Abstract

Jet and Heavy-Flavor Measurements in pp and Pb–Pb Collisions with ALICE

Salvatore Aiola

2019

Quantum Chromo-Dynamics (QCD) is the field theory that describes the nuclear interactions, responsible for holding together quarks and gluons inside the atomic nuclei. Despite significant progress made in over four decades of experimental and theoretical work since QCD was established, there remain many open questions, especially regarding the fragmentation process of quarks and gluons and the behavior of QCD in the high-temperature regime. Jets are produced from hard-scattered quarks and gluons as a consequence of the confinement property of QCD, that banishes the possibility of free quarks at ordinary temperatures. However, at high energy densities, like those achieved in ultra-relativistic heavy-ion collisions, QCD predicts a transition to a phase of free quarks and gluons, called the Quark-Gluon Plasma (QGP).

This thesis presents two measurements performed with the ALICE detector at the CERN Large Hadron Collider (LHC). Charm jets were tagged using D^0 mesons. Their cross section and fragmentation function in pp collisions at the center-of-mass energy $\sqrt{s} = 7$ TeV were measured and compared with theoretical predictions obtained with Monte Carlo generators based on QCD. A general agreement was found, confirming that we understand the general features of jet and heavy-flavor production in the framework of QCD. Another measurement was performed in Pb–Pb collisions at a center-of-mass energy per nucleon $\sqrt{s_{\mathrm{NN}}} = 2.76$ TeV. Jets were reconstructed and their yield compared to a pp reference measurement. A strong suppression was observed, which is interpreted as caused by energy loss of hard-scattered quarks and gluons in the QGP.

Jet and Heavy-Flavor Measurements in pp and Pb–Pb Collisions with ALICE

A Dissertation
Presented to the Faculty of the Graduate School
of
Yale University
in Candidacy for the Degree of
Doctor of Philosophy

by
Salvatore Aiola

Dissertation Director: John W. Harris

May 2019

Niuna cosa maggiormente dimostra la grandezza e la potenza dell'umano intelletto, né l'altezza e nobiltà dell'uomo, che il poter l'uomo conoscere e interamente comprendere e fortemente sentire la sua piccolezza. Quando egli considerando la pluralità de' mondi, si sente essere infinitesima parte di un globo ch'è minima parte d'uno degl'infiniti sistemi che compongono il mondo [...] si trova come smarrito nella vastità incomprensibile dell'esistenza; allora con questo atto e con questo pensiero egli dà la maggior prova possibile della sua nobiltà, della forza e della immensa capacità della sua mente, la quale, rinchiusa in sì piccolo e mènomo essere, è potuta pervenire a conoscere e intender cose tanto superiori alla natura di lui.

Nothing is more revealing of the greatness and power of human intellect, of the stature and nobility of man, than the ability of knowing, deeply understanding and feeling his own nothingness. When he, pondering the multitudes of worlds, considers himself as an infinitesimal part of a world, that is an infinitesimal part of one of the countless systems that make the universe, he finds himself lost in the incomprehensible vastness of the existence; it is then, in this precise act and thought, that he gives the greatest possible proof of his nobility, strength and immense capacity of his mind, that, limited in such a small and diminished individual, could come to know and understand things so much superior than its own nature.

Giacomo Leopardi, *Zibaldone di Pensieri*
The translation is mine.

Acknowledgements

A number of people have made this work possible. I will avoid making a long list of names, which would simply demean the unique and invaluable contribution that each person has given. I will only make few exceptions. The first exception is for John Harris and Helen Caines, my advisors and mentors at Yale, who trusted me in many ways and gave me an example of how to be a true scientist and a true teacher, which I hope one day to be able to imitate. Reina Maruyama and Ramamurti Shankar kindly read this thesis and contributed insightful questions and comments during the defense, something that I am truly thankful for. I would like to thank my wife, who has brought a new beginning and adventure in my life, teaching me once more that "the unexpected is the only hope"[1]. I am forever grateful to my parents, who made this whole adventure possible by giving me life, and who first introduced me to the vastness of the world around me, with few words and much practice. The last exception is for the Author of the Universe and all it contains, who entrusted us with the freedom and intellect to explore the universe and make the best use of it. As Pope Benedict XVI said in one occasion: "...the universe itself is structured in an intelligent manner, such that a profound correspondence exists between our subjective reason and the objective reason in nature. It then becomes inevitable to ask oneself if there might not be a single original intelligence that is the common font of them both"[2].

1. "Un imprevisto è la sola speranza", from the poem "Prima del viaggio" by Eugenio Montale.

2. Address Of His Holiness Benedict XVI to the Participants in the Forth National Ecclesial Convention. Verona, October 19th, 2006. `http://w2.vatican.va/content/benedict-xvi/en/speeches/2006/october/documents/hf_ben-xvi_spe_20061019_convegno-verona.html`.

Contents

Introduction

The Standard Model of Particle Physics is a paramount example of a theory based on a simple idea that is the ultimate explanation of a wealth of physical phenomena, from the nature of light and radio waves, to the nuclear decays, from the force that keeps the nuclei together, to the chemical bonds that form the molecules. Only the gravitational phenomena are left out of this comprehensive description of nature. Despite its undeniable elegance and success, there remain many open questions, more than can be listed in a single thesis – left alone being addressed. Why are there exactly three generations of matter particles (quarks and leptons)? Are there more? Why do particles have the mass that they have, and why is the mass of the top quark so much higher than the other quarks? What is the origin of the matter-antimatter asymmetry in the Universe? Does the strong nuclear force violate the charge-parity (CP) symmetry? If not, why? These questions point to the fact that, despite its great success, the Standard Model is *not* the *ultimate* theory. We know that the Standard Model is destined to be superseded, sooner or later, by a more complete theory that can give a natural and simple explanation to the questions that remain open, and perhaps include also a quantum theory of gravity. In the meantime, we must use the Standard Model as a guidance to formulate our questions and design our approach to try and answer them.

Within the Standard Model, a whole set of questions is related to the theory of strong interactions, Quantum Chromo-Dynamics (QCD). Despite the theory is well understood in its formal unfolding from a gauge invariant principle, some of its phenomenological consequences are still beyond our reach. These phenomenological aspects are related to two intriguing properties of QCD, which are a direct consequence of the $SU(3)$ gauge symmetry group: confinement and asymptotic freedom. Confinement is at the origin of the parton-hadron transition in the fragmentation process and of the internal structure of the hadrons. Its counterpart, asymptotic freedom, applies in processes occurring at small distances or involving a large momentum transfer; this is also the case of the high temperature and density regime where the QCD matter undergoes a transition of phase characterized by the presence of free quarks and gluons, called the Quark-Gluon Plasma (QGP). This exotic state of matter existed in the early Universe, a few microseconds after the Big Bang, when the conditions of density and temperature were those typical of the QGP formation.

This thesis is born in an effort to contribute to this quest. It attempts to do so by experimentally studying the properties of rare processes that occur in high-energy collisions: jet and heavy-flavor production. Jets are the result of QCD confinement; therefore studying their properties, and in particular how they fragment into hadrons, is crucial to progress our understanding of this aspect of the theory.

Jets and heavy-flavor particles are also excellent probes of the QGP. By smashing heavy ions at ultra-relativistic energies we create a small droplet of this exotic state of matter. Energetic partons (gluons or quarks), produced by the same heavy-ion collision, traverse the QGP and scatter multiple times through it. By means of measuring the modification that they undergo along this path we can infer the properties of the plasma itself. The experimental challenges of such a task become apparent once we consider the spatial and time constraints in which these phenomena occur: the dimensions of the QGP are about 12 fm and it lasts for $\sim 10^{-23}$ seconds before decaying into a gas of hadrons. Therefore its properties can only be inferred from the final state measured by the experimental apparatus at a much longer time scale.

An additional challenge comes from the complexity of the final state: the bulk of the particle production amounts to thousands of particles in a central Pb–Pb collision at the LHC. These challenges, and the solutions adopted to overcome them, will be discussed in the course of this thesis.

The thesis is organized as follows. A brief overview of the Standard Model of Particle Physics, which is at the heart of the physics being explored at the LHC, is given in Chapter 1. A particular emphasis is given to the topics related to the study of the QCD, and specifically its behavior in the regime of very high energy density and temperature. The LHC and the experimental apparatuses are machines of unprecedented complexity and precision, suitable to overcome the challenges of nuclear and particle physics. Both the accelerator complex and the ALICE apparatus are described in Chapter 2, focusing in particular on the subsystems relevant for the analyses presented in this thesis. Chapter 3 dives into the first measurement presented in this thesis: the p_{T}-differential cross section and fragmentation function of jets containing D^0 mesons in pp collisions at center-of-mass energy $\sqrt{s} = 7$ TeV. The analysis is described in detail and was developed roughly during the last three years of this PhD program, in the years 2015-2018. The challenges of reconstructing jets in heavy-ion collisions are discussed in Chapter 4, where the measurement of jet production in Pb–Pb collisions at center-of-mass energy per nucleon $\sqrt{s_{\mathrm{NN}}} = 2.76$ is presented. This is the first ALICE measurement of jet suppression using fully reconstructed jets. This analysis was initiated in 2012, immediately after the first Pb–Pb run with the fully-commissioned ALICE electromagnetic calorimeter[3]. The analysis was brought into a final publication in 2015. The results of both analyses are discussed in relation to theoretical models and other experimental results in Chapter 5. In Chapter 6 we will look ahead in the future of the LHC and ALICE. During the

3. During the 2010 Pb–Pb run, only a small portion (about 1/5) of the calorimeter was taking data.

Long Shutdown 2 (2019-2020) ALICE will undergo extensive upgrades, in preparation for the LHC Run-3 and beyond. These upgrades will allow the experiment to take data at a rate 150 times higher, opening the possibility of studying new and rarer probes, crucial to pin down the fundamental properties of the QGP, in terms of its transport properties and dynamical evolution. The emphasis on this Chapter is on the R&D performed at Yale for the upgrade of the Time Projection Chamber. The last Chapter concludes this thesis, summarizing the results obtained and proposing some pointers for future continuation.

Chapter 1

Physics at the Large Hadron Collider

1.1 The Standard Model

The Standard Model of Particle Physics is a theory describing three of the four forces of nature (electromagnetism, strong nuclear and weak nuclear) and all the visible matter in the Universe[1]. Figure 1.1 shows a schematic overview of the Standard Model. It includes three generations of leptons (electron, muon, tau) and three generations of quarks, that together constitute the "matter" particles (half-spin fermions); four interaction bosons (with spin 1); and the Higgs boson (with spin 0), responsible for the mass of all fundamental particles.

All the matter around us, as well as our bodies, are made of *up* and *down* quarks, held together inside the nuclei by *gluons*, and *electrons*, bound to the nuclei inside the atoms by the electromagnetic interaction mediated by *photons*. The matter particles belonging to the second and third generations have identical properties as those of their counterparts in the first generation, except for the mass. They are routinely produced in a variety of astrophysical phenomena (such as through the nuclear interactions in the Sun) or at human-made colliders. They are unstable and tend to

1. Dark matter and dark energy, which comprise more than 95% of the energy in the Universe by some estimates, are not contemplated by the Standard Model.

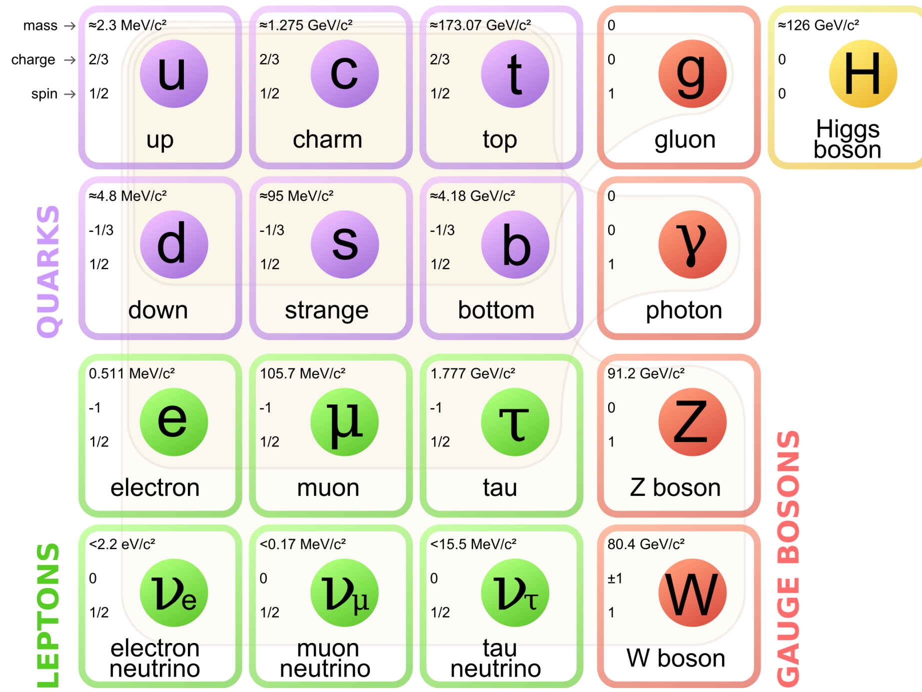

Figure 1.1: Standard Model of Particle Physics [1].

eventually decay into the lighter particles of the first generation.

The Standard Model is formulated through quantum field theories. Its Lagrangian is obtained combining the electro-weak (EW) theory and Quantum Chromo-Dynamics (QCD). The EW part is invariant under the local gauge group $SU_W(2) \times U_Y(1)$. The symmetry group forbids the presence of mass terms in the Lagrangian. The Higgs mechanism is responsible for a spontaneous symmetry breaking: even though the formulation of the Lagrangian maintains its symmetry under the gauge group, the state of minimum energy (ground or "vacuum" state) breaks the symmetry leading to the separation of the weak force from the electromagnetic force. When expanding the Lagrangian around the ground state, mass terms appear for the Z^0 and $W^{\pm}$ bosons, that are proportional to the interaction strength with the Higgs boson. No mass term is associated with the photon: in fact the electromagnetic force remains symmetric under $U_{em}(1)$, which is a copy of the original $U_Y(1)$ group. Using a similar mechanism, masses can be assigned also to the quarks and leptons, as interaction terms with the

Higgs.

The Standard Model has passed many experimental tests. In particular, experiments at the CERN Large Electron-Positron Collider (LEP) were able to test the theory of electro-weak interactions with an unprecedented and unsurpassed precision. The Higgs boson, the last building block of the Standard Model, was observed for the first time in 2012 by ATLAS and CMS at the CERN Large Hadron Collider (LHC) [2, 3]. This observation marked the first big success of the LHC, recognized by a Nobel Prize, which was conferred in 2013 to François Englert and Peter Higgs, who in the 1960s made the theoretical predictions about the long-sought boson.

1.2 Quantum Chromo-Dynamics

Quantum Chromo-Dynamics (QCD) is a non-abelian quantum field theory, invariant under the local gauge group $SU(3)$. From the symmetry group, it follows that there are three conserved charges, called *colors*, and eight carriers of the color charges, called *gluons*. They serve the same role as the photon in electromagnetism; however unlike the photon, which is electrically neutral, gluons carry color charge themselves. This particular property is crucial for the QCD phenomenology because it implies that gluons can interact with themselves.

The strength of the interactions is mediated by the QCD coupling constant α_s. As is typical for quantum field theories, cross section amplitudes of measurable physical processes are calculated in perturbation theory, where each interaction vertex contributes a factor $\sqrt{\alpha_\mathrm{s}}$. Because of the gluon self-coupling, higher-order contributions including gluon and fermion-antifermion loops are divergent. To overcome this limitation, a renormalization scale μ is introduced in the calculation. The renormalization group equation enforces the fact that any observable must be independent of μ. The

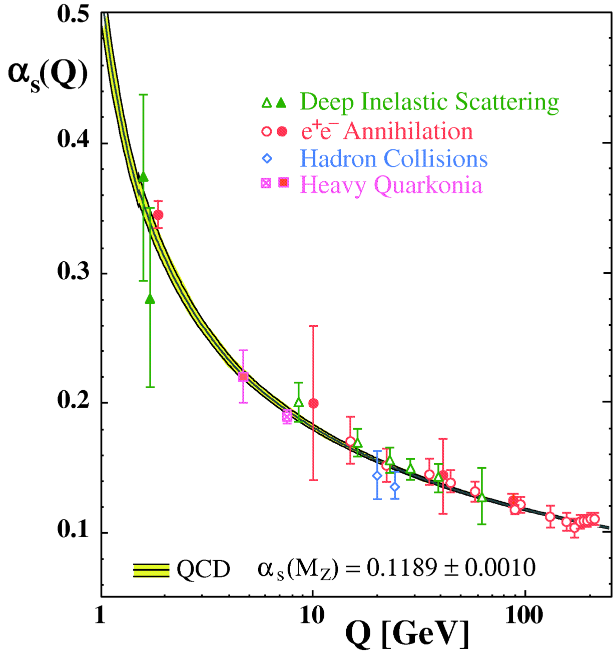

Figure 1.2: Summary of measurements of $\alpha_\mathrm{s}(Q)$ as a function of the respective energy scale Q. The curves are the QCD predictions for the combined world average value of $\alpha_\mathrm{s}(M_{\mathrm{Z}^0})$ [4].

solution of this equation implies a running coupling constant:

$$\alpha_\mathrm{s}(Q^2) = \frac{12\pi}{(11N_\mathrm{c} - 2N_\mathrm{f}) \log\left(\frac{Q^2}{\Lambda^2_{\mathrm{QCD}}}\right)}, \tag{1.1}$$

where $N_\mathrm{c} = 3$ is the number of color charges, N_f is the number of EW quark flavors[2] and $\Lambda_{\mathrm{QCD}} \approx 1$ GeV is the QCD scale parameter, which can be related directly to μ. The coupling "constant" α_s is shown as a function of the momentum transfer Q in Fig. 1.2, where it is compared with several independent experimental estimates spanning a wide range of Q.

There are two phenomenological consequences of the non-abelianity of QCD.

2. $N_\mathrm{f} = 6$ if all quarks are accessible, i.e. $\mu > m_\mathrm{q}$ for all quark masses m_q; otherwise the number of flavors is reduced excluding those quarks with mass larger than the energy scale of the process.

Confinement From Eq. 1.1 we see that as Q^2 approaches Λ^2_{QCD} from above, α_{s} increases and exceeds unity. At large distances, or - equivalently - at low momentum transfer in interactions mediated by QCD, the existence of free quarks is banished: trying to separate two quarks from each other, for instance in Deep-Inelastic Scattering (DIS) experiments, apparently results in an increase of the QCD field's energy. This can be interpreted as a consequence of gluon self-interaction, which results in an "anti-screening" effect (opposite of what happens in Quantum Electro-Dynamics). The empty space between the two separating quarks is filled with quantum "virtual" quark pairs and gluons and at a certain point the energy of the system is large enough that it becomes energetically more favorable to create a real quark-antiquark pair than moving the two quarks further apart (i.e. transforming some of their kinetic energy into new particles). The initial quarks "dress" up with other quarks to build hadrons. These hadrons exhibit no net color charge to the outside. For this reason quarks and gluons are never observed freely, but always bound inside a hadron. The whole process is called *hadronization* and it gives the theoretical grounds to explain hadron production in all kinds of particle collisions (ep, $\mathrm{e}^+\mathrm{e}^-$, pp, ...). In particular, it is the basis of the *jet* production in high-energy collisions, where, after a high momentum transfer between two partons occurs, the hadronization process gives rise to a collimated spray of hadrons.

Asymptotic freedom For large Q^2, Eq. 1.1 shows that α_{s} tends to zero. QCD predicts that the interaction between quarks and gluons becomes weaker as they come close together, or - equivalently - at large momentum transfer. Also this feature is confirmed by experimental observations: the dynamics of DIS of electrons off a proton, reveal that the electron scattering occurs at point-like and massless constituents, the quarks, rather than at a homogeneous object with the size of a proton. Apparently, at sufficiently high momentum transfers, quarks behave like free or weakly bound point-like particles.

1.2.1 Jets and Heavy-Flavor Production

We have seen that jet production is one of the direct consequences of QCD confinement. In this Section, the techniques used to calculate the jet cross section in the perturbative expansion of QCD (pQCD) will be briefly outlined. The fundamental idea comes from the QCD factorization theorem [5], which states that the perturbative terms of the calculation can be factorized from the non-perturbative ones because they occur at different energy scales. Under this assumption the hadron or jet inclusive production cross section in pp collisions takes the form:

$$\mathrm{d}\sigma^{\mathrm{pp}\to\mathrm{h/jet+X}} \propto f_{\mathrm{a}}(x_1, Q^2) \otimes f_{\mathrm{b}}(x_2, Q^2) \otimes \mathrm{d}\sigma^{\mathrm{ab}\to\mathrm{c+X}}(x_1, x_2) \otimes D_{\mathrm{c}\to\mathrm{h/jet}}(z, \mu^2). \quad (1.2)$$

The term $\mathrm{d}\sigma^{\mathrm{ab}\to\mathrm{c+X}}(x_1, x_2)$ represents the cross section for the production of parton c from the scattering of partons a and b; it is calculable in perturbative QCD at any given order in α_{s}. The two non-perturbative terms are:

- $f_{\mathrm{a}}(x_1, Q^2)$: the parton distribution function (PDF). It represents the probability of finding parton a inside the proton with momentum fraction $x_1 = p_{\mathrm{a}}/p_{\mathrm{p}}$.

- $D_{\mathrm{c}\to\mathrm{h/jet}}(z, \mu^2)$: the fragmentation function (FF). It represents the probability that parton c fragments into a final state hadron or jet with momentum fraction $z = p_{\mathrm{h/jet}}/p_{\mathrm{c}}$.

The PDF appears twice in Eq. 1.2 for parton a in the first proton and for parton b in the other proton. The final cross section must be summed over all possible combinations of a, b and c. The FF depends on the hadron species or on the jet definition (see Appendix A for an overview of jet definitions). They must be determined experimentally at a particular energy scale: PDFs are typically determined in Deep

Inelastic Scattering (DIS) of electrons off protons or nuclei, while the most precise FFs come from jet measurements in high-energy e^+e^- collisions. Both the PDF and the FF are universal, but must be evolved to the energy scales of interest, indicated in Eq. 1.2 with Q^2 and μ^2, respectively. Even though they are non-perturbative, their evolution to a different energy scale is calculable in perturbation theory. This evolution is performed via the DGLAP equations, named after the initials of their authors [6–8]. In the absence of collective nuclear effects (such as those discussed in the next Section), the above considerations are fully valid also for proton-nucleus (p–A) and nucleus-nucleus (A–A) collisions, provided that the proton PDFs are replaced with the corresponding nuclear PDFs.

For the heavy-flavor production similar considerations apply with one crucial difference: in addition to the scale set by the parton momentum transfer, there is an additional scale given by the mass of the outgoing quark. Several approaches based on pQCD exists to deal with the presence of both scales in the calculation of the heavy-flavor cross section. FONLL (Fixed-Order plus Next-to-Leading-Log) [9–11] and GM-VFNS (General-Mass Variable-Flavor-Number Scheme) [12] rely both on the collinear-factorization approach. FONLL is a method to obtain the p_{T} spectrum of heavy-flavour production with Next-to-Leading-Order (NLO) accuracy in α_{s}, and with resummation of next-to-leading logarithms of $p_{\mathrm{T}}/m_{\mathrm{q}}$, where m_{q} is the quark mass. GM-VFNS combines the virtues of the Fixed-Flavor-Number Scheme (FFNS) [13], which is reliable close to the threshold of heavy-quark production, and the Zero-Mass Variable-Flavor-Number Scheme (ZM-VFNS) [14], which neglects the heavy-quark mass and is valid for $p_{\mathrm{T}} \gg m_{\mathrm{q}}$. In this way it is possible to obtain a cross section valid for both regimes.

1.3 The Quark-Gluon Plasma

The first accelerating machines able to provide ultra-relativistic nucleus-nucleus collisions became available in the early eighties: at CERN the Super Proton Synchrotron (SPS) and at BNL the Alternating Gradient Synchrotron (AGS). Both accelerators were first employed as proton colliders, unveiling milestone discoveries, like the electroweak bosons Z^0 and $W^{\pm}$ at the SPS and the charm quark at the AGS. Successively, they were modified to collide nuclei in fixed-target experiments. These experiments provided the first tantalizing evidence of a new state of matter, the *Quark-Gluon Plasma* (QGP).

Indeed models predict that when the nuclear matter is heated up to a limiting critical temperature $T_{\mathrm{c}} \approx 160$ MeV, a transition of phase occurs, characterized by new degrees of freedom. Although these ideas were proposed even before QCD was established [15, 16], the quantum field theory of strong interactions provides a more natural theoretical framework to explain this new state of matter, where quarks and gluons, which are usually bound inside hadrons, are deconfined and free to move in the fireball produced in heavy-ion collisions [17, 18]. In fact, at very high energy densities, like those achieved in ultra-relativistic heavy-ion collisions, quarks and gluons are packed together in a small volume and exchange large momenta: as discussed above, asymptotic freedom sets in and quarks are free.

As shown in Fig. 1.3, we can characterize the state of the hadronic matter by a phase diagram in the (T, μ_{B}) plane, where T is the temperature of the system expressed in MeV and μ_{B} is the baryonic chemical potential[3]. The QGP phase can be reached either by increasing μ_{B}, a condition perhaps found in the core of neutron stars, or by increasing the temperature, as done at ultra-relativistic heavy-ion colliders

3. The baryonic chemical potential μ_{B} is defined as the change in the energy E of the system when the total baryonic number N_{B} ($\equiv$ baryons – antibaryons) is increased by one unit: $\mu_{\mathrm{B}} = \frac{\partial E}{\partial N_{\mathrm{B}}}$.

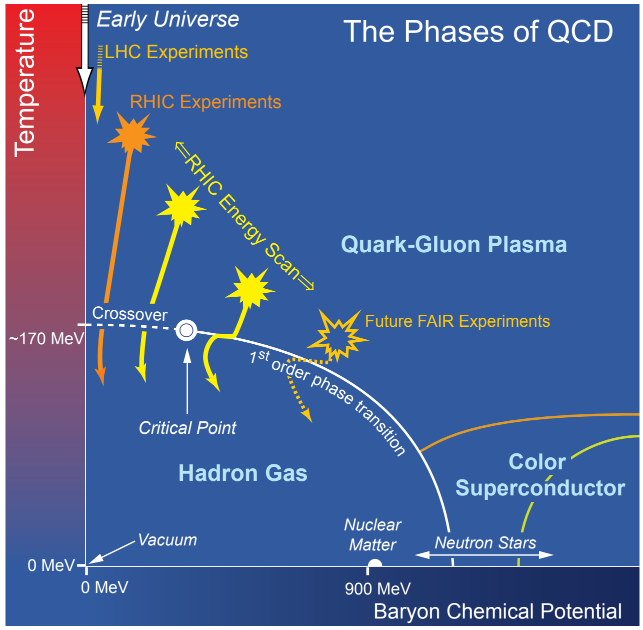

Figure 1.3: Schematic QCD phase diagram in the (T, μ_B) plan. The solid lines represent the phase boundaries for the indicated phases. The solid circle represents a possible critical point. Possible trajectories for systems moving in the QGP phase at different accelerator facilities are also shown. Source: [19] (with modifications).

(in this case $\mu_{\mathrm{B}} \approx 0)^4$.

The evolution of a nucleus-nucleus collision is sketched in Fig. 1.4. The two nuclei, traveling in opposite directions along parallel trajectories, appear to be compressed along the direction of motion because of the relativistic Lorentz contraction. After a pre-equilibrium phase, dominated by the initial fluctuations in the partonic structure of the nuclei, thermalization occurs: this is where the QGP degrees of freedom are expected to set in. This phase is dominated by a rapid hydrodynamic expansion due to its high internal pressure. The hydrodynamic behavior has been confirmed by experimental evidence that indicate that the momentum distributions of the final-state particle are compatible with the expansion of a nearly perfect liquid. The energy density reduces, until the temperature drops again below T_{c}, transitioning back to a hadron gas phase, in which hadrons interact with each other through both elastic and

4. This is also the case for the QGP phase of the early Universe.

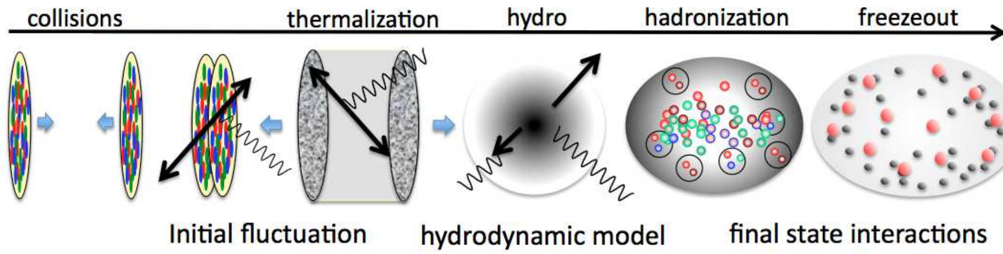

Figure 1.4: Phases of a ultra-relativistic nucleus-nucleus collision. Source: [20].

inelastic processes. Eventually the temperature decreases at a point where inelastic interactions between hadrons stop. The particle species ratios are fixed at this point and we refer to this transition as *chemical freeze-out*. After further expansion and cooling, the elastic interactions stop as well, fixing the momentum and energy of all particles. We refer to this phase as a *thermal freeze-out*. After this point, particles travel through space, until they are detected, without further interactions.

1.3.1 Implications for Cosmology and Astrophysics

The study of the QGP has also some astrophysical and cosmological interests.

The QGP in the evolution of the Universe The early stages of the evolution of the Universe are described by the well established Big Bang scenario, which is based on a number of empirical observations. Hadrons were formed in the quark-hadron transition when the Universe was about 10^{-5} seconds old. Before this transition, all matter in the Universe was contained in a small region with an enormous density, compatible with the formation of a QGP [21]. Among the many phase transitions that have occurred in the evolution of the Universe, this is the only one that is reproducible in a laboratory with the current technology.

Neutron stars In their last phase, very heavy stars can undergo an extreme compression due to gravity. This happens after they have used all the available nuclear combustion and the gravitational pressure is not balanced by the radiation pressure anymore. In this phase electrons are captured by protons in the core of the star, through the inverse β decay. The density of the core of a neutron star is enormous ($\sim 10^{15}$ g/cm^3), which means that the energy density inside a neutron star could be high enough for a QGP to form [22].

1.3.2 Early Experimental Observations

The Quark-Gluon Plasma is an unstable phase of matter, evolving into ordinary hadrons in a time scale of few fm/c. It is thus impossible to study this phase of the matter directly. Its existence is inferred by the measurement of the final-state particles generated by the cooling down of the hot medium.

Strangeness enhancement

The temperature of the QGP is expected to be above 160 MeV, which is greater than the mass of the strange quark ($m_\mathrm{s} \approx 96$ MeV). In addition, a large number of gluons are present in the QGP. As a consequence, thermal production of s quarks via the gluon fusion process ($\mathrm{gg} \rightarrow \mathrm{s\bar{s}}$) is significantly enhanced in the QGP [23, 24]. This is one of the first signatures of the QGP to be observed in heavy-ion collisions at the SPS energies [25], later confirmed at RHIC [26] and LHC [27, 28].

Quarkonia

Bound states of quark-antiquark pairs are known as *quarkonia*. The J/Ψ is one of the lowest energy states of a bound $\mathrm{c\bar{c}}$ pair[5]. J/Ψ suppression was predicted [29] at SPS energies as a consequence of the screening of the color field in the QGP state, which interferes with the resonance interaction of the $\mathrm{c\bar{c}}$ pair. This signature was

5. It is the lowest energy state with the quantum numbers that allow a decay into a di-lepton final state.

first observed at the SPS [30]. This observation was replicated also at RHIC [31, 32] and at the LHC [33, 34]; however the phenomenology of the J/Ψ in the QGP turned out to be more complex than initially thought, because of the possibility of thermal recombination of $c\bar{c}$ pairs produced in two incoherent high-momentum scatterings [35, 36]. These findings have increased the interest in the study of quarkonia production in the presence of a QGP.

1.3.3 A new energy regime: RHIC and LHC

The results of the SPS program at CERN, particularly strangeness enhancement and J/Ψ suppression, brought convincing evidence for a new state of matter, that pushed CERN to issue a press release on the subject in 2000 [37].

In the meantime, the Relativistic Heavy-Ion Collider (RHIC) at BNL was starting operations, colliding gold ions at center-of-mass energies ranging from 19.6 GeV to 200 GeV per nucleon. In 2009 the Large Hadron Collider (LHC) at CERN started its experimental effort, which included a rich heavy-ion physics program.

The much larger center-of-mass energy allowed the RHIC and LHC experiments to provide solid results on the phenomenology of ultra-relativistic heavy-ion collisions, confirming the early observations of the expected signatures of the QGP formation [38–43]. More importantly, new, yet unexplored, observables became available, opening a new era of measurements in ultra-relativistic heavy-ion physics.

Hard Probes[6]

In the new energy regimes of RHIC and LHC, the production cross section of high p_{T} partons is considerably larger, making it possible to use these processes as probes of the QGP. Because they involve a large momentum transfer, hard partons are produced

6. Hard probes are particles produced in parton scatterings involving large momentum transfers and that can be used to probe the medium. They typically include jets and heavy-flavor particles.

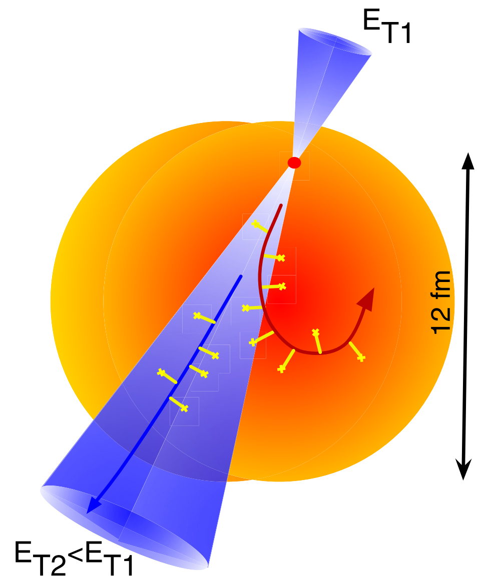

Figure 1.5: Hard scattered partons interact with the QGP generated in ultra-relativistic heavy-ion collisions.

in very short time-scales, before the formation time of the QGP. This property makes hard-scattered partons excellent probes of the QGP, because they witness the full dynamical evolution of the medium.

Two such hard-scattered partons are pictured in Fig. 1.5, immersed in the hot and dense QGP. Energy-momentum conservation requires that the partons coming out of the hard scattering are emitted back-to-back with the same momentum. The hard scattering can happen at any spatial point of the nuclear overlap region: in the example illustrated by Fig. 1.5, parton 1 is at the edge of the QGP surface and is not much affected by it; on the other hand parton 2 has to travel a longer path through the medium, which interferes with its parton shower.

Parton energy loss in the medium occurs via two mechanisms, which have different dependence on the path length and parton species [44]. They both depend on a parameter called the transport coefficient:

$$\hat{q} \propto \frac{1}{\lambda} = \frac{1}{\rho\sigma}, \tag{1.3}$$

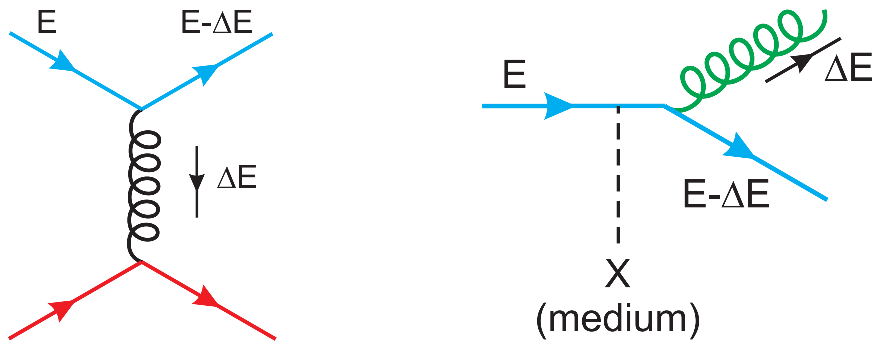

Figure 1.6: Diagrams for collisional (left) and radiative (right) energy losses of a quark of energy E traversing a quark-gluon medium [44].

where λ is the mean free path of a parton traveling through the medium, ρ is the medium density and σ is the cross section of the interaction of the parton with the medium.

Collisional energy loss Elastic scatterings with the medium constituents cause a net energy transfer from the hard parton to the medium, as shown in the left diagram of Fig. 1.6. For both quarks and gluons the average collisional energy loss takes the form:

$$\langle \Delta E_{\mathrm{coll}} \rangle \propto C_{\mathrm{R}} \alpha_{\mathrm{s}} \hat{q} L \log E, \tag{1.4}$$

where the color charge $C_{\mathrm{R}} = 4/3$ for quarks and $C_{\mathrm{R}} = 3$ for gluons; L is the path length of the parton through the QGP; and E is the initial energy of the parton.

Radiative energy loss The dominant mechanism of energy loss of a fast parton (gluon or light quark) in a QCD environment is of radiative nature, by medium-induced multiple gluon emission, as depicted by the right diagram of Fig. 1.6. For light quarks and gluons the average collisional energy has been calculated by various authors in different approximations; however we can extract the common features in

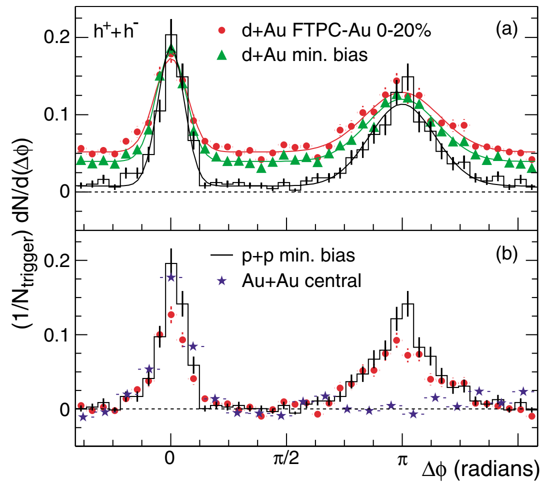

Figure 1.7: (a) Efficiency-corrected two-particle azimuthal distributions for minimum bias and central d–Au collisions, and for pp collisions. (b) Comparison of two-particle azimuthal distributions for central d–Au collisions to those seen in pp and central Au–Au collisions. The respective pedestals have been subtracted [45].

the formula:

$$\langle \Delta E_{\mathrm{rad}} \rangle \propto C_{\mathrm{R}} \alpha_{\mathrm{s}} \hat{q} L^2 \log E. \tag{1.5}$$

This expression differs from the collisional energy loss because of the L^2 dependence.

Due to kinematic constraints, gluon emission from a heavy quark differs from that of a massless parton, already in the vacuum. The radiation is suppressed at angles smaller than the ratio of the quark mass to its energy. In the medium, the reduction of the radiative energy loss for charm and beauty quarks has been estimated to be of the order of 25% and 75%, respectively, for momenta of the quarks comparable to their mass [44].

Experimental results Since jet measurements in heavy-ion collisions must contend with the large background coming from the underlying event (see Section 4.4), jet studies at RHIC and LHC have initially focused on high-p_{T} hadrons, used as proxies for the jets. One of the first and most iconic measurement of jet quenching, is the observation of the disappearance of the away-side ($\Delta\phi \approx 180^{\circ}$) peak from hadron-

hadron correlations in Au–Au collisions at $\sqrt{s_{\mathrm{NN}}} = 200$ GeV [45], shown in Fig. 1.7. The Au–Au result is compared with similar measurements performed in pp and d–Au collisions, that show a prominent peak in the away-side region, expected from the back-to-back jet kinematics. Another classical signature of jet quenching measured both at RHIC and LHC is the suppression of the overall yield of hadrons in A–A collisions compared to expectations from pp collisions scaled to account for the number of binary nucleon-nucleon collisions [46–49]. More recently, full jet reconstruction was made possible due to the advancement of the experimental and analysis techniques, particularly at the LHC, which benefits from a significantly larger jet rate thanks to the higher center-of-mass energy. Energy imbalance in the jet-jet and photon-jet systems was reported early on after the first Pb–Pb run at the LHC [50–52]. In more recent years the focus has shifted towards an understanding of the modification of the jet internal substructure [53, 54], which promises to bring more quantitative insights on the nature of jet quenching [55].

Chapter 2

The LHC and the ALICE Apparatus

2.1 The Accelerator Complex

The *Large Hadron Collider* (LHC) [56–58] at CERN is the world's largest particle collider. It is housed in a tunnel with a circumference of about 27 km, between 50 and 175 m beneath the France-Switzerland border near the city of Geneva. The tunnel was built in the 1980s and was used until the late 1990s to house the Large Electron-Positron Collider (LEP). The construction of the LHC took about 10 years. It started in the late 1990s, during the decommissioning phase of LEP, and was completed in 2008.

Figure 2.1 shows a schematic view of the LHC. Particles travel in opposite directions in two parallel beam pipes, intersecting at four interaction points (IPs), where experiments are located to detect and measure the collisions: ALICE [59], ATLAS [60], CMS [61], LHCb [62].

2.1.1 Injection chain

Protons and ions undergo several pre-acceleration steps before being injected into the LHC. The first accelerator step happens in the linear accelerator (Linac) 2. The Linac

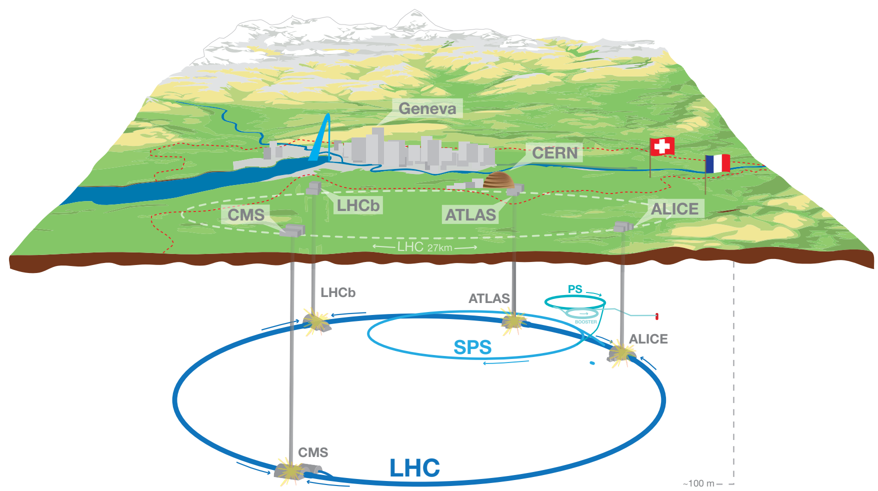

Figure 2.1: 3D schematic view of the LHC accelerator complex and experiments. Source: CERN graphic service, `https://cds.cern.ch/record/1708849`.

uses radio frequency cavities to accelerate protons to an energy of 50 MeV. Proton beams are passed to the Proton Synchrotron Booster (PSB) in which they travel in closed orbits and are focused as well as accelerated to an energy of 1.4 GeV. The proton beams continue to the Proton Synchrotron (PS) where they are accelerated further to 25 GeV, an energy suitable for injection into the Super Proton Synchrotron (SPS). The SPS is the last acceleration step before injection into the LHC, at which point protons have reached an energy of 450 GeV. They are injected in bunches, spaced by 25 ns (or multiple thereof) for a maximum of $2,808$ bunches when operating at full luminosity in pp collision mode. Ion beams follow a similar injection chain, except for the first two steps. A different linear accelerator, Linac 3, is used to accelerate ions, originating from the source at an energy of a few keV/n (per nucleon), to 4.2 MeV/n. Then, they are injected into the Low Energy Ion Ring (LEIR), where they are accelerated to 72 MeV/n. After that, they are injected into the PS and follow the same injection chain as the protons. Ions are progressively stripped of their electrons during the various acceleration steps; before being injected into the SPS they are fully ionized (bare nuclei). When injected into the LHC, ions have the same magnetic rigidity of protons with 450 GeV; for Pb ions this corresponds to an energy of 177 GeV/n. During Run-1 the ion bunch separation was 200 ns.

2.1.2 Magnets

The superconducting magnets, made of copper-clad niobium-titanium, are at the heart of the LHC technology masterwork. The cryogenic facility uses approximately 96 tonnes of superfluid helium-4 to maintain the magnets at their operating temperature of 1.9 K. Particles are kept in their circular trajectories around the LHC thanks to the magnetic field generated by $1,232$ superconducting dipole magnets. At the highest energy achieved during the LHC Run-2 (6.5 TeV for proton beams) the dipole magnets generate a magnetic field of 7.7 T. In addition, 858 superconducting quadrupole and higher-multipole magnets serve the purpose of keeping the beams tightly focused and provide other optical corrections to the orbits.

2.1.3 Radio Frequency System

Acceleration in the LHC is provided through 16 radio frequency (RF) cavities. A pulsating voltage, synchronized with the beam revolution frequency, is applied to the cavities. The RF cavities are synchronized such that if the dipole magnets are kept at fixed current no net acceleration is achieved. Particles that are slightly late or early to the RF cavities are accelerated and decelerated at each passage, keeping their momentum oscillating around the nominal value. By smoothly increasing the magnetic field provided by the dipole magnet, the beam particles follow a shorter path, arriving earlier to the RF cavities. This time shift will cause the particles to receive a small acceleration at each passage.

Collision system	Years	$\sqrt{s}$ (TeV)
Run-1		
pp	2009	0.9
	2010, 2011	7
	2011	2.76
	2012	8
Pb–Pb	2010, 2011	2.76
p–Pb	2012[1], 2013	5.02
Run-2		
pp	2015-2018	13
	2015, 2017	5.02
Pb–Pb	2015, 2018[2]	5.02
p–Pb	2016	5.02, 8
Xe–Xe	2018[3]	5.44

Table 2.1: LHC Run-1 and Run-2 operations.

2.1.4 Operational Phases

The LHC started operations in September 2008. A serious accident occurred during the first magnet ramp up. Subsequent reparations and new quality assurance checks on all electrical connections between the magnets took another full year. After this initial false start, the LHC has been operating with excellent performance, in some cases exceeding design expectations [63]. The first operational phase of the LHC (Run-1) started in November 2009 and was concluded in February 2013. In this first phase the LHC successfully provided pp, p–Pb and Pb–Pb collisions. Between 2013 and 2015 the LHC operations were stopped to allow for upgrades to the machine and to the four experiments (Long Shutdown 1, or LS1). Run-2 started in April 2015 and is scheduled to extend until the end of 2018. Table 2.1 shows details of the LHC operations in Run-1 and Run-2. After Run-2, another 2-year stop is foreseen (LS2)

1. Pilot run.

2. Planned for November 2018.

3. Single 8-hour run.

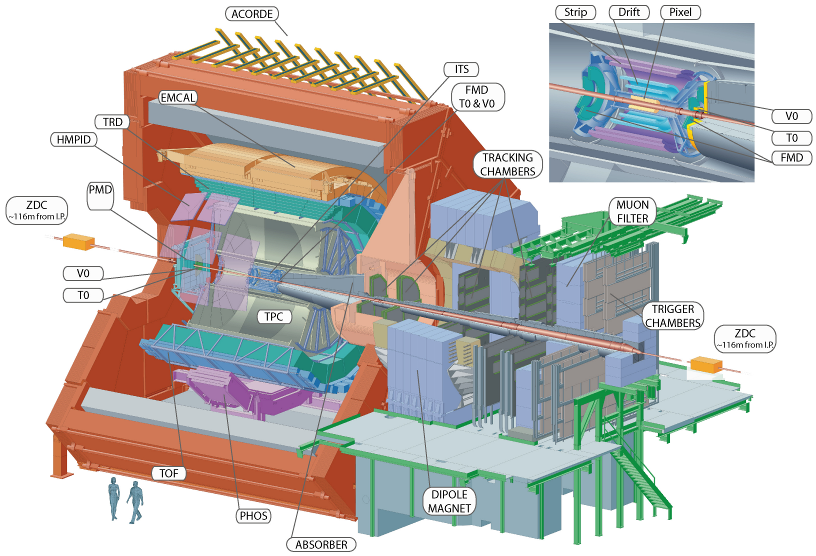

Figure 2.2: 3D schematic view of the ALICE detector during the LHC Run-1 [64]. Central-barrel detectors are visible inside the red solenoid magnet; the muon tracking station is on the right side. In the upper-right corner a zoomed inlay of the ITS is visible.

to allow for more upgrades, before the third operational phase, which is scheduled to start in 2021.

2.2 A Large Ion Collider Experiment

ALICE (*A Large Ion Collider Experiment*) [59, 64] is the experiment dedicated to the study of heavy-ion collisions at the LHC. Figure 2.2 shows a schematic view of the ALICE detector during the LHC Run-1. ALICE is a complex experiment made of several independent detector sub-systems that are operated synchronously. Each sub-detector is labelled in Fig. 2.2.

The main detectors are located in the central barrel, immersed in a moderate magnetic field (0.5 T), and covering the mid-rapidity region ($|\eta| \lesssim 1$). The Inner Tracking System (ITS) consists of six layers of silicon detectors and it is the closest to the interaction point (IP); it provides the first space points of the charged-particle tracks and it is crucial for the determination of the primary and secondary vertices.

The Time Projection Chamber (TPC) is a large-volume gaseous detector surrounding the ITS and serves as the main ALICE tracking detector. Both the ITS and the TPC have excellent particle identification (PID) capabilities via the measurement of the specific energy loss $\mathrm{d}E/\mathrm{d}x$. On the outside of the TPC, there are two full-azimuth PID detectors: the Transition Radiation Detector (TRD), used for electron identification and the Time-Of-Flight (TOF) detector, which provides pion, kaon and proton identification. ALICE has two electromagnetic calorimeters: the Photon Spectrometer (PHOS), a small-acceptance ($|\eta| < 0.12$, $220° < \phi < 320°$) high-granularity detector designed for the precise measurement of photons, and the Electromagnetic Calorimeter (EMCal) which has larger acceptance ($|\eta| < 0.7$, $80° < \phi < 187°$) and is used also for jet reconstruction, in addition to the measurement and identification of electrons, photons and π^0. A third calorimeter called DCal ($|\eta| < 0.7$, $253° < \phi < 320°$), which uses the same technology as that of the EMCal, was added during the LS1 on the opposite side of the EMCal to allow for jet correlation measurements. The High-Momentum Particle Identification Detector (HMPID) is a single-arm detector in the central region and uses the measurement of the Cherenkov light to provide PID of hadrons up to $3 - 5$ GeV/c depending on the particle species.

Additional detectors located at forward rapidity are complementary to the central detectors for characterizing the collision and providing interaction triggers. The T0 detector, consisting of two arrays of Cherenkov counters, measures the starting time of a collision (with a fixed time delay), which is then fed back to the TOF to calculate particles' time-of-flight. Two arrays of scintillators compose the V0 detector, which is used to provide interaction triggers, as well as to determine the geometry of the Pb–Pb collision (centrality and reaction plane). The Zero-Degree Calorimeter (ZDC), sitting at 113 m away from the IP, is used only in p–Pb and Pb–Pb collisions to detect the spectators (nucleons not participating in the collision). The Photon Multiplicity Detector (PMD) and Forward Multiplicity Detector (FMD), measure the photon

Detector	Pseudo-rapidity	Technology	Main purpose
SPD	$\|\eta\| < 2.0$	Si pixel	tracking, vertex
SDD	$\|\eta\| < 0.9$	Si drift	tracking, PID
SSD	$\|\eta\| < 1.0$	Si strip	tracking, PID
TPC	$\|\eta\| < 0.9$	gas drift+MWPC	tracking, PID
TOF	$\|\eta\| < 0.9$	MRPC	PID
EMCal	$\|\eta\| < 0.7$	Pb+scint.	$e^{\pm}$, γ, jets
V0	$2.8 < \eta < 5.1$, $-3.7 < \eta < -1.7$	scint.	trigger, vertex, multiplicity
T0	$4.6 < \eta < 4.9$, $-3.3 < \eta < -3.0$	quartz	trigger, vertex, time
ZDC	$\|\eta\| > 8$	W+quartz	forward neutrons
	$6.5 < \eta < 7.5$	brass+quartz	forward protons

Table 2.2: List of the ALICE detector subsystems relevant for the jet and heavy flavor measurements during the LHC Run-1. All detectors have full azimuthal coverage, except the EMCal which covers $80^{\circ} < \phi < 187^{\circ}$.

multiplicity and the charged-particle multiplicity, respectively, in the forward-rapidity region.

Finally, a muon spectrometer (MCH) is used to detect and identify muons to study open heavy flavor and quarkonia. It covers a pseudo-rapidity range of $-4.0 < \eta < -2.4$, and consists of five components: an absorber, a dipole magnet, tracking chambers, a muon filter and trigger chambers (MTR).

For the jet measurements, the charged constituents are detected by the tracking system (ITS and TPC); the EMCal is used to measure the neutral constituents that shower in it, particularly π^0s. For the D-meson reconstruction, the PID of the decay products is provided by the TPC $\mathrm{d}E/\mathrm{d}x$ and by TOF; ITS is used to reconstruct the decay topology, through the determination of the primary and secondary vertices. The trigger is provided by the SPD and the V0 for pp collisions; for Pb–Pb collisions the ZDC is used in addition. Table 2.2 lists the ALICE detector subsystems relevant for the jet and heavy-flavor analyses presented in this thesis. They will be described further in the following Sections.

2.2.1 The Tracking System

The Inner Tracking System

The working principle of semiconductor detectors relies on the formation of a diode junction. A pn-junction is created by the juxtaposition of a p-type with an n-type semiconductor. Without the application of any voltage, there is an initial diffusion of holes into the n-region and electrons into the p-region. This generates an electric field gradient across the junction. The diffusion process of holes and electrons stops once an equilibrium is reached due to the presence of the electric field itself. The depletion zone corresponds to the region across the pn-junction where there is an electric potential gradient. By applying an external reverse-biased voltage, a diode can be fully depleted of free carriers. This is the typical working state of a silicon detector. When a charged particle traverses the diode, electron-hole pairs are liberated and swept out by the electric field. An electric current signal proportional to the ionization can be extracted using external electric contacts on either side of the pn-junction.

The ITS is made of six cylindrical layers, covering the central rapidity range ($|\eta| < 0.9$). Figure 2.3 shows a 3D layout of the ITS.

Silicon Pixel Detector The two innermost layers are located at an average distance of 3.9 cm and 7.6 cm from the beam axis, respectively. They operate in a region where the track density is the highest, 50 tracks/cm^2, and the design of the SPD takes this condition into account, including its high radiation levels. The SPD is made from hybrid silicon pixels in the form of two dimensional matrices of reverse-biased diodes. In total, there are 9.8 million pixel cells, which ensures large acceptance coverage and high granularity. The spatial precision is 12 and 100 μm in the directions transverse and longitudinal to the beam, respectively. The average amount of material experienced by a straight charged particle following a trajectory perpendicular to the SPD is about 1% of a radiation length per layer. The read-out of the SPD is logical,

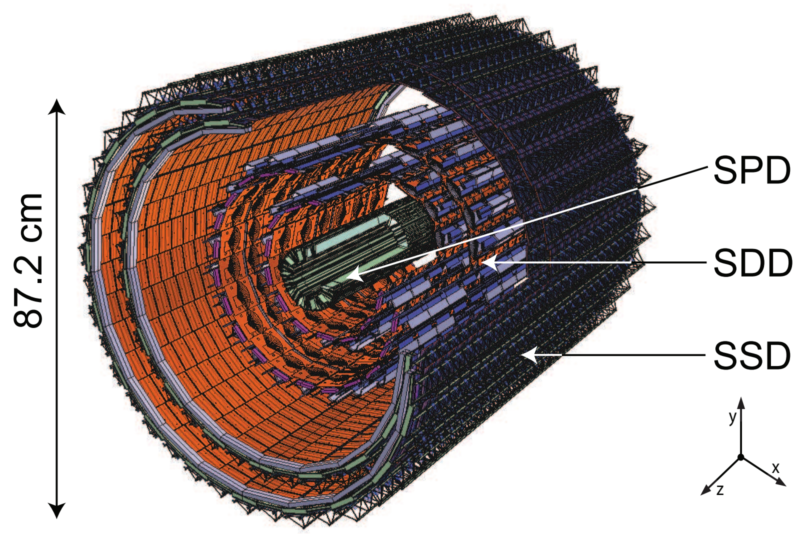

Figure 2.3: 3D layout of the ITS. Source: [65].

therefore it does not provide any information for the energy loss measurements.

Silicon Drift Detector The two intermediate layers of the ITS sit at average radii of 15.0 cm and 23.9 cm, respectively. Strips of p^+-type silicon (+ stands for heavily doped material) are attached to the bulk of n-type silicon on both sides. The p^+ strips fully deplete the detector volume and generate an electric drift field parallel to the surface. The sensitive volume is divided into two regions by the central cathode strip with a nominal bias voltage of -2.4 kV. When a charged particle goes through the sensitive volume, pairs of electrons and holes are produced. The holes are collected by the nearest p^+ electrode, while the electrons are forced into the middle plane and drift to the edge of the detector. An array of anodes made from n^+ pads along the edge collects the electrons and sends the signals to front-end electronics. The coordinate perpendicular to the drifting direction is reconstructed as the centroid of the collected charges in all the anodes (electrons spread over multiple anodes due to diffusion). The drift time of the charge is used to determine the spatial coordinate along the drift direction, given a fixed drift velocity. In this way, a silicon drift detector can measure two coordinates of the passing particle. Furthermore, the signal measured by the SDD is proportional to the energy deposited by the particles, making it possible to use it to measure the specific energy loss $\mathrm{d}E/\mathrm{d}x$. The average spatial resolutions along the azimuthal direction (drift direction) and that along the beam direction (anode axis) are $35\,\mu$m and $25\,\mu$m, respectively. The material budget amounts to 1.13% of a radiation length per layer.

Silicon Strip Detector The two outermost layers of the ITS are located at average radii of 38 and 43 cm. The fundamental sensor of the SSD is made of n-type bulk, where p^+-type and n^+-type silicon strips are implanted on each side. Electrons and holes generated by the passage of a charged particle are collected at the n^+-type and p^+-type strips, respectively. Signals are produced and collected on both sides, which can be used to reduce fake signals. The two types of strips do not run parallel, but rather at an angle of 35 mrad. This arrangement makes it possible to measure the two spatial coordinates. The average spatial resolutions along the azimuthal direction (perpendicular to the strips) and that along the beam direction (along the strips) are $20\,\mu$m and $830\,\mu$m, respectively. The energy deposited by the particles is measured as well. The material budget amounts to 0.8% of a radiation length per layer.

The Time Projection Chamber

The TPC is the main tracking detector. It provides tracking of charged particles, momentum measurement, particle identification via $\mathrm{d}E/\mathrm{d}x$ and secondary vertex determination of strange particle decays. A 3D layout of the TPC is shown in Fig. 2.4. It is 510 cm long, with an inner radius of 90 cm and an outer radius of 250 cm. The total inner volume (88 m^3) is filled with a mixture 90/10 of Ne-CO_2[4]. The TPC field cage provides stability and extremely precise positioning of the end-cap read-out

4. The gas mixture was changed to Ar-CO_2 for some of the data taking during the LHC Run-2.

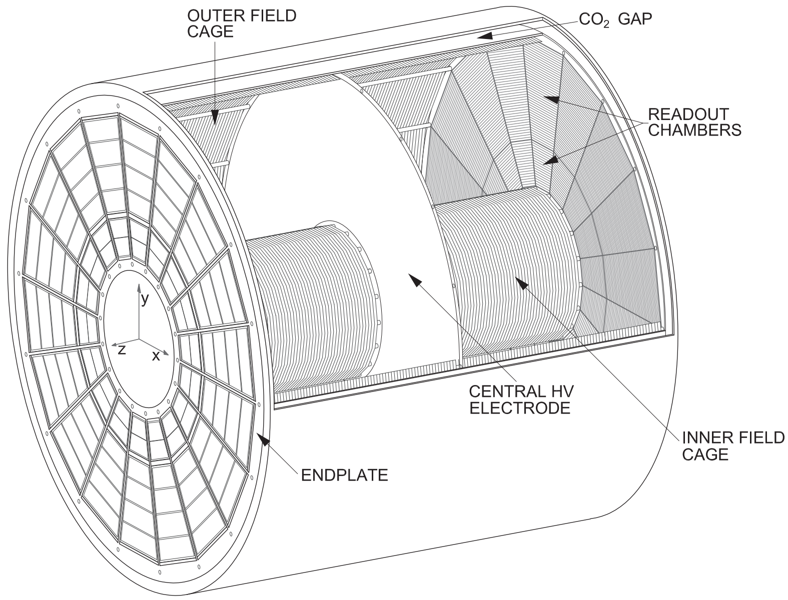

Figure 2.4: 3D layout of the TPC. Source: [66].

pads, essential to maintain a good spatial resolution, while maintaining the materials at a minimum in order to avoid scattering or absorption of the particles when crossing the TPC.

A nominal negative voltage of 100 kV is applied to the central membrane, creating an electric field of 400 V/cm parallel to the beam line directed towards the membrane. Charged particles traversing the gas produce a (primary) ionization: ions drift towards the central membrane, whereas electrons drift towards the end caps with a drift velocity of $\approx$ 3 cm/μs. Each end-cap is equipped with Multi-Wire Proportional Chambers (MWPCs) segmented into 72 readout pads, arranged into two crowns each of 18 sectors. A total of 5.7×10^5 channels are read out independently. The pad size is $7 \times 4.5\,\mathrm{mm}^2$. When the electrons reach close to the anode wires, an avalanche (secondary) ionization occurs, producing an amplified induced signal on the readout pads. The x, y coordinates of each tracking point are given by the position of the readout pads that collect the signal, while the z coordinate is determined from the drift time of the electrons. A large number of ions are generated with the avalanche.

They drift back to the bulk of the TPC with a much smaller drift velocity (inversely proportional to their mass). If not stopped, these ions would produce a large amount of space charge in the gas volume, which would take a long time (> 100 ms) to recombine in the gas or be collected by the central cathode. The presence of space charge would compromise the spatial resolution by distorting the electric field lines in the TPC volume. To avoid this, a metallic gating grid is positioned at a distance of 3 mm from the anode wires. After the electrons from the primary ionization go through, the grid is "closed" by applying a voltage bias: ions, drifting back from the avalanche ionization, are trapped by the grid. During this time the grid is opaque also to electrons coming from the bulk of the TPC, therefore the detector is not able to record any subsequent event until the grid is open again. This limits the read-out rate of the TPC to ≈ 3.5 kHz (the gating grid stays closed for $\approx 300\,\mu$s)[5]. A major upgrade planned to be installed during LS2 and start operations during the LHC Run-3 will push this limit up to about 50 kHz, effectively allowing a continuous read-out in Pb–Pb data-taking mode.

2.2.2 Particle Identification

dE/dx in the TPC

The mean specific energy loss $\langle \frac{\mathrm{d}E}{\mathrm{d}x} \rangle$ of charged particles traveling through a medium is well described by the Bethe-Bloch formula [67]:

$$\left\langle -\frac{\mathrm{d}E}{\mathrm{d}x} \right\rangle = K z^2 \frac{Z}{A} \frac{1}{\beta^2} \left[\frac{1}{2} \log \frac{2 m_\mathrm{e} c^2 \beta^2 \gamma^2 W_\mathrm{max}}{I^2} - \beta^2 - \frac{\delta(\beta\gamma)}{2} \right], \tag{2.1}$$

where:

- K is a function of universal constants ($K \approx 0.307$ MeV mol $^{-1}$ cm ^{2});

5. During Run-1 and Run-2, the front-end electronics further limited the read-out rate to about 300 Hz.

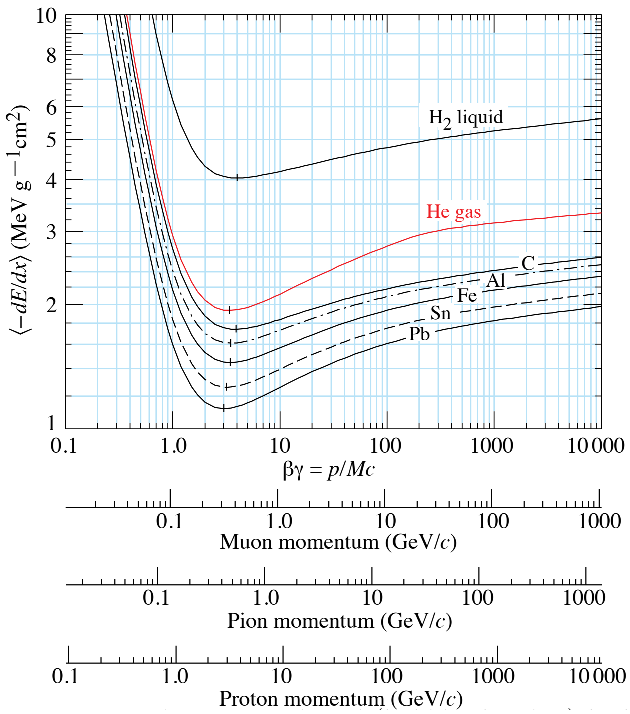

Figure 2.5: Mean energy loss rate in liquid (bubble chamber) hydrogen, gaseous helium, carbon, aluminum, iron, tin, and lead [67].

- z is the charge number of the incident particle;
- Z is the atomic number of the absorber;
- A is the mass number of the absorber;
- $\beta = v/c$ is the velocity of the incident particle;
- $m_e = 0.51$ MeV$/c^2$ is the mass of the electron;
- $\gamma = \frac{1}{\sqrt{1-\beta^2}}$ is the Lorentz factor;
- W_{max} is the maximum energy transfer to an electron in a single collision and it depends only on the mass and velocity of the incident particle via several fundamental constants;
- I is the mean excitation energy of the medium and it is determined experimentally or through empirical formulae;

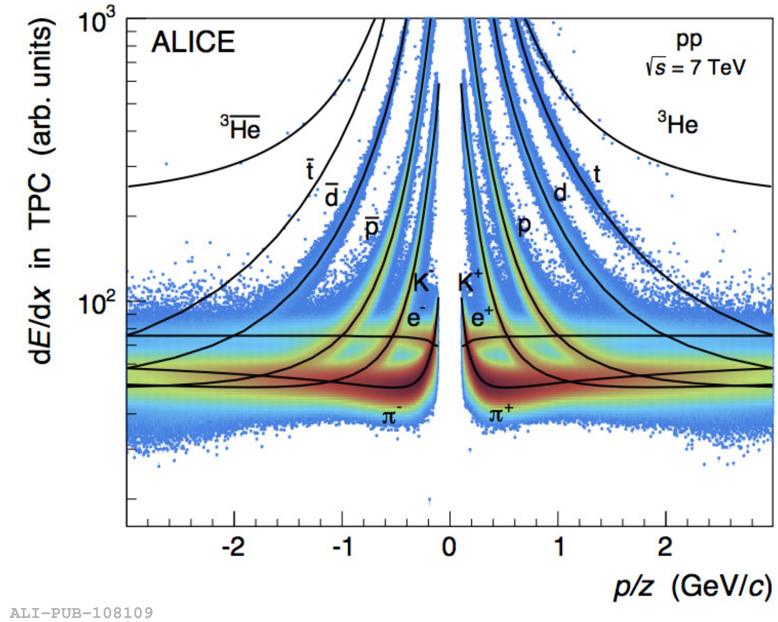

Figure 2.6: Specific energy loss ($\mathrm{d}E/\mathrm{d}x$) vs. rigidity (momentum/charge) for TPC tracks from pp collisions at $\sqrt{s} = 7$ TeV. The solid curves represent a parametrization of the Bethe-Bloch curve [68].

- $\delta(\beta\gamma)$ is the density effect correction due to the polarization of the medium caused by the passage of the particle.

Figure 2.5 shows the mean specific energy loss calculated with the Bethe-Bloch formula for various materials. Three regions can be identified:

1. at low velocity $-\left\langle \frac{\mathrm{d}E}{\mathrm{d}x} \right\rangle \propto \frac{1}{\beta^2}$;

2. for $\beta\gamma \approx 3$, the specific energy loss is minimum and a particle in this regime is called a Minimum Ionizing Particle (MIP);

3. at larger velocities, the energy loss increases again with $-\left\langle \frac{\mathrm{d}E}{\mathrm{d}x} \right\rangle \propto \log \beta$ (relativistic rise).

In a drift chamber, such as the TPC, the specific energy loss of the particle along the trajectory is measured via the magnitude of the signals induced by the particle at each sampling point. The mean of the energy loss, obtained through this sampling method, is affected by rare processes with large energy deposition in a single scattering. To overcome this instability, a truncated mean is typically used, i.e. only a fraction of the sampling points with the smaller signals are used (70% for the ALICE TPC). By plotting the mean energy loss as a function of the rigidity (momentum/charge), the distributions for different particle species can be separated in certain momentum regions according to their mass. An example of the specific energy loss measurement in pp collisions at $\sqrt{s} = 7$ TeV is shown in Fig. 2.6. Particles can be distinguished on a track-by-track basis for $p \lessapprox 1$ GeV/c. At higher momenta, particles can still be separated on a statistical basis with multi-Gaussian fits. This method allows for the measurement of p_{T} spectra of identified particle up to ~ 20 GeV/c [69].

Time Of Flight

The Time of Flight Detector provides particle identification capabilities in the intermediate momentum range $0.5 < p_{\mathrm{T}} < 2.5$ GeV/c for pion and kaons, and up to 4 GeV/c for protons. The TOF detector measures the transit time of individual particles with a very good time resolution (~ 100 ps), made possible by the use of Multi-gap Resistive Plate Chambers (MRPC), located at $370 - 399$ cm from the beam axis and covering the full azimuth. The start time for the TOF measurement is provided by the T0 detector, which consists of two arrays of Cherenkov counters, positioned at forward rapidities on opposite sides of the interaction point. Each array has 12 cylindrical counters equipped with a quartz radiator and photomultiplier tube. The start time of the event is also estimated using the particle arrival times at the TOF detector, when at least three particles reach the TOF detector, to provide increased resolution and efficiency at larger multiplicity [70].

The efficiency of matching TPC tracks to TOF is shown in Fig. 2.7 for p–Pb collisions at $\sqrt{s_{\mathrm{NN}}} = 5.02$ TeV where it is also compared with a Monte Carlo simulation.

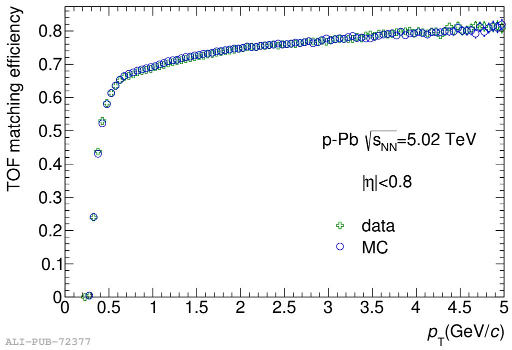

Figure 2.7: Matching efficiency (including the geometric acceptance factor) at TOF for tracks reconstructed in the TPC in p–Pb collisions at $\sqrt{s_{\rm NN}} = 5.02$ TeV, compared to a Monte Carlo simulation [64].

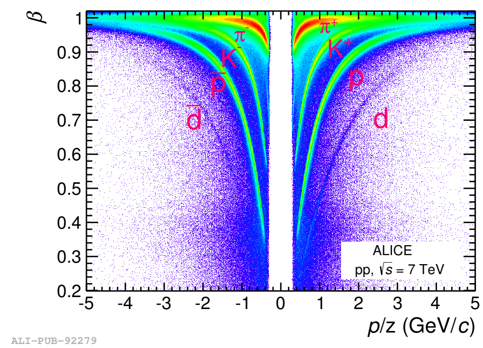

Figure 2.8: Particle velocity β measured by the TOF detector as a function of the rigidity p/z, where z is the particle charge, for $|\eta| < 0.9$ [71].

At $p_{\rm T} < 0.7$ GeV/c, the matching efficiency is dominated by energy loss and the rigidity cutoff generated by the magnetic field. At higher transverse momenta it reflects a slightly reduced efficiency due to the geometrical acceptance (dead space between sectors), the inactive modules, and the intrinsic efficiency of the MRPCs (98.5% on average).

Figure 2.8 illustrates the performance of the TOF detector by showing the measured velocity β distribution as a function of momentum (measured by the ITS-TPC).

2.2.3 The Electromagnetic Calorimeter

The ALICE Electromagnetic Calorimeter (EMCal) [72] was not present in the first design of the experiment. The EMCal project was approved in 2006 to become an integral part of the ALICE apparatus. It allows for the measurement of neutral hadrons (via their decay into photons), which would otherwise go undetected in the central barrel. The detection of neutral hadrons provides a more precise measurement of the jet energy scale. In addition, the EMCal can measure the inclusive production of photons as well as identify electrons by determining the ratio p/E, where the

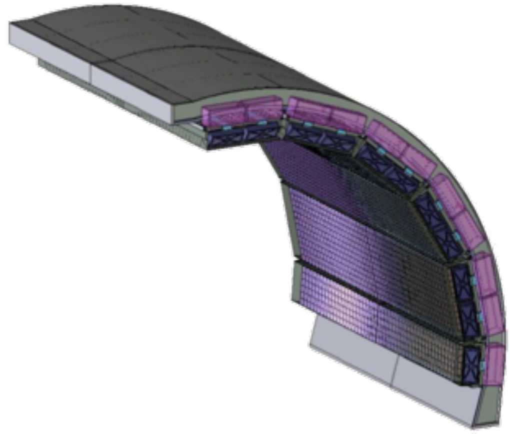

Figure 2.9: Schematic view of the EMCal.

momentum p is measured by the tracking system and the energy E by the calorimeter. Finally, it provides a fast and efficient trigger for jets, photons and electrons, allowing ALICE to fully exploit the hard momentum processes, which are abundantly produced at LHC. The layout of the EMCal during the LHC Run-1, sketched in Fig. 2.9, consists of 10 full-size Super Modules (SMs). Additional 2 “one-third” size SMs where added during LS1 .

The EMCal occupies a cylindrical integration volume approximately 110 cm deep in the radial direction, with front face 450 cm from the beam line. The azimuthal EMCal coverage is 107 degrees. In the longitudinal direction the EMCal has a length $\approx$ 700 cm, covering $|\eta| < 0.7$. The full size SMs span $\Delta\eta = 0.7$ and $\Delta\phi = 20°$, whereas the 1/3 modules span a smaller azimuthal range of $\Delta\phi = 7°$. Each full-sized SM is assembled from $12 \times 24 = 288$ modules. Each one-third size SM is assembled from $4 \times 24 = 96$ modules. Each module comprises four independent energy-measuring channels called “towers”. A total of $1,152$ towers are in each full-size SM and 384 in the one-third-size ones, for a total of $12,288$ towers. The total thickness of the calorimeter corresponds to 20 radiation lengths and incorporates on average a moderate active volume density of $5.68\,\mathrm{g/cm}^2$, which results from $\approx 1 : 1.22$ Pb to scintillator ratio by volume.

The scintillation light produced in each tower is collected by an array of wavelength shifting (WLS) fibers that run longitudinally through the tower and transmit the light to a 5×5 mm^2 active area Avalanche Photo-Diode (APD).

2.2.4 Trigger System

. The Central Trigger Processor (CTP) provides the trigger decision logic, generating triggers for the readout detectors by evaluating inputs from triggering detectors. The trigger decision is then delivered to all readout detectors through a dedicated network.

The earliest trigger decision (Level 0, or L0) is issued $1.2\,\mu$s after the event, L1 is issued at $6.5\,\mu$s, and L2 is issued at $88\,\mu$s. L1 and L2 decisions provide rejection of L0 triggers[6]. Higher trigger levels allow for more complex algorithms to identify rare events of interest.

The High Level Trigger (HLT) is a computer farm whose main object is to reduce the data volume that is stored permanently. Real-time event reconstruction is required for more elaborate compression algorithms that employ reconstructed event properties. This compression is particularly important for the TPC data, whose volume would otherwise be very difficult to cope with.

6. During Run-1 and Run-2 no L2 trigger was active.

Chapter 3

D^0-Meson Tagged Jets in pp Collisions

3.1 Introduction

At hadron colliders, charm quarks are produced as a result of a hard scattering of partons. Like lighter quarks or gluons, charm quarks fragment into jets. The charm content of the jet is conserved throughout the fragmentation chain, which is dominated by QCD processes. The charm content of a jet can be identified by looking for the presence of charmed hadrons, i.e. hadrons that have a charm quark among their valence quarks. Since all charmed hadrons have short lifetimes ($\tau \lesssim 10^{-12}$ s) their presence is inferred using a combination of Particle Identification (PID) techniques and selection of specific kinematics and topological patterns of their decay products.

The production cross-section of charm jets is significantly smaller than that of lighter quarks or gluons. The internal jet substructure is also influenced by the mass of the parent parton. In particular the fragmentation is expected to be "harder" for jets originating from massive quarks, i.e. to split the total jet momentum into fewer final-state particles sharing each a larger fraction of momentum.

3.1.1 Physics Goals

Perturbative QCD The measurement of the charm production cross section in pp collisions is an important sensitive test of perturbative QCD (pQCD). At the LHC energies, the measurement of charm production at low p_{T} probes the parton distribution functions (PDFs) of the proton at small values of parton fractional momentum, x, and squared momentum transfer, Q^2. For illustration, using a simplified $2 \to 2$ kinematics at leading order, charm quarks ($m_{\mathrm{c}} \approx 1.5$ GeV/c^2) with $p_{\mathrm{T}} \sim 2$ GeV/c and rapidity $y \sim 0$ probe the parton distribution functions at $x \sim 7 \times 10^{-4}$ and $Q^2 \sim (5 \text{ GeV})^2$. Perturbative QCD calculations have substantial uncertainties at low p_{T}, owing to both the large effect of the choice of the factorization and renormalization scales at low Q^2 and to the sizeable uncertainties on the gluon PDFs at small x [73].

Quark-Gluon Plasma Heavy quarks are also an ideal probe of the QGP, that is created in ultra-relativistic heavy-ion collisions. Hard-scattered partons, including heavy quarks, are produced early in the collision. They interact with the QGP and lose energy via radiative and collisional processes. At an energy comparable to its own mass, the charm quark is expected to interact less strongly with the QGP because of the so-called the dead-cone effect [74] which suppresses gluon radiation at small angles. Contrary to initial expectations [75–78], experimental evidence from both RHIC [79–81] and LHC [82–87] exhibit a strong suppression of D-meson production in heavy-ion collisions, similar to that of light-flavor hadrons. Furthermore, evidence of non-zero D-meson elliptic flow has been reported [81, 86, 88–90]. This evidence forced a rethinking of the energy loss mechanism of heavy quarks in the QGP [91–94]. In the context of the study of the QGP, the measurement of the charm cross section in pp collisions provides a baseline to look for collective effects in ultra-relativistic heavy-ion collisions. The total charm-production cross section in pp collisions is also crucial to model charmonium regeneration in the QGP [36]. Furthermore, it must be noted that following the discovery of the away-side ridge in high-multiplicity p–Pb and pp collisions [95–99], the search for collective effects in these small(er) collision systems has become a research topic of utmost interest. The simple scheme in which pp and p–Pb collisions can be used as a QCD-vacuum baseline, free from any hot-medium effects, has been upset by these findings. A different picture arises: a continuum in which (some of) the QGP signatures slowly turn on while the system multiplicity increases without any clear "singular" point [100]. The search for collective effects in high-multiplicity pp and p–Pb collisions is active also in the heavy-flavor sector. The elliptic flow of D-mesons was shown to be non-zero in high multiplicity p–Pb collisions [85, 101, 102]. However no evidence of high-p_{T} D-meson suppression has been reported so far in these collisions [103–107].

Astrophysics Finally, the measurement of the charm differential cross section down to low p_{T} is relevant for cosmic-ray and neutrino astrophysics: high-energy neutrinos from the decay of charmed hadrons produced in particle showers in the atmosphere constitute an important background for neutrinos from astrophysical sources [108, 109].

3.1.2 State of the Art

The p_{T}-differential production cross sections of D mesons from charm-quark fragmentation (referred to as "prompt" D mesons) has been measured in pp and $\mathrm{p\bar{p}}$ collisions at several center-of-mass energies, from $\sqrt{s} = 0.2$ TeV at RHIC up to $\sqrt{s} = 13$ TeV at the LHC [106, 110–118]. The data are described reasonably well by calculations based on perturbative QCD (pQCD), such as FONLL[1] [9–11] and GM-VFNS[2] [12].

In comparison to single-particle measurements, the reconstruction of jets containing charm hadrons allows for more differential studies to characterize the heavy quark production and fragmentation. The kinematic properties of jets are closer to those of the parent charm quark, when compared to the measurement of the charmed hadrons alone. Therefore, by measuring the kinematic properties of jets containing charmed hadrons one reduces the dependence on the details of the fragmentation, which is a highly non-perturbative phenomenon, known only with large uncertainties [119]. The study of the charm jet fragmentation can also reveal information on the charm production mechanism [120, 121]. A particularly relevant observable is the fraction ($z_{||}$) of jet momentum ($\vec{p}_{\rm jet}$) carried by the D meson along the jet axis direction:

$$z_{||} = \frac{\vec{p}_{\rm jet} \cdot \vec{p}_{\rm D}}{\vec{p}_{\rm jet} \cdot \vec{p}_{\rm jet}}. \tag{3.1}$$

The STAR experiment at RHIC measured the $\mathrm{D}^{*\pm}$-meson production in jets in pp collisions at $\sqrt{s} = 200$ GeV [122]. The jets were measured in the interval $8 < p_{\rm T,jet} < 20$ GeV/c. The data exhibit a rate at low $z_{||}$ values that is higher than that obtained with a Monte Carlo simulation performed with Pythia 6 [123] using only the direct charm flavor creation processes, $\mathrm{gg} \to \mathrm{c\bar{c}}$ and $\mathrm{q\bar{q}} \to \mathrm{c\bar{c}}$, suggesting that higher order processes (gluon splitting, flavor excitation) are not negligible in charm production at RHIC energies. In a more recent analysis, the PHENIX collaboration has measured azimuthal correlations of charm and bottom semi-leptonic decays using unlike- and like-sign muon pairs [124]. Overall they found a good agreement with a Pythia 6 [123] simulation. Through a Bayesian analysis based on Pythia 6 templates they found that while leading-order pair creation is dominant for bottom,

1. Fixed-Order plus Next-to-Leading-Log

2. General-Mass Variable-Flavor-Number Scheme

higher order processes dominate for charm production. At the LHC, the analysis of the angular correlations of b-hadron decay vertices, measured by CMS [125], indicated that the collinear region, where the contributions of gluon splitting processes are expected to be large, is not adequately described by PYTHIA 6 nor by predictions based on Next-To-Leading (NLO) order pQCD calculations. The ATLAS experiment measured the $\mathrm{D}^{*\pm}$-meson production in jets in pp collisions at $\sqrt{s} = 7$ TeV [126] finding that the $z_{||}$ distribution differs from expectations of PYTHIA 6, HERWIG 6 [127, 128] and POWHEG [129–132] event generators, both in overall normalization and shape, with data displaying a higher probability for low $z_{||}$ values and a steeper decrease towards $z_{||} = 1$. The discrepancy between data and generator expectations is maximum in the lowest jet p_{T} interval, $25 < p_{\mathrm{T}} < 30$ GeV/c. ATLAS data are well described in a recent global QCD analysis of fragmentation functions based on the ZM-VFNS [133] scheme, in which the in-jet fragmentation data were combined with previous D-meson measurements in a global fit [134]. The authors highlight the importance of this type of data in order to pin down the otherwise largely unconstrained momentum fraction dependence of the gluon fragmentation function.

This Chapter is dedicated to the measurement of the D^0-meson tagged charged-jet p_{T}- and $z_{||}^{\mathrm{ch}}$-differential cross sections in pp collisions at $\sqrt{s} = 7$ TeV with the ALICE experiment at the LHC. The observable $z_{||}^{\mathrm{ch}}$ is defined as in Eq. 3.1 but using the momentum of the charged jet, $\vec{p}_{\mathrm{ch\,jet}}$. Charged jets are reconstructed with only their charged-particle constituents [135].

3.2 Data Sample

Beam parameters The data used for this analysis were recorded by the ALICE detector during a data-taking campaign that was performed from March to August 2010. During that time, the LHC delivered the first pp collisions at the center-of-mass energy $\sqrt{s} = 7$ TeV. These first collisions were characterized by low proton bunch densities and small number of bunches injected in the machine. In fact, proton bunches were injected one by one into the LHC, with inter-bunch distances much larger than the minimum bunch separation of 25 ns reached during the LHC Run-2. The instantaneous luminosity delivered by the LHC to the high-luminosity experiments ATLAS and CMS was ramped up from 2.5×10^{27} to 1.0×10^{31} cm^{-2}s^{-1} [136]. When the instantaneous luminosity delivered by the LHC became higher than the maximum allowed by the ALICE data acquisition infrastructure, leveling of the luminosity delivered to ALICE was achieved by separating the beams in the plane orthogonal to the beam direction by up to 3.8 times the r.m.s of their transverse profile. In this way the instantaneous luminosity in ALICE was kept in the range $0.2 - 1.2 \times 10^{29}$ cm^{-2}s^{-1} [64, 112]. The average number of interactions per bunch crossing in ALICE varied in the range $0.04 - 0.08$, with probability of collision pile-up below 4% per triggered event.

Trigger Throughout this data-taking period ALICE collected events using the minimum-bias trigger, internally coded `CINT1`. The conditions for the `CINT1` trigger are met when at least one hit is recorded in either of the two V0 counters or in the SPD detector, in coincidence with an LHC bunch crossing at IP2. The minimum-bias trigger efficiency was estimated to be 85% for inelastic hadronic collisions [137]. Furthermore, Monte Carlo simulations based on the PYTHIA 6.4.21 event generator [123] (with Perugia 0 tune [138]) verified that the minimum-bias trigger is 100% efficient for events containing a D meson with $p_{\mathrm{T,D}} > 1$ GeV/c and $|y| < 0.5$.

Data reconstruction The ALICE Run Coordination grouped these data in 4 periods, characterized by uniform beam parameters and/or detector conditions: LHC10b, LHC10c, LHC10d, LHC10e. Several physics data reconstruction passes were performed for these datasets. The last one was name-coded `pass4` and was performed in

2014 after various improvements in the track reconstruction code and event selection.

Event selection Background events generated by the interaction of beam particles with the residual gas present in the interaction point (beam-gas) were rejected at reconstruction time using the timing information from the V0 and the correlation between the number of hits and track segments (tracklets) in the SPD detector. Beam-gas events are characterized by a large number of SPD hits not associated with any tracklet. The offline event selection was based on pile-up rejection and on the reconstructed primary vertex. The pile-up condition is met when a second vertex is found, with at least 3 associated tracklets and separated from the first by more than 8 mm. The primary vertex of the collision was required to be within 10 cm from the center of the ALICE detector along the beam direction, $|V_z| < 10$ cm. This condition ensures uniformity in the tracking performance within the fixed pseudo-rapidity window $|\eta| < 0.9$. Events in which a primary vertex could not be reconstructed (e.g. because there were too few hits in the ITS) were also rejected because they cannot be used to reconstruct the D^0 mesons[3]. However the fraction of such events whose (experimentally inaccessible) primary vertices meet the condition $|V_z| < 10$ cm contribute to the inelastic hadronic cross section and should be included in the cross section normalization factor. Assuming that the fraction of events with $|V_z| > 10$ cm over the total is the same in events with or without a reconstructed vertex, the adjusted number of events used for the normalization of the cross sections is:

$$N_{\text{adjusted}} = N_{\text{accepted}} + N_{\text{no vertex}} \frac{N_{\text{accepted}}}{N_{\text{accepted}} + N_{\text{rejected}\,Vz}}, \tag{3.2}$$

where $N_{\text{rejected}\,Vz}$ is the number of events rejected because $|V_z| > 10$ cm. Table 3.1 shows the total number of accepted and rejected events in each period as well as the

3. As we shall see later, selection cuts on the D^0-meson candidates are based on the reconstruction of a secondary decay vertex displaced from the primary vertex.

Table 3.1: Number of events analyzed (in millions) selected using the `CINT1` trigger class.

Period	LHC10b	LHC10c	LHC10d	LHC10e	Total
Accepted	23.91	62.44	134.93	118.04	339.33
Rejected: pile-up	0.10	1.16	2.24	1.69	5.19
Rejected: no vertex	3.32	8.66	22.32	19.14	53.45
Rejected: $\lvert V_z \rvert > 10$ cm	0.12	0.71	18.34	17.63	36.80
Adjusted no. of events (see text)					387.55

total obtained combining the four periods. The adjusted number of events obtained combining all four periods is $N_{\text{adjusted}} = 3.88 \times 10^8$.

Luminosity determination The LHC luminosity at the interaction point can be determined precisely only through dedicated runs called Van der Meer scans [139]. During these scans the beams are displaced in the plane orthogonal to the beam direction and the interaction rate is measured as a function of the displacement. This allows for the measurement of the effective transverse widths in the two directions orthogonal to the beam direction, h_x and h_y, which enter the calculation of the luminosity $\mathscr{L} = f N_1 N_2 / h_x h_y$, where N_i are the number of protons in each bunch and f is the revolution frequency of the accelerator. The inelastic cross section σ_{INEL} is obtained inverting the Equation:

$$\frac{\mathrm{d}N}{\mathrm{d}t} = \epsilon_{\text{CINT1}} \times \sigma_{\text{INEL}} \times \mathscr{L} = \sigma_{\text{CINT1}} \times \mathscr{L}, \tag{3.3}$$

where $\mathrm{d}N/\mathrm{d}t$ is the rate measured by the `CINT1` trigger and ϵ_{CINT1} is the trigger efficiency. Two Van der Meer scans were performed in ALICE during the 2010 data-taking campaign. The results are reported in [137], including the measurement of $\sigma_{\text{CINT1}} = 62.2 \pm 2.2$ mb. Once σ_{CINT1} is known, we can calculate the integrated luminosity for all data taken at the same center-of-mass energy and trigger conditions:

$$\mathscr{L}_{\text{int}} = \frac{N}{\sigma_{\text{CINT1}}}, \tag{3.4}$$

where N is the number of triggers collected. Using Eq. 3.4 and the adjusted number of events $N = N_{\text{adjusted}} = 3.88 \times 10^8$ calculated above, the integrated luminosity is $\mathscr{L}_{\text{int}} = 6.23 \pm 0.22\ \text{nb}^{-1}$.

3.3 Monte Carlo Simulations

3.3.1 Central Productions

The ALICE Collaboration takes care of centrally producing Monte Carlo simulations for general purpose or for use in a specific analysis or group of analyses. These productions typically include the event generation and the transport of the generated particles through a detailed simulation of the detector elements. Productions are anchored to specific data-taking periods, to accurately simulate the detector and data-taking conditions and, if needed, the beam parameters. The final result of the particle transport is the generation of detector signals in the form of digits that are calibrated to provide physical signals. The calibration and physics reconstruction of the detector signals is performed with the same code used for the reconstruction of the real data. Throughout this Chapter we will speak of "generator-level" event and "detector-level" event: the former refers to the event made of all the particles produced in the pp scattering, for which we know all properties (four-momentum, particle type, all quantum numbers etc.); the latter refers to the event as seen by the detector (calibrated detector signals, reconstructed objects such as tracks). Several event generators have been implemented and used for central productions. The most common for the simulation of pp collisions is Pythia 6 [123], although Pythia 8 [140] is now replacing it for newer productions. For the particle transport GEANT 3 [141] is used. For this analysis two productions anchored to the 2010 data-taking periods were used, both obtained with PYTHIA 6.4.25 using the Perugia 2011 tune [138].

Minimum-bias This is a general-purpose production, mimicking the minimum-bias trigger selection used in real data taking. Single-diffractive, double-diffractive and $2 \rightarrow 2$ QCD processes are included[4]. About 300 million events were generated with these settings.

Charm-enhanced This production was performed specifically for analyzing jets tagged with D mesons. The charm content was enhanced by requiring either a charm or a bottom quark. In addition all D hadrons were forced to decay into hadronic channels. The production was divided into 9 bins, each with 5 million events. The first bin was generated with minimum-bias settings, as in the minimum-bias production described above. The remaining 8 bins were generated with the hard-QCD process[5]. Each bin was set with different $p_{\mathrm{T,hard}}$ limits[6] in order to generate sufficient statistics at all jet momenta.

Throughout this Chapter we shall indicate these two productions simply as the "minimum-bias Monte Carlo production" and the "charm-enhanced Monte Carlo production".

3.3.2 Custom Productions

A number of custom Monte Carlo simulations were produced for the purpose of this analysis. These productions include only the generator-level event simulation, i.e.

4. $\texttt{MSEL} = 0$ and $\texttt{ISUB} = 92, 93, 94, 95$ in Section 8.2.4 of [123].

5. $\texttt{MSEL} = 1$, which includes $\texttt{ISUB} = 11, 12, 13, 28, 53, 68, 96$ in Section 8.2.1 of [123].

6. $\texttt{CKIN}(3)$ and $\texttt{CKIN}(4)$ in Section 3.6 of [123]. The limits of the 8 bins were: $[5, 11, 21, 36, 57, 84, 117, 152, 191]$.

particles are not transported through the detector geometry. They were used primarily for two purposes:

1. estimate the contribution coming from the decay of B hadrons into D mesons (B feed-down);
2. compare the final results with expectations obtained with Monte Carlo event generators implementing QCD processes at LO and/or NLO.

These simulations will be described in detail when introducing the B feed-down correction in Section 3.8.2 and in Chapter 5 where the final results will be discussed and interpreted.

3.4 Analysis Overview

3.4.1 Aim of the Analysis

The aim of the analysis is to identify and reconstruct jets containing prompt D^0 mesons produced in pp collisions. We will refer to *prompt* D^0 mesons to indicate those that are the direct product of the fragmentation of a charm quark and subsequent hadronization of the colored partons. In contrast *non-prompt* D^0 mesons are the decay product of B hadrons

D^0 mesons were identified in the exclusive decay channel:

$$\mathrm{D}^0 \rightarrow \mathrm{K}^-\pi^+, \tag{3.5}$$

which has a branching ratio BR $= 3.89 \pm 0.04\%$ [67]. In this analysis both the D^0 meson and its antiparticle $\overline{\mathrm{D}^0}$ (which decays as in Eq. 3.5 with the same BR, taking the charge conjugates of all particles involved) are included indifferently. In the following "D^0 meson" will indicate both the particle and its antiparticle $\overline{\mathrm{D}^0}$, unless otherwise specified. Jets were reconstructed using the anti-k_{T} algorithm [142] with a resolution parameter $R = 0.4$, using only the charged-particle constituents measured by the tracking system. For a historical review and technical description of the jet finding algorithms see Appendix A. The main observable of interest is the production cross section, differential in the jet transverse momentum ($p_{\mathrm{T,jet}}^{\mathrm{ch}}$) and in the jet momentum fraction carried by the D^0 meson in the direction of the jet axis ($z_{||}^{\mathrm{ch}}$), defined as:

$$z_{||}^{\mathrm{ch}} = \frac{\vec{p}_{\mathrm{jet}}^{\,\mathrm{ch}} \cdot \vec{p}_{\mathrm{D}}}{\vec{p}_{\mathrm{jet}}^{\,\mathrm{ch}} \cdot \vec{p}_{\mathrm{jet}}^{\,\mathrm{ch}}}, \tag{3.6}$$

where $\vec{p}_{\mathrm{jet}}^{\,\mathrm{ch}}$ and $\vec{p}_{\mathrm{D}}$ are the vectors representing the jet and the D^0-meson momenta, respectively. The "ch" superscript indicates that jets are reconstructed using only their charged-particle constituents. The ingredients needed to measure the p_{T}-differential cross section are explicit in the following formula:

$$\frac{\mathrm{d}^2\sigma^{\mathrm{D}^0}}{\mathrm{d}p_{\mathrm{T,jet}}^{\mathrm{ch}}\mathrm{d}\eta_{\mathrm{jet}}}(p_{\mathrm{T,jet}}^{\mathrm{ch}}) = \frac{1}{\mathscr{L}_{\mathrm{int}}}\frac{1}{\mathrm{BR}}\frac{N^{\mathrm{D}^0}(p_{\mathrm{T,jet}}^{\mathrm{ch}})}{\Delta\eta_{\mathrm{jet}}\Delta p_{\mathrm{T,jet}}^{\mathrm{ch}}}, \tag{3.7}$$

where $N^{\mathrm{D}^0}(p_{\mathrm{T,jet}}^{\mathrm{ch}})$ is the measured yield in each bin of $p_{\mathrm{T,jet}}^{\mathrm{ch}}$; $\Delta p_{\mathrm{T,jet}}^{\mathrm{ch}}$ is the width of the histogram bin; $\Delta\eta_{\mathrm{jet}}$ is the width of the jet pseudo-rapidity acceptance window. Similarly the $z_{||}^{\mathrm{ch}}$-differential cross section is obtained from:

$$\frac{\mathrm{d}^3\sigma^{\mathrm{D}^0}}{\mathrm{d}z_{||}^{\mathrm{ch}}\mathrm{d}p_{\mathrm{T,jet}}^{\mathrm{ch}}\mathrm{d}\eta_{\mathrm{jet}}}(p_{\mathrm{T,jet}}^{\mathrm{ch}}, z_{||}^{\mathrm{ch}}) = \frac{1}{\mathscr{L}_{\mathrm{int}}}\frac{1}{\mathrm{BR}}\frac{N^{\mathrm{D}^0}(p_{\mathrm{T,jet}}^{\mathrm{ch}}, z_{||}^{\mathrm{ch}})}{\Delta\eta_{\mathrm{jet}}\Delta p_{\mathrm{T,jet}}^{\mathrm{ch}}\Delta z_{||}^{\mathrm{ch}}}, \tag{3.8}$$

where $N^{\mathrm{D}^0}(p_{\mathrm{T,jet}}^{\mathrm{ch}}, z_{||}^{\mathrm{ch}})$ is the measured yield in each bin of $p_{\mathrm{T,jet}}^{\mathrm{ch}}$ and $z_{||}^{\mathrm{ch}}$; $\Delta z_{||}^{\mathrm{ch}}$ is the width of the histogram bin. We have already seen in Section 3.2 how the integrated luminosity $\mathscr{L}_{\mathrm{int}}$ was determined. The experimental procedure to measure $N^{\mathrm{D}^0}(p_{\mathrm{T,jet}}^{\mathrm{ch}})$ and $N^{\mathrm{D}^0}(p_{\mathrm{T,jet}}^{\mathrm{ch}}, z_{||}^{\mathrm{ch}})$ will be detailed in the following. Another observable of interest is the rate of D^0-meson tagged jets relative to the inclusive jet production as a function of $p_{\mathrm{T,jet}}^{\mathrm{ch}}$ and $z_{||}^{\mathrm{ch}}$. As a function of $p_{\mathrm{T,jet}}^{\mathrm{ch}}$ it coincides with the ratio of the p_{T}-differential

Table 3.2: Kinematic cuts of the differential cross sections of D^0-meson tagged jets reported in this thesis.

Cross Section	$p_{\mathrm{T,D}}$ (GeV/c)	$p_{\mathrm{T,jet}}^{\mathrm{ch}}$ (GeV/c)	η_{jet}
$p_{\mathrm{T,jet}}^{\mathrm{ch}}$-differential	$p_{\mathrm{T,D}} > 3$	/	$\lvert\eta_{\mathrm{jet}}\rvert < 0.5$
$z_{\vert\vert}^{\mathrm{ch}}$-differential	$p_{\mathrm{T,D}} > 2$	$5 < p_{\mathrm{T,jet}}^{\mathrm{ch}} < 15$	$\lvert\eta_{\mathrm{jet}}\rvert < 0.5$
$z_{\vert\vert}^{\mathrm{ch}}$-differential	$p_{\mathrm{T,D}} > 6$	$15 < p_{\mathrm{T,jet}}^{\mathrm{ch}} < 30$	$\lvert\eta_{\mathrm{jet}}\rvert < 0.5$

cross sections of D^0-meson tagged jets and inclusive jets:

$$R(p_{\mathrm{T,jet}}^{\mathrm{ch}}) = \frac{\mathrm{d}^2\sigma^{\mathrm{D}^0}/\mathrm{d}p_{\mathrm{T,jet}}^{\mathrm{ch}}\mathrm{d}\eta_{\mathrm{jet}}(p_{\mathrm{T,jet}}^{\mathrm{ch}})}{\mathrm{d}^2\sigma^{\mathrm{jet}}/\mathrm{d}p_{\mathrm{T,jet}}^{\mathrm{ch}}\mathrm{d}\eta_{\mathrm{jet}}(p_{\mathrm{T,jet}}^{\mathrm{ch}})} = \frac{N^{\mathrm{D}^0}(p_{\mathrm{T,jet}}^{\mathrm{ch}})}{\mathrm{BR}\cdot N^{\mathrm{jet}}(p_{\mathrm{T,jet}}^{\mathrm{ch}})}, \tag{3.9}$$

where $N^{\mathrm{jet}}(p_{\mathrm{T,jet}}^{\mathrm{ch}})$ is the measured yield of inclusive jets. It is obtained as a function of $z_{||}^{\mathrm{ch}}$ by dividing the $z_{||}^{\mathrm{ch}}$-differential cross section by the inclusive jet cross section integrated in the $p_{\mathrm{T,jet}}^{\mathrm{ch}}$ interval under consideration:

$$R(z_{||}^{\mathrm{ch}})_{a<p_{\mathrm{T,jet}}^{\mathrm{ch}}<b} = \frac{\int_a^b \mathrm{d}p_{\mathrm{T,jet}}^{\mathrm{ch}} \frac{\mathrm{d}^3\sigma^{\mathrm{D}^0}}{\mathrm{d}p_{\mathrm{T,jet}}^{\mathrm{ch}}\mathrm{d}\eta_{\mathrm{jet}}\mathrm{d}z_{||}^{\mathrm{ch}}}(z_{||}^{\mathrm{ch}})}{\int_a^b \mathrm{d}p_{\mathrm{T,jet}}^{\mathrm{ch}} \frac{\mathrm{d}^2\sigma^{\mathrm{jet}}}{\mathrm{d}p_{\mathrm{T,jet}}^{\mathrm{ch}}\mathrm{d}\eta_{\mathrm{jet}}}} = \frac{N^{\mathrm{D}^0}(z_{||}^{\mathrm{ch}})_{a<p_{\mathrm{T,jet}}^{\mathrm{ch}}<b}}{\mathrm{BR}\cdot N^{\mathrm{jet}}_{a<p_{\mathrm{T,jet}}^{\mathrm{ch}}<b}}. \tag{3.10}$$

The kinematic cuts are summarized in Table 3.2.

3.4.2 Analysis Workflow

The analysis workflow is structured as follows:

1. Event selection (as described in previous Section)
2. For each event: identification of D^0-meson candidates among pairs of opposite-charge tracks; apply kinematic, topological and PID cuts
3. Reconstruction of the jet that contains each identified D^0-meson candidate:

apply kinematic cuts

4. For each D^0-meson tagged jet candidate, compute and store the variables of interest:

   $\boldsymbol{m_{\mathrm{inv}}}$ Invariant mass of the kaon-pion pair

   $\boldsymbol{p_{\mathrm{T,D}}}$ Transverse momentum of D^0-meson candidate

   $\boldsymbol{p_{\mathrm{T,jet}}^{\mathrm{ch}}}$ Transverse momentum of the charged jet candidate

   $\boldsymbol{z_{||}^{\mathrm{ch}}}$ Jet momentum fraction carried by the D^0-meson candidate

5. Extraction of the raw yield as a function of the variables of interest ($z_{||}^{\mathrm{ch}}$, $p_{\mathrm{T,jet}}^{\mathrm{ch}}$) via a statistical analysis performed by fitting the invariant mass distributions with appropriate functional forms

6. Application of efficiency and acceptance corrections

7. Subtraction of the B feed-down contribution estimated from Monte Carlo simulations

8. Correction for finite detector resolution, applied via statistical unfolding of the final distributions

9. Normalization of the distributions according to Eqs. 3.7, 3.8, 3.9, 3.10

In the following Sections all of the above points will be discussed.

3.4.3 Software

The analysis was performed making use of the ALICE grid infrastructure [143] and the LEGO analysis train system [144]. The analysis software used to reconstruct the D^0-meson tagged jets is part of the `AliPhysics` and `AliRoot` packages which are based on `ROOT` [145] and are hosted in publicly available `github` repositories [146, 147]. These packages are written in `C++`. For jet reconstruction `FastJet` 3.2.1 [148, 149] was used. The post-processing (items 5–9 of the previous enumeration) and the assessment of systematic uncertainties was performed using ad-hoc programs written in `python` and `C++` and based on `ROOT` libraries. The code is available in [150]. For the unfolding part the `RooUnfold` [151] package was used.

3.5 Tracking

3.5.1 Track finding

The tracking algorithm of the ALICE central barrel is described in detail in [64]. Here the main steps will be summarized. Before tracking can be performed, "cluster" reconstruction is performed for all ALICE sub-detectors. A cluster is characterized by a position, signal time and signal amplitude. The Kalman filter technique [152] is used for track finding and fitting. The first tracking step starts from the outermost TPC clusters and follows the tracks inward. Some quality cuts are applied to ensure that tracks contain a sufficiently large number of TPC clusters and that the fraction of clusters shared among multiple tracks is low. TPC-only tracks are the result of this first step. These tracks are propagated farther inward to the outermost ITS layer and used as seeds for track finding in the ITS. Each TPC track is assigned a tree of possible track projections to the ITS and the one with the smallest χ^2 is selected. At this stage additional standalone ITS track finding is performed using those ITS clusters that were not matched to a TPC track. In fact, tracks with $p_{\mathrm{T}} \lesssim 0.4$ GeV/c have very low reconstruction efficiency in the TPC due to energy loss and multiple scattering in the detector material. ITS standalone tracking allows for the reconstruction of tracks down to about 80 MeV/c. Global TPC-ITS tracks are propagated outward and matched with the other central barrel detectors (TOF, TRD, EMCal, HMPID) to provide additional PID information. Finally, tracks are propagated back inward

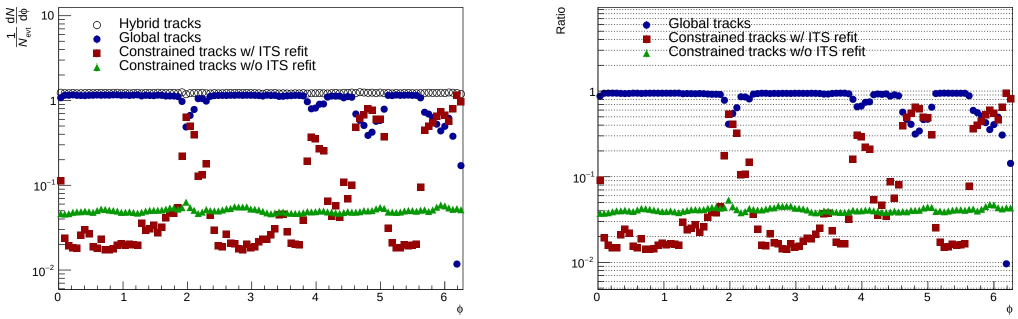

(a) Distribution (b) Ratio

Figure 3.1: Comparison of the reconstructed track distributions as a function of ϕ for the hybrid track selection and its sub-components.

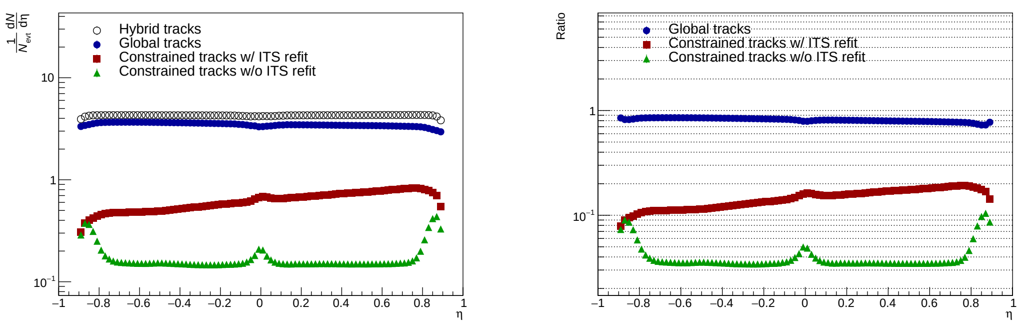

(a) Distribution (b) Ratio

Figure 3.2: Comparison of the reconstructed track distributions as a function of η for the hybrid track selection and its sub-components.

from the outer TPC radius to the ITS and refitted to calculate the final position, direction, curvature and covariance matrix. The primary vertex is then calculated using global TPC-ITS tracks.

3.5.2 Track selection criteria for jet finding

Jet finding requires uniform and high tracking efficiency with good track momentum resolution. The uniformity requirement is important to avoid jet clustering around higher efficiency acceptance spots. Standard track quality selection cuts include the following:

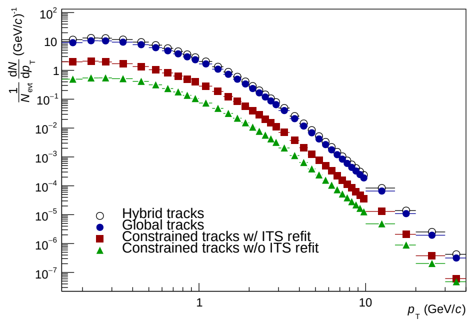

(a) Distribution

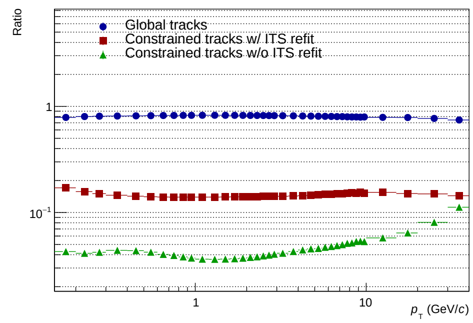

(b) Ratio

Figure 3.3: Comparison of the reconstructed track distributions as a function of p_T for the hybrid track selection and its sub-components.

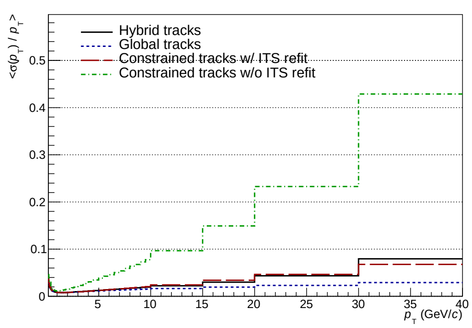

(a) p_T resolution vs. p_T

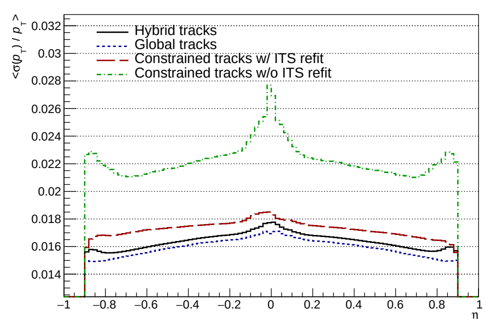

(b) p_T resolution vs. η

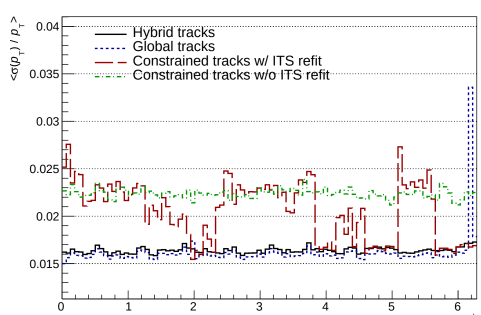

(c) p_T resolution vs. ϕ

Figure 3.4: Transverse momentum resolution of hybrid tracks and each sub-component.

- at least 70 associated TPC space points (out of a maximum of 159);
- χ^2/ndf < 2 in the TPC (where ndf is the number of degrees of freedom involved in the tracking procedure);
- at least one hit in either of the two layers of the SPD;
- a minimum of 3 hits in the entire ITS.

These tracks are called *global* tracks. Due to some inactive sectors in the SPD, the efficiency of this track sample is not uniform as a function of φ and η. This effect is apparent from the track distributions as a function of φ and η shown with the blue circles in Figs. 3.1 and 3.2, respectively. In order to improve uniformity a *hybrid* approach was employed. For the acceptance windows corresponding to inactive SPD sectors, less stringent requirements were imposed on the track quality, particularly lifting the SPD hit requirement and constraining the tracks to the primary vertex to improve their momentum resolution (impacted by the lack of space points close to the vertex). This *complementary* set of tracks is further sub-divided according to whether the refit of the ITS tracking procedure was successful or not. A successful ITS refit implies at least 3 hits in the 4 outer layers (the SPD being inactive for these tracks). Uniform tracking was obtained with these track selection criteria in the full azimuth for $|\eta| < 0.9$, as can be appreciated from the open black symbols in Figs. 3.1 and 3.2. The two complementary track sample distributions are also shown, with their efficiency matching the low efficiency regions of the global tracks. Tracks are reconstructed in the transverse momentum range $0.15 < p_{\mathrm{T}} < 100$ GeV/c, although for this analysis only tracks up to $p_{\mathrm{T}} = 30$ GeV/c are relevant. Figure 3.3 shows the distribution of hybrid tracks and global/complementary sub-samples as a function of p_{T}. Overall tracks without SPD hits with and without successful ITS refit make up 14.6% and 4.1%, respectively, of the total hybrid track selection. Figure 3.4 shows the transverse momentum resolution as a function of p_{T}, η and ϕ. The momentum

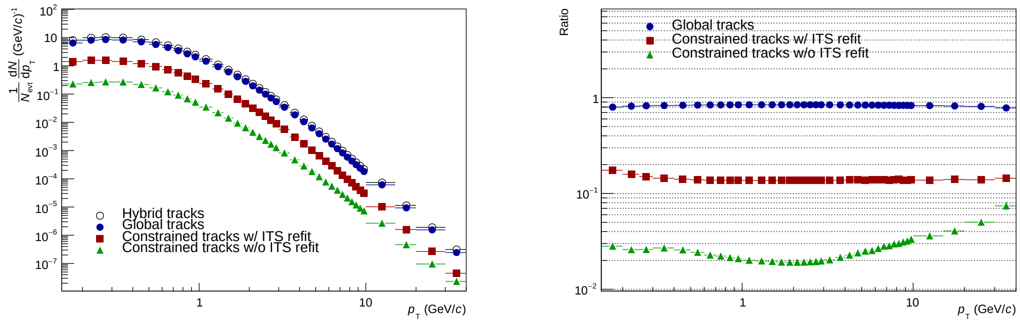

(a) Distribution (b) Ratio

Figure 3.5: Comparison of the reconstructed track distributions as a function of p_{T} for the hybrid track selection and its sub-components obtained from the minimum-bias Monte Carlo production.

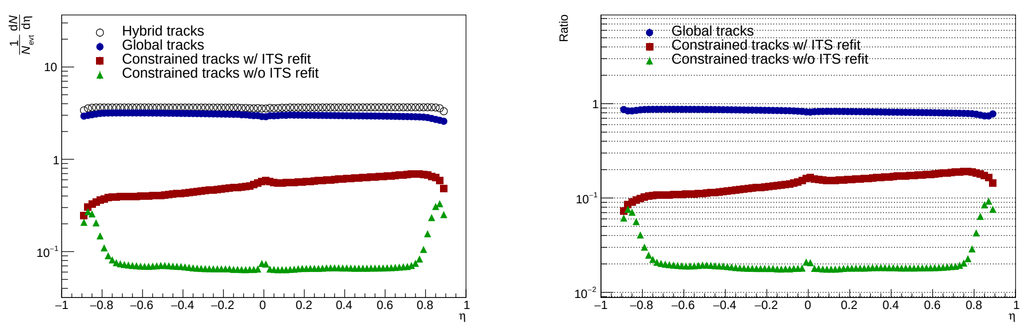

(a) Distribution (b) Ratio

Figure 3.6: Comparison of the reconstructed track distributions as a function of η for the hybrid track selection and its sub-components obtained from the minimum-bias Monte Carlo production.

resolution is estimated from the diagonal elements of the covariance matrix of the tracking fit procedure. As expected, global tracks show the best transverse momentum resolution, which stays in the range $1-3\%$ for $0.3 < p_{\mathrm{T}} < 40$ GeV/c. It must be noted that due to the vertex constraining procedure, the momentum resolution estimation for constrained tracks is biased. The η dependence of the track p_{T} resolution is not fully understood and it is under investigation. A possible explanation is that tracks close to the TPC central membrane are likely to contain fewer space points, making their momentum measurement less precise.

Figures 3.5, 3.6 and 3.7 show the distribution of hybrid tracks as a function of

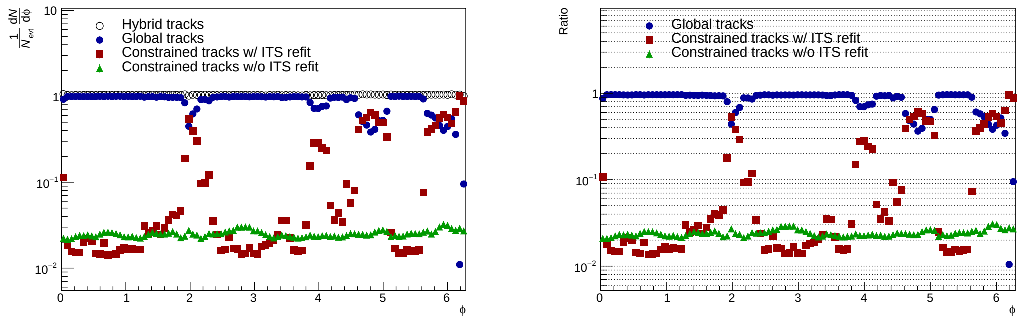

(a) Distribution

(b) Ratio

Figure 3.7: Comparison of the reconstructed track distributions as a function of ϕ for the hybrid track selection and its sub-components obtained from the minimum-bias Monte Carlo production.

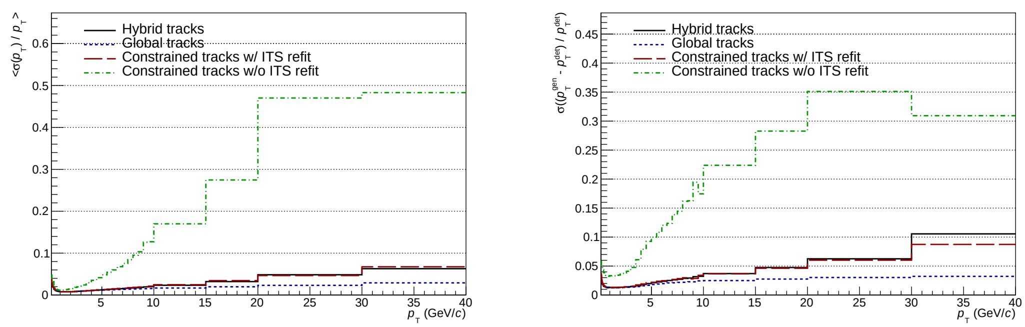

(a) Tracking fit.

(b) Relative difference from truth.

Figure 3.8: Transverse momentum resolution of hybrid tracks and of each sub-component as a function of p_{T} obtained from the minimum-bias Monte Carlo production.

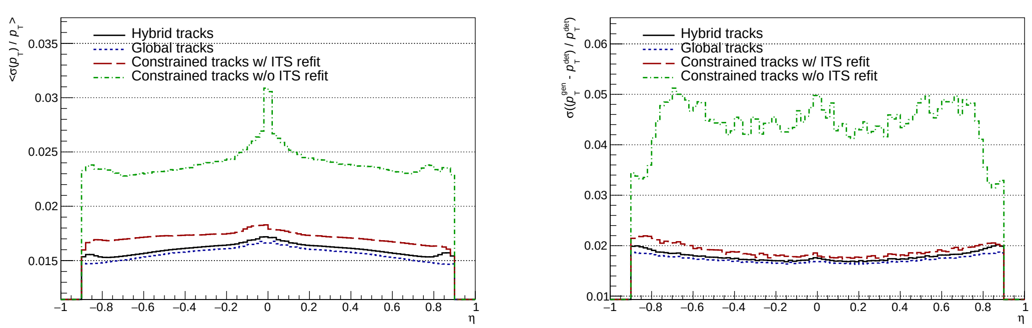

(a) Tracking fit.

(b) Relative difference from truth.

Figure 3.9: Transverse momentum resolution of hybrid tracks and of each sub-component as a function of η obtained from the minimum-bias Monte Carlo production.

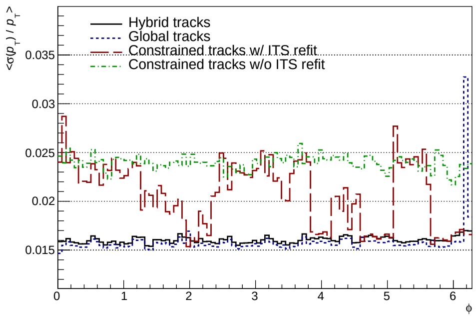

(a) Tracking fit.

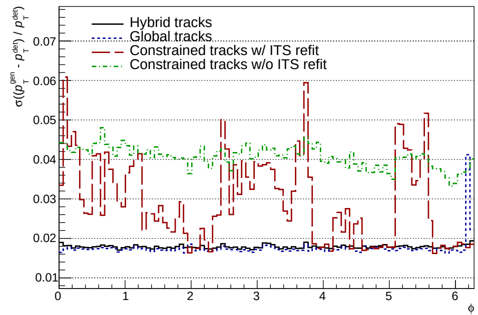

(b) Relative difference from truth.

Figure 3.10: Transverse momentum resolution of hybrid tracks and of each sub-component as a function of ϕ obtained from the minimum-bias Monte Carlo production.

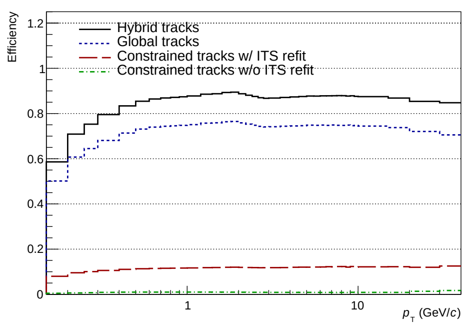

(a) Efficiency vs. p_{T}

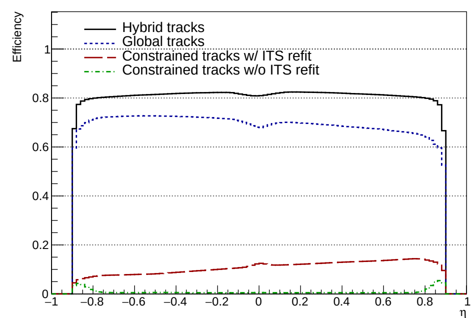

(b) Efficiency vs. η

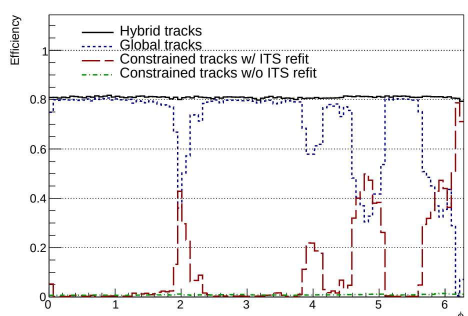

(c) Efficiency vs. ϕ

Figure 3.11: Track reconstruction efficiency of hybrid tracks and of each sub-component obtained from the minimum-bias Monte Carlo production.

p_{T}, η and ϕ, respectively, from the minimum-bias Monte Carlo production. The distributions are very similar to those obtained from data. The overall fraction of constrained tracks is 14.4% and 2.4% for tracks with and without ITS refit, respectively. Figures 3.8, 3.9 and 3.10 show the transverse momentum resolution of hybrid tracks as a function of p_{T}, η and ϕ, respectively, estimated from the minimum-bias Monte Carlo production. The resolution is estimated both from the tracking fit covariance matrix (as done in data) and from the width of the distribution of the relative difference between the detector-level and the generator-level (truth) momenta. The small discrepancies between the momentum resolutions obtained using the two methods, particularly as a function of η, are not fully understood and are under investigation. Figure 3.11 shows the tracking reconstruction efficiency of hybrid tracks as a function of p_{T}, η and ϕ from the minimum-bias Monte Carlo production. The efficiency is about 70% for $p_{\mathrm{T}} = 0.2$ GeV/c, approaches its maximum of 90% for $p_{\mathrm{T}} \approx 2$ GeV/c and then it decreases and reaches a plateau at about 85%.

3.5.3 Track selection criteria for $\mathbf{D^0}$ mesons

For the identification of the decay products of the D^0 mesons, stricter track selections were utilized to achieve the best possible momentum resolution. In this case, tracking uniformity is not a requirement, therefore only the global tracks described above were used. Tracks were required to have $|\eta| < 0.8$ and $p_{\mathrm{T}} > 0.7$ GeV/c.

Both track selection criteria were tuned and used extensively in several analyses published by ALICE, including measurements of jets in pp [153, 154] and Pb–Pb [155, 156] collisions and the D-meson p_{T}-differential cross sections in pp collisions at $\sqrt{s} = 7$ TeV [106].

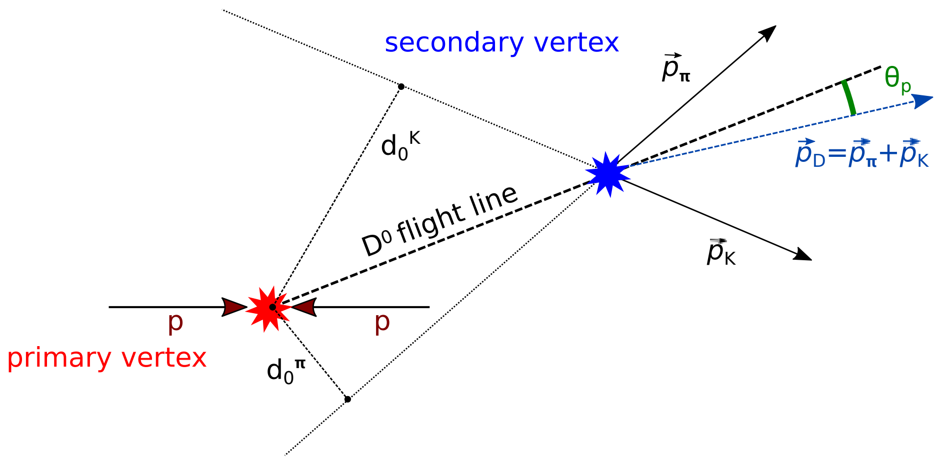

Figure 3.12: Schematics of the decay topology of a D^0 meson.

3.6 Raw Yield Extraction

3.6.1 D^0 Meson Reconstruction

During the physics data reconstruction, tracks of opposite charge were paired into decay-vertex candidates. The large majority of these vertices is made of combinatorial background, i.e. pairs that do not correspond to the final state of a D^0-meson decay. Later, these vertices were analyzed to extract a sample of D^0-meson decay-vertex candidates, where the signal is enhanced compared to the combinatorial background. In the following we will go through the kinematic, topological and PID cuts used in this analysis.

Kinematic Cuts

A fiducial acceptance cut was applied on the D^0-meson candidate rapidity, $|y_{\rm D}| < y_{\rm fid}(p_{\rm T,D})$, with $y_{\rm fid}(p_{\rm T,D})$ increasing from 0.5 to 0.8 in the D^0-meson transverse momentum interval $2 < p_{\rm T,D} < 5$ GeV/c and $y_{\rm fid}(p_{\rm T,D}) = 0.8$ for $p_{\rm T,D} > 5$ GeV/c. Outside of this selection the efficiency drops rapidly as a consequence of the detector acceptance and the kinematic cuts applied to the tracks.

Table 3.3: Topological cuts applied to the D^0-meson candidates. The last column refers to both residuals of the impact parameters, i.e. tr = K, π.

$p_{\mathrm{T,D}}$ (GeV/c)	DCA (μm)	$\cos(\theta^*)$	$d_0^{\mathrm{K}} d_0^{\pi}$ (μm^2)	$\cos(\theta_{\mathrm{p}})$	L^{xy}/σ	$(d_{0,\mathrm{tr}}^{xy,\mathrm{exp}} - d_{0,\mathrm{tr}}^{xy})/\sigma_{\Delta}$
$2-3$	300	0.8	-20000	0.90	–	2
$3-4$	300	0.8	-12000	0.90	–	2
$4-5$	300	0.8	-8000	0.85	–	2
$5-6$	300	0.8	-8000	0.85	–	3
$6-7$	300	0.8	-8000	0.85	–	3
$7-8$	300	0.8	-7000	0.85	–	3
$8-10$	300	0.9	-5000	0.85	–	3
$10-12$	300	0.9	-5000	0.85	–	3
$12-16$	300	–	10000	0.85	–	4
$16-20$	300	–	–	0.85	–	3
$20-24$	300	–	–	0.85	–	2.5
$24-30$	300	–	–	0.85	1	2.5

Decay Topology

The D^0 meson has a mean proper decay length of $c\tau = 123$ μm. Its decay vertex (also referred to as *secondary vertex*) is typically displaced from the primary vertex of the collision by a few hundreds μm. This displacement results in a specific topology of the system composed of the primary and secondary vertices that was exploited to sift the signal out of the combinatorics. The typical decay topology is illustrated in Fig. 3.12, where some of the variables used in the selection cuts are also defined. Table 3.3 shows the full list of the decay topology selection cuts.

Distance-of-Closest-Approach (DCA) The DCA between the pion and kaon tracks is used to reject pairs of tracks originating from different vertices, e.g. one from the primary vertex and one from the decay of a long-lived hadron. Within the experimental uncertainties it should be very close to zero for tracks originating from the same vertex.

Cosine of θ^* The cosine of the angle between the kaon momentum in the D^0-meson rest frame and the D^0-meson boost direction is uniformly distributed between -1 and 1: the kaon and the pion are emitted isotropically back-to-back in the D^0-meson rest frame. For pairs of tracks belonging to the combinatorial background, the cosine of θ^* is not uniformly distributed and peaks at values close to either -1 and 1.

Decay length The decay length L is the distance between the primary and the secondary vertex. Since the best vertex resolution is obtained in the plane transverse to the beam direction, the cut was applied only on the projection of the decay length to this plane, L^{xy}. It is normalized dividing by the experimental resolution σ^{xy}. The cut $L^{xy}/\sigma^{xy} > 1$ was applied only to the D^0-meson candidates with $24 < p_{\mathrm{T,D}} < 30$ GeV/c.

Impact parameters d_0^{K} and d_0^{π} The distances between the trajectories of each of the decay products and the primary vertex are of the same order of magnitude as the displacement of the secondary vertex from the primary vertex, i.e. $\sim 100\ \mu m$. Furthermore, the projections of the primary vertex into either trajectories are always found on opposite sides with respect to the primary vertex in the decay plane. A selection cut based on the (signed) product of the two impact parameters is thus more powerful then selecting on each impact parameter separately.

Residuals of the impact parameters Fixing the angles between the momentum of the D^0 meson and the momenta of each of the decay products $\theta^{xy}_{\mathrm{D,K}}$, $\theta^{xy}_{\mathrm{D},\pi}$, the expected impact parameters of the kaon and pion can be calculated using the measured decay length:

$$d^{xy,\mathrm{exp}}_{0,\mathrm{K}} = L^{xy}\sin(\theta^{xy}_{\mathrm{D,K}}), d^{xy,\mathrm{exp}}_{0,\pi} = L^{xy}\sin(\theta^{xy}_{\mathrm{D},\pi}). \tag{3.11}$$

Table 3.4: D^0-meson candidates classified according to the PID selection outcomes.

Minimum $p_{T,D}$ (GeV/c)	D^0	$\overline{D^0}$	No-PID
0	486318	474822	111290
fraction:	4.53×10^{-1}	4.43×10^{-1}	1.04×10^{-1}
1	120215	119392	43127
fraction:	4.25×10^{-1}	4.22×10^{-1}	1.53×10^{-1}
2	38404	38576	26677
fraction:	3.70×10^{-1}	3.72×10^{-1}	2.57×10^{-1}
3	30185	30353	20894
fraction:	3.71×10^{-1}	3.73×10^{-1}	2.57×10^{-1}
4	13234	13389	8036
fraction:	3.82×10^{-1}	3.86×10^{-1}	2.32×10^{-1}

The xy superscript indicates that variables are projected in the plane transverse to the beam direction. The residuals are defined as:

$$(d_{0,K}^{xy,\exp} - d_{0,K}^{xy})/\sigma_\Delta, (d_{0,\pi}^{xy,\exp} - d_{0,\pi}^{xy})/\sigma_\Delta, \tag{3.12}$$

where $d_{0,K}^{xy}$ and $d_{0,\pi}^{xy}$ are the measured impact parameters of the kaon and the pion, respectively; σ_Δ is the experimental resolution of the residuals. Requiring these residuals to be smaller than $3-4$ significantly reduces both the combinatorial background and the fraction of D^0 mesons originating from B-hadron decays, while cutting almost no signal.

Pointing angle $\boldsymbol{\theta_p}$ For real D^0 mesons the angle between the direction obtained connecting the primary and secondary vertex (D^0-meson flight direction) and the direction of the momentum of D^0-meson $\vec{p}_D = \vec{p}_K + \vec{p}_\pi$ is very small but non-zero because of finite detector resolution. This is a rather powerful selection cut, since for the combinatorial background the distribution of the $\cos(\theta_p)$ is flat.

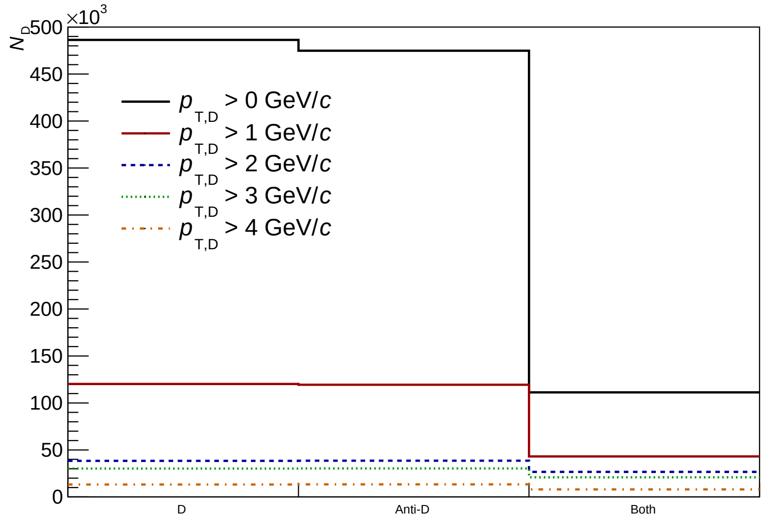

Figure 3.13: D^0-meson candidates classified according to the PID selection outcomes.

Particle Identification

The Particle Identification (PID) of pions and kaons was performed using the measurements of the specific energy loss $\mathrm{d}E/\mathrm{d}x$ in the TPC and the time-of-flight provided by the TOF detector. The following variable was defined for both observables:

$$N_{\sigma,\mathrm{det}} = \frac{S_{\mathrm{det}} - S_{\mathrm{det}}(H_i)}{\sigma_{\mathrm{det}}}, \tag{3.13}$$

where det is either TPC or TOF, S_{det} is the measured PID signal, $S_{\mathrm{det}}(H_i)$ is the expected PID signal for particle hypothesis H_i and σ_{det} is the experimental resolution. $N_{\sigma,\mathrm{det}}$ is expected to be distributed as a Gaussian centered at zero with width equal to one. When both observables are available, a combined discriminator is defined:

$$N_{\sigma,\mathrm{comb}} = \sqrt{N^2_{\sigma,\mathrm{TPC}} + N^2_{\sigma,\mathrm{TOF}}}. \tag{3.14}$$

The pion or kaon hypothesis was rejected when $N_{\sigma,\mathrm{comb}} > 3$. This cut corresponds to a circular cut in the $N_{\sigma,\mathrm{TPC}} - N_{\sigma,\mathrm{TOF}}$ plane, rather than a rectangular cut that would

Table 3.5: D^0-meson candidates classified according to the PID selection outcomes obtained from the minimum-bias Monte Carlo production.

Minimum $p_{T,D}$ (GeV/c)	D^0	$\overline{D^0}$	No-PID	Wrong-PID
0	506777	490442	111969	80
fraction:	4.57×10^{-1}	4.42×10^{-1}	1.01×10^{-1}	7.21×10^{-5}
1	108538	107385	38549	77
fraction:	4.27×10^{-1}	4.22×10^{-1}	1.51×10^{-1}	3.03×10^{-4}
2	37470	37666	24754	65
fraction:	3.75×10^{-1}	3.77×10^{-1}	2.48×10^{-1}	6.51×10^{-4}
3	30286	30453	19980	55
fraction:	3.75×10^{-1}	3.77×10^{-1}	2.48×10^{-1}	6.81×10^{-4}
4	14048	14093	8457	38
fraction:	3.84×10^{-1}	3.85×10^{-1}	2.31×10^{-1}	1.04×10^{-3}

result if each variable was used separately. If only one of the two PID observables was available for a specific track (typically the TPC $\mathrm{d}E/\mathrm{d}x$), then $N_{\sigma,\mathrm{det}} > 3$ was used instead. In some cases the PID was inconclusive, i.e. neither the pion nor the kaon hypothesis could be excluded. In such cases both mass combinations were considered: the pair is counted twice with the two possible mass assignments. If the pair does not correspond to a real D^0 meson, it produces two background entries; otherwise it produces a signal entry and a background entry. In much rarer cases the wrong mass hypothesis is accepted while the correct one is rejected. In such cases the real D^0 meson is lost and the entry contributes to the background only. In either case – inconclusive or wrong PID of real decay products – the sample of D^0-meson candidates will include *reflections*, defined as pion-kaon pairs that come from the decay of a real D^0 meson, but with the reflected mass hypothesis.

Figure 3.13 and Table 3.4 show a summary of how D^0-meson candidates are classified according to the PID selection. The identification of the sign of the charge of the kaon and the pion forces the candidate to be either a D^0 or a $\overline{D^0}$. For this reason they are indicated as D^0 or $\overline{D^0}$. For $p_{T,D} > 2$ GeV/c about 74% of the candidates are classified uniquely as either D^0 or $\overline{D^0}$ candidates. For the remaining candidates the PID analysis was inconclusive and therefore both mass hypotheses were taken into

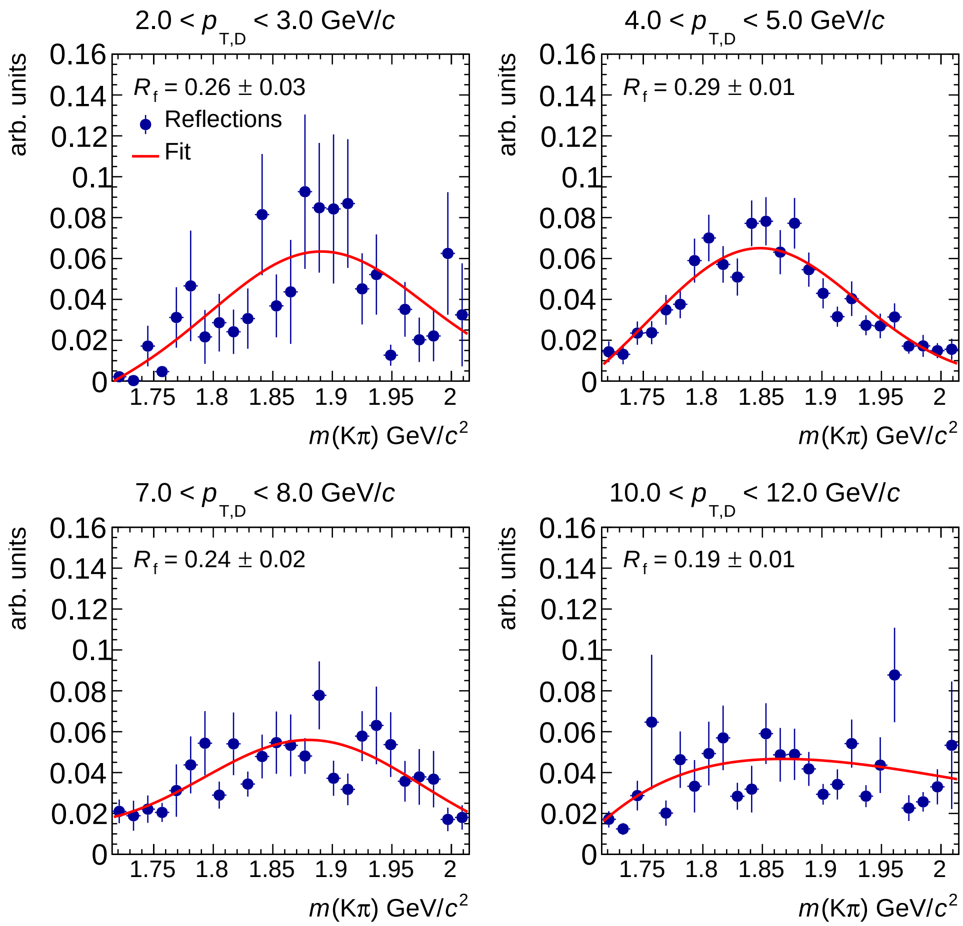

Figure 3.14: Invariant mass distribution of D^0-meson reflections in different ranges of $p_{T,D}$ obtained from the charm-enhanced Monte Carlo production. The distributions are shown as blue symbols. The red curve represents a fit with a double Gaussian function.

consideration resulting in two D^0-meson candidates for a single pair of tracks. The detector PID performance from data was also compared with the PID performance observed in the minimum-bias Monte Carlo production. Table 3.5 shows a summary of the PID performance obtained from the simulation. The last column shows also the rate of the PID misidentification, i.e. candidates that correspond to real D^0 or $\overline{D^0}$ for which the PID selection returned the wrong (reflected) mass hypothesis. This rate is about 6.5 of every $10,000$ (for $p_{T,D} > 2$ GeV/c).

It is important to study the invariant mass distribution of the D^0-meson reflections to look for structures that may arise, in that they constitute a source of correlated background as opposed to the combinatorial background coming from unrelated track pairs. Figure 3.14 shows the invariant mass distribution of D^0-meson reflections for different $p_{T,D}$ ranges. They include candidates for which PID was either inconclusive or wrong. These distributions were obtained from the charm-enhanced Monte Carlo production. The invariant mass distribution of the D^0-meson reflections shows a broad peak around the D^0 mass, which becomes even broader at higher momenta. R_f is defined as the ratio of the reflections over the real D^0 mesons in the invariant mass interval $1.715 < m_{inv} < 2.015$ GeV/c^2. It shows a non-monotonic pattern: it is about 0.26 for $2 < p_{T,D} < 3$ GeV/c, reaches its maximum 0.29 for $4 < p_{T,D} < 5$ GeV/c and then decreases again for higher momenta reaching 0.17 for $15 < p_{T,D} < 30$ GeV/c. This pattern is explained by the better PID performance at low momenta, which reduces the chances of inconclusive or wrong PID. On the other hand the invariant mass of the D^0 reflections becomes broader at higher momenta because of the kinematics, causing the reflections entries to spread farther away from the D^0-meson mass peak region. These distributions were fit with a double Gaussian function to smooth out statistical fluctuations and templates were generated from them. As we shall see in Section 3.6.3, these templates were used in the statistical analysis of the invariant mass distributions in data to model more accurately this component of the background.

3.6.2 Jet Finding and Tagging

Similar measurements performed in the past by other experiments implemented separate reconstruction chains for the D mesons and the jets. The tagging of the charm jets was typically achieved via a geometrical matching between the jet and the D meson [120, 122, 126, 157]. This technique comes with some important drawbacks, especially for low-momentum jets and/or low-momentum D mesons. Figure 3.15 shows the probability density distribution of the angle between the kaon/pion mo-

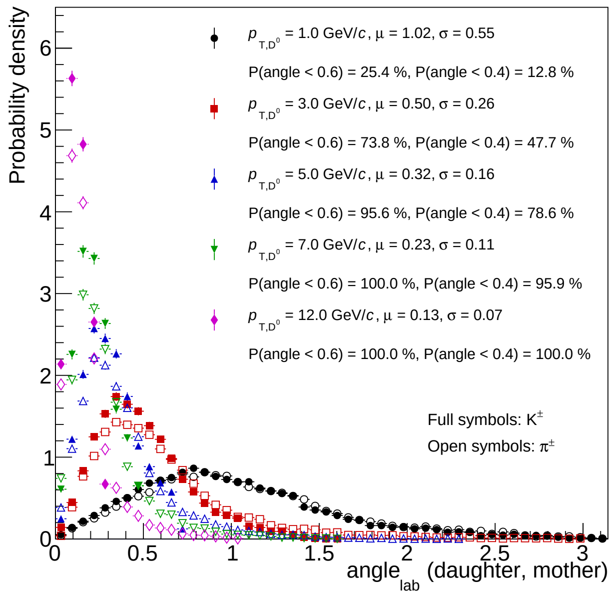

Figure 3.15: Probability density distribution of the angle between the momentum of the kaon (full symbols) or the pion (open symbols) and the momentum of the D^0 meson for different transverse momenta of the D^0 meson.

mentum and the D^0-meson momentum, for different transverse momenta of the D^0 meson. These distributions were obtained from a simple kinematic simulation of the D^0-meson decay. More than 50% of the D^0 mesons with $p_{T,D} = 3$ GeV/c have their decay products emitted at an angle larger than 0.4 rad with respect to the D^0-meson momentum direction. The decay products of low-momentum D^0 mesons are often found outside of the reconstructed jet cone (typically $R < 1$) that is physically correlated with the D^0 meson. As a result the jet momentum misses the fraction carried by the D^0 meson, which degrades the jet momentum resolution and the angular resolution of the jet axis. The geometrical matching efficiency between the jet axis and the D^0 momentum direction is also affected.

In this analysis a different approach was used. Once the D^0-meson candidates were identified, their four-momenta were used to replace their own decay products in the set of tracks that constitutes the input of the anti-k_T algorithm. Tagging was simply achieved looking for the jet that contains the D^0-meson candidate among its

Table 3.6: Classification of the analyzed events according to the number of D^0-meson candidates that pass all the selections (including topological and PID).

Minimum $p_{T,D}$ (GeV/c)	1 candidates	2 candidates	3 candidates	4 candidates
0	1032119	19239	571	30
fraction:	3.04×10^{-3}	5.67×10^{-5}	1.68×10^{-6}	8.84×10^{-8}
1	276900	2828	54	4
fraction:	8.16×10^{-4}	8.34×10^{-6}	1.59×10^{-7}	1.18×10^{-8}
2	101804	891	21	2
fraction:	3.00×10^{-4}	2.63×10^{-6}	6.19×10^{-8}	5.90×10^{-9}
3	79946	712	18	2
fraction:	2.36×10^{-4}	2.10×10^{-6}	5.31×10^{-8}	5.90×10^{-9}
4	34026	293	13	2
fraction:	1.00×10^{-4}	8.64×10^{-7}	3.83×10^{-8}	5.90×10^{-9}

constituents. For this analysis, the jet resolution parameter was $R = 0.4$ and the p_T recombination scheme was used.

This procedure is repeated independently for each D^0-meson candidate, i.e. each candidate is treated as if it was the only one in the event. This is done because multiple candidates can potentially share the same decay track, although this is a very rare occurrence. Figure 3.16 and Table 3.6 show a summary of the distribution of the number of candidates found in a single event. Of all the analyzed events, only about 0.3% contain at least one candidate of any momentum passing all analysis cut. This fraction reduces further to 0.03% when we require the candidates to have momentum $p_{T,D} > 2$ GeV/c. Out of the events that contain at least one candidate, only about 1.9% (0.87%) of them contain 2 or more candidates for $p_{T,D} > 0$ ($p_{T,D} > 2$ GeV/c).

3.6.3 Statistical Analysis of the Invariant Mass Distributions

In the previous Section we have seen how the sample of D^0-meson tagged jet candidates is constructed from the data. For each D^0-meson tagged jet candidate the following variables were measured:

$\boldsymbol{m_{\mathrm{inv}}}$ Invariant mass of the kaon-pion pair

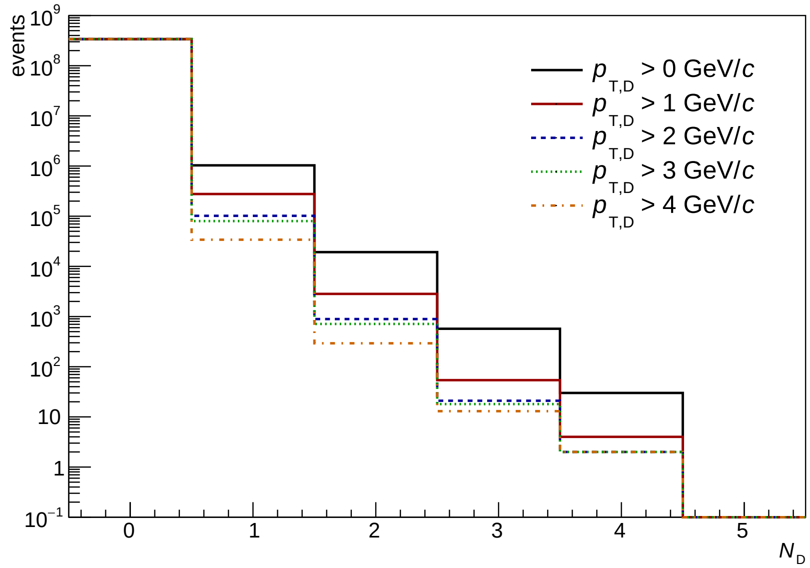

Figure 3.16: Classification of the analyzed events according to the number of D^0-meson candidates that pass all the selections (including topological and PID) in pp collisions at $\sqrt{s}$ = 7 TeV. The different lines corresponds to different cuts on the minimum $p_{T,D}$ as indicated in the legend.

$\boldsymbol{p_{T,D}}$ Transverse momentum of D^0-meson candidate

$\boldsymbol{p^{ch}_{T,jet}}$ Transverse momentum of the charged jet candidate

$\boldsymbol{z^{ch}_{||}}$ Jet momentum fraction carried by the D^0-meson candidate

This Section focuses on the statistical analysis aimed at separating the signal from the combinatorial background.

Invariant Mass Fits

The distribution of the invariant mass m_{inv} in the range $1.715 < m_{inv} < 2.015$ GeV/c^2 is shown in Fig. 3.17a, for $5 < p^{ch}_{T,jet} < 30$ GeV/c, separately for various intervals of $p_{T,D}$ spanning the range $2 < p_{T,D} < 30$ GeV/c. In Fig. 3.17b candidates are instead classified according to $p^{ch}_{T,jet}$ and the invariant mass distributions shown for different intervals of this variable. Finally the invariant mass distributions are also shown in Figs. 3.17c and 3.17d in various intervals of $z^{ch}_{||}$, for $5 < p^{ch}_{T,jet} < 15$ GeV/c and

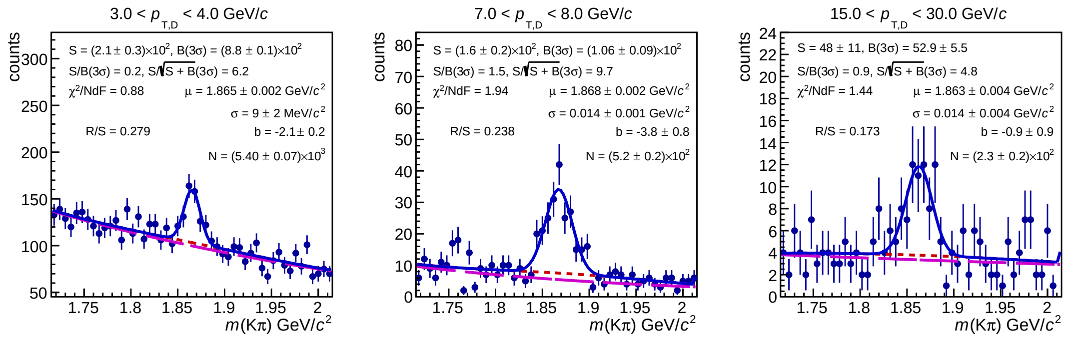

(a) Intervals of $p_{\mathrm{T,D}}$, with $5 < p_{\mathrm{T,jet}}^{\mathrm{ch}} < 30$ GeV/c.

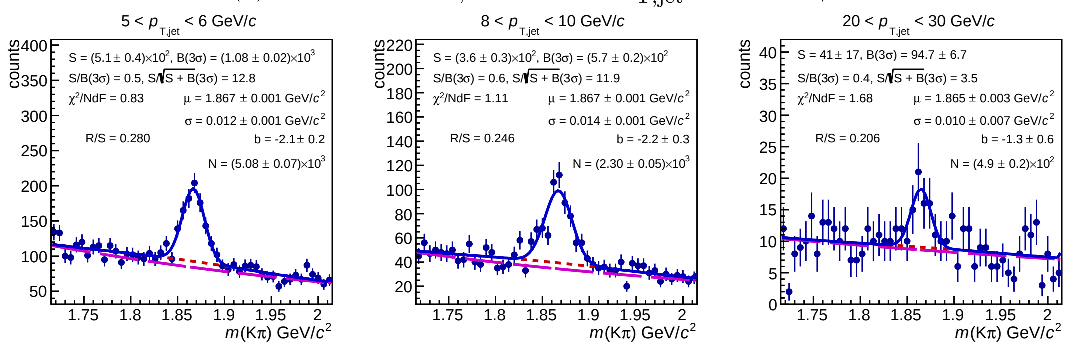

(b) Intervals of $p_{\mathrm{T,jet}}^{\mathrm{ch}}$, with $p_{\mathrm{T,D}} > 3$ GeV/c.

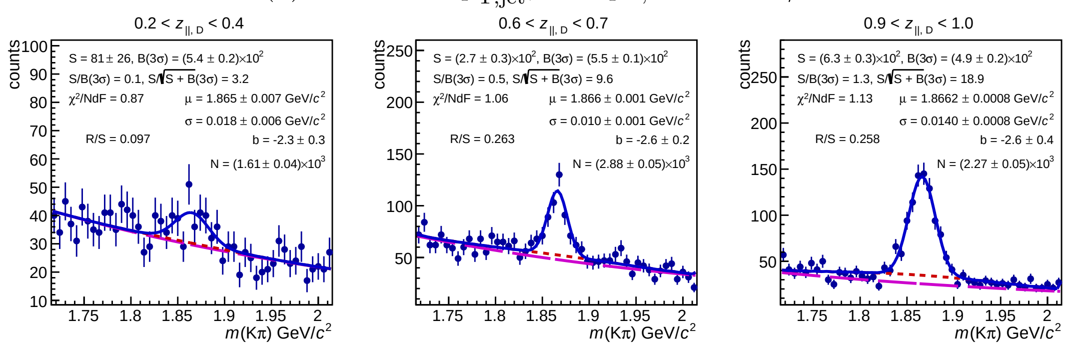

(c) Intervals of $z_{||}^{\mathrm{ch}}$, with $p_{\mathrm{T,D}} > 2$ GeV/c and $5 < p_{\mathrm{T,jet}}^{\mathrm{ch}} < 15$ GeV/c.

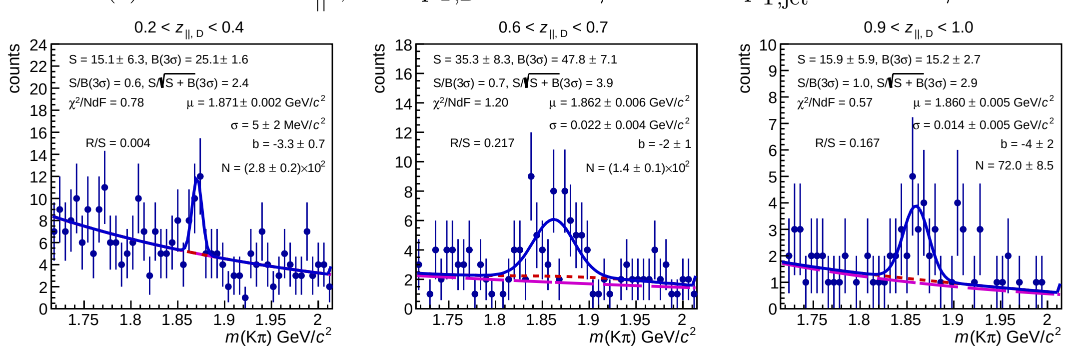

(d) Intervals of $z_{||}^{\mathrm{ch}}$, with $p_{\mathrm{T,D}} > 6$ GeV/c and $15 < p_{\mathrm{T,jet}}^{\mathrm{ch}} < 30$ GeV/c.

Figure 3.17: Invariant mass distributions of D^0-meson tagged jets.

$15 < p_{\mathrm{T,jet}}^{\mathrm{ch}} < 30$ GeV/c, respectively. The invariant mass distributions feature a peak around the D^0-meson mass $m_{\mathrm{D}^0} = 1.865$ GeV/c^2 [67]. The peak is more or less prominent depending on the kinematic ranges considered. It lies on top of a smooth background, whose shape is regular and also depends on the kinematic ranges considered. Since the D^0-meson lifetime is long, the intrinsic width of its peak is zero. The observed width depends solely on the experimental resolution. The shape of the peak can thus be approximated by a Gaussian function. The background includes two main components:

combinatorial background track pairs that are not the decay products of any particle;

D^0-meson reflections track pairs that are the decay products of a D^0 meson but with the wrong mass assignments, i.e. the mass of the pion was assigned to the kaon and viceversa (because of inconclusive or wrong PID).

The first source of background can be modeled with an exponential function. Other choices are also possible, such as a polynomial of order N, and will be considered when assessing the systematic uncertainties. The second source of background features a broad peak around the D^0-meson mass, as we have seen in Section 3.6.1 and particularly Fig. 3.14. Templates were constructed using the Monte Carlo charm-enhanced production for each kinematic range of interest. The templates were fit with a double Gaussian function (sum of two Gaussian functions) to smooth out statistical fluctuations.

The invariant mass distributions were fit with a function which is the sum of a Gaussian, modeling the signal, and the two background components described above:

$$f(m_{\mathrm{inv}}) = a m_{\mathrm{inv}}^{b} + \frac{S}{\sigma_0\sqrt{2\pi}} e^{-\left(\frac{m-m_0}{2\sigma_0}\right)^2} + S \cdot R_{\mathrm{f}} \cdot T(m_{\mathrm{inv}}), \tag{3.15}$$

where m_{inv} is the invariant mass, a, b, S, m_0, σ_0 are free parameters; R_{f} and $T(m_{\mathrm{inv}})$

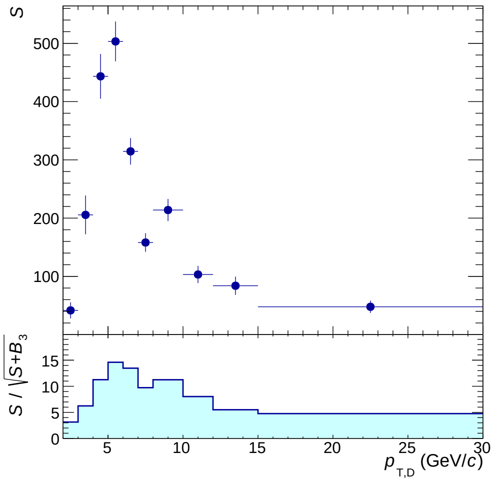

(a) Signal (top) and significance (bottom).

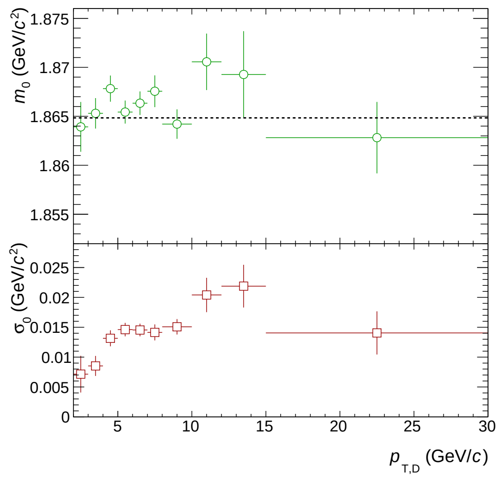

(b) m_0 (top) and σ_0 (bottom).

Figure 3.18: Parameters extracted from the fit of the invariant mass distributions in bins of $p_{\mathrm{T,D}}$ for $5 < p_{\mathrm{T,jet}}^{\mathrm{ch}} < 30$ GeV/c.

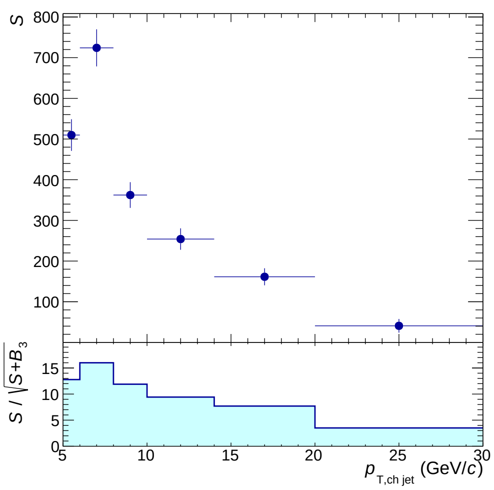

(a) Signal (top) and significance (bottom).

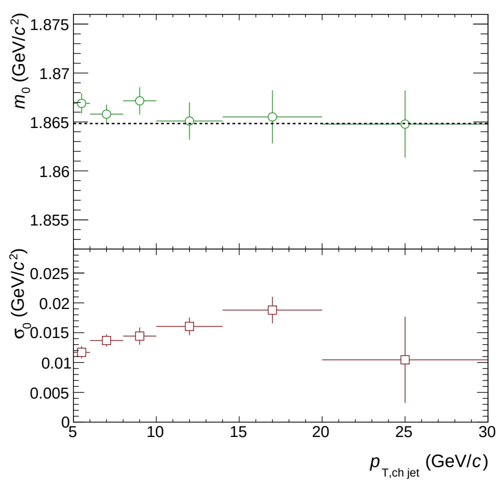

(b) m_0 (top) and σ_0 (bottom).

Figure 3.19: Parameters extracted from the fit of the invariant mass distributions in bins of $p_{\mathrm{T,jet}}^{\mathrm{ch}}$ for $p_{\mathrm{T,D}} > 3$ GeV/c.

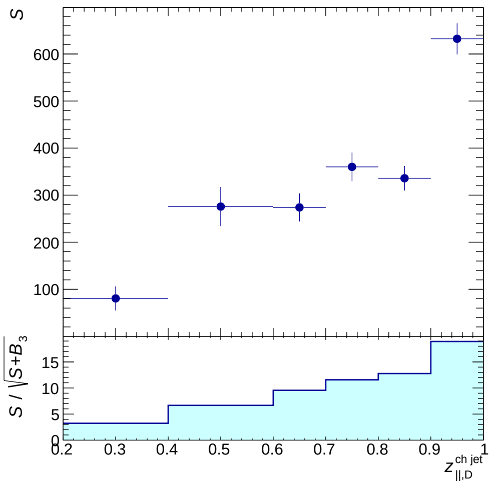

(a) Signal (top) and significance (bottom).

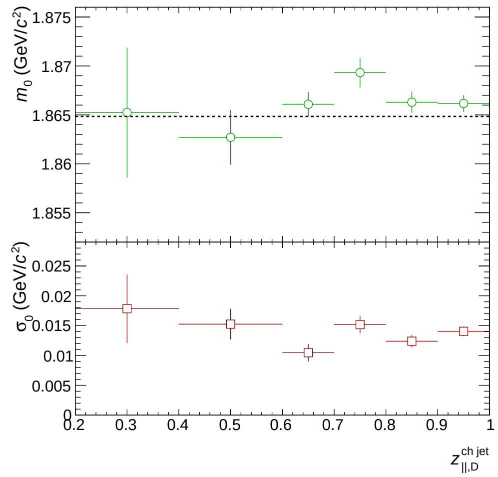

(b) m_0 (top) and σ_0 (bottom).

Figure 3.20: Parameters extracted from the fit of the invariant mass distributions in bins of $z_{||}^{\mathrm{ch}}$ for $5 < p_{\mathrm{T,jet}}^{\mathrm{ch}} < 15$ GeV/c and $p_{\mathrm{T,D}} > 2$ GeV/c.

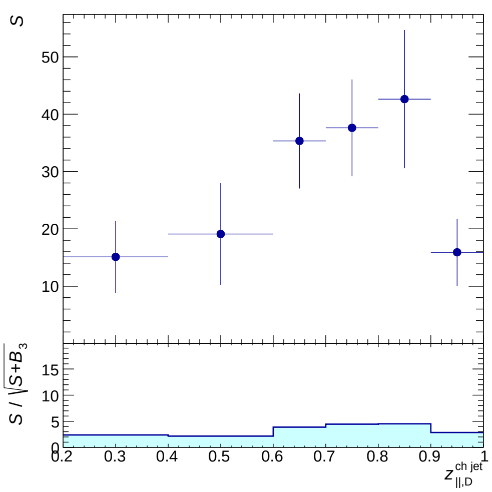

(a) Signal (top) and significance (bottom).

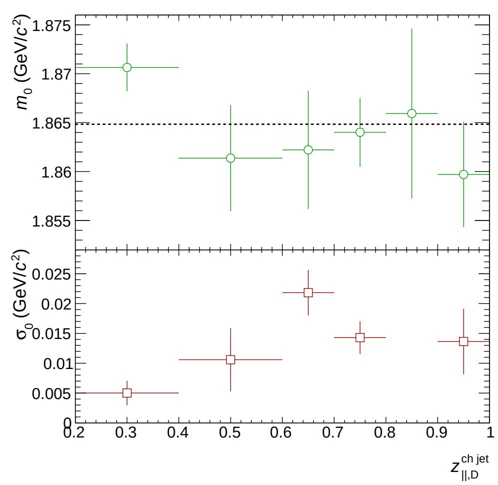

(b) m_0 (top) and σ_0 (bottom).

Figure 3.21: Parameters extracted from the fit of the invariant mass distributions in bins of $z_{||}^{\mathrm{ch}}$ for $15 < p_{\mathrm{T,jet}}^{\mathrm{ch}} < 30$ GeV/c and $p_{\mathrm{T,D}} > 6$ GeV/c.

are the ratio reflections over signal and the double Gaussian template modeling the reflections, respectively, and are different for each kinematic range ($p_{\mathrm{T,D}}$, $p_{\mathrm{T,jet}}^{\mathrm{ch}}$, $z_{||}^{\mathrm{ch}}$) considered. The normalization factor in front of the Gaussian function is such that the parameter S corresponds to the integral of the Gaussian function itself. The fit functions are shown with blue curves in Figs. 3.17a, 3.17b, 3.17c and 3.17d. The red dotted curves and the magenta dashed curves represent the background functions, with and without the reflection component, respectively.

The results of the invariant mass fits are summarized in Figures 3.18, 3.19, 3.20 and 3.21 for the kinematic selections defined above. The mass parameter is in agreement with the expected D^0-meson mass within the uncertainties. The peak widths tend to increase with $p_{\mathrm{T,D}}$ because of the track parameter resolution, which becomes larger at higher momenta. It varies in the range $8 - 20$ MeV/c^2. The significance of the fits is defined as:

$$\frac{S}{\sqrt{S + B_3}}, \tag{3.16}$$

where B_n is the integral of the background function (including the reflection component) in the $n\sigma_0$ window around the peak center m_0. It varies between 3 and 16. Relative statistical uncertainties on the raw yields vary from a few percent to about 45%.

Side-Band Subtraction Method

An alternative method to extract raw yields as a function of any variable x is the side-band subtraction. The symbol x represents any measurable property of the D^0-meson tagged jets, e.g. $x = z_{||}^{\mathrm{ch}}$ or $x = p_{\mathrm{T,jet}}^{\mathrm{ch}}$. The invariant mass analysis was performed as a function of the D^0-meson transverse momentum. The peak region and the side-band regions were established from the invariant mass fits for each $p_{\mathrm{T,D}}$ interval considered. They are defined as:

$$|m_{\mathrm{inv}} - m_0| < 2\sigma_0 \tag{3.17}$$

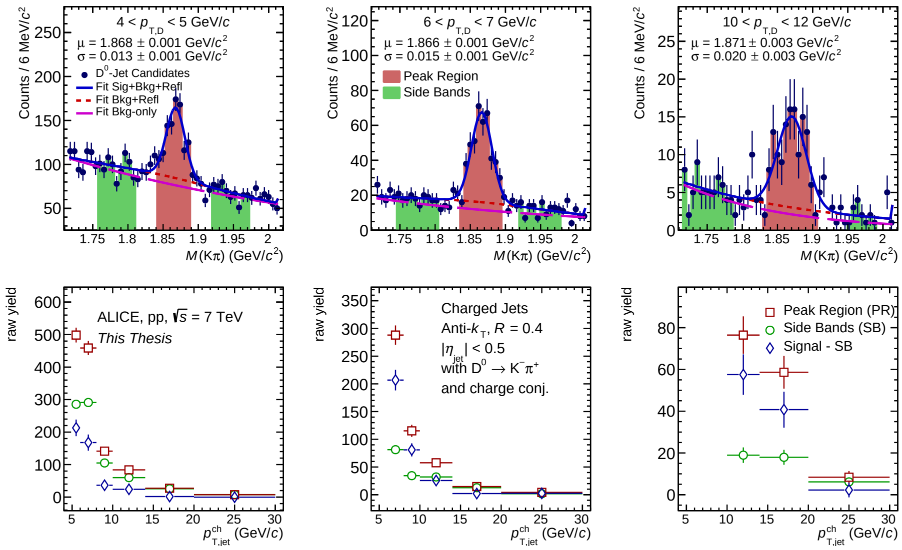

Figure 3.22: Top: invariant mass distributions of D^0-meson tagged jets for different intervals of $p_{\mathrm{T,D}}$, as indicated in each panel. The shaded green (red) areas represent the side-band (peak) regions. Bottom: $p_{\mathrm{T,jet}}^{\mathrm{ch}}$ distributions of D^0-meson tagged jet candidates in the side-band (green) and peak (red) regions for the same $p_{\mathrm{T,D}}$ intervals as the corresponding top panels; the blue symbols represent the subtracted raw yields.

and

$$4\sigma_0 < |m_{\mathrm{inv}} - m_0| < 8\sigma_0, \tag{3.18}$$

respectively. The D^0-meson tagged jet candidates belonging to the peak region comprise a mixture of signal and background. Conversely, the side bands are practically signal-free since they are far enough from the D^0-meson mass peak. Distributions as a function of x were constructed separately for candidates belonging to the peak region and candidates belonging to the side bands. The side-band distributions were normalized to B_2, the integral of the background function in the $2\sigma_0$ window around the peak center m_0. The raw yield as a function of x was obtained as:

$$N_x^{\mathrm{raw}} = \sum_{p_{\mathrm{T,D}}} \left[N_x^{\mathrm{PR}}(p_{\mathrm{T,D}}) - \frac{B_2(p_{\mathrm{T,D}}) \cdot N_x^{\mathrm{SB}}(p_{\mathrm{T,D}})}{\sum_x N_x^{\mathrm{SB}}(p_{\mathrm{T,D}})} \right], \tag{3.19}$$

where $N_x^{\mathrm{PR}}(p_{\mathrm{T,D}})$ and $N_x^{\mathrm{SB}}(p_{\mathrm{T,D}})$ are the peak-region and side-band distributions, respectively, as a function of x in each interval of $p_{\mathrm{T,D}}$.

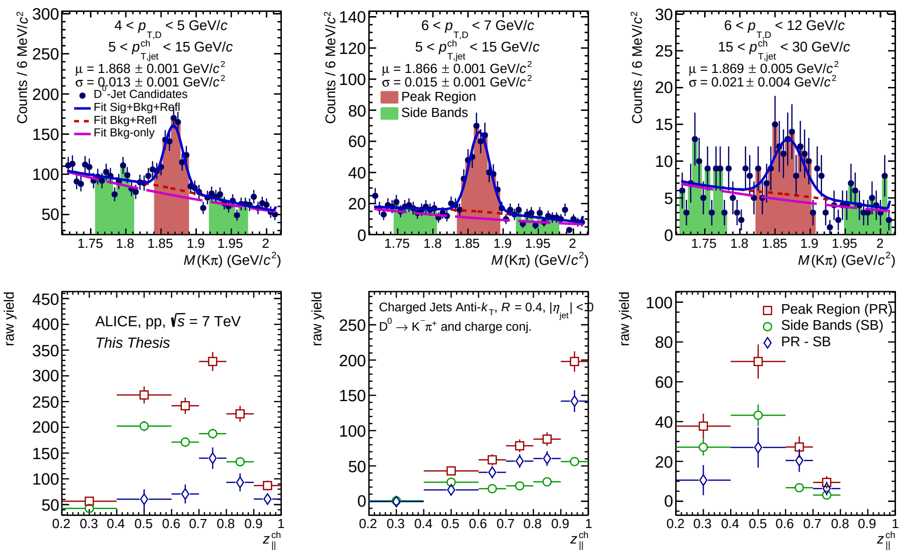

Figure 3.23: Top: invariant mass distributions of D^0-meson tagged jets for different intervals of $p_{\mathrm{T,D}}$ and $p^{\mathrm{ch}}_{\mathrm{T,jet}}$, as indicated in each panel. The shaded green (red) areas represent the side-band (peak) regions. Bottom: $z^{\mathrm{ch}}_{||}$ distributions of D^0-meson tagged jet candidates in the side-band (green) and peak (red) regions for the same $p_{\mathrm{T,D}}$ and $p^{\mathrm{ch}}_{\mathrm{T,jet}}$ intervals as the corresponding top panels; the blue symbols represent the subtracted raw yields.

The peak and side-band regions are indicated as shaded areas in the invariant mass distributions for various ranges of $p_{\mathrm{T,D}}$ and $p^{\mathrm{ch}}_{\mathrm{T,jet}}$ in the top panels of Figs. 3.22 and 3.23. The side-band regions are represented by the green-shaded areas, while the peak regions are represented by the red-shaded areas. The bottom panels of Fig. 3.22 shows the peak-region (red) and side-band (green) $p^{\mathrm{ch}}_{\mathrm{T,jet}}$ distributions in the same $p_{\mathrm{T,D}}$ ranges of the corresponding top panels. The subtracted raw yields are shown in blue (corresponding to the argument of the sum on the right side of Eq. 3.19). Similarly, the bottom panels of Fig. 3.23 show the distributions as a function of $z^{\mathrm{ch}}_{||}$.

The two methods were shown to yield equivalent results within their statistical uncertainties. Figure 3.24 show the comparison between the raw yields obtained with the direct invariant mass fits and with the side-band subtraction method.

The advantage of the side-band method is twofold. First it allows one to extract raw yields also for cases with low statistical precision where a direct invariant mass

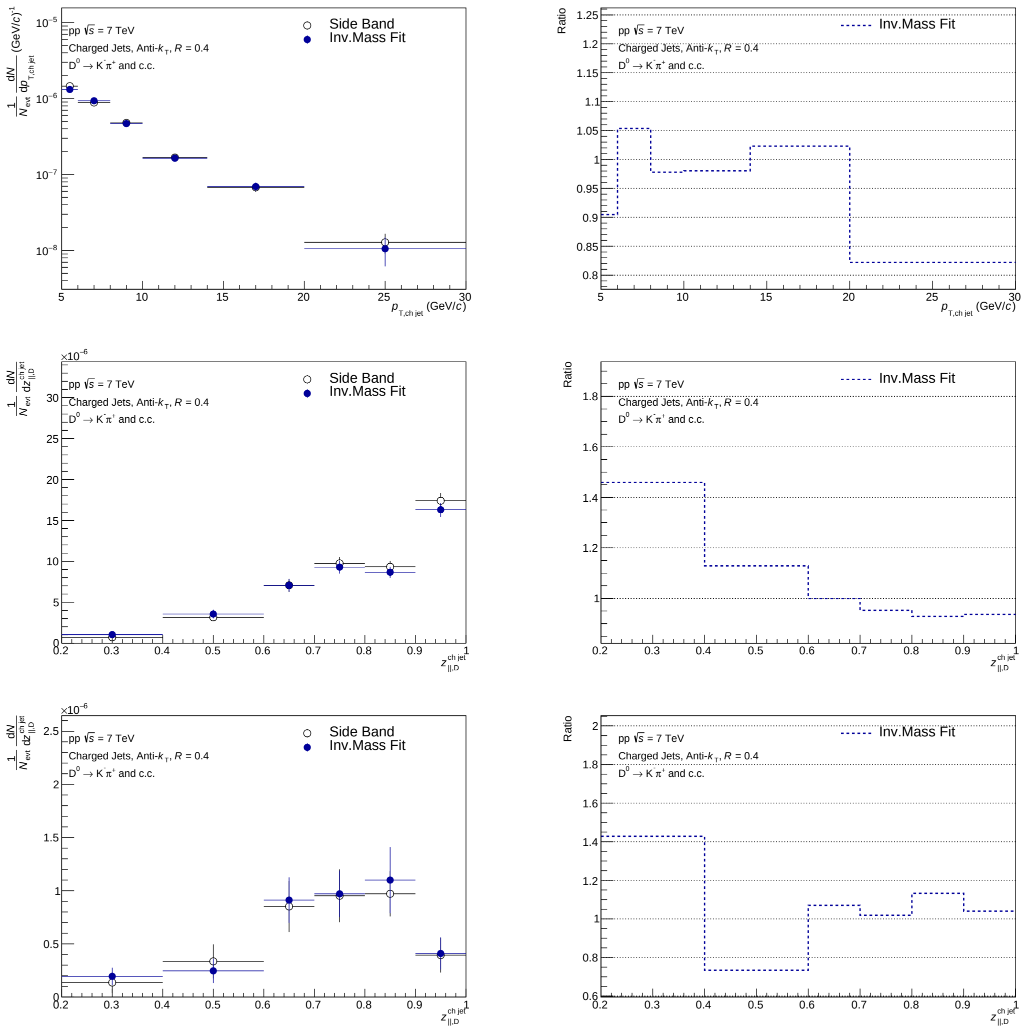

Figure 3.24: Comparisons between the raw yields extracted with the direct invariant mass fits (blue solid symbols) and those with the side-band subtraction method (empty black symbols). Yields are shown on the left. The ratio of the yields obtained with the direct invariant mass fit over those obtained the side-band method are shown on the right. Top: raw yields vs. $p_{\mathrm{T,jet}}^{\mathrm{ch}}$ with $p_{\mathrm{T,D}} > 3$ GeV/c. Middle: raw yields vs. $z_{||}^{\mathrm{ch}}$ with $p_{\mathrm{T,D}} > 2$ GeV/c and $5 < p_{\mathrm{T,jet}}^{\mathrm{ch}} < 15$ GeV/c. Bottom: raw yields vs. $z_{||}^{\mathrm{ch}}$ with $p_{\mathrm{T,D}} > 6$ GeV/c and $15 < p_{\mathrm{T,jet}}^{\mathrm{ch}} < 30$ GeV/c.

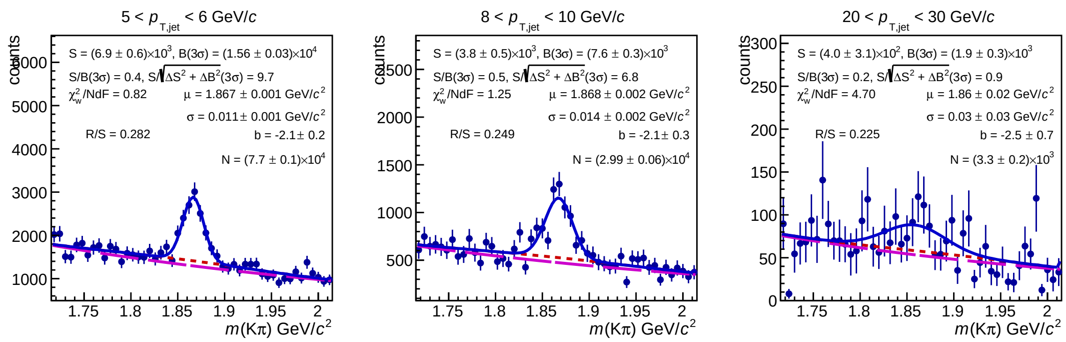

Figure 3.25: Invariant mass distributions weighted by $1/\epsilon(p_{\mathrm{T,D}})$ of D^0-meson tagged jets for different intervals of $p_{\mathrm{T,jet}}^{\mathrm{ch}}$, as indicated in each panel. For all panels $p_{\mathrm{T,D}} > 3$ GeV/c.

fit would be unstable and unreliable because of the low signal significance. This is the case for the distributions as a function of $z_{||}^{\mathrm{ch}}$ for $15 < p_{\mathrm{T,jet}}^{\mathrm{ch}} < 30$ GeV/c. The invariant mass fits shown in Fig. 3.17d features a very low significance; in fact, the D^0-meson mass peak barely emerges from the background. The second advantage is that the reconstruction efficiency can be easily applied before merging the distributions in $p_{\mathrm{T,D}}$:

$$N_x^{\mathrm{raw}} = \sum_{p_{\mathrm{T,D}}} \frac{1}{\epsilon^{\mathrm{prompt}}(p_{\mathrm{T,D}})} \left[N_x^{\mathrm{PR}}(p_{\mathrm{T,D}}) - \frac{B_2(p_{\mathrm{T,D}}) \cdot N_x^{\mathrm{SB}}(p_{\mathrm{T,D}})}{\sum_x N_x^{\mathrm{SB}}(p_{\mathrm{T,D}})} \right], \tag{3.20}$$

where $\epsilon^{\mathrm{prompt}}(p_{\mathrm{T,D}})$ is the prompt D^0-meson reconstruction efficiency.

In fact, applying the efficiency correction to the yields extracted using the direct invariant mass fits in bins of $p_{\mathrm{T,jet}}^{\mathrm{ch}}$ or $z_{||}^{\mathrm{ch}}$ is problematic. D^0-meson candidates in fixed ranges of $z_{||}^{\mathrm{ch}}$ or $p_{\mathrm{T,jet}}^{\mathrm{ch}}$ include contributions from a wide range of $p_{\mathrm{T,D}}$. The efficiency as a function of these variables can only be estimated making assumptions on the relative contributions as a function of $p_{\mathrm{T,D}}$ within each $z_{||}^{\mathrm{ch}}$ or $p_{\mathrm{T,jet}}^{\mathrm{ch}}$ interval under consideration[7]. This approach would be model-dependent and was not considered. Alternatively, the invariant mass distributions could be filled weighting each entry by

7. We will see how the reconstruction efficiency was estimated in Section 3.8. For the moment it is enough to point out that the reconstruction efficiency depends strongly on the D^0-meson transverse momentum, while its dependence on the other variables of interest ($z_{||}^{\mathrm{ch}}$, $p_{\mathrm{T,jet}}^{\mathrm{ch}}$) is negligible.

the inverse of the reconstruction efficiency $\epsilon^{\rm prompt}(p_{\rm T,D})$. In this way the efficiency correction is applied as a function of $p_{\rm T,D}$ directly on the invariant mass distributions, so that the raw signal extracted from the fit parameters is already efficiency-corrected. The drawback of this approach is that the significance of the invariant mass fits is negatively affected. In fact, low-momentum $\rm D^0$-meson candidates, which have a much lower signal/background ratio, get a large weight (as we shall see, the efficiency decreases sharply at low $p_{\rm T,D}$). As a consequence, the signal/background ratio decreases for all $p_{\rm T,jet}^{\rm ch}$ intervals when the efficiency weight is applied. This is apparent in Fig. 3.25, which shows the invariant mass distributions as a function of $p_{\rm T,jet}^{\rm ch}$ where each entry was weighted by $1/\epsilon^{\rm prompt}(p_{\rm T,D})$. Comparing with Fig. 3.17b the degradation of the fit performance is obvious.

3.7 Detector Performance

In the previous Section we have seen how the raw yield was extracted from data. In this Section we will discuss two important aspects of the detector performance: the reconstruction efficiency and the resolution.

The detector performance in reconstructing $\rm D^0$-meson taggged jets was studied in the charm-enhanced Monte Carlo simulation. At detector-level, the reconstruction of the $\rm D^0$ mesons and of the jets was performed following the same procedure described in Sections 3.6.1 and 3.6.2, respectively, with one important difference: only $\rm D^0$-meson candidates corresponding to real $\rm D^0$ mesons were analyzed. This is possible in the simulation because tracks at detector-level retain a label to match them back to the particle at generator-level that produced the signal in the detector. Therefore, it is relatively straightforward to check whether a track pair at detector-level corresponds to a kaon-pion pair emitted by a $\rm D^0$-meson decay. At generator-level the analysis is performed in a similar way. All selection cuts (kinematic, topological) are neglected.

Detector-level D^0-meson tagged jets are matched with their generator-level counterparts by following in reverse the transport of the decay products of the D^0 meson in the detector.

The detector performance was studied separately for prompt and non-prompt D^0-meson tagged jets.

3.7.1 Reconstruction Efficiency

The tracking efficiency (see Fig. 3.11) limits the reconstruction efficiency of D^0 mesons. Since the reconstruction of a D^0 meson requires the reconstruction of the tracks of both decay products (pion and kaon) its reconstruction efficiency is limited roughly by the product of the reconstruction efficiencies of those two tracks. However, tracking efficiency is not the only factor that plays a role in the reconstruction of D^0 mesons. The kinematic and topological cuts discussed in Section 3.6.1 further reduce the reconstruction efficiency, eliminating part of the signal. On the other hand, PID cuts have a negligible effect on the efficiency.

The generator-level D^0-meson tagged jets that have a matched detector-level counterpart form the *reconstructed* sample. The *generated* sample is simply obtained taking all the generator-level D^0-meson tagged jets that pass the kinematic selections summarized in Table 3.2. The reconstructed sample is for the most part a sub-sample of the generated sample. It is not an exact sub-sample because the kinematic selections of Table 3.2 are applied to detector-level variables for the reconstructed sample, while they are applied to the generator-level variables in the generated sample. This choice allows the representation of both the reconstruction efficiency and the acceptance correction by a single ratio between the reconstructed and the generated samples.

Figure 3.26 shows the product of the reconstruction efficiency and acceptance correction for prompt D^0-meson tagged jets as a function of $p_{\mathrm{T,D}}$. In the following we

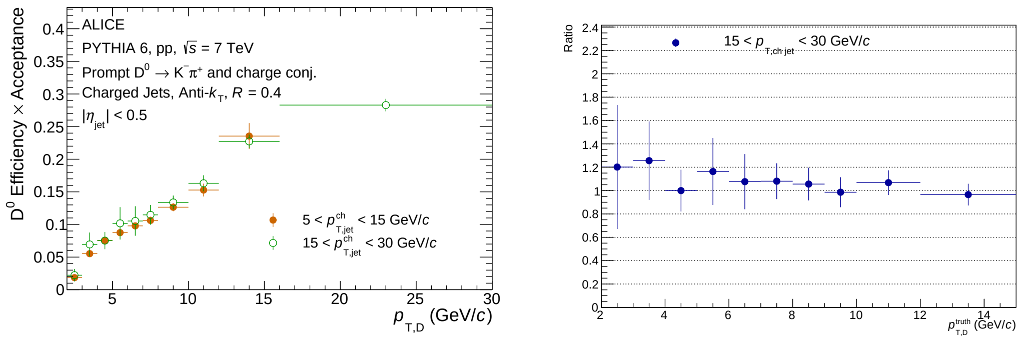

Figure 3.26: Left: reconstruction efficiency and acceptance correction as a function of $p_{\mathrm{T,D}}$ for D^0-meson tagged jets with $5 < p_{\mathrm{T,jet}}^{\mathrm{ch}} < 15$ GeV/c (orange solid symbols) and $15 < p_{\mathrm{T,jet}}^{\mathrm{ch}} < 30$ GeV/c (green open symbols). Right: ratio between the two reconstruction efficiencies.

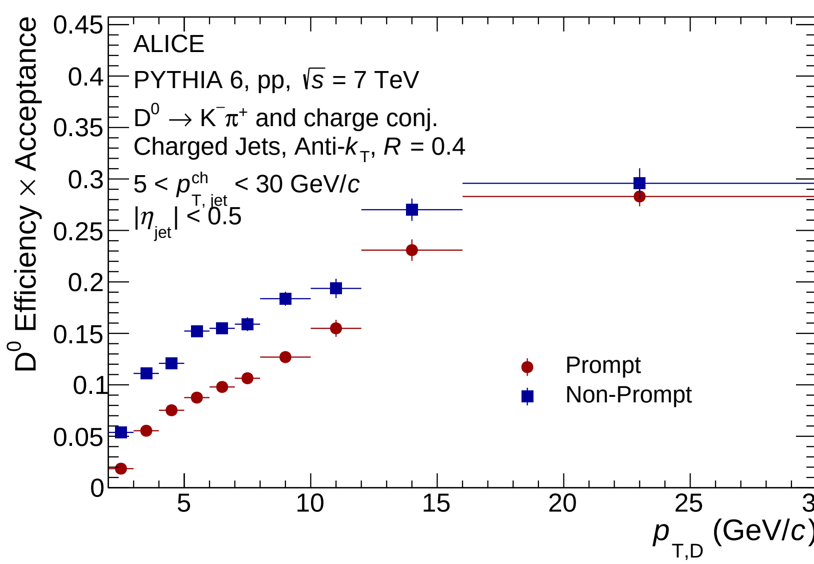

Figure 3.27: Reconstruction efficiency and acceptance correction as a function of $p_{\mathrm{T,D}}$ for prompt (red circles) and non-prompt (blue squares) D^0-meson tagged jets with $5 < p_{\mathrm{T,jet}}^{\mathrm{ch}} < 30$ GeV/c.

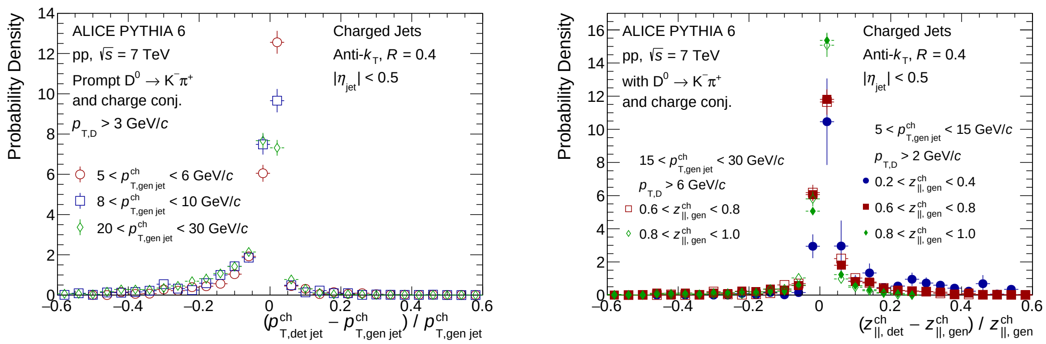

Figure 3.28: Probability density distributions of the residuals 3.21 (left) and 3.22 (right) for prompt D^0-meson tagged jets for different intervals of $p^{\mathrm{ch}}_{\mathrm{T,gen\,jet}}$ and $z^{\mathrm{ch}}_{||,\mathrm{gen}}$.

shall refer to this quantity as simply the "efficiency". The efficiency is shown separately for $5 < p^{\mathrm{ch}}_{\mathrm{T,jet}} < 15$ GeV/c and for $15 < p^{\mathrm{ch}}_{\mathrm{T,jet}} < 30$ GeV/c to highlight the fact that it has negligible dependence on $p^{\mathrm{ch}}_{\mathrm{T,jet}}$. As a function of $p_{\mathrm{T,D}}$ it increases monotonically from about 2% for $2 < p_{\mathrm{T,D}} < 3$ GeV/c to about 30% for $15 < p_{\mathrm{T,D}} < 30$ GeV/c. This sharp increase is a consequence of the topological cuts (see Table 3.3) that are much stricter at low $p_{\mathrm{T,D}}$ to deal with the much larger combinatorial background.

The prompt and non-prompt reconstruction efficiencies are compared in Fig. 3.27. The non-prompt efficiency turns out to be higher than the prompt efficiency. This is purely due to the specific topological selection cuts used to enhance the signal over the combinatorial background. We will come back to this issue later in Section 3.8.2.

3.7.2 $p^{\mathrm{ch}}_{\mathrm{T,jet}}$ and $z^{\mathrm{ch}}_{||}$ Resolution

Tracking efficiency is also the main factor impacting the experimental precision of the jet momentum measurement. Tracking momentum resolution is a secondary factor, which becomes important only for jets with few constituents and/or high-momentum tracks. This is an important difference when comparing with jet reconstruction performed using the energy flow measured through calorimetry. In fact, calorimetric efficiency is nominally 100%, while the energy resolution is a prominent factor, especially for hadronic calorimeters.

The detector resolution was studied comparing variables determined at detector-level with those determined at generator-level for the D^0-meson tagged jets belonging to the reconstructed sample described above. In particular, the resolution of the measurement of $p_{\mathrm{T,jet}}^{\mathrm{ch}}$ and $z_{||}^{\mathrm{ch}}$ was studied, by looking at the probability density distributions of the residuals:

$$(p_{\mathrm{T,det\,jet}}^{\mathrm{ch}} - p_{\mathrm{T,gen\,jet}}^{\mathrm{ch}})/p_{\mathrm{T,gen\,jet}}^{\mathrm{ch}}, \tag{3.21}$$

$$(z_{||,\mathrm{det}}^{\mathrm{ch}} - z_{||,\mathrm{gen}}^{\mathrm{ch}})/z_{||,\mathrm{gen}}^{\mathrm{ch}}, \tag{3.22}$$

where the gen and det subscripts refer to the generator-level and detector-level variables, respectively. The probability density distributions of 3.21 and 3.22 are shown in Fig. 3.28 for prompt D^0-meson tagged jets separately for different intervals of $p_{\mathrm{T,gen\,jet}}^{\mathrm{ch}}$ and $z_{||,\mathrm{gen}}^{\mathrm{ch}}$. We observe that the distributions of the residuals for $p_{\mathrm{T,jet}}^{\mathrm{ch}}$ (Eq. 3.21) feature a sharp peak at 0 and are prominently asymmetric. The longer tails at negative values are a direct consequence of tracking inefficiency. The entries at positive values are instead largely due to jet clustering effects and to a lesser extent to track momentum resolution. Unreconstructed particles may cause a shift of the jet axis at detector-level; this shift occasionally causes two jets to cluster together, leading to an apparent larger jet momentum at detector-level. The distributions of the residuals of for $z_{||}^{\mathrm{ch}}$ (Eq. 3.22) are very similar to those obtained for $p_{\mathrm{T,jet}}^{\mathrm{ch}}$ and can be described in the same terms.

In order to characterize the distribution of the residuals, shown in Fig. 3.28, the mean, median and variance were calculated. The mean and the median of the jet transverse momentum residuals are shown in Fig. 3.29 as a function of $p_{\mathrm{T,gen\,jet}}^{\mathrm{ch}}$ for the prompt (left) and non-prompt (right) D^0-meson tagged jets. The mean (median) for the prompt D^0-meson tagged jets is about +0.5% (−2%) for $p_{\mathrm{T,gen\,jet}}^{\mathrm{ch}} = 5$ GeV/c and decreases monotonically down to −2% (−7%) for $p_{\mathrm{T,gen\,jet}}^{\mathrm{ch}} = 30$ GeV/c. The

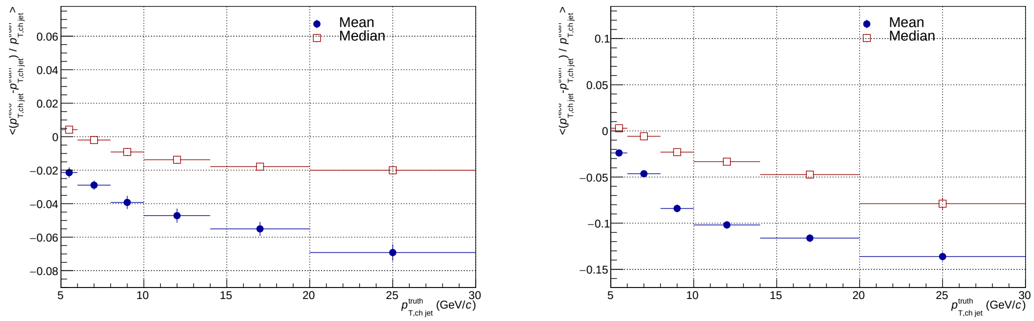

(a) Prompt (b) Non-prompt

Figure 3.29: Mean (blue solid circles) and median (red open squares) of the probability density distributions of the residuals 3.21 for D^0-meson tagged jets as a function of $p^{\mathrm{ch}}_{\mathrm{T,gen\,jet}}$.

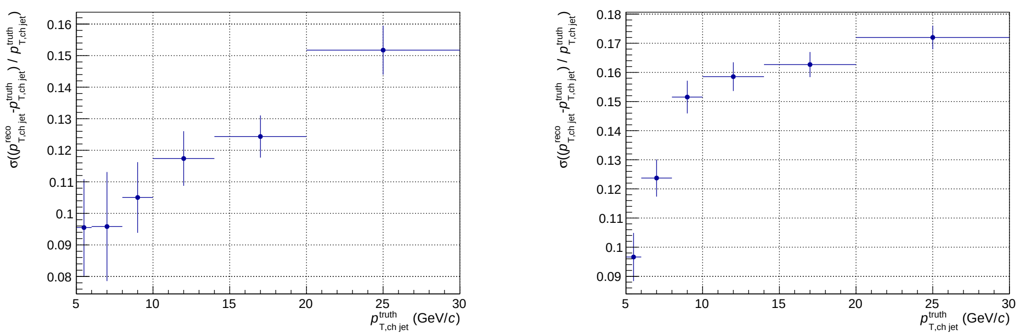

(a) Prompt (b) Non-prompt

Figure 3.30: Square root of the variance of the probability density distributions of the residuals 3.21 for D^0-meson tagged jets as a function of $p^{\mathrm{ch}}_{\mathrm{T,gen\,jet}}$.

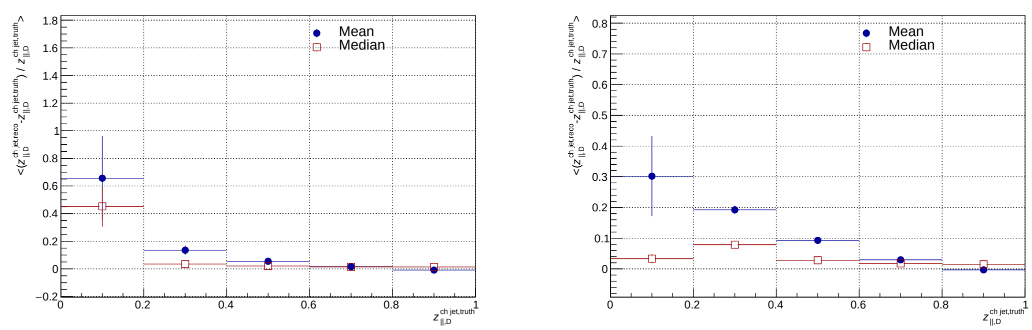

(a) Prompt (b) Non-prompt

Figure 3.31: Mean (blue solid circles) and median (red open squares) of the probability density distributions of the residuals 3.22 for D^0-meson tagged jets as a function of $z^{\mathrm{ch}}_{||,\mathrm{gen}}$ for $5 < p^{\mathrm{ch}}_{\mathrm{T,jet}} < 15$ GeV/c.

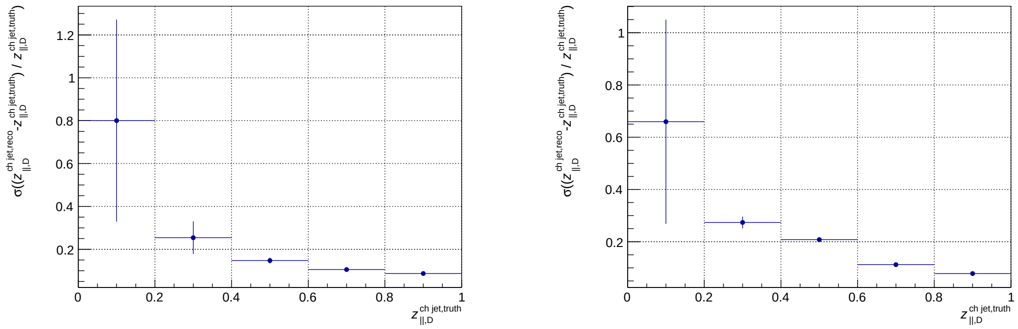

(a) Prompt (b) Non-prompt

Figure 3.32: Square root of the variance of the probability density distributions of the residuals 3.22 for D^0-meson tagged jets as a function of $z^{\mathrm{ch}}_{||,\mathrm{gen}}$ for $5 < p^{\mathrm{ch}}_{\mathrm{T,jet}} < 15$ GeV/c.

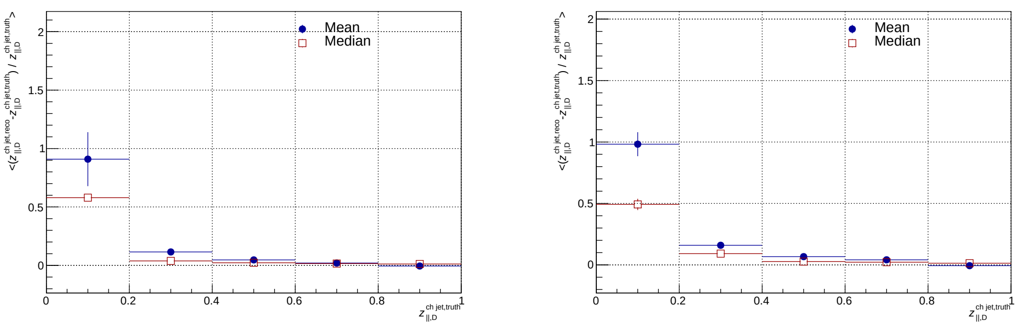

(a) Prompt (b) Non-prompt

Figure 3.33: Mean (blue solid circles) and median (red open squares) of the probability density distributions of the residuals 3.22 for D^0-meson tagged jets as a function of $z^{\mathrm{ch}}_{||,\mathrm{gen}}$ for $15 < p^{\mathrm{ch}}_{\mathrm{T,jet}} < 30$ GeV/c.

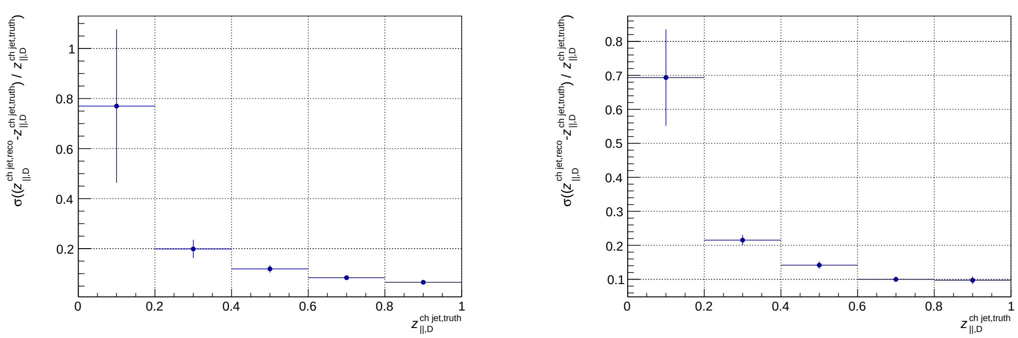

(a) Prompt (b) Non-prompt

Figure 3.34: Square root of the variance of the probability density distributions of the residuals 3.22 for D^0-meson tagged jets as a function of $z^{\mathrm{ch}}_{||,\mathrm{gen}}$ for $15 < p^{\mathrm{ch}}_{\mathrm{T,jet}} < 30$ GeV/c.

non-prompt D^0-meson tagged jets show substantially larger negative shifts, probably a consequence of the harder fragmentation of b quarks. The square root of the variance, which quantifies the experimental resolution for $p_{\mathrm{T,jet}}^{\mathrm{ch}}$, is shown in Fig. 3.30 as a function of $p_{\mathrm{T,gen\,jet}}^{\mathrm{ch}}$ for the prompt (left) and non-prompt (right) D^0-meson tagged jets. It varies from about 10% to 15% for prompt (slightly larger for non-prompt). Compared to the measurement of inclusive jets without D^0-meson tagging [154] the resolution is slightly better due to the requirement of a D^0-meson among the jet constituents, which ensures at least a jet constituent measured with good precision.

The mean, median and variance of the $z_{||}^{\mathrm{ch}}$ residual distributions are shown in Figs. 3.31, 3.32, 3.33 and 3.34 for both prompt and non-prompt and for the two $p_{\mathrm{T,jet}}^{\mathrm{ch}}$ intervals.

The smearing effect caused by the detector finite resolution was encoded in response matrices, like those shown in Fig. 3.35 for prompt D^0-meson tagged jets. Each entry of the response matrix corresponds to a generator-level D^0-meson tagged jet matched with its detector-level counterpart. The x axis represents its detector-level property (e.g. $p_{\mathrm{T,det\,jet}}^{\mathrm{ch}}$), while the y axis represents the corresponding generator-level property (e.g. $p_{\mathrm{T,gen\,jet}}^{\mathrm{ch}}$). The matrices were normalized such that each y slice has the integral equal to one: it represents the probability density distribution as a function of the detector-level variable, for a fixed interval of the generator-level variable. It can be expressed as a conditional probability that the variable is observed in bin j given that the true value is in bin i:

$$R_{ij} = P(\text{observed in bin } j \mid \text{true value in bin } i). \tag{3.23}$$

For what concerns $p_{\mathrm{T,D}}$, it was verified that the experimental resolution is much better than all other experimental uncertainties involved in the measurement. Since the momentum of the D^0 meson is measured experimentally by summing the momenta

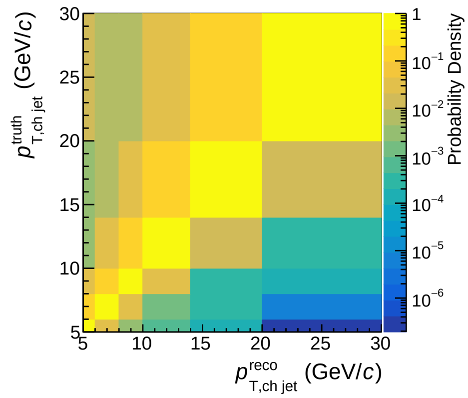

(a) $p_{\mathrm{T,jet}}^{\mathrm{ch}}$ response, $p_{\mathrm{T,D}} > 3$ GeV/c.

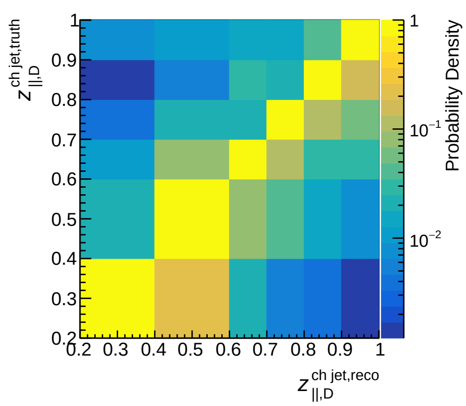

(b) $z_{||}^{\mathrm{ch}}$ response, $p_{\mathrm{T,D}} > 2$ GeV/c, $5 < p_{\mathrm{T,jet}}^{\mathrm{ch}} < 15$ GeV/c.

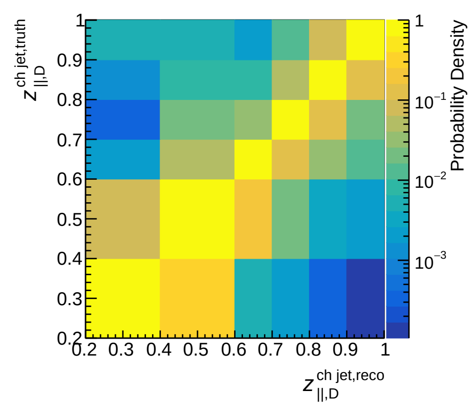

(c) $z_{||}^{\mathrm{ch}}$ response, $p_{\mathrm{T,D}} > 6$ GeV/c, $15 < p_{\mathrm{T,jet}}^{\mathrm{ch}} < 30$ GeV/c.

Figure 3.35: Response matrices encoding the smearing caused by the detector finite resolution in the measurement of D^0-meson tagged jet variables $p_{\mathrm{T,jet}}^{\mathrm{ch}}$ and $z_{||}^{\mathrm{ch}}$. The y slices are normalized such that the total integral (including overflow and underflow bins) is equal to one.

of two tracks, its absolute uncertainty is given by the sum in quadrature of the momentum uncertainties of the two tracks. Thus, the relative uncertainty on $p_{\mathrm{T,D}}$ is about $\sqrt{2}$ times smaller compared to the single-track momentum relative uncertainty (which is $1-3\%$ in the momentum range of interest).

3.8 Corrections

3.8.1 Reconstruction Efficiency

The efficiency correction was already discussed at the end of Section 3.6.3. The raw yield distributions as a function of $p_{\mathrm{T,jet}}^{\mathrm{ch}}$ or $z_{||}^{\mathrm{ch}}$ were extracted in small intervals of $p_{\mathrm{T,D}}$. Each distribution was weighted with the inverse of the efficiency calculated for each $p_{\mathrm{T,D}}$ interval before summing them all together. This procedure is represented by Eq. 3.20. Notice that at this step the prompt D^0-meson efficiency factor was used. The non-prompt D^0-meson efficiency, which is different from the prompt (see Fig. 3.27), was not used at this stage, even though the sample of reconstructed D^0 mesons contains an admixture of prompt and non-prompt. This apparent inconsistency is corrected in the following step, when the non-prompt contribution is subtracted.

3.8.2 B Feed-Down Subtraction

Non-prompt D^0 mesons belong to the fragmentation of beauty quarks through the decay of B hadrons, contrary to prompt D^0 mesons that come directly from the fragmentation of charm quarks. Figure 3.27 shows how the reconstruction efficiency of non-prompt D^0 mesons is significantly higher compared to that of prompt D^0 mesons. It is an unfortunate effect because it biases the natural admixture of prompt and non-prompt D^0 mesons in a detector- and analysis-specific way. In this analysis the non-prompt contribution was subtracted. With the ITS upgrade planned to be installed during the LHC Long Shutdown 2 and that will go into operation during the LHC

Run-3 phase (Chapter 6), ALICE will be able to experimentally distinguish between prompt and non-prompt D mesons [158]. Until then we have to make assumptions on the non-prompt fraction using theoretical models.

Calculation of the B feed-down cross section

In previous analyses of D mesons published by the ALICE Collaboration [82, 103, 112, 115], the non-prompt fraction was estimated and subtracted using predictions from FONLL [9]. The FONLL formalism allows one to include the fragmentation and hadronization of the heavy-flavor quarks in order to calculate D meson p_{T}-differential cross sections. It has been shown to be in reasonable agreement with measurements of heavy-flavor cross sections at the LHC [11]. However it is very difficult – if not impossible – to include the effect of jet reclusterization according to a specific jet finding algorithm in a purely analytical formalism such as FONLL. This is needed in order to subtract the B feed-down as a function of $p_{\mathrm{T,jet}}^{\mathrm{ch}}$ and $z_{||}^{\mathrm{ch}}$, variables that depend on the particular jet definition used in the data analysis (anti-k_{T} algorithm with $R = 0.4$ in this case). Therefore, a different approach was used. The POWHEG method [129, 130, 159] allows one to match pQCD NLO calculations with a parton shower Monte Carlo generator. For this analysis the software implementation POWHEG-BOX V2 [131] was used. POWHEG was configured with the mass of the beauty quark $m_{\mathrm{b}} = 4.75$ GeV/c^2; the renormalization and factorization scales were kept at the nominal value $\mu_{\mathrm{R}} = \mu_{\mathrm{F}} = \mu_0 = \sqrt{p_{\mathrm{T}}^2 + m_{\mathrm{b}}^2}$. The parton distribution function (PDF) was obtained using the LHAPDF 6 [160] interpolator with the PDF set CT10nlo [161]. POWHEG-BOX generates partonic events, which include parton splittings and gluon radiation at NLO. These partonic events were loaded in PYTHIA 6, which takes over for the remaining parton shower and hadronization into colorless particles. In addition, PYTHIA 6 was used for the generation of the underlying event via its multi-parton interaction (MPI) scheme. Particle decays were also handled by PYTHIA 6, except for the decays of B hadrons, which were simulated by EvtGen [162].

Figure 3.36 compares the non-prompt D^0-meson production cross section calculated using FONLL[8] [11, 73] with that obtained with the POWHEG + PYTHIA 6 simulation. The systematic uncertainty is shown only for FONLL as a cyan band. It includes the uncertainty on the renomalization and factorization scales, the quark masses and the PDFs. A reasonable agreement is confirmed by this calculation, especially taking into consideration that the p_{T}-differential cross section spans almost six orders of magnitude and that the POWHEG simulation is affected by systematic uncertainties at the same level of FONLL.

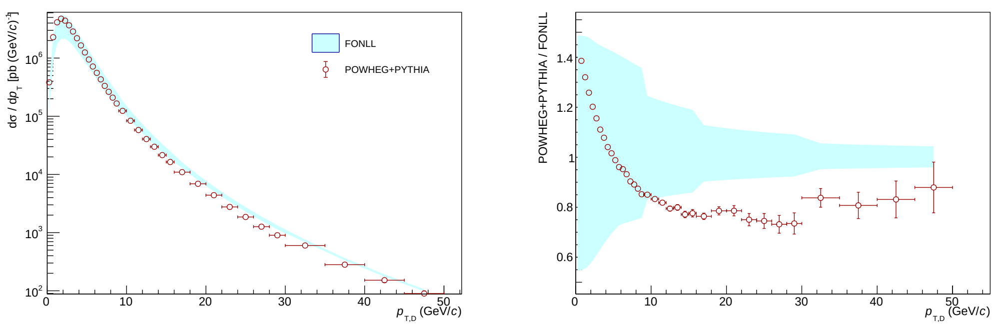

Figure 3.36: Left: D^0 spectrum generated by POWHEG+PYTHIA $b\bar{b}$ events (red points) compared with a FONLL calculation (cyan band); the band of the FONLL calculation includes the uncertainties due to the renormalization and factorization scales, the quark mass and the PDFs. Right: ratio of POWHEG + PYTHIA 6 over FONLL; the band at unity represents the FONLL uncertainty.

Subtraction

To limit the use of computing resources, the POWHEG + PYTHIA 6 simulation was performed as a "fast" simulation, skipping the transport of the particles through the detector. The detector response was applied using parametrizations obtained from the charm-enhanced Monte Carlo production. A $p_{\mathrm{T,D}}$-dependent weight corre-

8. `http://www.lpthe.jussieu.fr/~cacciari/fonll/fonllform.html`

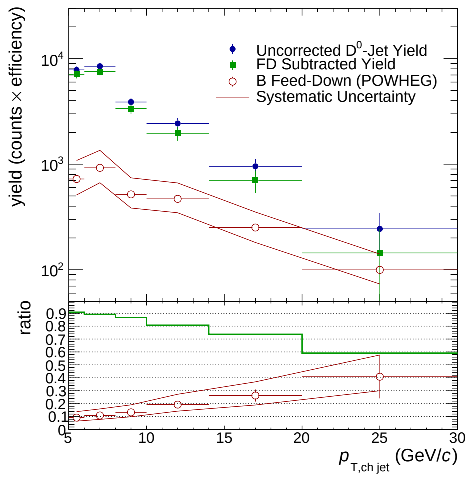

(a) $p_{\mathrm{T,D}} > 3$ GeV/c

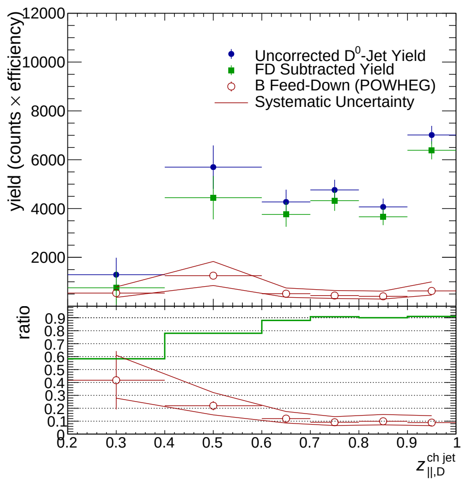

(b) $p_{\mathrm{T,D}} > 2$ GeV/c and $5 < p_{\mathrm{T,jet}}^{\mathrm{ch}} < 15$ GeV/c

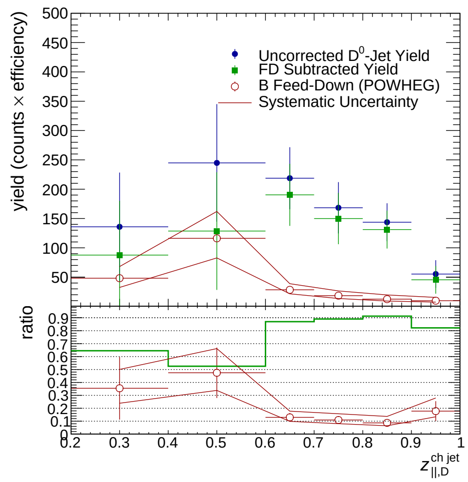

(c) $p_{\mathrm{T,D}} > 6$ GeV/c and $15 < p_{\mathrm{T,jet}}^{\mathrm{ch}} < 30$ GeV/c

Figure 3.37: Efficiency-corrected measured D^0-meson tagged jet raw yields in pp collisions at $\sqrt{s} = 7$ TeV without B feed-down correction (blue full circles) and after correction (green full squares). The B feed-down yield (red open circles) is obtained with the POWHEG + Pythia 6 simulation (see text for details).

sponding to the ratio of the non-prompt over the prompt reconstruction efficiencies $\epsilon_{\text{non-prompt}}\left(p_{\mathrm{T,D}}\right)/\epsilon_{\text{prompt}}\left(p_{\mathrm{T,D}}\right)$ was applied to each entry when filling histograms. The inverse of the prompt efficiency was used because the sample of D^0 mesons reconstructed in data was collectively corrected using the inverse of the prompt efficiency (see Eq. 3.20), which was thus applied to both the prompt and the non-prompt fractions. As a consequence, when comparing the efficiency-corrected raw yield from data with the non-prompt yield from the simulation, we need to multiply the latter by the same factor. The effect of the finite detector resolution in the measurement of $p_{\mathrm{T,jet}}^{\mathrm{ch}}$ and $z_{||}^{\mathrm{ch}}$ was accounted for by applying the non-prompt detector response matrices represented by the symbols $R_{p_{\mathrm{T,jet}}^{\mathrm{ch}}}^{\text{non-prompt}}$ and $R_{z_{||}^{\mathrm{ch}}}^{\text{non-prompt}}$, respectively.

The b feed-down yield was then subtracted from the efficiency-corrected D^0-meson tagged jet yield:

$$N_{p_{\mathrm{T,det\,jet}}^{\mathrm{ch}}}^{\text{prompt}} = N_{p_{\mathrm{T,det\,jet}}^{\mathrm{ch}}}^{\text{raw}} - N_{p_{\mathrm{T,det\,jet}}^{\mathrm{ch}}}^{\text{non-prompt}}, \tag{3.24}$$

where:

$$N_{p_{\mathrm{T,det\,jet}}^{\mathrm{ch}}}^{\text{non-prompt}} = R_{p_{\mathrm{T,jet}}^{\mathrm{ch}}}^{\text{non-prompt}} \cdot \sum_{p_{\mathrm{T,D}}} \frac{\epsilon_{\text{non-prompt}}\left(p_{\mathrm{T,D}}\right)}{\epsilon_{\text{prompt}}\left(p_{\mathrm{T,D}}\right)} N_{p_{\mathrm{T,gen\,jet}}^{\mathrm{ch}}}^{\text{non-prompt}}(p_{\mathrm{T,D}}). \tag{3.25}$$

$N_{p_{\mathrm{T,gen\,jet}}^{\mathrm{ch}}}^{\text{non-prompt}}(p_{\mathrm{T,D}})$ is the vector representing the b feed-down yields obtained by multiplying the POWHEG + PYTHIA 6 differential cross section by the data integrated luminosity $\mathscr{L}_{\mathrm{int}}$ and discretizing it in bins of $p_{\mathrm{T,D}}$ and $p_{\mathrm{T,gen\,jet}}^{\mathrm{ch}}$.

Figure 3.37 shows $N_{p_{\mathrm{T,det\,jet}}^{\mathrm{ch}}}^{\text{prompt}}$ (green solid squares), $N_{p_{\mathrm{T,det\,jet}}^{\mathrm{ch}}}^{\text{raw}}$ (blue solid circles) and $N_{p_{\mathrm{T,det\,jet}}^{\mathrm{ch}}}^{\text{non-prompt}}$ (red open circles) as a function of $p_{\mathrm{T,jet}}^{\mathrm{ch}}$ (top) and $z_{||}^{\mathrm{ch}}$ (bottom). The bottom panels show the ratios $N_{p_{\mathrm{T,det\,jet}}^{\mathrm{ch}}}^{\text{non-prompt}}/N_{p_{\mathrm{T,det\,jet}}^{\mathrm{ch}}}^{\text{raw}}$ and $N_{p_{\mathrm{T,det\,jet}}^{\mathrm{ch}}}^{\text{prompt}}/N_{p_{\mathrm{T,det\,jet}}^{\mathrm{ch}}}^{\text{raw}}$. Systematic uncertainties on the b feed-down (represented by the red lines) will be described in detail in Section 3.9.1. The feed-down fraction shows an approximately linear increase as a function of $p_{\mathrm{T,jet}}^{\mathrm{ch}}$. The dependence on $z_{||}^{\mathrm{ch}}$ is weak and it only appears to increase slightly for $z_{||}^{\mathrm{ch}} < 0.6$.

3.8.3 Unfolding of the Detector Resolution

For sufficiently small histogram bins, the yield distribution of D^0-meson tagged jets as a function of $p_{\mathrm{T,jet}}^{\mathrm{ch}}$ or $z_{||}^{\mathrm{ch}}$ is affected by significant shape distortions caused by the finite detector resolution. These distortions are experiment-specific and can potentially deceive the interpretation of the data especially when it is compared to other experimental results or theoretical calculations. If we represent the measured yield as a function of $p_{\mathrm{T,det\,jet}}^{\mathrm{ch}}$ in a vector $N_{p_{\mathrm{T,det\,jet}}^{\mathrm{ch}}}$ and the true yield as a function of $p_{\mathrm{T,gen\,jet}}^{\mathrm{ch}}$ in a vector $N_{p_{\mathrm{T,gen\,jet}}^{\mathrm{ch}}}$ then they are related by a linear transformation:

$$N_{p_{\mathrm{T,det\,jet}}^{\mathrm{ch}}} = R_{p_{\mathrm{T,jet}}^{\mathrm{ch}}}^{\mathrm{prompt}} \cdot N_{p_{\mathrm{T,gen\,jet}}^{\mathrm{ch}}}, \tag{3.26}$$

where $R_{p_{\mathrm{T,jet}}^{\mathrm{ch}}}^{\mathrm{prompt}}$ is a linear operator and coincides with the detector response matrix. A similar relation can be written for $z_{||}^{\mathrm{ch}}$ or any other measurable variable of the D^0-meson tagged jets. The *unfolding* (or *unsmearing*) of the measured distribution corresponds mathematically to the operation of matrix inversion:

$$N_{p_{\mathrm{T,gen\,jet}}^{\mathrm{ch}}} = \left(R_{p_{\mathrm{T,jet}}^{\mathrm{ch}}}^{\mathrm{prompt}}\right)^{-1} \cdot N_{p_{\mathrm{T,det\,jet}}^{\mathrm{ch}}}. \tag{3.27}$$

There are however some practical problems that typically arise when one attempts to follow this approach. First the matrix may not be regular, i.e. $\left(R_{p_{\mathrm{T,jet}}^{\mathrm{ch}}}^{\mathrm{prompt}}\right)^{-1}$ may simply not exist. One can sometimes get around this issue by rebinning the vectors and the matrix until a regular matrix is obtained. However this is insufficient. As shown in [163], after inverting the matrix and applying it to $N_{p_{\mathrm{T,det\,jet}}^{\mathrm{ch}}}$, the result $N_{p_{\mathrm{T,gen\,jet}}^{\mathrm{ch}}}$ is typically affected by wild statistical fluctuations. Once the uncertainties of $N_{p_{\mathrm{T,det\,jet}}^{\mathrm{ch}}}$ are properly propagated to $N_{p_{\mathrm{T,gen\,jet}}^{\mathrm{ch}}}$, correspondingly large statistical uncertainties are obtained. This result may appear surprising at first. In practice, there is a large number of "true" distributions with a very fine structure of peaks and valleys that

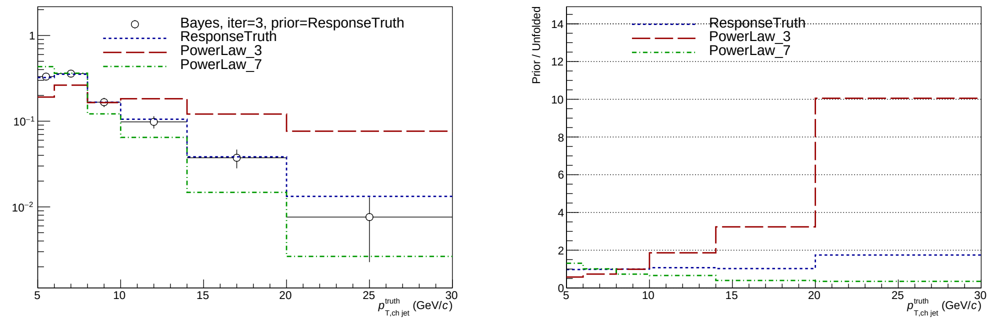

(a) Yield (b) Ratio

Figure 3.38: $p_{\mathrm{T,jet}}^{\mathrm{ch}}$ spectra used as priors for the unfolding compared with the unfolded prompt D^0-meson tagged jet spectrum (black): PYTHIA 6 spectrum (blue), modified power-law spectra with index 3 (blue) and 7 (red). The ratios between each prior and the unfolded spectrum are shown on the right. See text for details.

would result in the same smooth "measured" distribution once the detector smearing is applied. Smaller histogram bins – and larger statistical uncertainties – will invariably lead to more potential candidates of true distributions with a very fine structure. The solution proposed by various authors is to "regularize" the unfolding procedure by adding certain assumptions about the real distribution that is being sought, for example excluding distributions that do not adhere to a given "smoothness" criterion. Some care must be taken as to avoid introducing biases, which must be estimated and considered as potential sources of systematic uncertainties.

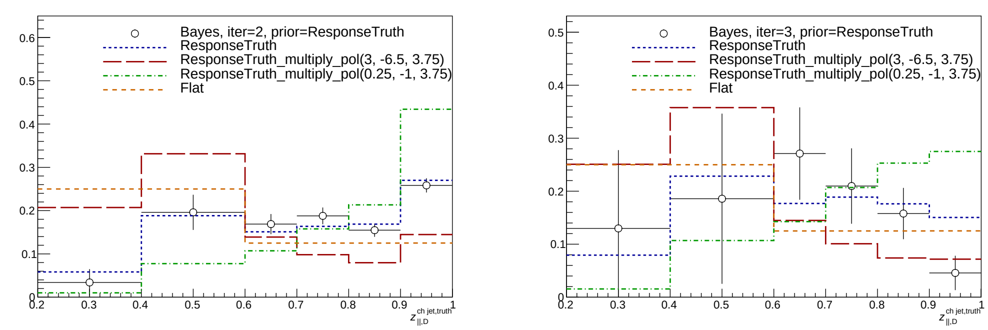

(a) $5 < p_{\mathrm{T,jet}}^{\mathrm{ch}} < 15$ GeV/c (b) $15 < p_{\mathrm{T,jet}}^{\mathrm{ch}} < 30$ GeV/c

Figure 3.39: $z_{||}^{\mathrm{ch}}$ spectra used as priors for the unfolding compared with the unfolded prompt D^0-meson tagged jet spectrum (black): PYTHIA distribution (blue), harder fragmentation (green), softer fragmentation (red), flat (orange). See text for details.

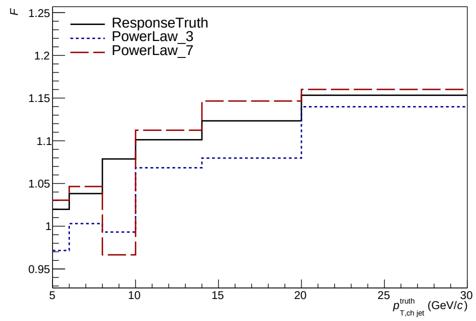

(a) $p^{\mathrm{ch}}_{\mathrm{T,jet}}$

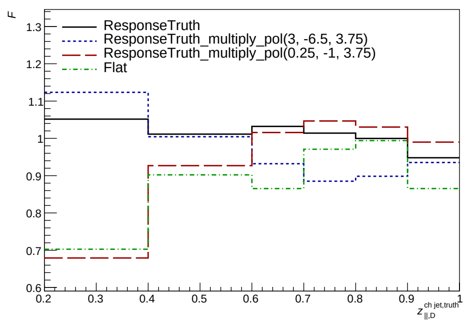

(b) $z^{\mathrm{ch}}_{||}$, $5 < p^{\mathrm{ch}}_{\mathrm{T,jet}} < 15$ GeV/c

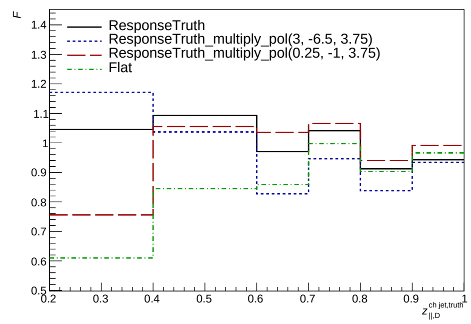

(c) $z^{\mathrm{ch}}_{||}$, $15 < p^{\mathrm{ch}}_{\mathrm{T,jet}} < 30$ GeV/c

Figure 3.40: Comparison of the bin-by-bin correction factors for different prior choices. For the $p^{\mathrm{ch}}_{\mathrm{T,jet}}$ spectrum (top): PYTHIA 6 spectrum (black), and modified power-law spectra with index 3 (blue) and 7 (red). For the $z^{\mathrm{ch}}_{||}$ spectra (bottom): PYTHIA 6 spectra (blue), harder fragmentation (green), softer fragmentation (red), flat (orange). See text for details.

For this analysis the Bayesian iterative technique [164, 165] was used. The result was also cross-checked with the regularized Singular Value Decomposition (SVD) technique [166] and with a simple bin-by-bin correction.

Bin-by-bin correction Bin-by-bin correction factors are defined as:

$$F_{p^{\mathrm{ch}}_{\mathrm{T,jet}}} = \frac{N^{\mathrm{MC}}_{p^{\mathrm{ch}}_{\mathrm{T,gen\,jet}}}}{N^{\mathrm{MC}}_{p^{\mathrm{ch}}_{\mathrm{T,det\,jet}}}}, \tag{3.28}$$

where $N^{\mathrm{MC}}_{p^{\mathrm{ch}}_{\mathrm{T,gen\,jet}}}$ and $N^{\mathrm{MC}}_{p^{\mathrm{ch}}_{\mathrm{T,det\,jet}}}$ are the generator-level and detector-level distributions, respectively, obtained from the Monte Carlo simulation. Similarly for the $z^{\mathrm{ch}}_{||}$ distributions:

$$F_{z_{||}^{\mathrm{ch}}} = \frac{N^{\mathrm{MC}}_{z^{\mathrm{ch}}_{||,\mathrm{gen}}}}{N^{\mathrm{MC}}_{z^{\mathrm{ch}}_{||,\mathrm{det}}}}. \tag{3.29}$$

The correction is performed by simply multiplying the F_x factors with the raw yield vector extracted from data. The bin-by-bin correction method is potentially affected by severe biases, because it tends to "pull" the result towards the Monte Carlo distribution used to calculate the bin-by-bin factors. In order to estimate such an effect, bin-by-bin correction factors were calculated with different assumptions on $N^{\mathrm{MC}}_{p^{\mathrm{ch}}_{\mathrm{T,gen\,jet}}}$ ($N^{\mathrm{MC}}_{z^{\mathrm{ch}}_{||,\mathrm{gen}}}$) that correspond to different $N^{\mathrm{MC}}_{p^{\mathrm{ch}}_{\mathrm{T,det\,jet}}}$ ($N^{\mathrm{MC}}_{z^{\mathrm{ch}}_{||,\mathrm{det}}}$) counterparts. The baseline $N^{\mathrm{MC}}_{p^{\mathrm{ch}}_{\mathrm{T,gen\,jet}}}$ distribution was extracted from the Monte Carlo charm-enhanced production (PYTHIA 6 Perugia 2011). For the variations, the spectra were obtained from a modified power-law function:

$$f(p_{\mathrm{T,jet}}) = p_{\mathrm{T,jet}}^{-a} e^{-\frac{ab}{p_{\mathrm{T,jet}}}}, \tag{3.30}$$

where a is the power-law index (two variations were used: $a = 3, 7$) and $b = 3$ GeV/c is the position of the local maximum of the distribution. The exponential factor $e^{-\frac{ab}{p_{\mathrm{T,jet}}}}$ was added to avoid infinities at $p^{\mathrm{ch}}_{\mathrm{T,jet}} \to 0$ and to have a more realistic spectrum (the physical cross-section goes to zero for $p^{\mathrm{ch}}_{\mathrm{T,jet}} \to 0$). Figure 3.38 compares the baseline $N^{\mathrm{MC}}_{p^{\mathrm{ch}}_{\mathrm{T,gen\,jet}}}$ distribution with the other variations and with the unfolded final spectrum (obtained with the Bayesian iterative technique described below). Also for the $z^{\mathrm{ch}}_{||}$ distribution the baseline prior was obtained from the Monte Carlo charm-enhanced production. Variations were obtained by applying a distortion to the baseline to make it represent a softer or harder fragmentation. In addition a flat distribution was used. These variations are compared with the unfolded distributions in Fig. 3.39. The bin-by-bin correction factors obtained with all the different choices of $N^{\mathrm{MC}}_{p^{\mathrm{ch}}_{\mathrm{T,gen\,jet}}}$ or $N^{\mathrm{MC}}_{z^{\mathrm{ch}}_{||,\mathrm{gen}}}$ are compared in Fig. 3.40. We observe significant differences between the correction factors obtained with the different prior choices, especially for the $z^{\mathrm{ch}}_{||}$ distributions.

Bayesian iterative technique The Bayes' theorem is used to estimate the conditional probability that the true value is in bin i given that the measurement was in bin j:

$$P(\text{true value in bin } i \mid \text{observed in bin } j) = \frac{p_i R_{ij}}{\sum_k p_k R_{kj}}, \tag{3.31}$$

where the vector p_i represents an initial guess of the true distribution (*prior*) with its integral normalized to one and R_{ij} represents the response matrix. For a given response R_{ij} and prior p_i, the conditional probability defined in Eq. 3.31 allows one to calculate an updated estimate of p_i, by multiplying this probability with the measured distribution. The procedure is repeated a few times until it converges, i.e. the χ^2 value between two successive updates of p_i is small. Typically a few $(3-5)$ iterations are sufficient for the procedure to converge. The number of iterations is the regularization parameter.

Regularized SVD technique A singular value decomposition (SVD) of a real $m \times n$ matrix R is its factorization of the form

$$R = USV^{\mathrm{T}}, \tag{3.32}$$

where U is an $m \times m$ orthogonal matrix, V is an $n \times n$ orthogonal matrix, while S is an $m \times n$ diagonal matrix with non-negative diagonal elements:

$$UU^{\mathrm{T}} = U^{\mathrm{T}}U = I, VV^{\mathrm{T}} = V^{\mathrm{T}}V = I, \tag{3.33}$$

$$S_{ij} = 0 \text{ for } i \neq j, S_{ii} \geq 0 \tag{3.34}$$

The quantities S_{ii} are called singular values of the matrix R. This decomposition allows one to eventually calculate the inverse of R. The interesting fact is that, after appropriate linear algebra manipulations (which can be found in detail in [166]), the

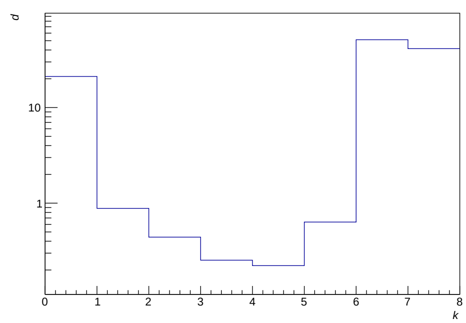

(a) $p_{\mathrm{T,jet}}^{\mathrm{ch}}$

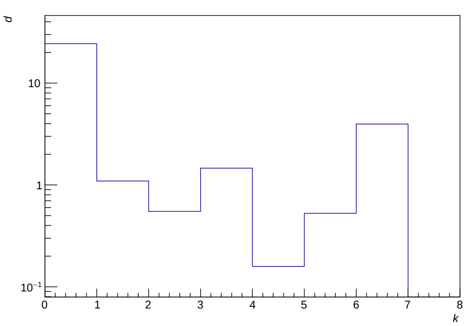

(b) $z_{||}^{\mathrm{ch}}$, $5 < p_{\mathrm{T,jet}}^{\mathrm{ch}} < 15$ GeV/c

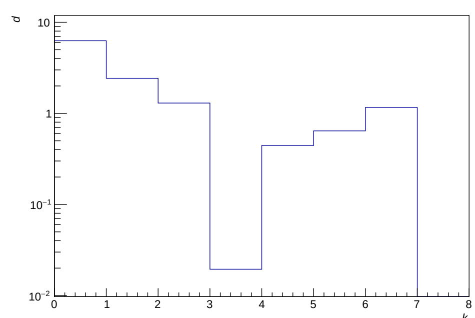

(c) $z_{||}^{\mathrm{ch}}$, $15 < p_{\mathrm{T,jet}}^{\mathrm{ch}} < 30$ GeV/c

Figure 3.41: Vector d_i (see text for details) of the detector response matrices of D^0-meson tagged jets.

origin of the difficulty of the unfolding problem becomes apparent. The solution can be written as the sum of n linear terms, where n is the number of bins in the measured histogram. It can be shown that if bins are small compared to the detector resolution and at the same time statistical uncertainties are large, some of these terms are not significant and should be neglected to obtain a sensible result. The regularization parameter k coincides with the number of terms kept in the linear expansion of the solution. A simple quantitative measure of how many terms should be retained is given by the d_i values, which are the coefficients of the rescaling and the rotation of the vector representing the measured histogram. It is expected that the first few d_i values are large, then they drop exponentially and form a plateau around unity. Since their statistical uncertainty is one by construction, only the first few d_i terms are significant. Figure 3.41 shows the d_i vectors obtained from the detector response matrices of D^0-meson tagged jets. For the $p_{\mathrm{T,jet}}^{\mathrm{ch}}$ response the d_i vector does not correspond to the expected pattern described above. It is possible that the large statistical uncertainty of the last bin of the measured $p_{\mathrm{T,jet}}^{\mathrm{ch}}$ distribution (almost 70%) breaks down some of the assumptions made in the algebraic manipulations. Another possibility is that the code used for the regularized SVD unfolding (`RooUnfold` [151]) assumes Poisson's statistics for each bin (the measured spectrum does not conform to Poisson's statistics because statistical uncertainties come from the signal extraction in the invariant mass fits). Unfortunately it is not clear from the documentation of `RooUnfold` whether Poisson's statistics is assumed and it was not possible to get an answer from the author. No further investigation was done on this issue because it is used only as a cross check, while the unfolding method used for the final results is the Bayesian iterative method described above. For the $z_{||}^{\mathrm{ch}}$ distributions, the d_i vectors seem to conform more closely with the expected behavior.

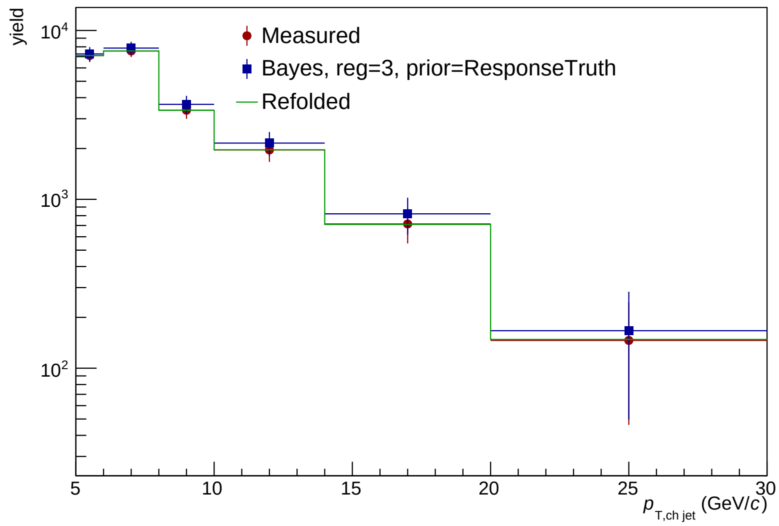

(a) Efficiency-corrected yields

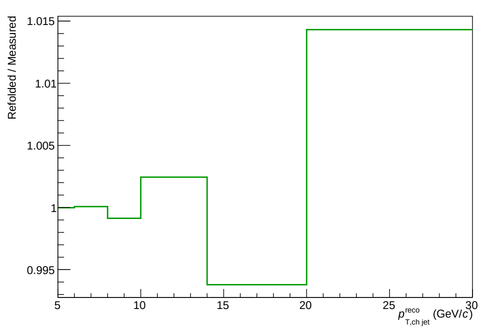

(b) Ratio Refolded / Measured

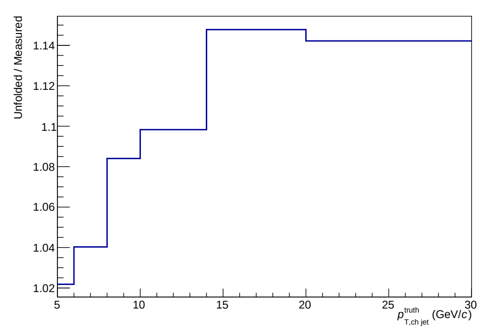

(c) Ratio Unfolded / Measured

Figure 3.42: Top: measured prompt D^0-jet p_{T} spectrum in pp collisions at $\sqrt{s}$ = 7 TeV, corrected for reconstruction efficiency and B feed-down (red symbols), compared with the unfolded (blue symbols) spectrum. The green line is the refolded spectrum, which is obtained by applying the response matrix to the unfolded distribution. Bottom left: ratio between the refolded and measured spectra. Bottom right: ratio between the unfolded and measured spectra.

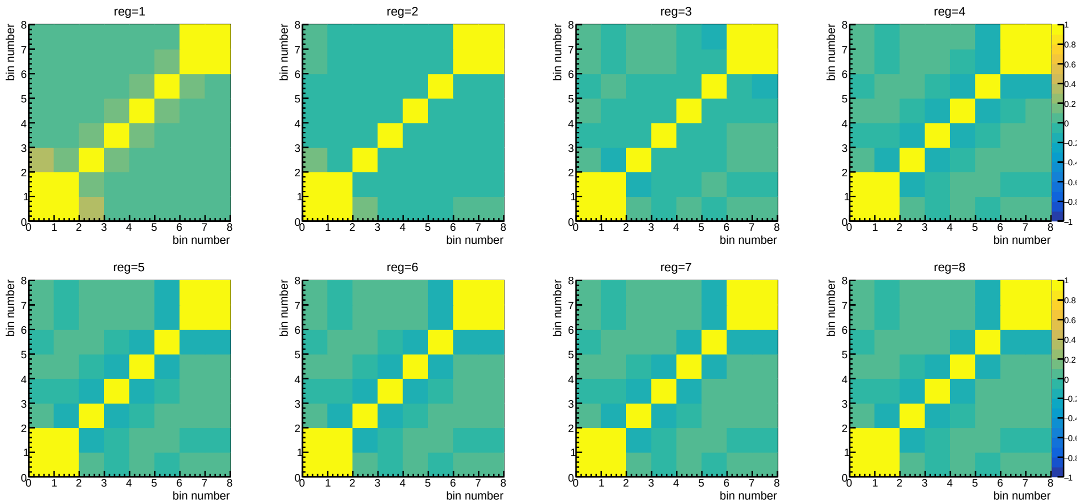

Figure 3.43: Pearson correlation coefficients obtained from the unfolding of the $p_{\mathrm{T,jet}}^{\mathrm{ch}}$ distribution of D^0-meson tagged jets with the Bayesian iterative method for different numbers of iterations. Starting from top left to bottom right: from 1 to 8 iterations.

Unfolding of the jet p_{T}-differential cross section

The prompt D^0-meson tagged jet spectrum unfolded with the Bayesian iterative method (blue solid squares) is compared in Fig. 3.42a with the measured spectrum (red solid circles) and the refolded spectrum (green line). The iterative unfolding procedure converged after 3 iterations. The prior distribution was taken to coincide with the spectrum from the Monte Carlo charm-enhanced production. The refolded spectrum is obtained applying the detector response matrix to the unfolded spectrum and it should be compatible with the original measured spectrum. The ratio of the refolded spectrum over the measured spectrum is shown in Fig. 3.42b. The largest deviation is 1% in the last bin. Deviations smaller than the statistical uncertainties are expected because of the regularization of the unfolding procedure. Figure 3.42c shows the ratio of the unfolded spectrum over the measured spectrum. From this ratio we see that the overall correction resulting from the unfolding of the detector response is 2% in the low-$p_{\mathrm{T,jet}}^{\mathrm{ch}}$end of the spectrum and increases up to 14% in the high-$p_{\mathrm{T,jet}}^{\mathrm{ch}}$ end. For all bins these correction factors are smaller than the statistical uncertainties.

After unfolding, bins become correlated with each other. The yield in any given bin of the unfolded spectrum depends in principle on the yield of the full measured spectrum. Of course the correlation is stronger between neighboring bins and depends on the detector resolution. Pearson correlation coefficients measure the correlations between bins in the unfolded result. They are defined as:

$$\rho_{i,j} = \frac{\mathrm{cov}(i,j)}{\sigma_i \sigma_j}, \tag{3.35}$$

where $\mathrm{cov}(i,j)$ is the covariance between bins i and j and σ_i is the standard deviation of bin i (square of the statistical uncertainty of its content). The interpretation of the Pearson correlation coefficients is the following:

$\mathbf{1} =$ maximum level of correlation between two bins;

$\mathbf{0} =$ no correlation;

$\mathbf{-1} =$ maximum level of anti-correlation between two bins.

Positive (negative) values in between these limits represent increasing levels of correlation (anti-correlation). It is expected that all bins have strong autocorrelations, i.e. diagonal elements ≈ 1. A mild correlation is expected between neighboring bins. More extreme structures in these matrices indicate that the unfolding regularization was too strong (too few iterations) or too weak (too many iterations). A strong regularization will lead to a strong correlation between all bins and the presence of a potential bias in the result. A weak regularization is signaled by the appearance of a mild or strong anti-correlation between neighboring bins; correspondingly, artificial fine structures and large statistical fluctuations will appear in the unfolded result. These observations are confirmed by Fig. 3.43 that show the Pearson correlation coefficients, represented by 8×8 matrices, obtained for the unfolded $p_{\mathrm{T,jet}}^{\mathrm{ch}}$ distributions of D^0-meson tagged jets for the different iterations of the Bayesian unfolding. The x, y

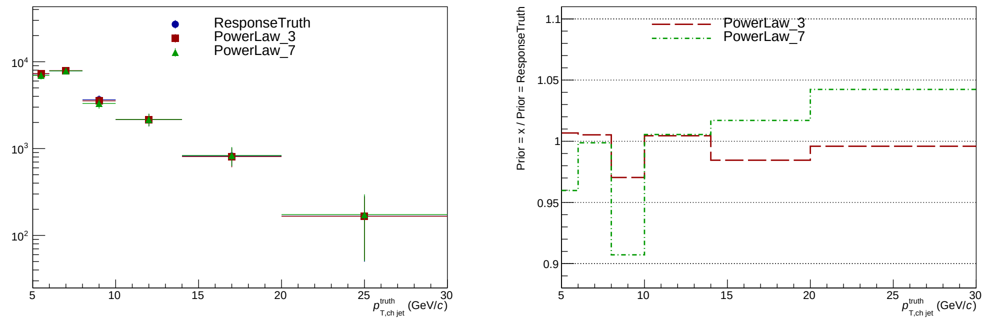

(a) Yield (b) Ratio

Figure 3.44: Unfolded prompt D^0-meson tagged jet p_T spectra; unfolding is performed using the iterative Bayesian method. Three different prior choices are compared: the PYTHIA 6 spectrum (open symbols) and the modified power-law spectra with index 3 (blue) and 7 (red). The ratios between the spectra unfolded with the power-law priors and the baseline unfolded with the PYTHIA 6 prior are shown on the right.

axes represent the bin numbers and the color axis represents the value of the Pearson correlation coefficient. The first and last bins are the underflow ($p_{T,jet}^{ch} < 5$ GeV/c) and overflow ($p_{T,jet}^{ch} > 30$ GeV/c) bins, respectively. They are empty by construction in the measured spectrum and are filled in the unfolded results as a result of the resolution unsmearing. Thus they are almost fully correlated with the next and previous bins, respectively. At the first iteration we observe a high level of correlation between bins. For $2, 3$ iterations we see healthy-looking Pearson coefficients. Increasing the number of iterations we start observing increasing levels of anti-correlation between neighbouring bins, a sign of a weak regularization strength.

Figure 3.44 compares the unfolded results obtained starting with the three different priors described above (see Fig. 3.38): the PYTHIA 6 spectrum and the modified power-law spectra with indexes 3 and 7. No significant difference in the results is observed, contrary to the effect shown for the bin-by-bin correction factors in Fig. 3.44.

Figure 3.45 exhibits how the unfolded spectrum evolves with increasing number of iterations. The procedure converges very quickly: after three iterations the change in the unfolded results is $< 1\%$.

Figure 3.46 compares the baseline unfolded result (obtained using the Bayesian

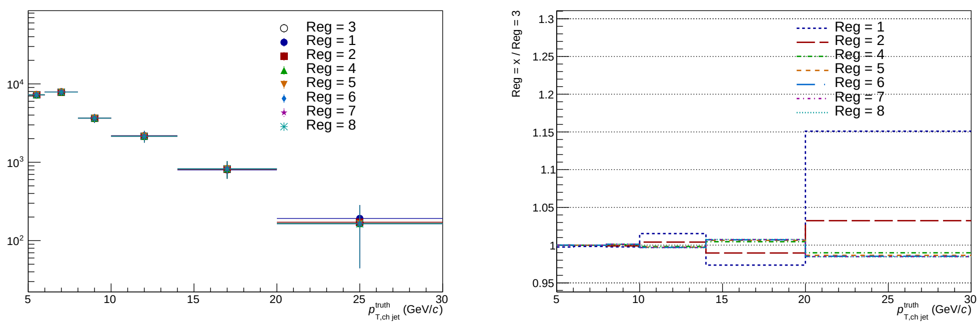

(a) Yield (b) Ratio

Figure 3.45: Unfolded prompt D^0-meson tagged jet p_{T} spectra; unfolding is performed using the iterative Bayesian method. The evolution of the unfolded spectrum with increasing number of iterations is shown in different colors from 1 to 8 iterations. The ratios between each iteration and the baseline (3 iterations) are shown on the right.

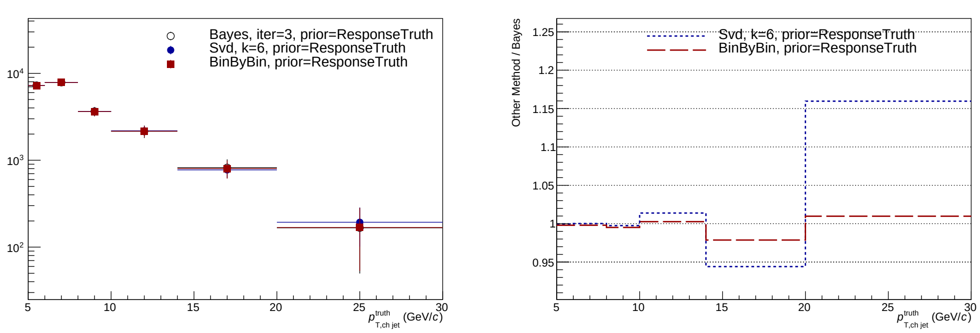

(a) Yield (b) Ratio

Figure 3.46: Unfolded prompt D^0-meson tagged jet p_{T} spectra. Three unfolding methods are compared: iterative Bayesian (3 iterations, open symbols), regularized SVD ($k = 6$, blue symbols), bin-by-bin correction (red symbols). The ratios between SVD/Bayesian and bin-by-bin/Bayesian are shown on the right.

iterative approach with 3 iterations) with the result obtained with the regularized SVD method and with the bin-by-bin correction method. The three methods agree well with each other, despite very large statistical uncertainties.

Unfolding of the D^0 momentum fraction distribution

A completely equivalent procedure was performed to unfold the $z_{||}^{\mathrm{ch}}$ distribution of D^0-meson tagged jets, separately for the two jet momentum ranges: $5 < p_{\mathrm{T,jet}}^{\mathrm{ch}} < 15$ GeV/c and $15 < p_{\mathrm{T,jet}}^{\mathrm{ch}} < 30$ GeV/c. The details will be omitted here. They are available in the dedicated Appendix B.

3.9 Systematic Uncertainties

3.9.1 Sources of Systematic Uncertainties

Sources of systematic uncertainties can be ascribed to the following issues:

1. limited knowledge of the detector performance;

2. potential and unavoidable biases introduced by the analysis procedure.

The first point is typically a consequence of the limitations of the simulation software in accurately reproducing all aspects of particle detection provided by the experimental apparatus. The track-reconstruction efficiency and the D^0-meson reconstruction efficiency, particularly its dependence on the topological and PID selections, are examples of sources of this kind of uncertainty. In the analysis procedure a number of unavoidable assumptions are made, e.g. the shape of the combinatorial background and of the signal components in the invariant mass distribution. These assumptions introduce potential biases that must be quantified and included in the systematic uncertainty.

The distinction drawn above should only be considered as a conceptual guidance. In practice, uncertainties were identified and quantified empirically by applying specific variations on the analysis parameters, which are expected to expose a particular source of systematic uncertainty. In the following we will discuss all sources of systematic uncertainties that were identified.

Track-reconstruction efficiency

The uncertainty on the track-reconstruction efficiency is mainly a consequence of the limited detector knowledge: simulation of the particle transport in the tracking detectors (gas and silicon), conversion into electronic signals, calibration. Uncertainties on the track-reconstruction efficiency affect the measurement in two ways.

D^0-meson reconstruction efficiency A previous estimate made by other ALICE collaborators was used. This estimate was made specifically for the measurement of the D^0-meson p_T-differential cross section in pp collisions at $\sqrt{s} = 7$ TeV [115], which was performed using the same dataset and the same analysis techniques for what concerns the D^0-meson reconstruction part. These earlier studies found a p_T-independent systematic uncertainty of 4% for the D^0-meson reconstruction efficiency. The fact that this uncertainty was found to be p_T-independent allows us to apply it directly to the present measurement without further investigations.

Jet momentum resolution The effect was estimated using the following technique. In the simulation used to extract the detector response matrix (see Section 3.7.2), tracks reconstructed at detector level were randomly rejected with a frequency equal to the uncertainty on the track-reconstruction efficiency. The relative systematic uncertainty on the track-reconstruction efficiency for the set of hybrid tracks used for jet reconstruction (see Section 3.5) was estimated to be 5% in earlier works published by the ALICE Collaboration based on the same dataset [154]. A detector response matrix was obtained with the artificially reduced tracking efficiency. As a result, the jet momentum shifted by a net negative 1% on average, while the change in the momentum resolution was negligible. Unfolding was repeated using this modified response matrix, both for the $p_{\mathrm{T,jet}}^{\mathrm{ch}}$ and $z_{||}^{\mathrm{ch}}$ distributions. The distributions unfolded with the modified response matrix were compared with the distributions unfolded with the normal response matrix: the relative difference between the two was taken as a systematic uncertainty. The uncertainties on the yield were found to be less than 7% in most cases. It must be noted that this technique allows us to directly assess the uncertainty for the case in which the track-reconstruction efficiency was over-estimated. The uncertainty on the track-reconstruction efficiency is however symmetric (equal probabilities of being under- or over-estimated). It was assumed that also its effect on the jet yield (as estimated with the technique described above) is symmetric.

$\mathbf{D^0}$-meson selection cuts

The D^0-meson reconstruction efficiency strongly depends on the selection cuts applied to the decay topology of the D^0-meson decay products (Section 3.7.1). Therefore the estimation of the reconstruction efficiency from the Monte Carlo simulation relies on the accurate simulation of the detector performance in reconstructing the decay topology. The uncertainty arising from the limited accuracy of the detector simulation was determined repeating the analysis using different sets of cuts consistently in data and simulation. In fact, a small variation of the selection cuts, when consistently applied both to the data analysis chain and to the simulation analysis chain should have a negligible net effect once the efficiency correction is applied to the data. Any discrepancy can be ascribed to inaccuracies in the detector simulation. This study was performed for the measurement of the D^0-meson p_{T}-differential cross section [115]. A relative difference of about 5% was found when cuts were varied consistently in

Table 3.7: Variations of the fitting parameters of the invariant mass distributions to evaluate the systematic uncertainties on the raw yield extraction. $m_{\rm inv}^{\rm min}$ and $m_{\rm inv}^{\rm max}$ are the lower and upper limits, respectively, of the invariant mass fit range.

Parameter	Default	Variation(s)
$m_{\rm inv}^{\rm min}$ (GeV/c^2)	1.715	1.739, 1.691
$m_{\rm inv}^{\rm max}$ (GeV/c^2)	2.015	1.991, 2.039
Invariant mass bin width (MeV/c^2)	6	12
Background fit function	exponential	1st & 2nd order polynomial
m_0 and σ_0	free parameters	see table 3.8

data and simulation. A negligible $p_{\rm T}$ dependence was observed. This study was not repeated in the context of this analysis and the same uncertainty estimation was employed.

Raw yield extraction

The raw yield was extracted via a statistical analysis of the invariant mass distributions as described in Section 3.6.3. The invariant mass distributions were fit using functional forms that are empirical, i.e. not based on any "first-principle" prescription. This technique introduces a potential bias in the extraction of the raw yield: it is unavoidable and it can and should be quantified. The systematic uncertainties on the raw yield extraction were estimated by repeating the fitting procedure of the invariant mass distributions several times, with different fitting conditions. The fitting parameters and their variations are listed in Table 3.7 and Table 3.8. Several combinations of these variations were taken into account, totaling over 300 trials. The ratios of the signal yield obtained in each of these trials over the signal yield obtained with the default fitting conditions are shown in Figs. 3.47 and 3.48, for the $p_{\rm T,jet}^{\rm ch}$ and $z_{||}^{\rm ch}$ distributions, respectively. The root-mean-square of the differences between signal-yield distributions obtained from the successful trials was taken as the systematic uncertainty. Trials with large χ^2 or unsuccessful fit were excluded.

Table 3.8: Variations of the parameters of the Gaussian fit function of the invariant mass distributions. The first row corresponds to the default choice; the other variations are used to evaluate the systematic uncertainties on the raw yield extraction. σ_{MC} is obtained fitting with a Gaussian function the invariant mass distribution of the signal (without background) in the charm-enhanced Monte Carlo production; m_{PDG} is the value of the D^0-meson mass reported in [67].

m_0	σ_0
free	free
free	σ_{MC}
free	$1.15 \times \sigma_{\mathrm{MC}}$
free	$0.85 \times \sigma_{\mathrm{MC}}$
m_{PDG}	free
m_{PDG}	σ_{MC}

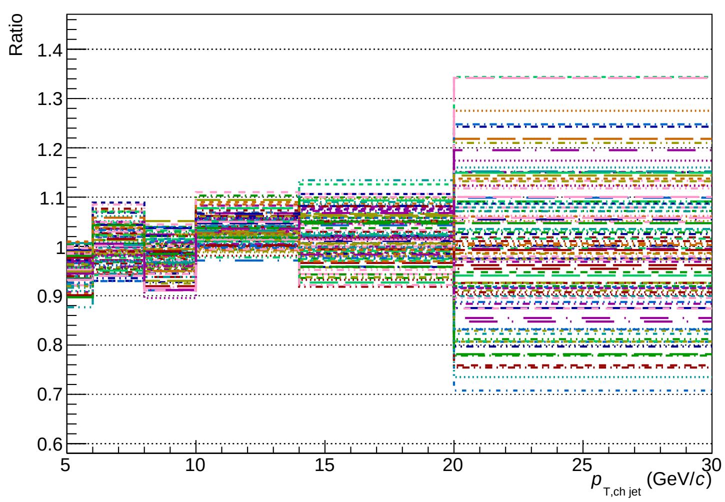

Figure 3.47: Ratio of the signal yield as a function of $p_{\mathrm{T,jet}}^{\mathrm{ch}}$ obtained with each of several hundreds of trials over the yield obtained with the default fitting conditions of the invariant mass distribution. The root-mean-square of the relative differences is used to estimate the systematic uncertainty. See text for details.

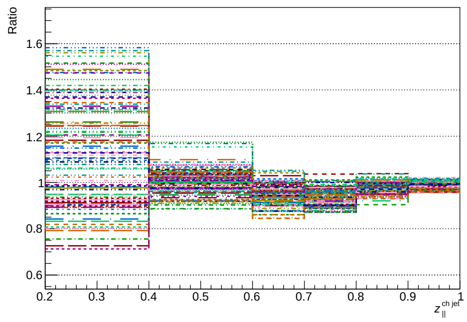

(a) $5 < p_{\mathrm{T,jet}}^{\mathrm{ch}} < 15$ GeV/c

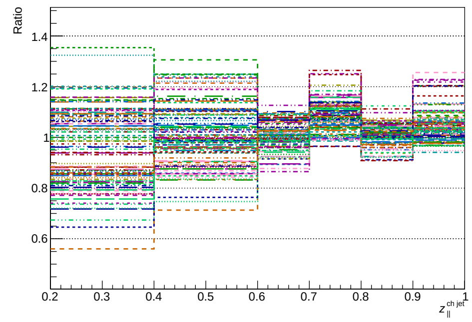

(b) $15 < p_{\mathrm{T,D}} < 30$ GeV/c

Figure 3.48: Ratio of the signal yield as a function of $z_{||}^{\mathrm{ch}}$ obtained with each of several hundreds of trials over the yield obtained with the default fitting conditions of the invariant mass distribution. The root-mean-square of the relative differences is used to estimate the systematic uncertainty. See text for details.

Furthermore a separate study was performed to estimate the systematic uncertainty arising from the modeling of the D^0-meson reflections. The reflections were included in the fit function using templates built from the Monte Carlo charm-enhanced production (see Section 3.6.3). The templates were obtained fitting the invariant mass distribution of the D^0-meson reflection with a double Gaussian function and fixing the ratios of the reflections over the signal to the value obtained from the same Monte Carlo simulation. Both the shape of the templates and the ratios of the reflections over signal were varied: the shape was varied replacing the double Gaussian with a simple Gaussian, a 3rd and a 6th order polynomial; the ratios were varied by $\pm$ 50%. Figures 3.49 and 3.50 show the ratio of the raw yields obtained with each of these reflection template variations and the default raw yield, for the $p_{\mathrm{T,jet}}^{\mathrm{ch}}$ and $z_{||}^{\mathrm{ch}}$ distributions, respectively. Also the case in which the reflection templates are not included at all in the fit function is shown: it is not part of the systematic uncertainty evaluation and it is reported only to show the effect of excluding the reflection templates from the fit. For the final evaluation of the systematic uncertainty only the $\pm$50% variation of the reflections-over-signal ratio was taken into account since it produces a variation on the yield that is the largest.

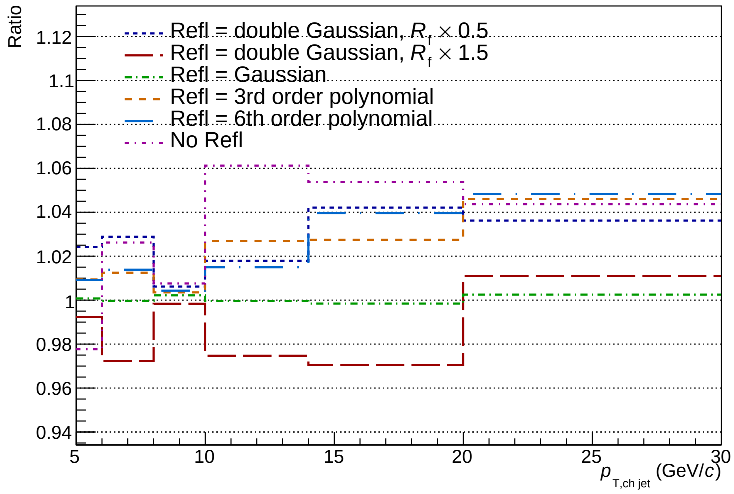

Figure 3.49: Ratio of the signal yield as a function of $p_{\mathrm{T,jet}}^{\mathrm{ch}}$ obtained with each variation of the $\mathrm{D^0}$-meson reflection templates over the yield obtained with the default fitting conditions of the invariant mass distribution. Variations of the ratio reflections over signal: -50% (blue), $+50\%$ (red). Variations of the template shape: simple Gaussian (green), 3rd order polynomial (green), 6th order polynomial (azure). The case without reflection templates in the fit function is also shown (violet). See text for details.

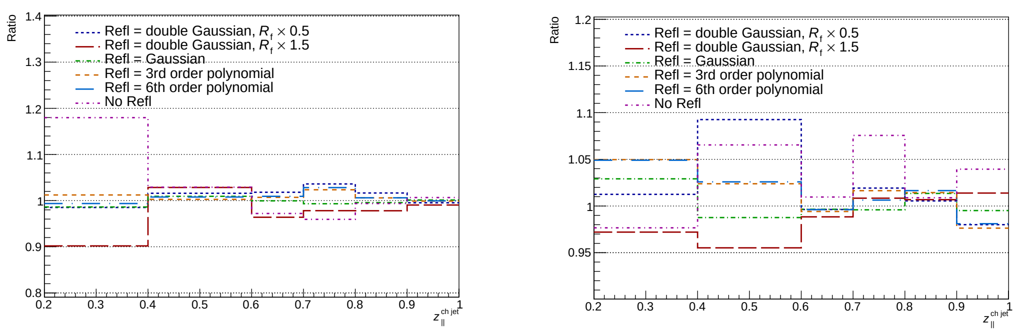

(a) $5 < p_{\mathrm{T,jet}}^{\mathrm{ch}} < 15$ GeV/c

(b) $15 < p_{\mathrm{T,D}} < 30$ GeV/c

Figure 3.50: Ratio of the signal yield as a function of $z_{||}^{\mathrm{ch}}$ obtained with each variation of the $\mathrm{D^0}$-meson reflection templates over the yield obtained with the default fitting conditions of the invariant mass distribution. Variations of the ratio reflections over signal: -50% (blue), $+50\%$ (red). Variations of the template shape: simple Gaussian (green), 3rd order polynomial (green), 6th order polynomial (azure). The case without reflection templates in the fit function is also shown (violet). See text for details.

Table 3.9: Variations of the parameters of the POWHEG + PYTHIA 6 simulation to evaluate the systematic uncertainties on the B feed-down.

Parameter	Default	Variation(s)
m_{b} (GeV/c^2)	4.75	4.5, 5.0
(μ_{F}, μ_{S})	(1, 1)	(0.5, 0.5), (0.5, 1), (1, 0.5), (2, 2), (2, 1), (1, 2)
PDF	CT10nlo [161]	MSTW2008nlo68cl [167]
Decay model	EvtGen	PYTHIA 6

B feed-down correction

The feed-down from b-hadron decays was subtracted using the production cross section estimated from a POWHEG + PYTHIA 6 simulation, as described in Section 3.8.2. The simulation parameters and the range in which they were varied to estimate the systematic uncertainties are listed in Table 3.9. The b-jet feed-down was calculated with each of these variations independently. The systematic uncertainty was obtained by taking the largest upward and downward variations from the central points. Figures 3.51 and 3.52 (left) show the ratios of the yields obtained with each of these variations over the central points, as a function of $p_{\mathrm{T,jet}}^{\mathrm{ch}}$ and $z_{||}^{\mathrm{ch}}$, respectively; the final b-jet feed-down yields with their systematic uncertainties are shown on the right.

Unfolding

In Section 3.8.3 we discussed the unfolding procedure used to correct the distortions on the shapes of the signal distributions as a function of $p_{\mathrm{T,jet}}^{\mathrm{ch}}$ and $z_{||}^{\mathrm{ch}}$caused by the detector finite resolution. As discussed there, several tests were performed to verify the stability of the unfolding procedure and the possible presence of biases. These tests included the variation of the regularization parameter, the variation of the prior distribution, the variation of the regularization technique (iterative Bayesian and regularized SVD). All these variations did not expose any instability neither the

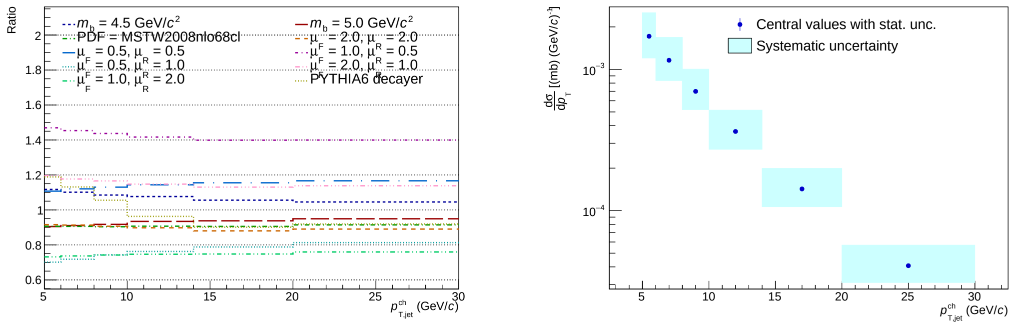

Figure 3.51: Left: ratios of the b-jet feed-down yields obtained with several variations of the Monte Carlo parameters and the default as a function of $p_{\mathrm{T,jet}}^{\mathrm{ch}}$. Right: final yield as a function of $p_{\mathrm{T,jet}}^{\mathrm{ch}}$ with the systematic uncertainties represented by cyan boxes.

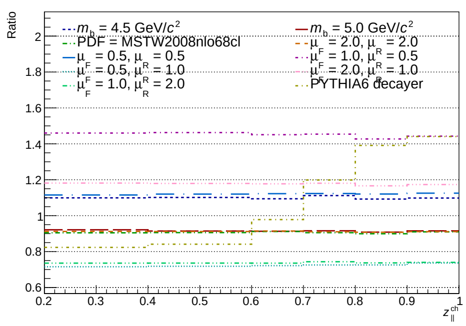

(a) Ratios: $5 < p_{\mathrm{T,jet}}^{\mathrm{ch}} < 15$ GeV/c

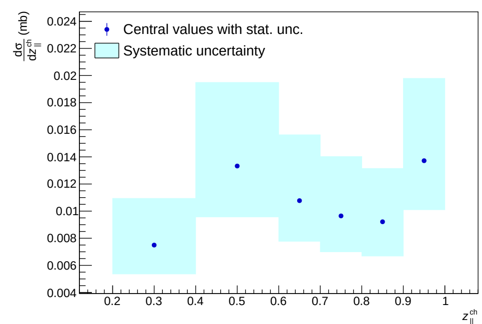

(b) Yield: $5 < p_{\mathrm{T,jet}}^{\mathrm{ch}} < 15$ GeV/c

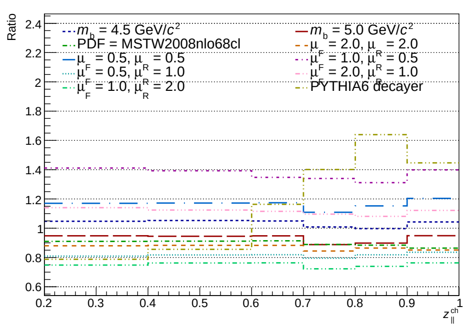

(c) Ratios: $15 < p_{\mathrm{T,D}} < 30$ GeV/c

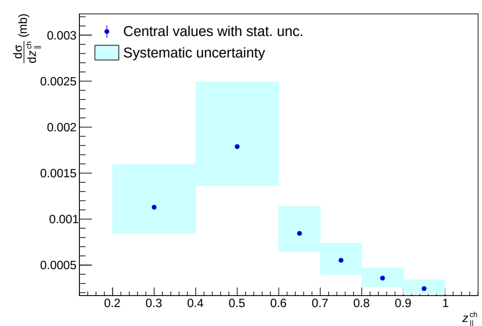

(d) Yield: $15 < p_{\mathrm{T,D}} < 30$ GeV/c

Figure 3.52: Left: ratios of the b-jet feed-down yields obtained with several variations of the Monte Carlo parameters and the default as a function of $z_{||}^{\mathrm{ch}}$. Right: final yield as a function of $z_{||}^{\mathrm{ch}}$ with the systematic uncertainties represented by cyan boxes.

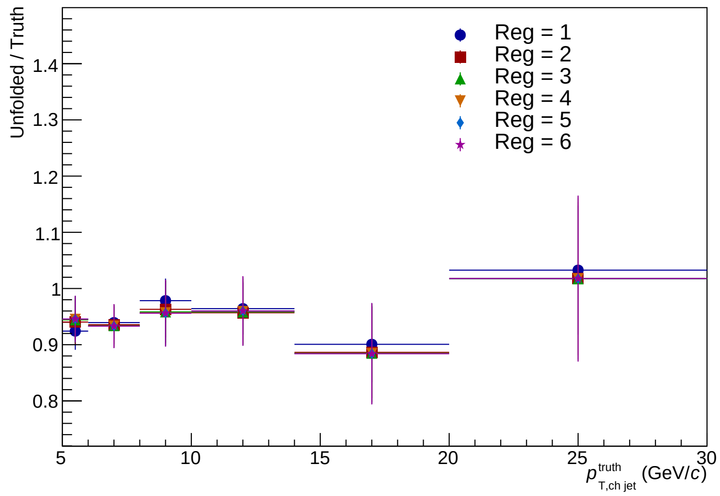

Figure 3.53: The D^0-meson tagged jet distribution as a function of $p_{\mathrm{T,jet}}^{\mathrm{ch}}$ as obtained from the minimum-bias Monte Carlo production was unfolded using the response matrix from the charm-enhanced Monte Carlo production. The ratios between the unfolded distribution and the generator-level distribution are shown for different number of iterations of the Bayesian iterative procedure (see text for details).

presence of significant biases.

In addition a Monte Carlo closure test was performed. The D^0-meson tagged jets reconstructed from the minimum-bias Monte Carlo production (which has a statistical precision comparable to the data) was unfolded using a detector response matrix obtained from the charm-enhanced Monte Carlo production. The unfolded results were compared to the generator-level distributions of the minimum-bias Monte Carlo production, as shown in Fig. 3.53. A p_{T}-independent 5% systematic uncertainty was assigned based on the maximum deviations observed between the unfolded result and the truth.

Cross-section normalization

The normalization of the differential cross sections is affected by uncertainties on the $D^0 \rightarrow K^-\pi^+$ branching ratio (1% [67]) and on the minimum-bias cross section (3.5% [137]).

The total systematic uncertainties were obtained by summing in quadrature the uncertainties estimated for each of the sources outlined above.

3.9.2 p_T-differential cross section

A summary of the uncertainties affecting the p_T-differential cross section is given in Table 3.10. The uncertainties are also compared graphically in Fig. 3.54.

The systematic uncertainty affecting the jet energy scale via the track-reconstruction efficiency increases with $p_{\mathrm{T,jet}}^{\mathrm{ch}}$ from 1% to 7%. This behavior is explained by the fact that, as we shall see in the next Section, at low $p_{\mathrm{T,jet}}^{\mathrm{ch}}$ there is a large contribution of jets having the D^0 meson as single constituent. For these jets, any uncertainty on the track-reconstruction efficiency has no effect on the reconstructed jet energy scale since the jet momentum coincides with the D^0-meson momentum[9].

The uncertainties due to the raw yield extraction and D^0-meson reflections are roughly constant in the range $5 < p_{\mathrm{T,jet}}^{\mathrm{ch}} < 14$ GeV/c, at about 4% and $2-3$%, respectively. In the last two bins the uncertainty due to the raw yield extraction increases significantly up to 15%. There is a variety of reasons that could explain this pattern: a change in shape of the invariant mass distribution of the combinatorial background or an inaccurate description of the invariant mass resolution in the Monte Carlo simulation – just to mention two possible explanations. At high $p_{\mathrm{T,jet}}^{\mathrm{ch}}$ the statistical uncertainty increases sharply as well: it is also possible that statistical fluctuations uncorrelated between different trials interfere with the estimation of the systematic uncertainty. In this case the systematic uncertainty may have been over-estimated.

The b-jet feed-down uncertainty increases with $p_{\mathrm{T,jet}}^{\mathrm{ch}}$ from 5% to 21%. The uncertainty on the theoretical b-jet cross section does not increase and actually shows

9. The track-reconstruction efficiency uncertainty still has a direct effect on the yield via the D^0-meson reconstruction efficiency, which is estimated and reported in Table 3.10 separately.

Table 3.10: Summary of systematic uncertainties as a function of $p_{\mathrm{T,jet}}^{\mathrm{ch}}$.

Source	Uncertainty (%)					
$p_{\mathrm{T,jet}}^{\mathrm{ch}}$ (GeV/c)	5 - 6	6 - 8	8 - 10	10 - 14	14 - 20	20 - 30
Tracking Eff. (Jet Energy Scale)	1	2	3	4	6	7
Raw Yield Extraction	4	4	4	4	11	15
Reflections	3	2	2	3	5	6
B Feed-Down (POWHEG)	5	5	7	9	17	21
B Feed-Down (decayer)	1	1	1	2	4	6
Unfolding	5	5	5	5	5	5
Selection Cuts	5	5	5	5	5	5
Tracking Eff. (D-Meson)	4	4	4	4	4	4
Normalization (BR & lumi)	3.6					
Total Systematic Uncertainty	11	11	13	14	24	29
Statistical	10	9	12	16	24	71
Total Uncertainty	15	14	17	22	34	77

a mild decrement with $p_{\mathrm{T,jet}}^{\mathrm{ch}}$. However, as shown in Fig. 3.37a, the b-jet fraction increases approximately from 10% to 40%. Therefore at large $p_{\mathrm{T,jet}}^{\mathrm{ch}}$ the b-jet feed-down subtraction is the dominant source of uncertainty.

The total systematic uncertainty rises slightly with increasing $p_{\mathrm{T,jet}}^{\mathrm{ch}}$ and is comparable to the statistical uncertainties, except for $20 < p_{\mathrm{T,jet}}^{\mathrm{ch}} < 30$ GeV/c, where the statistical uncertainty dominates.

3.9.3 $z_{||}^{\mathrm{ch}}$-differential cross section

The uncertainties affecting the $z_{||}^{\mathrm{ch}}$-differential cross section are reported in Table 3.11 and Fig. 3.55, for both ranges of $p_{\mathrm{T,jet}}^{\mathrm{ch}}$. Similar considerations already drawn for the p_{T}-differential cross section apply to the uncertainties affecting the $z_{||}^{\mathrm{ch}}$-differential cross section. An interesting fact is that the uncertainty due to the track-reconstruction efficiency (via the jet energy scale) features an inverted pattern in the two $p_{\mathrm{T,jet}}^{\mathrm{ch}}$ ranges: it decreases with increasing $z_{||}^{\mathrm{ch}}$ for $5 < p_{\mathrm{T,jet}}^{\mathrm{ch}} < 15$ GeV/c, while it increases with increasing $z_{||}^{\mathrm{ch}}$ for $15 < p_{\mathrm{T,jet}}^{\mathrm{ch}} < 30$ GeV/c. This can be explained by the fact that the

Table 3.11: Summary of systematic uncertainties as a function of $z_{||}^{\mathrm{ch}}$.

(a) $5 < p_{\mathrm{T,jet}}^{\mathrm{ch}} < 15$ GeV/c

Source	Uncertainty (%)					
$z_{\vert\vert}^{\mathrm{ch}}$	0.2 - 0.4	0.4 - 0.6	0.6 - 0.7	0.7 - 0.8	0.8 - 0.9	0.9 - 1.0
Tracking Eff. (Jet Energy Scale)	6	4	1	1	2	2
Raw Yield Extraction	23	17	5	3	2	2
Reflections	9	8	4	3	2	2
B Feed-Down (POWHEG)	23	17	7	4	4	4
B Feed-Down (decayer)	8	5	2	2	3	4
Unfolding	5	5	5	5	5	5
Selection Cuts	5	5	5	5	5	5
Tracking Eff. (D-Meson)	4	4	4	4	4	4
Normalization (BR & lumi)	3.6					
Total Systematic Uncertainty	36	28	13	11	11	11
Statistical	91	21	13	10	10	6
Total Uncertainty	98	35	19	15	15	13

(b) $15 < p_{\mathrm{T,jet}}^{\mathrm{ch}} < 30$ GeV/c

Source	Uncertainty (%)					
$z_{\vert\vert}^{\mathrm{ch}}$	0.2 - 0.4	0.4 - 0.6	0.6 - 0.7	0.7 - 0.8	0.8 - 0.9	0.9 - 1.0
Tracking Eff. (Jet Energy Scale)	3	3	2	3	9	13
Raw Yield Extraction	24	17	11	5	6	7
Reflections	11	8	7	2	2	2
B Feed-Down (POWHEG)	30	20	13	2	5	6
B Feed-Down (decayer)	13	9	6	4	7	8
Unfolding	5	5	5	5	5	5
Selection Cuts	5	5	5	5	5	5
Tracking Eff. (D-Meson)	4	4	4	4	4	4
Normalization (BR & lumi)	3.6					
Total Systematic Uncertainty	43	30	21	12	17	20
Statistical	114	87	31	34	31	70
Total Uncertainty	122	92	38	36	35	73

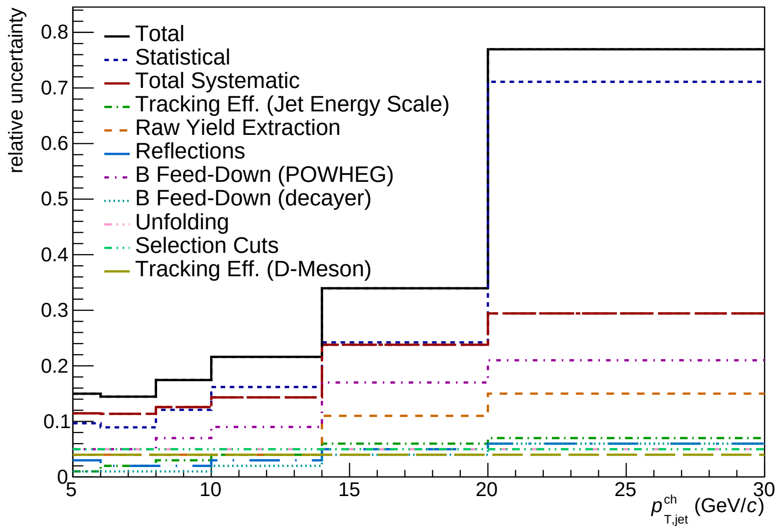

Figure 3.54: Relative uncertainties of the p_{T}-differential cross section of D^0-meson tagged jets in pp collisions at $\sqrt{s} = 7$ TeV.

two different ranges correspond to different jet constituent multiplicities: very small for the lower $p_{\mathrm{T,jet}}^{\mathrm{ch}}$ interval and larger from the higher $p_{\mathrm{T,jet}}^{\mathrm{ch}}$ interval.

For $5 < p_{\mathrm{T,jet}}^{\mathrm{ch}} < 15$ GeV/c, statistical and systematic uncertainties have similar magnitudes, except for $0.2 < z_{||}^{\mathrm{ch}} < 0.4$ where the statistics are very poor. For $15 < p_{\mathrm{T,jet}}^{\mathrm{ch}} < 30$ GeV/c, statistical uncertainties dominate over the entire $z_{||}^{\mathrm{ch}}$ range; the statistical uncertainty of the bin $0.2 < z_{||}^{\mathrm{ch}} < 0.4$ exceeds 100%, therefore this bin will be ignored in the following discussions and comparisons with theory.

3.10 Results

3.10.1 p_{T}-differential cross section

Figure 3.56 shows the p_{T}-differential cross section of D^0-meson tagged jets in pp collisions at $\sqrt{s} = 7$ TeV. Jets were measured in the pseudo-rapidity range $|\eta_{\mathrm{jet}}| < 0.5$ and tagged with D^0 mesons with $p_{\mathrm{T,D}} > 3$ GeV/c. The statistical uncertainties are shown with error bars, while systematic uncertainties are shown with gray boxes.

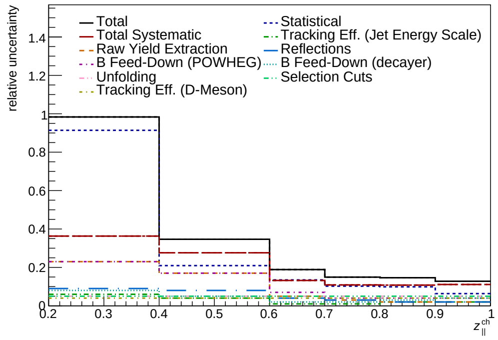

(a) $5 < p_{\mathrm{T,jet}}^{\mathrm{ch}} < 15$ GeV/c

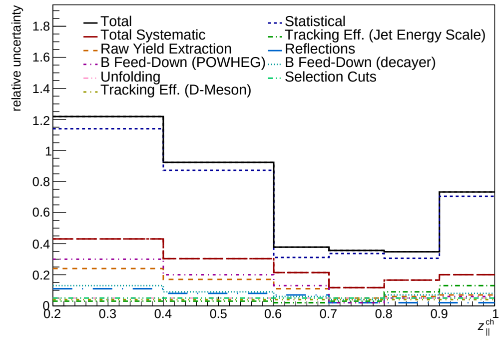

(b) $15 < p_{\mathrm{T,jet}}^{\mathrm{ch}} < 30$ GeV/c

Figure 3.55: Relative uncertainties of the $z_{||}^{\mathrm{ch}}$-differential cross section of D^0-meson tagged jets in pp collisions at $\sqrt{s} = 7$ TeV.

Transverse-momentum spectra of hard scattering processes typically follow a power law:

$$Cp_{\mathrm{T}}^{-a}. \tag{3.36}$$

The fit yields $a = 3.6 \pm 0.1$ (only statistical uncertainties), with $\chi^2/\mathrm{ndf} = 2.5$. Because of the finite charm quark mass, the differential cross section does not diverge for $p_{\mathrm{T}} \to 0$; in fact, the differential cross section is zero for $p_{\mathrm{T}} \to 0$. A better fit is thus obtained with a modified power law:

$$Cp_{\mathrm{T}}^{-a} e^{\frac{-ab}{p_{\mathrm{T}}}}, \tag{3.37}$$

where the exponential factor regularizes the function for $p_{\mathrm{T}} \to 0$ while being negligible for large p_{T}. The parameter b corresponds to the position of the local maximum of the function. The fit yields $a = 5.9 \pm 0.9$ and $b = 3.5 \pm 0.7$ GeV/c (only statistical uncertainties), with $\chi^2/\mathrm{ndf} = 0.2$.

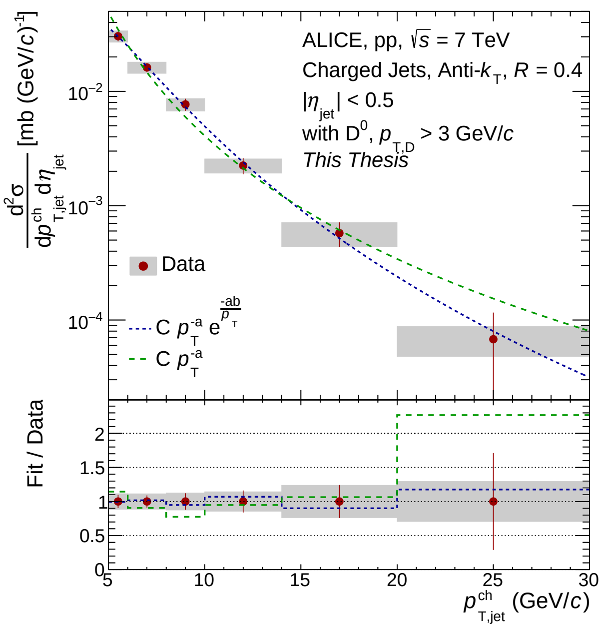

Figure 3.56: p_{T}-differential cross section of D^0-meson tagged jets in pp collisions at $\sqrt{s} = 7$ TeV.

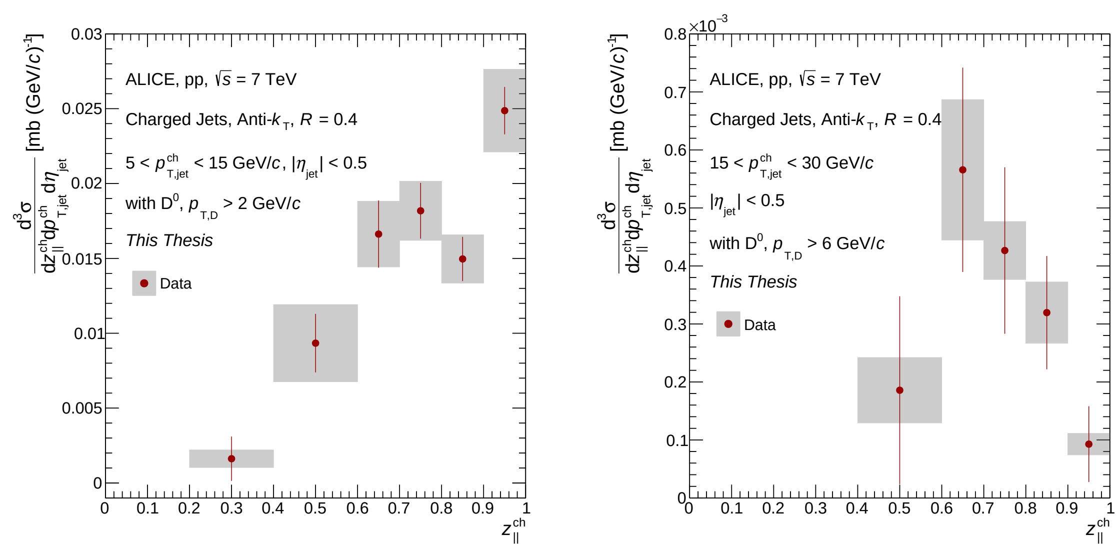

(a) $5 < p_{\mathrm{T,jet}}^{\mathrm{ch}} < 15$ GeV/c

(b) $15 < p_{\mathrm{T,jet}}^{\mathrm{ch}} < 30$ GeV/c

Figure 3.57: $z_{||}^{\mathrm{ch}}$-differential cross sections of D^0-meson tagged jets in pp collisions at $\sqrt{s} = 7$ TeV for two bins of $p_{\mathrm{T,jet}}^{\mathrm{ch}}$ as indicated below the panels.

3.10.2 $z_{||}^{\mathrm{ch}}$-differential cross section

Figure 3.57 shows the $z_{||}^{\mathrm{ch}}$-differential cross section of D^0-meson tagged jets in pp collisions at $\sqrt{s} = 7$ TeV. Jets were measured in the pseudo-rapidity range $|\eta_{\mathrm{jet}}| < 0.5$ and tagged with D^0 mesons with $p_{\mathrm{T,D}} > 2$ GeV/c and $p_{\mathrm{T,D}} > 6$ GeV/c, for $5 < p_{\mathrm{T,jet}}^{\mathrm{ch}} < 15$ GeV/c and $15 < p_{\mathrm{T,jet}}^{\mathrm{ch}} < 30$ GeV/c, respectively. The cuts on the minimum $p_{\mathrm{T,D}}$, allow us to probe the $z_{||}^{\mathrm{ch}}$-differential cross section without any bias for $z_{||}^{\mathrm{ch}} > 0.4$ for both $p_{\mathrm{T,jet}}^{\mathrm{ch}}$ intervals. For $5 < p_{\mathrm{T,jet}}^{\mathrm{ch}} < 15$ GeV/c, also the bin $0.2 < z_{||}^{\mathrm{ch}} < 0.4$ is reported with the caveat that the yield in this bin is biased because of the missing contribution of D^0 mesons with $1 < p_{\mathrm{T,D}} < 2$ GeV/c. The statistical uncertainties are shown with error bars, while systematic uncertainties are shown with gray boxes.

For $5 < p_{\mathrm{T,jet}}^{\mathrm{ch}} < 15$ GeV/c the cross section features a sharp peak at $z_{||}^{\mathrm{ch}} \approx 1$. This peak is populated by jets that contain only the D^0 meson as single constituent. The peak is not present for $15 < p_{\mathrm{T,jet}}^{\mathrm{ch}} < 30$ GeV/c, which instead has very low cross section for $z_{||}^{\mathrm{ch}} > 0.9$. If we neglect the bin $0.9 < z_{||}^{\mathrm{ch}} < 1$, we observe a local maximum in both distributions. The position of the local maximum is at $0.7 < z_{||}^{\mathrm{ch}} < 0.8$ for $5 < p_{\mathrm{T,jet}}^{\mathrm{ch}} < 15$ GeV/c and moves to $0.6 < z_{||}^{\mathrm{ch}} < 0.7$ for the higher $p_{\mathrm{T,jet}}^{\mathrm{ch}}$ interval. This pattern is expected: for higher jet momenta the effect of the mass of the D^0 meson becomes less important and the fragmentation function tends to the massless case, which diverges for $z_{||}^{\mathrm{ch}} \to 0$.

Chapter 4

Jets in Pb–Pb Collisions

4.1 Introduction

This Chapter describes the measurement of jet production in Pb–Pb collisions at $\sqrt{s_{\mathrm{NN}}} = 2.76$ TeV with the ALICE detector [156]. Before diving into the analysis details, the dataset and the techniques used to extract global event properties are introduced in Section 4.2. Jets were reconstructed using tracks and calorimeter energy clusters: they will be described in Section 4.3. The problem of the underlying event and the jet finding will be addressed in Section 4.4. In Section 4.5 the detector response and the unfolding is discussed. Section 4.6 is dedicated to the systematic uncertainties. Finally, in Section 4.7 the fully corrected jet p_{T} spectrum is presented.

4.2 Data Sample

4.2.1 Centrality Determination

Since nuclei are extended objects, the volume of the interacting region depends on the impact parameter (b) of the collisions, defined as the distance between the centers of the two colliding nuclei in the plane transverse to the beam direction. The centrality is typically expressed as a percentage of the total nuclear interaction cross section:

$$c = \frac{\int_0^b \mathrm{d}\sigma/\mathrm{d}b'\,\mathrm{d}b'}{\int_0^{\inf} \mathrm{d}\sigma/\mathrm{d}b'\,\mathrm{d}b'} = \frac{1}{\sigma_{\mathrm{AA}}}\int_0^b \frac{\mathrm{d}\sigma}{\mathrm{d}b'}\mathrm{d}b'. \tag{4.1}$$

The Glauber model [168] is a purely geometric description of the heavy-ion collisions that are treated as a superposition of binary nucleon-nucleon interactions. Relevant variables in this model are:

- the number of participant nucleons N_{part}, which is proportional to the volume of the initial overlap region;
- the number of spectators $N_{\mathrm{spec}} = 2A - N_{\mathrm{part}}$, where A is the number of nucleons contained in each nucleus;
- the number of binary collisions N_{coll}.

In the Glauber model these variables are calculated as a function of the impact parameter for a realistic distribution of the nucleons inside the nuclei and assuming that they follow straight line trajectories.

None of the variables mentioned above are directly measurable. Experimentally the centrality is determined in ALICE by measuring the average charged-particle multiplicity in the V0 detector (N_{ch}) [169]. N_{ch} decreases monotonically with increasing b. Alternatively, another centrality estimator is obtained by measuring the energy deposited in the zero-degree calorimeters (E_{ZDC}), which is directly related to the number of spectators that do not participate in the interaction. However its relation with b is not monotonic because nuclear fragments with similar magnetic rigidity as the beam nuclei may remain inside the beam pipe and thus not detected by the ZDC.

Equation 4.1 can be expressed in terms of experimental quantities:

$$c \approx \frac{1}{\sigma_{\mathrm{AA}}}\int_0^b \frac{\mathrm{d}\sigma}{\mathrm{d}N'_{\mathrm{ch}}}\mathrm{d}N'_{\mathrm{ch}} \approx \frac{1}{\sigma_{\mathrm{AA}}}\int_0^b \frac{\mathrm{d}\sigma}{\mathrm{d}E'_{\mathrm{ZDC}}}\mathrm{d}E'_{\mathrm{ZDC}}. \tag{4.2}$$

Table 4.1: Geometric properties (N_{coll} and N_{part}) of Pb–Pb collisions at $\sqrt{s_{\mathrm{NN}}} = 2.76$ TeV for centrality classes defined by sharp cuts in the V0 charged-multiplicity distribution [169].

Centrality	$< N_{\mathrm{part}} >$	$< N_{\mathrm{coll}} >$
$0 - 5\%$	382	1684
$5 - 10\%$	329.7	1316
$10 - 20\%$	260.5	922.7
$20 - 40\%$	157.8	440
$40 - 60\%$	69.13	128.4
$60 - 80\%$	22.64	26.48

During data reconstruction the centrality percentile of each event was calculated based on the calibrated signal of the V0 charged multiplicity. The average N_{coll} and N_{part} of centrality classes defined by sharp cuts in the measured V0 charged multiplicity, are obtained by relating N_{ch} to the geometrical variables of the collision via a Glauber Monte Carlo simulation. Table 4.1 reports the average values of N_{coll} and N_{part} for the experimental centrality classes defined for Pb–Pb collisions at a center-of-mass energy per-nucleon $\sqrt{s_{\mathrm{NN}}} = 2.76$ TeV.

4.2.2 Data Taking Conditions

Beam Parameters The data used for this analysis was collected by the ALICE detector in a data-taking campaign that took place between November and December 2011. This corresponds to the second run of the LHC delivering Pb–Pb collisions at the center-of-mass energy per-nucleon $\sqrt{s_{\mathrm{NN}}} = 2.76$ TeV. Pb ions were injected in the LHC in 15 trains of 24 bunches, for a total of 358 bunches (the last train missing 2 bunches). The bunch separation within a train was 200 ns; trains were separated by 900 ns. The peak instantaneous luminosity delivered by the LHC was 4.6×10^{26} $\mathrm{cm}^{-2}\mathrm{s}^{-1}$ with a maximum of 336 colliding bunches per fill. The interaction rate reached $3 - 4$ kHz. The average number of interactions per bunch crossing was in the range $10^{-4} - 10^{-3}$ [64], with negligible probability of collision pile-up.

Trigger Throughout this data-taking period ALICE collected events using a combination of minimum-bias, centrality and rare triggers. The minimum-bias trigger required a coincidence signal in both V0 cluster arrays and in both ZDC stations. The ZDC requirement suppresses the electromagnetic interactions between the lead ions. The minimum-bias trigger allows one to collect most of the hadronic cross section ($\approx 90\%$, excluding the most peripheral collisions), with negligible contamination from electromagnetic interactions. Two triggers based on the centrality of the collision as estimated by the V0 detector were active: a central trigger designed to collect events in the $0 - 10\%$ centrality class and a semi-central trigger for the $0 - 50\%$ centrality class. Thresholds were applied separately to the signals measured by each side of the V0, then the coincidence between the two sides was required. Rare triggers were also used to collect events containing rare processes, such us high energy jets (EMCal), photons (EMCal, PHOS), electrons (EMCal, TRD), muons (MTR), high-multiplicity (SPD). The analysis described in this Chapter is based on events collected with the minimum-bias and the centrality triggers.

4.2.3 Event Selection

Events were accepted if the coordinate of the reconstructed collision vertex measured along the beam direction was within ± 10 cm around the nominal interaction point. The event vertex reconstruction was fully efficient for the event centralities covered. A total of 11.5×10^6 and 5.7×10^6 events were analyzed, with V0 amplitudes corresponding to the $0 - 10\%$ and $10 - 30\%$ centrality classes, respectively. The centrality percentile distribution of the analyzed events is shown in Fig. 4.1. Three steps are visibile, that correspond to the three active triggers: the two triggers based on the V0 event centrality ($0 - 10\%$ and $0 - 50\%$) and the minimum-bias trigger.

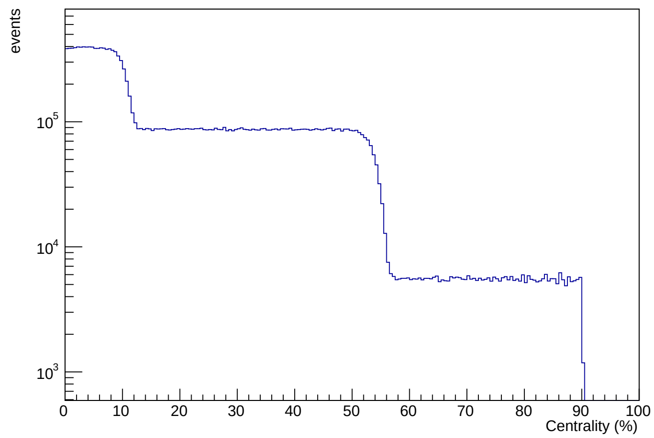

Figure 4.1: Centrality distribution of the analyzed Pb–Pb collision events at $\sqrt{s_{\mathrm{NN}}} =$ 2.76 TeV. The steps visible in the distribution are the result of the sum of three different triggers, as described in the text.

For a significant period of data taking, one of the TPC read-out chambers was not operating because of high voltage (HV) tripping issues. Events were still reconstructable, however a window in the (η,ϕ) plane was affected by low track-reconstruction efficiency. "Group `A`" events, reconstructed with the fully operational TPC, corresponds to roughly 60% of the total number of analyzed events; the rest of the events, recorded with one missing TPC read-out chamber, are classified as "group `B`". The missing chamber was reproduced in the detector simulation used to correct for instrumental effects (see Section 4.5.1). After correcting for instrumental effects, no significant difference was observed between jets reconstructed in group `A` and `B`.

4.2.4 Monte Carlo Simulations

Monte Carlo simulations were employed to assess the detector performance and calculate instrumental corrections to the measured quantities.

HIJING [170, 171] was used to simulate Pb–Pb collisions at $\sqrt{s_{\mathrm{NN}}} = 2.76$ TeV. The detector geometry and operational conditions were accurately reproduced in GEANT3 [141] in order to simulate the particle transport and detector response.

The ALICE Collaboration generated three Monte Carlo productions, one for each centrality class, name-coded as follows: `LHC12a17d_fix` ($0-10\%$), `LHC12a17e_fix` ($10-50\%$) and `LHC12a17f_fix` ($50-90\%$). Only limited statistics were made available through these productions (about 4 million events in total), because of their large computational cost. To simulate more accurately the detector response to jet reconstruction, another production was made by ALICE, using PYTHIA 6 [123] with the tune A to generate pp collisions at $\sqrt{s} = 2.76$ TeV. This production was name-coded `LHC12a15e_fix`. Also for this production, particles were transported by GEANT3. The ALICE geometry and operating conditions used in the simulation were set to reproduce those during the Pb–Pb data-taking campaign.

4.3 Preparation of the Jet Finder Input

Tracks and calorimeter energy clusters were used together as input for the jet finding. The combination of the tracking system with the electromagnetic calorimeter allows for the reconstruction of most of the particles produced by jet fragmentation, with the notable exception of K^0_L and neutrons. The missing momentum carried by those particles is corrected on a statistical basis using a Monte Carlo simulation, as explained in Section 4.5.1. The fraction of jet momentum carried by K^0_L and neutrons is in the range $3.6-6\%$ on average, according to a study performed by ALICE in pp collisions at $\sqrt{s} = 2.76$ TeV [153].

4.3.1 Tracking

Track Selection

A *hybrid* approach was used to obtain a uniform track-reconstruction efficiency in the (η,ϕ) plane. Global tracks, obtained by combining the ITS and TPC tracking, have the best momentum resolution. Standard track-quality cuts defined in ALICE require

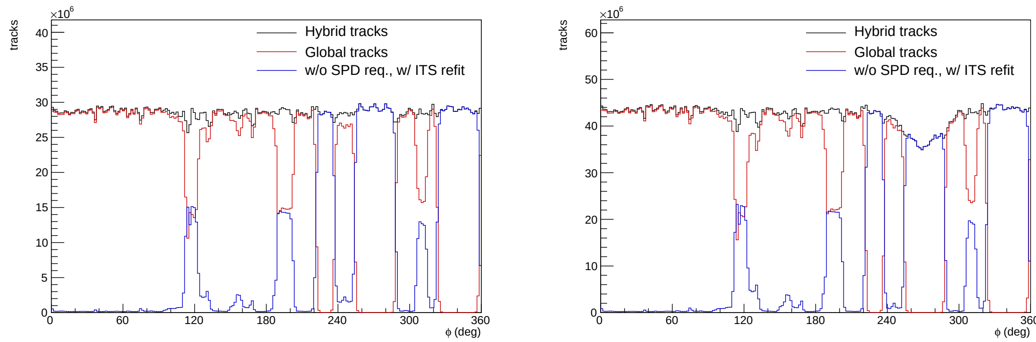

(a) Group A.

(b) Group B.

Figure 4.2: Track azimuthal distributions in Pb–Pb collisions at $\sqrt{s_{\mathrm{NN}}} = 2.76$ TeV. See text for details on the track selection and definition of Event Group A and B.

the presence of at least one SPD hit for the global tracks. Because of the presence of inactive SPD sectors, these quality cuts lead to a non-uniform track-reconstruction efficiency. The regions corresponding to inactive SPD sectors are supplemented with tracks selected with less strict cuts. A more detailed description of the tracking algorithm and track-quality selections was given when discussing the measurement of D^0-tagged jets in pp collisions at $\sqrt{s} = 7$ TeV, particularly in Section 3.5.2. Similar track-quality cuts were employed in this analysis, the only difference being that all complementary tracks were required to pass the ITS track refit.

Figures 4.2 and 4.3 show the azimuthal and pseudo-rapidity track distributions, respectively. For events in group B, the dip in the azimuthal distribution around $\phi \approx 270°$ and the drop at negative pseudorapidity are due to the missing read-out chamber in the TPC (see Section 4.2.3). The distributions are shown for the global tracks (red), for the complementary tracks without the SPD requirement (blue) and for the combination of the two, i.e. the hybrid sample (black).

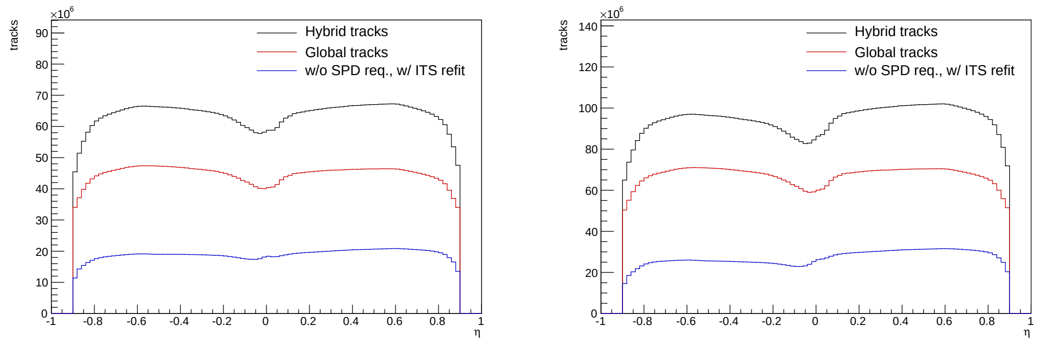

(a) Group `A`. (b) Group `B`.

Figure 4.3: Track pseudo-rapidity distributions in Pb–Pb collisions at $\sqrt{s_{\mathrm{NN}}} = 2.76$ TeV. See text for details on the track selection and definition of Event Group `A` and `B`.

Track-Reconstruction Performance

Figure 4.4 shows the track-reconstruction efficiency as a function of the track transverse momentum p_{T}, for different Pb–Pb centrality classes and for pp[1]. For the most central Pb–Pb collisions $(0-10\%)$, the track-reconstruction efficiency is about 56% for $p_{\mathrm{T}} = 0.15$ GeV/c; it increases to about 84% for $p_{\mathrm{T}} = 1.5$ GeV/c; then it decreases and reaches a local minimum of about 81% at $p_{\mathrm{T}} = 3$ GeV/c, after which it increases again and levels off at about 83% for $p_{\mathrm{T}} > 6.5$ GeV/c. The efficiency is slightly lower for larger event multiplicities. In particular, the Pb–Pb efficiency is lower by $2-4\%$ in the $0-10\%$ most central collisions when compared to pp collisions. The other Pb–Pb centrality classes have track-reconstruction efficiencies that lie in between these two extremes. The ratios between the track-reconstruction efficiencies in four Pb–Pb centrality classes $(0-10\%$, $10-30\%$, $30-50\%$ and $50-90\%)$ and that obtained from pp collisions is shown in the right panel of Fig. 4.4. The relative momentum resolution, estimated on a track-by-track basis using the covariance matrix of the track fit, is about 1% for $p_{\mathrm{T}} = 1.0$ GeV/c and about 3% for $p_{\mathrm{T}} = 50$ GeV/c. Tracks with $p_{\mathrm{T}} \gtrsim 100$ GeV/c have poor momentum resolution. However, rejecting them at

1. See Section 4.2.4 for details about the Monte Carlo productions used in this analysis

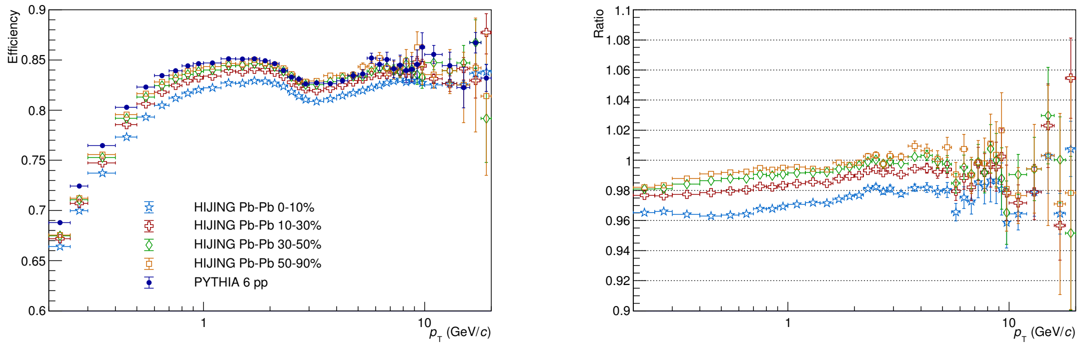

Figure 4.4: Left: track-reconstruction efficiency as a function of transverse momentum for four Pb–Pb centrality classes $0 - 10\%$ (azure stars), $10 - 30\%$ (red crosses), $30 - 50\%$ (green diamonds), $50 - 90\%$ (orange squares) and pp collisions (full blue circles). Right: ratio of the Pb–Pb track-reconstruction efficiencies over that of pp. The hybrid track selection is used in all cases.

this stage can potentially bias the jet finding. Instead, they are included in the jet finder input; later, jets containing tracks with $p_{\mathrm{T}} > 100$ GeV/c are rejected.

4.3.2 Calorimetry

The main purpose of the EMCal is to reconstructed electrons and photons, including the decay photons coming from hadrons, such as π^0 and η, via their electromagnetic (EM) showers.

The response of the EMCal to particles transversing its volume varies a lot depending on the particle type. Most of the energy of photons and electrons is eventually absorbed by the EMCal material. Unlike electrons and photons, charged hadrons deposit energy in the EMCal mostly via minimum ionization and occasionally via nuclear interactions that generate partially contained hadronic showers. This results in a complex detector response function, which will not be investigated here.

The energy resolution obtained from electron test beam data is about 15% at 0.5 GeV and better than 5% above 3 GeV.

Calibration

The EMCal calibration procedure includes the following steps.

Bad channel removal Criteria employed to identify and remove bad channels include: the presence of unexpected structures (e.g. peaks) in the energy distribution, larger-than-expected average energy, larger-than-expected number of hits per event.

Relative calibration The relative calibration of the EMCal cells was obtained correlating cells with each other to form an invariant mass distribution; then the relative calibration factors were set to fix the π^0 mass peak at its nominal value of 0.135 GeV/c^2.

Clustering A single EM shower typically extends over a few neighboring EMCal cells. A clustering algorithm was used to sum together energy deposits of cells that likely belong to the same shower. Cells with an energy deposit smaller than 50 MeV were not included by the clustering algorithm. The algorithm proceeds by aggregating cells together in all directions, starting from seeds chosen among cells with the largest energy deposits (with $E_{\mathrm{cell}} > 100$ MeV), until reaching a cell with more energy than the previous. The algorithm ensures that there is a single local maximum in each cluster.

Non-linearity correction The EMCal response is linear for photons and electrons with energy $3 \lessapprox E_{\mathrm{reco}} \lessapprox 100$ GeV. In fact, for initial particle energies $E \gtrapprox 100$ GeV, the EM shower is only partially contained, leaking also outside of the EMCal. The correction factors for the non-linearity were obtained from an electron beam test performed during the EMCal commissioning. For clusters with energy $E_{\mathrm{reco}} = 0.5$ GeV the non-linearity correction is about 7% and it is negligible for $E_{\mathrm{reco}} > 3$ GeV.

"Exotic" cluster removal Clusters with large apparent energy but anomalously small number of contributing towers are attributed to the interactions of slow neutrons or highly ionizing particles in the avalanche photodiode (APD) of the corresponding towers. These "exotic" clusters are not reproduced by the Monte Carlo simulations. A data-driven criterion was used to identify and remove these clusters.

Charged Particle Correction

Once they reach the EMCal, charged particles deposit part or all of their energy in a number of calorimeter cells, reconstructed in a cluster. In order to avoid double counting of the momentum carried by charged particles that are already reconstructed by the tracking system, a correction must be applied. The correction procedure follows a consolidated data-driven approach used also in the measurement of the jet p_{T}-differential cross section in pp collisions at $\sqrt{s} = 2.76$ TeV [153]. All tracks with $p_{\mathrm{T}} > 0.15$ GeV/c were propagated to the average shower depth within the EMCal, and then associated to clusters with $E_{\mathrm{T}} > 0.15$ GeV within the window $|\Delta\eta| < 0.015$ and $|\Delta\phi| < 0.025$, where $\Delta\eta = \eta_{\mathrm{track}} - \eta_{\mathrm{cluster}}$ and $\Delta\phi = \phi_{\mathrm{track}} - \phi_{\mathrm{cluster}}$. Tracks were always matched to their nearest cluster, while clusters were allowed to have multiple track matches. Clusters with matched tracks were corrected for charged particle contamination according to the following formula:

$$E_{\mathrm{corr}} = E_{\mathrm{reco}} - f \times \sum_{i} p_i, \tag{4.3}$$

where E_{reco} is the reconstructed cluster energy and p_i are the momenta of the matched tracks. The fraction f was fixed to 1. This choice is always correct for clusters generated by the energy deposit of a single charged particle. In particular, if the particle deposited only a fraction of its energy, the quantity in Eq. 4.3 is negative and the cluster is simply rejected. However if the showers generated by two or more particles overlap and are merged in a single cluster, an overcorrection may occur. Just as an example, consider a cluster resulting from the MIP energy deposit of a multi-GeV charged hadron plus the full energy deposited by a multi-GeV decay photon. The full energy of the charged hadron is subtracted according to Eq. 4.3, even though only the MIP energy deposit of few hundred MeV should have been subtracted. The overcorrection is however not so severe because the overlap probability is not very high, thanks to the good EMCal granularity. The overcorrection is amended on a statistical basis when applying the detector-resolution unsmearing, as we shall see in Section 4.5.1.

4.4 Underlying Event and Jet Finding

As we have seen in Table 4.1 more than a thousand nucleon-nucleon collisions occur in a single Pb–Pb collision event. High-energy jets ($p_{\mathrm{T,jet}} \gtrsim 40$ GeV/c) are extremely rare processes: one such jet is produced approximately every $\mathcal{O}(10^5)$ pp collisions at $\sqrt{s} = 2.76$ TeV. Therefore, in a typical central Pb–Pb collision most of the binary nucleon-nucleon collisions are characterized by soft processes that constitute the underlying event (UE). The UE is made of many low-p_{T} particles filling the entire phase space: jets sit on top of this diffuse background.

The challenge presented by the disentangling of the UE from the jets is both theoretical and experimental. In principle QCD does not allow for a qualitative distinction between soft and hard processes. In the perturbative expansion (pQCD) a distinction can be made between processes that are calculable and those that are divergent. In fact for $Q^2 \lesssim 1$ GeV^2 processes, $\alpha_s \gtrsim 1$, which makes impossible the perturbative expansion of the cross section amplitude. This distinction holds in the QCD vacuum. However, when following the parton fragmentation in the hot QCD matter, the hard process from which the jet originated becomes locally correlated with the bulk particle production via the parton energy loss mechanisms that are at play. These effects have been investigated theoretically and are in fact important in many practical situations [172, 173].

Experimentally there is no way to distinguish whether a specific track or calorimeter cell energy deposit is the result of jet fragmentation or is part of the UE. This ambiguity forces a statistical approach in the subtraction of the background.

4.4.1 Average Background Density

The approach proposed in [174] was used in this analysis to estimate the average background density due to the UE. The k_{T} and the Cambridge/Aachen jet finding algorithms are particularly suitable for the purpose of studying the UE because they have the tendency to naturally organize a uniform background of soft particles into clusters of variable area (see Appendix A for a review of jet finding algorithms). The median of the distribution of the transverse momentum density of the k_{T} clusters was used as an estimator of the event-by-event background density:

$$\rho = \text{median}\left[\left\{\frac{p_{\mathrm{T}j}}{A_j}\right\}\right], \tag{4.4}$$

where $p_{\mathrm{T}j}$ and A_j are the transverse momentum and the area, respectively, of the k_{T} cluster j. The median is used because it is less sensitive to outliers of the distribution, in particular k_{T} clusters with large p_{T} formed by jet fragments.

The ρ is estimated on an event-by-event basis; therefore, in order to be reliable, this method requires a sufficiently large acceptance. In fact, in a small-acceptance detector, like the EMCal, the occasional presence of a signal jet biases the estimation of ρ for that event. For this reason the average background ρ_{charged} was calculated using only charged particles reconstructed in the tracking system, which has a larger acceptance compared to the EMCal. To account for the background coming from

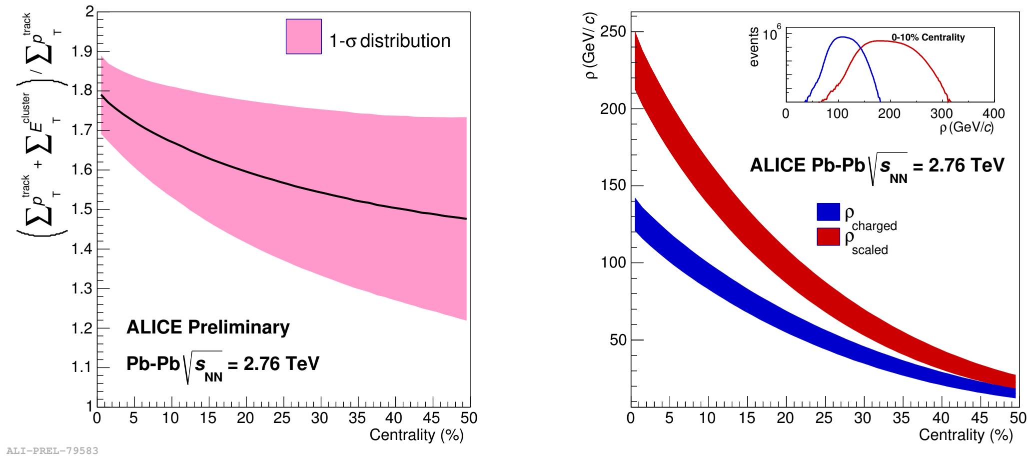

Figure 4.5: Left: scale factor $s_{\rm EMC}$ as a function of centrality. Right: average background $\rho_{\rm charged}$ (red) and $\rho_{\rm scaled}$ as a function of centrality. The inset shows the ρ distributions for the $0-10\%$ most central events. The bands represent the RMS of the distributions.

neutral particles measured by the EMCal, a data-driven scaling factor was estimated as a function of centrality as follows:

$$s_{\rm EMC} = \frac{\sum_i E_{\rm T}^i/A_{\rm EMC} + \sum_i p_{\rm T}^i/A_{\rm TPC}}{\sum_i p_{\rm T}^i/A_{\rm TPC}}, \tag{4.5}$$

where $E_{\rm T}^i$ are the EMCal cluster transverse energies, $p_{\rm T}^i$ are the track transverse momenta, $A_{\rm EMC}$ and $A_{\rm TPC}$ are the acceptances of the EMCal and of the TPC, respectively. The scaling factor distribution was fitted with a second order polynomial; this parametrization was used to calculate the scaled density $\rho_{\rm scaled}$ from $\rho_{\rm charged}$ measured event-by-event:

$$\rho_{\rm scaled} = \rho_{\rm charged} \times s_{\rm EMC}. \tag{4.6}$$

The profile of the scaling factor $s_{\rm EMC}$ as a function of centrality is shown in Fig. 4.5 (left), with the pink band representing the 1σ width of the distribution. The blue and red bands in Fig. 4.5 (right) show $\rho_{\rm charged}$ and $\rho_{\rm scaled}$, respectively, measured as a function of centrality in Pb–Pb collisions; the bands represent the 1σ width of the distributions. The inset panel shows the full ρ distributions for the $0-10\%$ most central events. The average UE density ρ allows us to estimate how much of the reconstructed jet p_{T} comes from the UE. From Fig. 4.5 (right) we can estimate for the $0-10\%$ centrality class, $\rho_{\mathrm{charged}} \approx 130$ GeV/c and $\rho_{\mathrm{scaled}} \approx 230$ GeV/c. For regular-shaped jets with $R = 0.2$ and area $A_{\mathrm{jet}} \approx \pi R^2 \approx 0.13$, the UE contribution to the reconstructed jet p_{T} is 17 and 30 GeV/c on average, respectively for charged-only (tracks) and full (tracks + EMCal) jets. These numbers are quite substantial, especially for jets with transverse momentum in the range $40-120$ GeV/c, that are the subject of this study.

4.4.2 Background Fluctuations

The UE is obviously not a uniform, continuous momentum flow, but rather it is made of discrete particles, which are reconstructed as either tracks or calorimeter energy clusters. Therefore, within a single event, the UE density fluctuates throughout the detector (η, ϕ) acceptance. These fluctuations smear the reconstructed jet momentum defined in Eq. 4.9. Two techniques were used to estimate such fluctuations.

Random Cones For each Pb–Pb event a cone is defined by fixing its axis to a random $(\eta_{\mathrm{cone}}, \phi_{\mathrm{cone}})$ position and its radius $R_{\mathrm{cone}} = R$, where R is the jet resolution parameter (see Appendix A). The transverse momentum of the cone ($p_{\mathrm{T,cone}}$) is obtained summing together the transverse momenta of all the reconstructed particles (tracks and/or calorimeter energy clusters) that are found within the cone size, i.e. $\sqrt{(\eta_{\mathrm{cone}} - \eta_{\mathrm{part}})^2 + (\phi_{\mathrm{cone}} - \phi_{\mathrm{part}})^2} < R_{\mathrm{cone}}$. The deviation between $p_{\mathrm{T,cone}}$ and the amount of background expected from the average background ρ is defined as follows:

$$\delta p_{\mathrm{T}}^{\mathrm{RC}} = p_{\mathrm{T,cone}} - A_{\mathrm{jet}} \times \rho. \tag{4.7}$$

Embedding A high-p_{T} "probe" (typically a single particle acting as a proxy for a jet) is embedded in a random (η, ϕ) position of each Pb–Pb event before running the

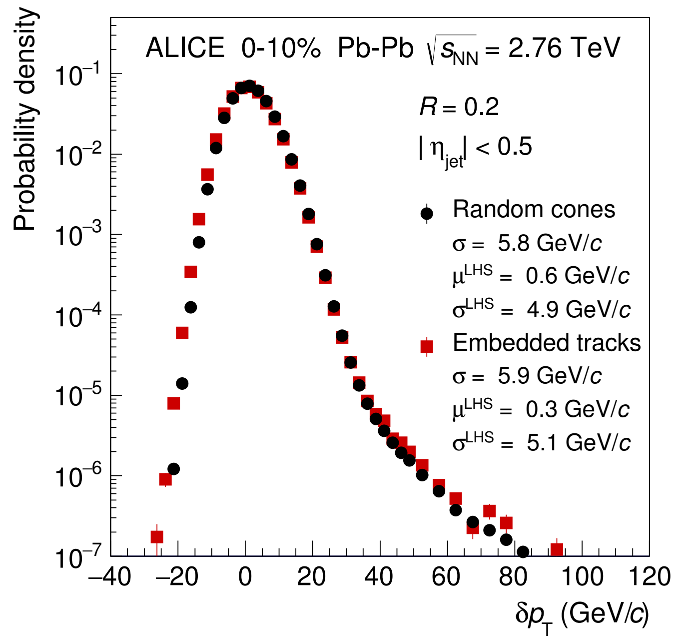

Figure 4.6: Background fluctuations estimated via δp_{T} distributions obtained with the random cone method (black circles) and with the embedding method (red squares) for jets with $R = 0.2$ in the most central $0-10\%$ Pb–Pb events.

anti-k_{T} jet finder. The jet containing the probe is used to calculate the deviation of the background in its vicinity compared to the event-averaged background ρ:

$$\delta p_{\mathrm{T}}^{\mathrm{emb}} = p_{\mathrm{T,jet}} - p_{\mathrm{T,probe}} - A_{\mathrm{jet}} \times \rho, \tag{4.8}$$

where $p_{\mathrm{T,jet}}$ and A_{jet} are the transverse momentum and the area of the jet containing the probe, respectively, and $p_{\mathrm{T,probe}}$ is the transverse momentum of the embedded probe.

Figure 4.6 compares the δp_{T} distributions obtained with the two methods described above for the $0-10\%$ most central Pb–Pb events. The $\delta p_{\mathrm{T}}^{\mathrm{emb}}$ distribution is shown for $p_{\mathrm{T,probe}} = 60$ GeV/c. The random-cone method does not rely on any assumptions about the structure of the background itself and gives approximately the same background fluctuations as embedding a probe with momentum much larger than the sum of the momenta of all the event particles. In fact, in this case the anti-k_{T} algorithm would make a perfectly round jet around the high-p_{T} probe. The embedding method should be able to reproduce the background as seen by the anti-k_{T} algorithm more directly. Probes of different p_{T} were tried; above 10 GeV/c the resulting $\delta p_{\mathrm{T}}^{\mathrm{emb}}$ distribution did not show any significant dependence on the p_{T} of the embedded particle. The two methods appear to provide the same quantitative response to the background fluctuations, with only marginal differences mainly due to small jet area fluctuations in the embedding track method.

Assuming that the estimation of the average background is not biased, the most probable values of $\delta p_{\mathrm{T}}^{\mathrm{RC}}$ and $\delta p_{\mathrm{T}}^{\mathrm{emb}}$ should be close to zero. The standard deviation of their distributions quantifies the region-by-region fluctuations, as seen by a high-p_{T} probe. The root-mean-square (RMS) of the full distributions is about 6 GeV/c. The distributions are clearly asymmetric, with a longer tail on the positive side. The tail is due to the occasional overlap of the region probed by the random cone or by the embedded particle with jet fragments present in the Pb–Pb events. A characterization of the left-hand-side (LHS) of the distributions allows us to quantify the UE properties, limiting the bias coming from the jet fragments. The LHS can be approximated by a Gaussian function. To determine the LHS width, the distributions were fitted recursively with a Gaussian function in the range $[\mu_{\mathrm{LHS}} - 3\sigma_{\mathrm{LHS}}, \mu_{\mathrm{LHS}} + \frac{1}{2}\sigma_{\mathrm{LHS}}]$ using the mean and width of the δp_{T} distribution as starting values for σ and μ. The LHS width is about 5 GeV/c in $0 - 10\%$, with negligible differences between the two methods.

The background fluctuations of the $0-10\%$ most central events are compared with those obtained in $10 - 30\%$ in Fig. 4.7 using the random-cone method. The RMS of the distributions is smaller for the semi-central case: 4.5 GeV/c, compared to about 6 GeV/c for the most central events. The two panels show the $\delta p_{\mathrm{T}}^{\mathrm{RC}}$ distributions obtained with two different cone radii, $R = 0.2$ (left) and $R = 0.3$ (right). Assuming a uniform and isotropic background, the width is expected to follow Poisson statistics,

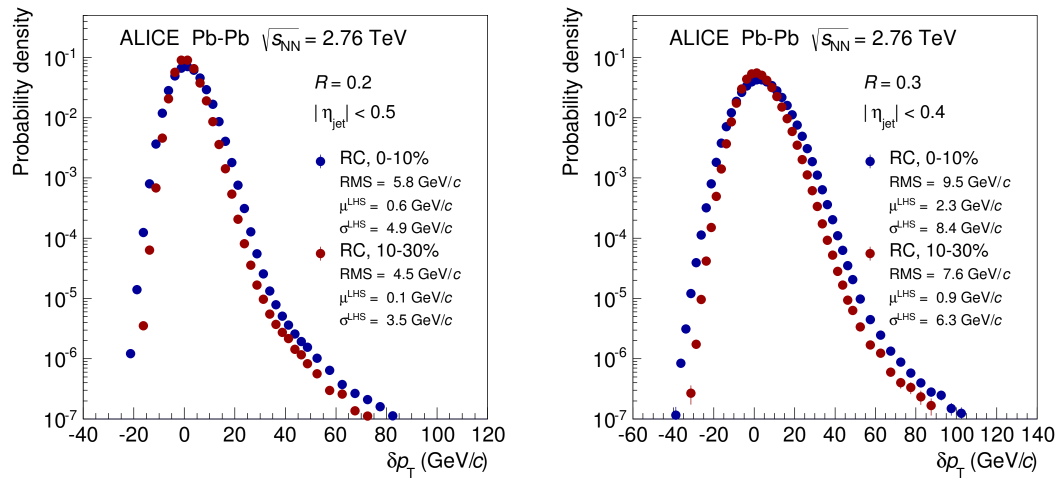

(a) $R = 0.2$ (b) $R = 0.3$

Figure 4.7: Background fluctuations estimated via δp_{T} random-cone distributions for the $0-10\%$ (blue) and $10-30\%$ (red) most central Pb–Pb events, for a) $R = 0.2$ and b) $R = 0.3$.

i.e. it is proportional to the square root of the expected number of particles contained in the cone, which is in turn proportional to the cone area $A_{\mathrm{cone}} = \pi R^2_{\mathrm{cone}}$. Therefore it is expected that the widths scale linearly with R_{cone}. This is approximately verified by the values obtained for the two cone radii shown in Fig. 4.7.

The presence of the tail at positive values of δp_{T} indicates that signal jets do occasionally overlap with other jet fragments coming from the same Pb–Pb collision. Jet fragments overlapping with other signal jets represent themselves a source of background. A question naturally arises: how can the measurement be possible at all if any jet can at the same time be part of the signal and also background to another jet? In fact, this issue poses a limit on the minimum jet transverse momentum $p^{\mathrm{min}}_{\mathrm{T,jet}}$ that can be measured in Pb–Pb using the techniques described here. This limit should be chosen such that the probability of two jets with $p^{\mathrm{reco}}_{\mathrm{T,jet}} \approx p^{\mathrm{min}}_{\mathrm{T,jet}}$ occurring in the same Pb–Pb event and sharing the same phase space is negligible[2]. When such condition is met, we can safely define signal jets as those with $p^{\mathrm{reco}}_{\mathrm{T,jet}} > p^{\mathrm{min}}_{\mathrm{T,jet}}$. All

2. The "reco" superscript indicates that this is the detector-level variable, not corrected for the detector and background resolution effects.

fragments of jets with $p_{\mathrm{T,jet}}^{\mathrm{reco}} < p_{\mathrm{T,jet}}^{\mathrm{min}}$ belong to the background and are expected to appear in the positive tail of the δp_{T} distributions [3].

4.4.3 Raw Jet p_{T} Spectrum

Clusters with $E_{\mathrm{T}} > 0.30$ GeV and tracks with $p_{\mathrm{T}} > 0.15$ GeV/c were assembled into jets using the anti-k_{T} algorithm with a resolution parameter of $R = 0.2$. Only those jets that were fully contained within the EMCal acceptance, at least R away from the EMCal boundaries of $|\eta| < 0.7$ and $1.4 < \phi < \pi$, were kept in the analysis. In addition, jets containing a track with $p_{\mathrm{T}} > 100$ GeV/c were rejected.

The transverse momentum of the reconstructed jets is affected by the contribution from the UE. The average contribution of the background was removed according to the following formula:

$$p_{\mathrm{T,jet}}^{\mathrm{reco}} = p_{\mathrm{T,jet}}^{\mathrm{raw}} - \rho_{\mathrm{scaled}} \times A_{\mathrm{jet}}, \tag{4.9}$$

where the event-by-event average background density ρ_{scaled} was determined according to the method described in Section 4.4.1.

Figure 4.8 shows the jet p_{T} spectra obtained after this correction. Figure 4.8 compares the inclusive raw jet p_{T} spectra obtained with different requirements on the transverse momentum of the leading charged jet constituent $p_{\mathrm{T,ch}}^{\mathrm{lead}}$, from none up to 10 GeV/c. A large bump is apparent at $p_{\mathrm{T,jet}}^{\mathrm{reco}} \approx 0$, which extends to negative values. The bump is suppressed with increasing minimum $p_{\mathrm{T,ch}}^{\mathrm{lead}}$. Negative values of the jet transverse momentum are of course unphysical: they are a consequence of background fluctuations (see Section 4.4.2) and combinatorial background. Local fluctuations of the UE density can go in either positive or negative directions with respect to the

3. By embedding a jet proxy to probe the background, the number of binary nucleon-nucleon collisions is effectively increased by a unit. In principle this increases slightly the effective centrality of the collision being probed and at the same time increases the jet-jet overlap probability. In central Pb–Pb collisions, where over $1,000$ binary collisions occur, this effect is negligible. For peripheral collisions or smaller systems (such as p–Pb) this effect may become important.

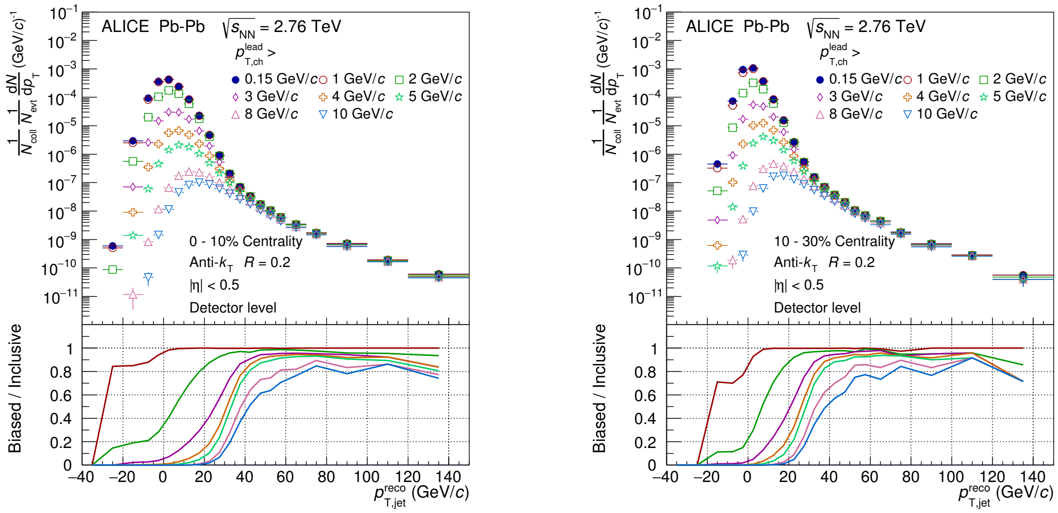

(a) $0-10\%$ centrality (b) $10-30\%$ centrality

Figure 4.8: Jet p_T spectra in Pb–Pb collisions at $\sqrt{s_{NN}} = 2.76$ TeV for two centrality classes as indicated under each panel. The spectra are normalized by the number of events and by the expected number of binary collisions N_{coll}. Full symbols represent the spectra obtained without any cut on the leading track; open symbols represent the "biased" spectra obtained requiring that the leading charged jet constituent has the minimum p_T as indicated in the legend. The bottom panels show the ratios of the biased spectra over the inclusive.

event average ρ, as evidenced by the δp_T distributions (Fig. 4.7). If a low p_T jet sits on top of a negative fluctuation of the UE, then it will be assigned a negative $p_{T,jet}^{reco}$ according to Eq. 4.9. In addition the sample obtained from the jet finder contains also jet candidates that were assembled using tracks and calorimeter clusters coming purely from the UE; in fact "combinatorial" jets are expected to make up a very large fraction of the jet candidates reconstructed at low momentum. These combinatorial jets are expected to be strongly suppressed when requiring a high p_T particle among the jet constituents. The bottom panels show the ratio between the spectra obtained with different minimum $p_{T,ch}^{lead}$ and the inclusive one. For $p_{T,ch}^{lead} > 5$ GeV/c, the yield is suppressed by more than 3 orders of magnitude for $p_{T,jet}^{reco} < 5$ GeV/c. The ratio increases sharply as a function of $p_{T,jet}^{reco}$ in the range $0 \lessapprox p_{T,jet}^{reco} \lessapprox 40$ GeV/c and then it stays approximately flat without reaching unity (except for $p_{T,ch}^{lead} > 1$ GeV/c, where the ratio reaches 1 for $p_{\mathrm{T,jet}}^{\mathrm{reco}} > 10$ GeV/c). A potential bias on the jet fragmentation is expected to arise from the requirement of minimum p_{T} for the leading charged constituent, which forces the presence of a "hard" core. The bias is expected to be stronger for low jet momenta.

4.5 Unfolding

The study of the jet momentum resolution was factorized into two parts: the detector response and the underlying event fluctuations.

4.5.1 Detector Response

Several detector limitations affect the measurement of the jet transverse momentum:

- track-reconstruction efficiency;
- calorimeter energy resolution;
- charged-particle double counting (tracking and calorimetry);
- unreconstructed neutral particles ($\mathrm{K}_{\mathrm{L}}^{0}$, neutrons).

Other limitations are present but they play a minor role compared to the those listed above. In particular, track-momentum resolution is much better than the calorimeter energy resolution; both are overshadowed by the track-reconstruction efficiency[4]. The jet p_{T} smearing caused by these detector limitations was studied using the PYTHIA 6 + GEANT3 simulation of pp collisions at $\sqrt{s} = 2.76$ TeV introduced in Section 4.2.4. The use of a pp simulation to extract the detector response is justified by the fact that, apart from second-order effects discussed below, the jet reconstruction performance should be independent of the collision system. In fact, in Section 4.3.1 we have seen

4. See Section 4.3

how the track-reconstruction efficiency depends slightly on the event track multiplicity. This effect was taken into account by reducing the track-reconstruction efficiency in the pp simulation to match the expected Pb–Pb efficiency in a given centrality class. This was achieved by randomly throwing away tracks from the detector-level pp simulation with a p_{T}-dependent frequency taken from a parametrization of the ratio between the Pb–Pb and pp efficiencies (see Fig. 4.4).

The detector response was encoded in a matrix correlating the jet transverse momentum reconstructed at detector-level $p_{\mathrm{T,jet}}^{\mathrm{reco}}$ (x axis) with its truth-level counterpart $p_{\mathrm{T,jet}}^{\mathrm{truth}}$ (y axis). This matrix was built following the procedure outlined below. The jet reconstruction was performed in the simulation using the same techniques employed for the data, both for the truth- and detector-level events. A truth-level jet A was matched to its detector-level counterpart jet B following a geometrical criterion:

- $d(\mathrm{A},\mathrm{B}) = \sqrt{(\eta_{\mathrm{A}} - \eta_{\mathrm{B}})^2 + (\phi_{\mathrm{A}} - \phi_{\mathrm{B}})^2} < 0.25$;
- A is the nearest particle-level jet to B and B is the nearest detector-level jet to A (in the sense of the distance defined above).

In the matching step, the following cuts were applied only at detector level: EMCal fiducial acceptance cut, $p_{\mathrm{T,ch}}^{\mathrm{lead}} > 5$ GeV/c and no track with $p_{\mathrm{T}} > 100$ GeV/c. When a valid matching is found, an entry is added to the response matrix correlating $p_{\mathrm{T,jet}}^{\mathrm{reco}}$ with $p_{\mathrm{T,jet}}^{\mathrm{truth}}$. The matrix is shown in Fig. 4.9a for $R = 0.2$ jets. Each row, i.e. a slice of the matrix within a $p_{\mathrm{T,jet}}^{\mathrm{truth}}$ range, is normalized to unity, so that its projection onto the $p_{\mathrm{T,jet}}^{\mathrm{reco}}$ represents the probability density distribution that a jet with true transverse momentum $p_{\mathrm{T,jet}}^{\mathrm{truth}}$ is seen by the detector as having transverse momentum $p_{\mathrm{T,jet}}^{\mathrm{reco}}$. Figure 4.9b shows the distributions of the residuals $(p_{\mathrm{T,jet}}^{\mathrm{reco}} - p_{\mathrm{T,jet}}^{\mathrm{truth}})/p_{\mathrm{T,jet}}^{\mathrm{truth}}$, for three selected ranges of $p_{\mathrm{T,jet}}^{\mathrm{truth}}$. The distributions are skewed towards negative values mainly because of unreconstructed particles (track-reconstruction inefficiency, unmeasured neutral particles that do not shower in the electromagnetic calorimeter).

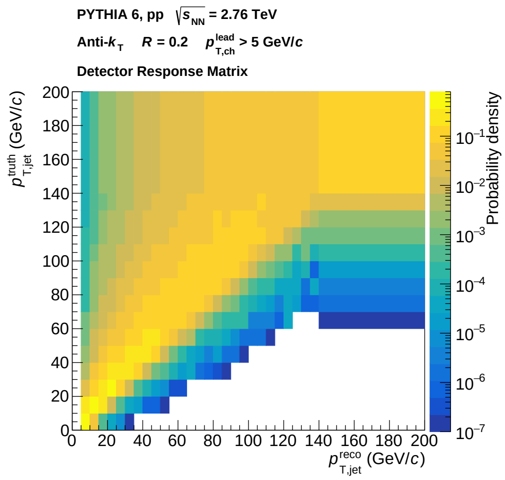

(a) Detector response matrix

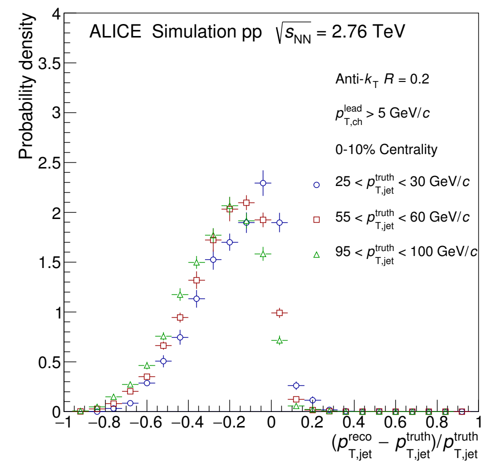

(b) Distributions of the residuals

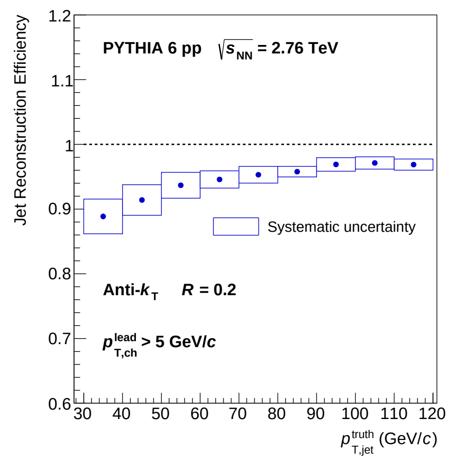

(c) Jet-reconstruction efficiency

Figure 4.9: Detector response for jets reconstructed in pp collisions at $\sqrt{s} = 2.76$ TeV. The track-reconstruction efficiency was artificially reduced to match that of Pb–Pb collisions in the $0-10\%$ centrality class. At detector level, jets are required to be within the EMCal fiducial acceptance, to have the leading charged constituent with $p^{\rm lead}_{\rm T,ch} > 5$ GeV/c and no track with $p_{\rm T} > 100$ GeV/c. At truth level, these requirements are applied only for the denominator used to calculate the efficiency, with the exception of $p_{\rm T,charged} < 100$ GeV/c which is never applied at truth level.

The jet-reconstruction efficiency was obtained dividing the p_{T} spectrum of the truth-level jets with a matched detector-level counterpart, by the p_{T} spectrum of all the truth-level jets. The truth-level jets used in the denominator of the efficiency calculation are required to pass the EMCal fiducial acceptance cut and $p_{\mathrm{T,ch}}^{\mathrm{lead}} > 5$ GeV/c. As the numerator is not an exact subset of the denominator this is a "generalized" efficiency, which coincides with the product of the actual efficiency with the "fake" rate of jets passing the selection cuts at detector level, but being matched with particle-level jets that do not pass the cuts. The efficiency is shown in Fig. 4.9c. The efficiency is about 87% at $p_{\mathrm{T,jet}}^{\mathrm{truth}} = 30$ GeV/c; it increases and reaches about 96% at $p_{\mathrm{T,jet}}^{\mathrm{truth}} = 90$ GeV/c, after which it stays approximately flat. At low $p_{\mathrm{T,jet}}^{\mathrm{truth}}$, the efficiency is limited by the track-reconstruction efficiency, especially because of the requirement $p_{\mathrm{T,ch}}^{\mathrm{lead}} > 5$ GeV/c. For $p_{\mathrm{T,jet}}^{\mathrm{truth}} > 100$ GeV/c the efficiency is also limited by the rejection of jets that contain tracks with $p_{\mathrm{T}} > 100$ GeV/c. The systematic uncertainty on the jet reconstruction efficiency is due to the uncertainty on the track-reconstruction efficiency[5].

4.5.2 Underlying Event Fluctuations

In addition to the detector resolution, the measurement of the jet p_{T} is affected by fluctuations in the UE density. The smearing due to these fluctuations was estimated using the data-driven method outlined in Section 4.4.2. The δp_{T} distribution was assembled into a response matrix by shifting it along the $p_{\mathrm{T,jet}}^{\mathrm{reco}}$ axis by the amount $p_{\mathrm{T,jet}}^{\mathrm{truth}}$ corresponding to each row (Toeplitz matrix). This matrix construction method assumes that the response of the jet p_{T} spectrum to the background fluctuations is independent of the jet momentum. This assumption is justified by the fact that the background fluctuations probed with embedded particles did not show any significant dependence on $p_{\mathrm{T,probe}}$ (see Section 4.4.2).

5. See Section 4.6 for more details.

4.5.3 Combined Resolution

A summary of the jet energy scale shift and jet p_{T} resolution is shown in Fig. 4.10 for Pb–Pb collisions at $\sqrt{s_{\mathrm{NN}}} = 2.76$ TeV in the $0-10\%$ centrality class. The results for the $10-30\%$ centrality class (not shown) exhibit a slightly better resolution due to the smaller UE fluctuations and marginally higher track-reconstruction efficiency, but otherwise they are similar to the results for the $0-10\%$ centrality class. The energy scale shift and resolution are shown separately for the detector effects and the UE fluctuations, as well as for the two combined. The jet energy scale shift due to the detector effects is negative by $10-30\%$ and it increases with $p_{\mathrm{T,jet}}^{\mathrm{truth}}$. The UE fluctuations cause a positive shift which, for low p_{T} jets, can be significant, but becomes very small at higher momenta. The jet detector resolution is approximately flat at $\approx 20\%$ as a function of the jet p_{T}. Conversely, the UE fluctuations bring an absolute momentum smearing that is constant as a function of $p_{\mathrm{T,jet}}^{\mathrm{truth}}$; therefore the resolution is proportional to $1/p_{\mathrm{T,jet}}^{\mathrm{truth}}$, improving from about 50% for $p_{\mathrm{T,jet}}^{\mathrm{truth}} = 10$ GeV/c to a few % at $p_{\mathrm{T,jet}}^{\mathrm{truth}} = 100$ GeV/c. The combined resolution is dominated by the UE fluctuations at low $p_{\mathrm{T,jet}}^{\mathrm{truth}}$, while the detector effects dominate at high $p_{\mathrm{T,jet}}^{\mathrm{truth}}$; the cross-over occurs at about 30 GeV/c.

4.5.4 Unfolding Procedure

Figure 4.11 shows the combined $\mathrm{RM}_{\mathrm{tot}}$ response matrices for the two centrality classes $0-10\%$ and $10-30\%$, obtained convoluting the matrix encoding the background fluctuations and that encoding the detector effects:

$$\mathrm{RM}_{\mathrm{tot}} = \mathrm{RM}_{\mathrm{bkg}} \times \mathrm{RM}_{\mathrm{det}}, \tag{4.10}$$

where "$\times$" represents the regular row-by-column matrix product. The kinematic efficiencies shown also in Fig. 4.11 are part of the response and represent the loss of

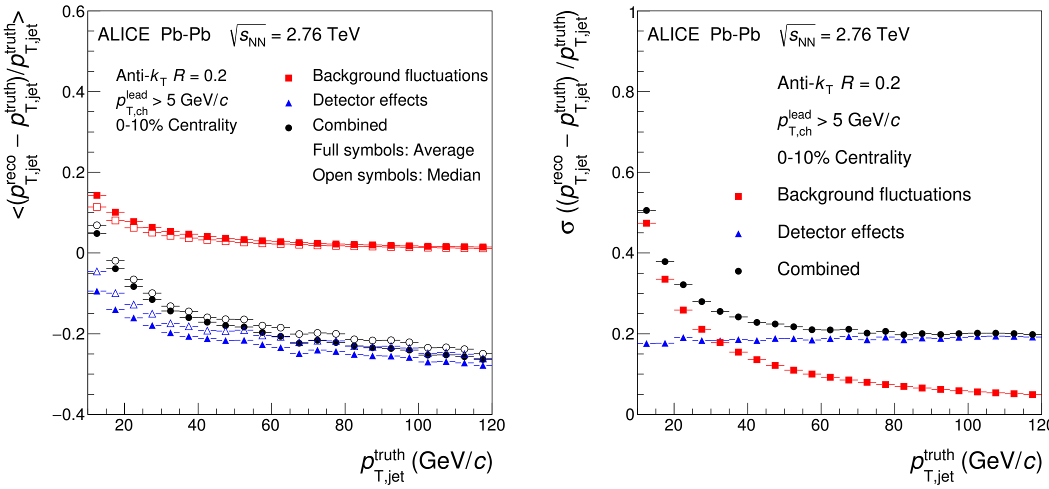

Figure 4.10: Left: jet energy scale shift quantified via the average (full symbols) or median (empty symbols) of the distribution of the relative differences between the truth-level and detector-level jet transverse momentum. Right: jet transverse momentum resolution quantified via the root-mean-square (RMS) of the distribution of the relative differences between the truth-level and detector-level jet transverse momentum. The red squares represent the effect of the UE fluctuations only; the blue triangles represent the detector effects only; the combined UE and detector effects are represented by the black circles. At detector level, jets are required to be within the EMCal fiducial acceptance, to have the leading charged constituent with $p_{\mathrm{T,ch}}^{\mathrm{lead}} > 5$ GeV/c and no track with $p_{\mathrm{T}} > 100$ GeV/c.

efficiency in the $p_{\mathrm{T,jet}}^{\mathrm{truth}}$ axis due to the fact that jets are measured only in a limited $p_{\mathrm{T,jet}}^{\mathrm{reco}}$ range: $30-120$ GeV/c for the $0-10\%$ centrality class and $20-100$ GeV/c for the $10-30\%$ centrality class. The high p_{T} limits were driven by the fact that statistics were insufficient above those values. Unfolding tests have shown that a minimum of 10 raw counts is necessary in each histogram bin to avoid instabilities. The low p_{T} limits were chosen to avoid the steepest part of the spectrum, which is very difficult to unfold. In fact a steep spectrum implies that a small uncertainty on the reconstructed jet p_{T} translates in a large uncertainty on the differential yield. Furthermore, even with the requirement $p_{\mathrm{T,ch}}^{\mathrm{lead}} > 5$ GeV/c, there is still a potentially large number of combinatorial jets, made entirely of particles from the UE. After unfolding, if not kept under control, combinatorial jets may contaminate the spectrum even at high jet p_{T}, spoiling the entire measurement. The minimum $p_{\mathrm{T,jet}}^{\mathrm{reco}}$ values were chosen to

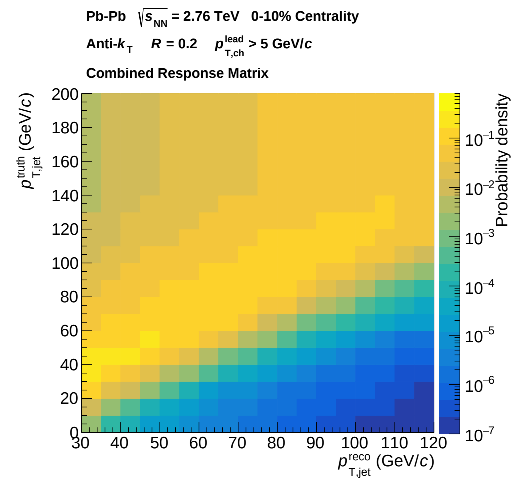

(a) $0-10\%$ centrality

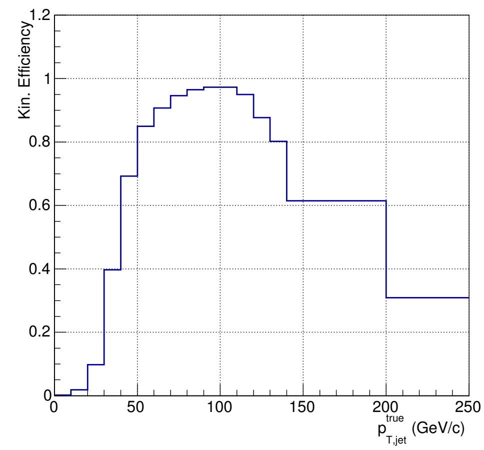

(b) $0-10\%$ centrality

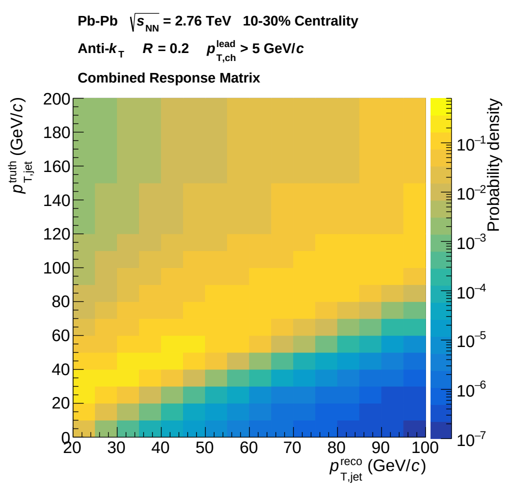

(c) $10-30\%$ centrality

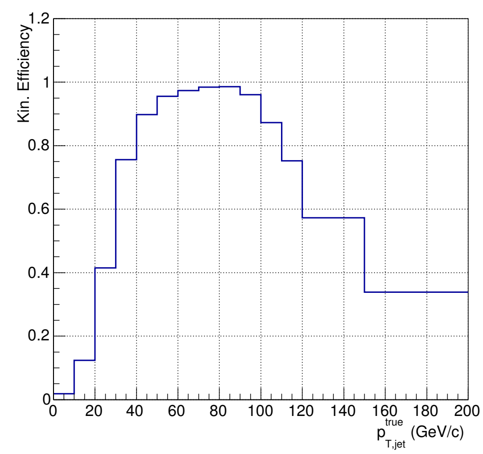

(d) $10-30\%$ centrality

Figure 4.11: Left: response matrices used to unfold the jet p_T spectrum. The response matrices include both the detector effects and the UE fluctuations. Right: reconstruction efficiency due to the kinematic limits on the reconstructed jet p_T spectrum. The response matrices and efficiencies are shown for two centrality classes as indicated below each panel. At detector level, jets are required to be within the EMCal fiducial acceptance, to have the leading charged constituent with $p_{T,ch}^{lead} > 5$ GeV/c and no track with $p_T > 100$ GeV/c.

be approximately equal to 5 times the RMS of the $\delta p_{\rm T}$ distributions, which is enough to guarantee a negligible contamination from combinatorial jets.

The measured jet $p_{\rm T}$ spectrum $N_{\rm reco}(p_{\rm T,det}^{\rm truth})$ is the result of the convolution of the true spectrum $N_{\rm truth}(p_{\rm T,jet}^{\rm truth})$ through the response matrix $\rm RM_{tot}$:

$$N_{\rm reco}(p_{\rm T,jet}^{\rm reco}) = {\rm RM}_{\rm tot} \times N_{\rm truth}(p_{\rm T,jet}^{\rm truth}). \tag{4.11}$$

A simple matrix inversion,

$$N_{\rm unfold}(p_{\rm T,jet}^{\rm truth}) = ({\rm RM}_{\rm tot})^{-1} \times N_{\rm reco}(p_{\rm T,jet}^{\rm reco}), \tag{4.12}$$

is not a viable option. The unfolded distribution $N_{\rm unfold}(p_{\rm T,jet}^{\rm truth})$ would be extremely sensitive to statistical fluctuations in the measured distribution. Even small statistical uncertainties would become unreasonably large after the matrix inversion[6]. For this analysis the regularized SVD method [166] was used. A smoothed version of the measured spectrum was used as the prior, so that the statistical fluctuations within the data were not magnified in the unfolding process.

The regularization parameter used for SVD unfolding was $k = 5$, with $k = 4, 6$ used for the systematic uncertainty. The value of k was chosen such that it corresponds to the d vector magnitude of 1, which is shown in Fig. 4.12 for both the $0-10\%$ and $10-30\%$ centrality classes. The Pearson correlation coefficients are shown in Fig. 4.13 for different choices of k. For $k = 5$ we observe mild or strong correlation between neighboring bins and a mild anti-correlation between bins that are 2 to 4 units apart. This pattern is expected given the bin widths and the $p_{\rm T,jet}$ resolution, which is $> 20\%$. Larger values of k lead to a strong anti-correlation pattern between neighboring bins, typical of a weak regularization strength.

6. A more comprehensive discussion, including the description of the regularized SVD unfolding method, is given in Section 3.8.3

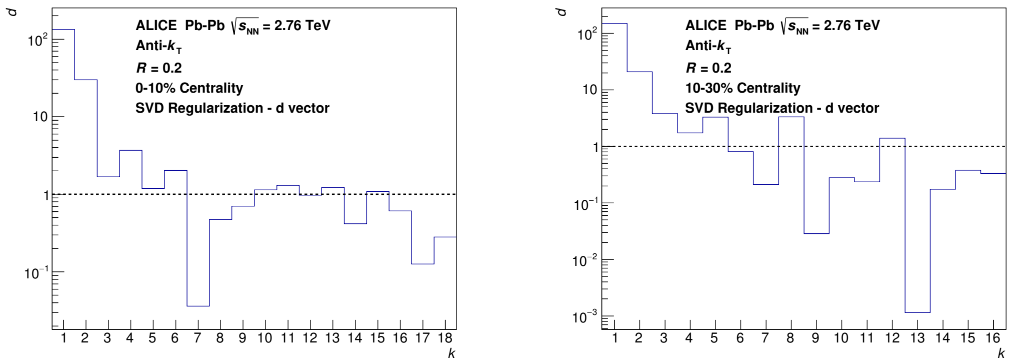

(a) $0-10\%$ centrality class.

(b) $10-30\%$ centrality class.

Figure 4.12: Vector d obtained in the SVD decomposition of the detector response matrices for the unfolding of the jet p_{T} spectra in Pb–Pb collisions at $\sqrt{s_{\mathrm{NN}}} = 2.76$ TeV.

4.6 Systematic Uncertainties

In this Section Figures and Tables will be shown only for the $0-10\%$ most central Pb–Pb collisions. Methods and results about the systematic uncertainties discussed in this Section are largely applicable and valid for the $10-30\%$ centrality class. Some of the Figures and Tables related to the $10-30\%$ centrality class are given for completeness in Appendix C.

The systematic uncertainties were divided into two categories: correlated uncertainties and shape uncertainties. The correlated uncertainties result predominantly from uncertainties on the jet energy scale, such as the uncertainty of the tracking efficiency, that will shift the entire jet spectrum in one direction. The shape uncertainties are related to the unfolding and can distort the slope of the spectrum. The systematic uncertainties on the jet spectrum are summarized in Table 4.2 for the $0-10\%$ centrality class.

4.6.1 Correlated Uncertainties

Several sources of correlated uncertainties were considered. Since they are assumed to be independent from each other, they were added in quadrature to obtain the

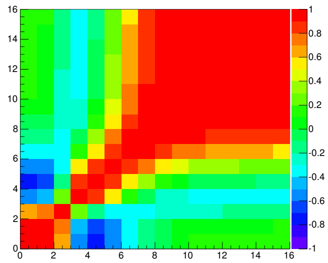

(a) $k = 3$

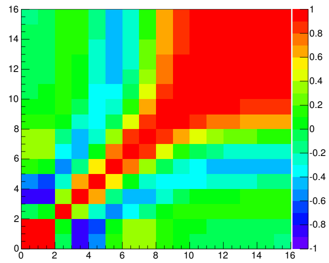

(b) $k = 4$ (syst. unc.)

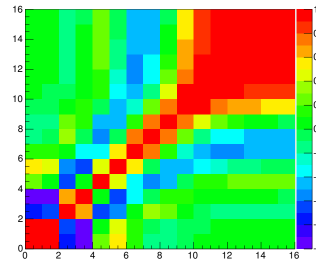

(c) $k = 5$ (nominal)

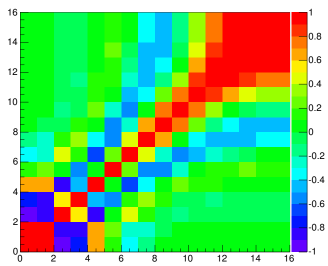

(d) $k = 6$ (syst. unc.)

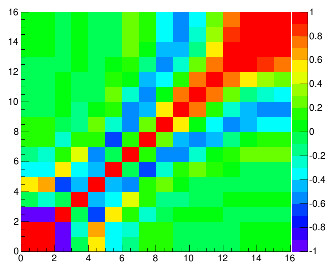

(e) $k = 7$

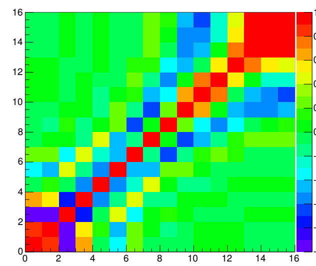

(f) $k = 8$

Figure 4.13: Pearson correlation coefficients obtained from the SVD unfolding of the jet p_{T} spectrum in the $0-10\%$ most central Pb–Pb collisions at $\sqrt{s_{\mathrm{NN}}} = 2.76$ TeV. Each panel corresponds to a different choice of the regularization parameter k.

final uncertainty. In the following each source of uncertainty and the method used to quantify it will be briefly described.

Track-reconstruction efficiency For this data sample it was estimated that the track-reconstruction efficiency in the Monte Carlo simulations is accurate within 5%. The track-reconstruction efficiency was artificially reduced by 5% in the simulation used to build the detector response matrix $\mathrm{RM}_{\mathrm{det}}$ and the jet reconstruction efficiency. The modified response matrix and efficiency were used to unfold the reconstructed jet p_{T} spectrum. The unfolded result was compared with the central points obtained with the nominal response matrix as shown in Fig. 4.14. The relative difference was found to be approximately $7-10\%$ with a weak p_{T} dependence. This difference was taken as the systematic uncertainty, under the assumption that the uncertainty is

Category	Relative uncertainty (%)				
	$p_{\mathrm{T,jet}}^{\mathrm{min}}$	$p_{\mathrm{T,jet}}^{\mathrm{max}}$	Min.	Max.	Avg.
Tracking efficiency	7.7	11.3	7.3	11.3	8.8
Track momentum resolution	1.0	1.0	1.0	1.0	1.0
Charged particle correction	0.7	2.7	0.7	6.4	3.7
EMCal clusterizer	3.2	1.8	0.1	3.2	1.4
EMCal response	4.4	4.4	4.4	4.4	4.4
Background fluctuations	3.9	2.7	2.3	3.9	2.8
Jet raw p_{T} cuts	2.6	6.7	1.5	6.7	3.6
Combinatorial jets	0.3	0.5	0.0	0.5	0.2
Total correlated uncertainty	10.6	14.5	10.6	14.5	12.0
Unfolding method	0.1	10.0	0.1	15.5	6.6
SVD reg. param. $k = 4$	3.6	11.7	2.4	11.7	6.0
SVD reg. param. $k = 6$	7.2	2.7	1.5	8.8	5.3
Prior choice 1	1.9	4.0	0.2	4.0	1.6
Prior choice 2	2.1	1.4	0.1	2.1	0.9
Total shape uncertainty	3.8	7.2	2.7	7.4	5.3

Table 4.2: Summary of systematic uncertainties for $0-10\%$ most central collisions. The first column is the uncertainty at the minimum $p_{\mathrm{T,jet}}^{\mathrm{min}}$ of 40 GeV/c, the second column is the uncertainty at the maximum $p_{\mathrm{T,jet}}^{\mathrm{max}}$ of 120 GeV/c. The minimum and maximum columns give the extremes, and the last column gives the average systematic uncertainty over the entire p_{T} range.

symmetric[7]. This is the largest source of correlated systematic uncertainty.

EMCal energy The uncertainties related to the EMCal response (particularly its limited linearity at low energy), EMCal energy scale and resolution were studied in detail in the context of the measurement of the jet p_{T}-differential cross section in pp collisions at $\sqrt{s} = 2.76$ TeV [153, 175]. The total uncertainty was estimated to be about 4.4%.

EMCal clustering algorithm The uncertainty arising from the choice of the EMCal clustering algorithm is determined by using a different algorithm, that forms clus-

7. Increasing the track-reconstruction efficiency is not as simple as reducing it; therefore the variation was done only in one direction and assuming that increasing the efficiency would have a symmetric effect.

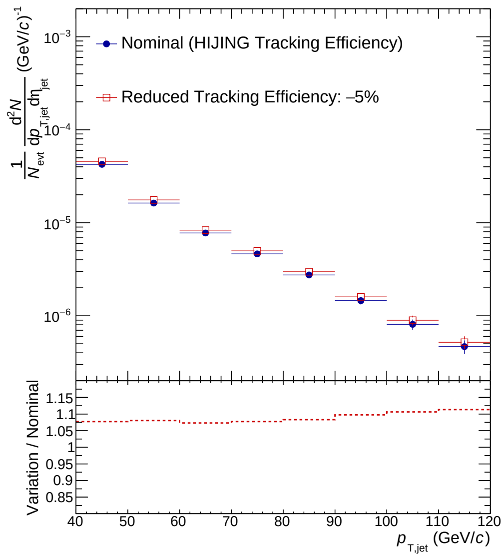

Figure 4.14: Comparison of the jet p_{T} spectra in the $0-10\%$ most central Pb–Pb collisions unfolded with the nominal detector response matrix (blue solid circles) and with the matrix obtained with the reduced track-reconstruction efficiency (red open squares) for the estimation of the systematic uncertainty.

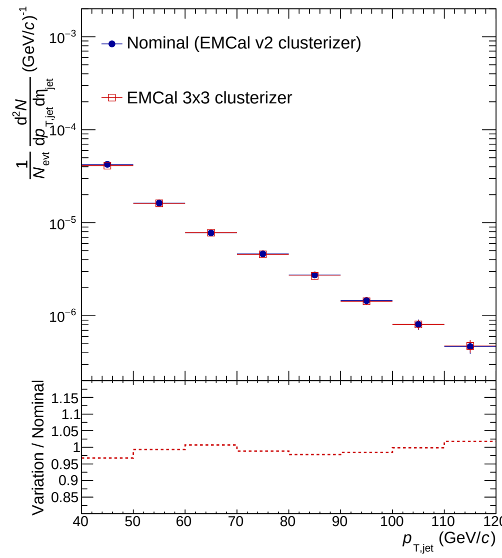

Figure 4.15: Comparison of the jet p_{T} spectra in the $0-10\%$ most central Pb–Pb collisions obtained using the nominal EMCal clustering algorithm (blue solid circles) and using the 3×3 algorithm (red open squares) for the estimation of the systematic uncertainty.

ters of fixed size. This algorithm scans the EMCal acceptance to find a cluster with the largest possible energy made of 3×3 towers. Then it removes it from the grid and proceeds with the next one until all towers above threshold have been assigned to a cluster. Figure 4.15 compares the effect of using a different EMCal clustering algorithm on the jet p_{T} spectrum after all corrections have been applied, including unfolding. The same clustering algorithm is consistently applied in all analysis steps (estimation of the background, detector response matrix, etc.). The effect on the final spectrum was found to be of few percent.

8. See Section 4.4.2 for details about the background fluctuations.

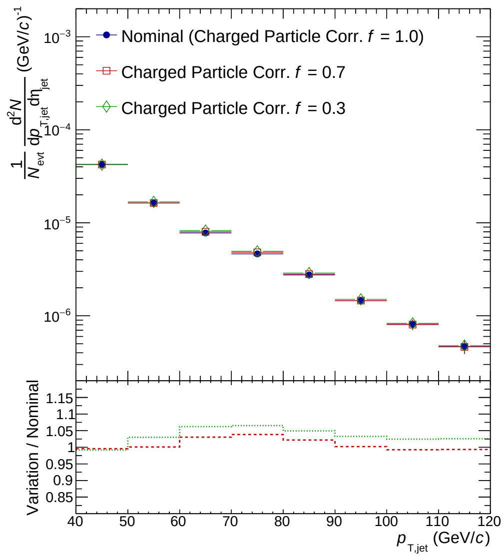

Figure 4.16: Comparison of the jet p_{T} spectra in the $0-10\%$ most central Pb–Pb collisions obtained using different values of the charged-particle correction factor f (see Eq. 4.3) for the estimation of the systematic uncertainty.

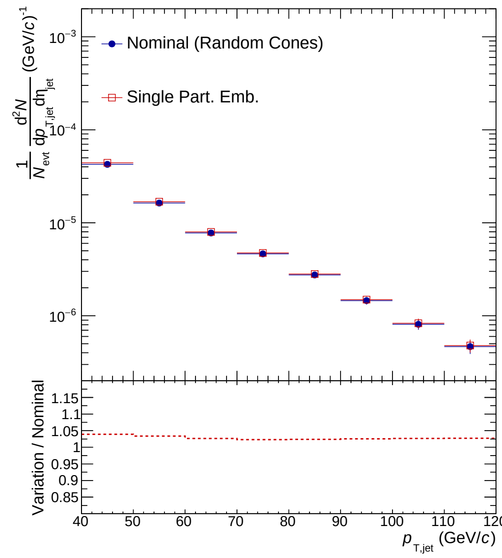

Figure 4.17: Comparison of the jet p_{T} spectra in the $0-10\%$ most central Pb–Pb collisions unfolded using the UE fluctuations quantified with random cones (blue solid circles) and with single-particle embedding (red open squares) for the estimation of the systematic uncertainty[8].

Charged particle correction The uncertainty due to the correction procedure for the charged particle double counting in the EMCal was determined to be about 4%. It was estimated by varying the charged-particle correction factor f (see Eq. 4.3) from 100% to 30% and 70% consistently in the measured spectrum and in the $\mathrm{RM}_{\mathrm{det}}$. The comparison between the unfolded spectra obtained with different choices of f is shown in Fig. 4.16.

Background fluctuations For the background fluctuations, the response matrix $\mathrm{RM}_{\mathrm{bkg}}$ was constructed with the single-particle embedding method for determining δp_{T} instead of the random-cone method. The comparison is shown in Fig. 4.17. The uncertainty estimated from this comparison is a few percent of the final yield.

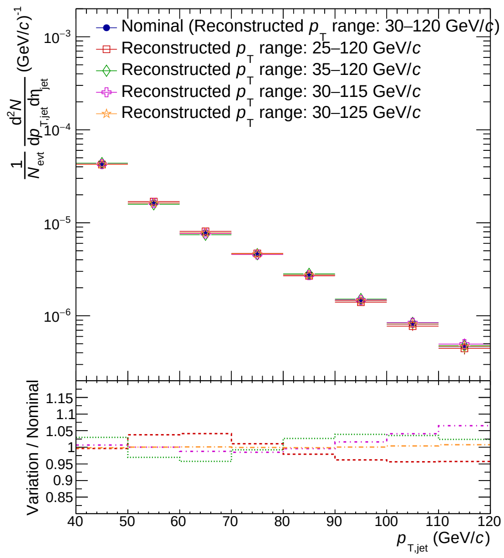

Figure 4.18: Comparison of the jet p_{T} spectra in the $0-10\%$ most central Pb–Pb collisions unfolded using different limits for the reconstructed axis for the estimation of the systematic uncertainty.

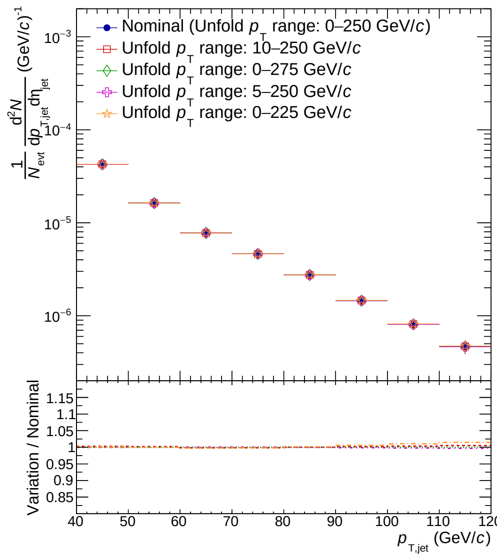

Figure 4.19: Comparison of the jet p_{T} spectra in the $0-10\%$ most central Pb–Pb collisions unfolded using different limits for the unfolded axis for the estimation of the systematic uncertainty.

p_{T} limits of the measured spectrum The p_{T} limits of the measured spectrum (the input for the unfolding procedure) were varied at both the low and high ends by ± 5 GeV/c. The importance of this variation is twofold: first it tests the sensitivity to the kinematic efficiency correction (see Fig. 4.11b), which is based on Monte Carlo and may be biased; second (for the low end limit only) it tests the sensitivity to a potentially increased/decreased contamination from combinatorial jets, which are more abundant at lower $p_{\mathrm{T,jet}}^{\mathrm{reco}}$. The comparison of the spectra obtained with the different limits on $p_{\mathrm{T,jet}}^{\mathrm{reco}}$ is shown in Fig. 4.18. The relative differences with the nominal choice were found to be between $1-7\%$ and were taken as the systematic uncertainty.

Combinatorial jets A more drastic way to test the presence of combinatorial jets is to force the unfolding procedure to distribute the measured counts in a restricted

$p_{\mathrm{T,jet}}^{\mathrm{truth}}$ interval. In particular, restricting the low end from 0 to a higher value is expected to shuffle combinatorial jets in the higher momentum bins. Both the low and high ends were varied as shown in Fig. 4.19. The relative differences between the various choices were found to be negligible.

4.6.2 Shape Uncertainties

The shape uncertainty is dominated by the regularization used in the unfolding procedure. The SVD method with regularization parameter $k = 5$ was used for the nominal result. The result was tested against a different regularization and unfolding technique based on the χ^2 minimization with a log–log regularization [176]. In this case the regularization is obtained by adding a penalty term in the calculation of the χ^2, calculated between the measured and refolded spectrum. This comparison is shown in Fig. 4.20a. The regularization parameter k was varied by ± 1: the comparison is shown in Fig. 4.20b. Finally, Fig. 4.20c shows the comparison between the spectra unfolded with the SVD method starting from different priors. The different priors were obtained varying the exponent of the power law function fitted to the reconstructed spectrum by ± 0.5.

These variations in the regularization strategy are combined assuming that they constitute independent measurements. The final shape uncertainty is thus obtained by summing them in quadrature and dividing by the square root of the number of variations. The total shape uncertainties vary between 3 and 7%.

4.7 Results

Figure 4.21 shows the jet p_{T} spectra measured in Pb–Pb collisions at $\sqrt{s_{\mathrm{NN}}} = 2.76$ TeV with the ALICE detector. The spectra are shown for two centrality classes: $0-10\%$ (central) and $10-30\%$ (semi-central) in the ranges $40-120$ and $30-100$ GeV/c,

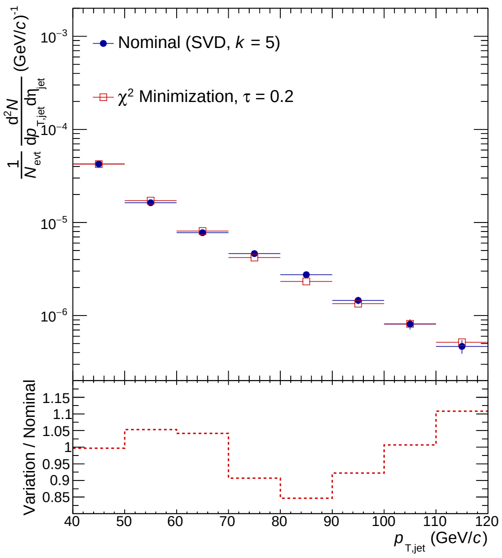

(a) Unfolding regularization method

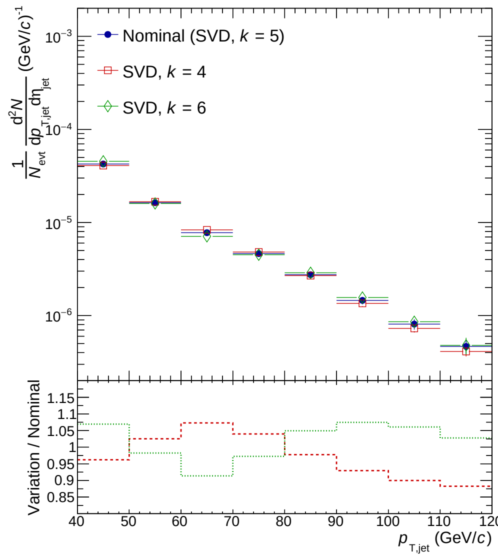

(b) SVD regularization parameter

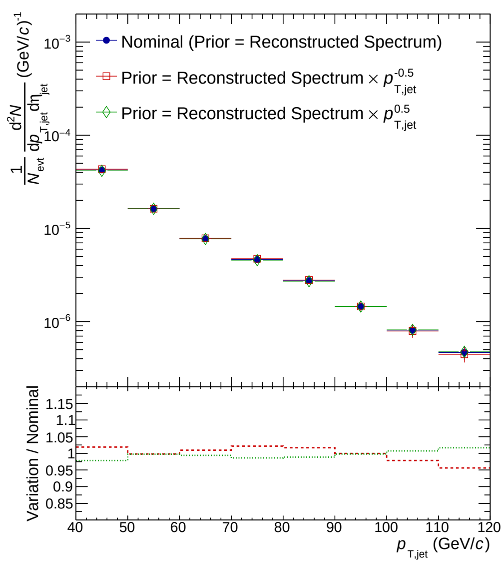

(c) Prior choice

Figure 4.20: Comparison of the jet p_{T} spectra in the $0-10\%$ most central Pb–Pb collisions unfolded using different parameters of the unfolding procedure for the estimation of the systematic uncertainty.

respectively. In the case of the semi-central collisions it was possible to push the low end to 30 GeV/c because of the smaller width of the background density fluctuations[9]; however, because of the smaller $N_{\rm coll}$ the statistics were insufficient above 100 GeV/c. Jets were assembled from tracks with $p_{\rm T} > 0.15$ GeV/c and EMCal energy clusters with $E_{\rm T} > 0.3$ GeV using the anti-$k_{\rm T}$ algorithm with resolution parameter $R = 0.2$. Jets were required to be within the EMCal fiducial acceptance, i.e. the jet axis was required to be R away from the edges of the calorimeter. Jets were also required to contain a leading track constituent with $p_{\rm T} > 5$ GeV/c. The average UE density was subtracted using a data-driven technique. An unfolding procedure was employed to correct for detector resolution effects and for fluctuations in the UE density. In particular, the detector resolution was estimated using a Monte Carlo simulation and included the corrections for the jet energy scale shift due to unreconstructed particles (track-reconstruction efficiency, neutral particles that do not shower in the EMCal, particles with momentum or energy below the thresholds, etc.). However the requirement of having a charged particle constituent with $p_{\rm T} > 5$ GeV/c was not removed in the correction, as this is considered part of the jet definition. The spectra are normalized by the number of events $N_{\rm evt}$ and by the number of binary collisions $N_{\rm coll}$ expected for each centrality class from the Glauber Monte Carlo[10]. The jet $p_{\rm T}$ spectrum in pp collisions at $\sqrt{s} = 2.76$ TeV is also reported in Fig. 4.21. The jet spectrum in pp collisions was measured by another ALICE collaborator, also a graduate student at Yale University (May 2014) [153, 175].

4.7.1 Leading Charged Particle $p_{\rm T}$

In order to investigate the effect of the leading charged-particle requirement for jets reconstructed in pp collisions, the ratio of the jet spectra with a 5 GeV/c leading

9. See Fig. 4.7a

10. See Section 4.2.1

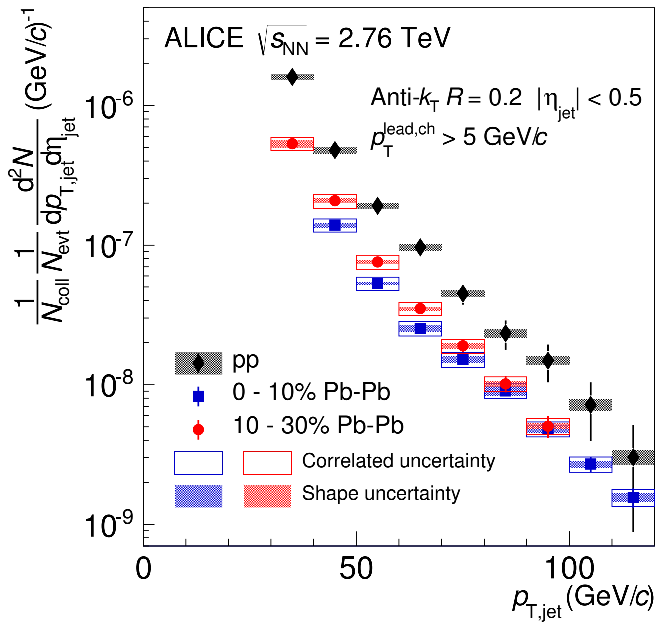

Figure 4.21: The spectra of $R = 0.2$ jets with a leading track requirement of 5 GeV/c in $0 - 10\%$ and $10 - 30\%$ most central Pb–Pb collisions scaled by $1/N_{\mathrm{coll}}$ and in inelastic pp collisions at $\sqrt{s_{\mathrm{NN}}} = 2.76$ TeV. The uncertainties on the normalization are about 11% for the Pb–Pb data from the uncertainty on N_{coll} and about 8% for the pp data from the total inelastic cross section.

charged-particle requirement (the biased jet sample), over the spectrum of jets without this requirement (the inclusive jet sample) was calculated. This ratio is reported in Figure 4.22 for jets with a resolution parameter $R = 0.2$. Systematic uncertainties in the ratio were evaluated by removing the uncertainties that are correlated between the spectra obtained with and without the cut on the leading particle. For $p_{\mathrm{T,jet}} > 50$ GeV/c more than 95% of all reconstructed jets have at least one charged particle with a p_{T} greater than 5 GeV/c. An estimate obtained with the PYTHIA 6 tune A is superimposed in Fig. 4.22 and accurately describes the measured ratio.

A similar exercise was performed for the measurement in $0-10\%$ most central Pb–Pb collisions. The ratios of jet spectra with the different leading charged-particle p_{T} biases over the nominal spectrum (with leading charged-particle p_{T} bias of 5 GeV/c) are shown in Fig. 4.23. The corrections to these different jet spectra were done using

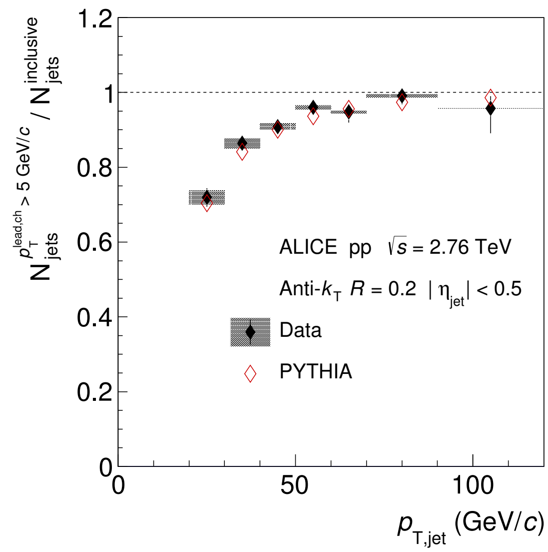

Figure 4.22: Ratio of the jet spectrum with a leading track $p_T > 5$ GeV/c over the inclusive jet spectrum for $R = 0.2$ in pp collisions at $\sqrt{s} = 2.76$ TeV.

the same unfolding procedure as the nominal spectrum. The statistical uncertainties were added in quadrature in the ratio. This approach is justified by the fact that the unfolding procedure weakens the statistical correlation between corresponding bins belonging to jet spectra with different leading track requirements. The systematic shape uncertainty, due to the unfolding procedure, was treated as completely uncorrelated in the ratio. The correlated uncertainty, primarily due to the uncertainty on the jet energy scale, is highly correlated between the various spectra. Therefore, the systematic variations discussed in Section 4.6.1 were applied consistently for both the denominator and the numerators, and the resulting relative differences in the ratios were taken as the systematic uncertainties. For lower requirements on the leading charged-particle p_T, the unfolding is not as stable as with a 5 GeV/c requirement, which leads to a larger systematic uncertainty due to the unfolding correction procedure. The ratio obtained for the jet spectra with leading charged-particle requirements of 3 GeV/c and 0 is consistent with unity within uncertainties. All measurements of the ratio of jet spectra with different leading charged-particle biases are well described by Pythia 6 (tune A), within one sigma of the total uncertainties or

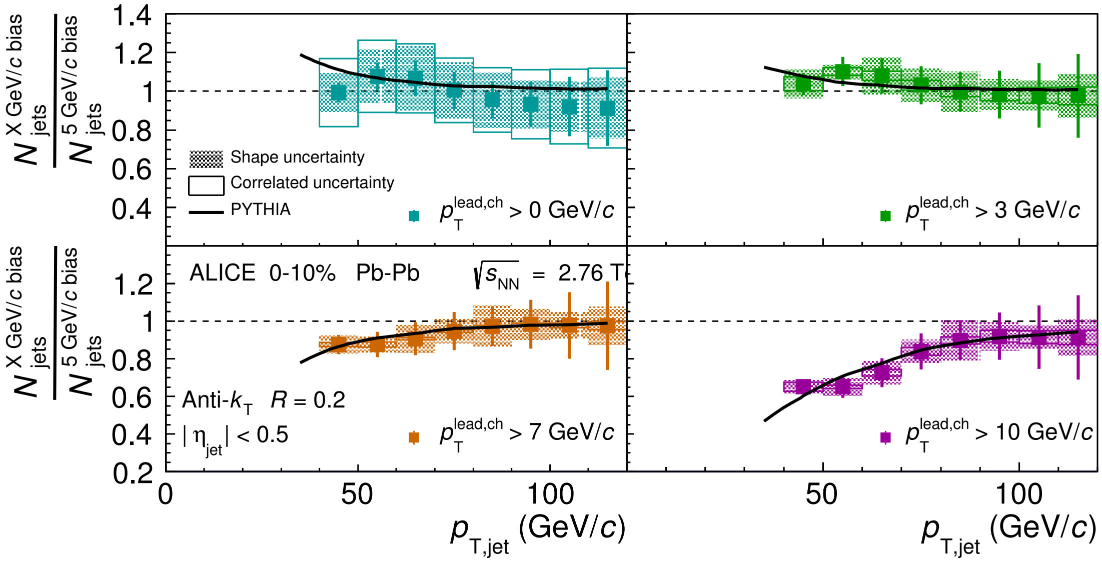

Figure 4.23: Ratios of jet spectra with different leading track pp requirements ("0 over 5", "3 over 5", "7 over 5" and "10 over 5") for $R = 0.2$ jets in $0-10\%$ Pb–Pb collisions at $\sqrt{s_{NN}} = 2.76$ TeV. The solid black curves represent predictions from PYTHIA 6 (tune A).

less.

Chapter 5

Discussion

5.1 D^0-Meson Tagged Jets in pp Collisions

The measurement of the D^0-meson tagged jets in pp collisions at $\sqrt{s} = 7$ TeV was compared with predictions from three Monte Carlo event generators. In the following the key points of each Monte Carlo generator are summarized.

Pythia The two versions of Pythia share the same phenomenology. Pythia 8 [177] (8.2.1) is the modern version, written in C++ and has superseded the old Pythia 6 written in Fortran. However comparing with Pythia 6 [123] (6.4.28) is valuable because it is still widely used by many experiments (including ALICE) for the determination of the detector performance. In addition, even though the underlying phenomenology is essentially the same, the tunes developed for Pythia 6 were not ported to Pythia 8, including relatively recent tunes, like the Perugia 2011 used in this study.

The hard-scattering process is calculated at Leading-Order (LO) in perturbative QCD (pQCD). In particular, the generic QCD $2 \to 2$ process was used ("minimum-bias" configuration) for this study. The parton shower is partially computed perturbatively, however important non-perturbative corrections are applied. Multi-parton interactions (MPIs) occurring between partons in the beam remnants generate the underlying event. These additional $2 \rightarrow 2$ scatterings are $p_\perp$-ordered[1], and limited between $p_{\perp\,\mathrm{max}}$ and $p_{\perp\,\mathrm{min}}$. The upper limit is determined by the $p_\perp$ of the hard scattering, while the lower limit is a free parameter that must be tuned from data ($p_{\perp\,\mathrm{min}} \approx 1.5 - 2.5$ GeV). Hadronization is performed using the Lund model [178, 179] and it is followed by the simulation of the decays of the unstable particles. In the Lund model, the fragmentation proceeds through the "breaking" of a color flux tube, represented by a string with the transverse dimensions of ≈ 1 fm, connecting a quark and an antiquark moving apart. As the quarks move farther apart from each other, the potential energy stored in the string increases and the string may break by generating a new quark-antiquark pair, leading to the formation of two mesons, or a new antidiquark-diquark pair, leading to the formation of a baryon and an antibaryon. The process continues iteratively until all the energy is used up. The string breaking is obtained invoking the idea of quantum-mechanical tunneling; hence the production of heavy-flavor quarks is strongly suppressed because the probability for a massive quark to overcome the potential barrier is very small (strange quarks are suppressed by $\sim 1/3$, while charm quarks are suppressed by 10^{-11}). This is an important aspect because it means that the overall charm production is not affected by this step of the event generation, but it only depends on the parton hard scattering and semi-perturbative parton shower. The fragmentation and hadronization steps require much tuning from existing data. The Perugia 2011 [138] and Monash 2013 [180] tunes were used for Pythia 6 and Pythia 8, respectively. Both tunes are based on LHC data available in the year they were published. For this study, the Parton Distribution Functions (PDFs) were not changed with respect to those used in the tuning: CTEQ5L [181] and NNPDF2.3 LO [182] for Pythia 6 and Pythia 8,

1. In this version of Pythia, as well as in all subsequent versions, also the parton shower and the initial- and final-state radiations are $p_\perp$-ordered.

respectively[2].

Herwig Similarly to PYTHIA, also Herwig 7.0 [184, 185] calculates the hard scattering at LO in pQCD[3]. Two choices of the main physics process have been used and compared with data: `MEMinBias` and `MEPP2QQ`. For the purpose of this study, the main relevant difference is that the former treats all partons as massless whereas the latter uses the correct masses of the heavy-flavor quarks (charm and beauty) in the matrix elements of the pQCD calculation. Parton showers are implemented fully perturbatively up to the infrared cut-off; for massive particles this means that the perturbative gluon emissions are calculated down to zero transverse momentum, which allows for an improved simulation of the dead-cone effect[4]. The underlying event is generated through multi-parton scatterings, computed perturbatively using the an eikonal approach, that gives rise to additional parton showers. The hadronization step is where Herwig differs substantially from PYTHIA. Partons that are close in momentum space are connected with each other in color-anticolor pairs. Clusters are formed from color singlets of connected (di)quarks and anti-(di)quarks. These clusters are regarded as highly excited hadron resonances. Each cluster is decayed into a pair of hadrons by popping a (di)quark-anti(di)quark from the vacuum. Quarks popping out from the vacuum are always up, down or strange. Also for Herwig a tuning is required for the non-perturbative aspects of the simulation. For this study the default tune shipped with Herwig 7.0 was used.

POWHEG The measurement was compared also with two NLO pQCD calculations obtained with the POWHEG-BOX V2 framework [131], which uses the POWHEG

2. The LHAPDF 5 [183] PDF interpolator was used for PYTHIA 6; PYTHIA 8 used an internal parametrization of the PDF without the use of any interpolator.

3. Herwig 7.0 allows also to calculate most processes at NLO accuracy, however this feature was not used in this study.

4. See Section 1.2.1.

method [129, 130] to match the NLO calculation with the parton shower generated by another Monte Carlo program. For this study, the parton event generated by POWHEG-BOX was passed to Pythia 6 (Perugia 2011 tune) for the parton shower, subsequent hadronization and particle decays, as well as the generation of the underlying event. The main problem of matching NLO calculations with a parton shower Monte Carlo is that of avoiding overcounting, since the parton shower routines typically include corrections equivalent to NLO, albeit potentially less accurate. This problem is resolved in the POWHEG formalism by generating first the emission with the largest $p_\perp$ using full NLO accuracy, and then using the shower Monte Carlo to generate subsequent radiation. For this method to work, also the shower Monte Carlo must be $p_\perp$-ordered, or alternatively a high-$p_\perp$ veto must be applied. The theoretical uncertainties on the POWHEG NLO calculation have been estimated by varying the renormalization and factorization scales ($0.5\mu_0 \leq \mu_{\mathrm{F,R}} \leq 2.0\mu_0$ with $0.5 \leq \mu_{\mathrm{R}}/\mu_{\mathrm{F}} \leq 2.0$), the mass of the charm quark ($m_{\mathrm{c}} = 1.3, 1.7$ GeV/c^2 with $m_{\mathrm{c},0} = 1.5$ GeV/c^2) and the PDF (central points: CT10nlo [161]; variation: MSTW2008nlo68cl [167]). Two process implementations of the POWHEG framework have been employed: the heavy-quark implementation [159] and the di-jet implementation [132], where the former computes the hard scattering for massive outgoing quarks (charm), while the latter treats all partons as if they were massless.

5.1.1 p_{T}-Differential Cross Section

Both versions of Pythia overestimate the yield by a factor ≈ 1.5 which appears to be approximately constant in the measured $p_{\mathrm{T,jet}}^{\mathrm{ch}}$ range as shown in Fig. 5.1 (left panel). However, since they also overestimate the inclusive jet cross section by a similar amount [186], they provide a good description of the rate of D^0-meson tagged jets over the inclusive jet production, as shown in Fig. 5.2 (left panel). Non-perturbative effects, such as hadronization and the underlying event, contribute similarly to both the D^0-

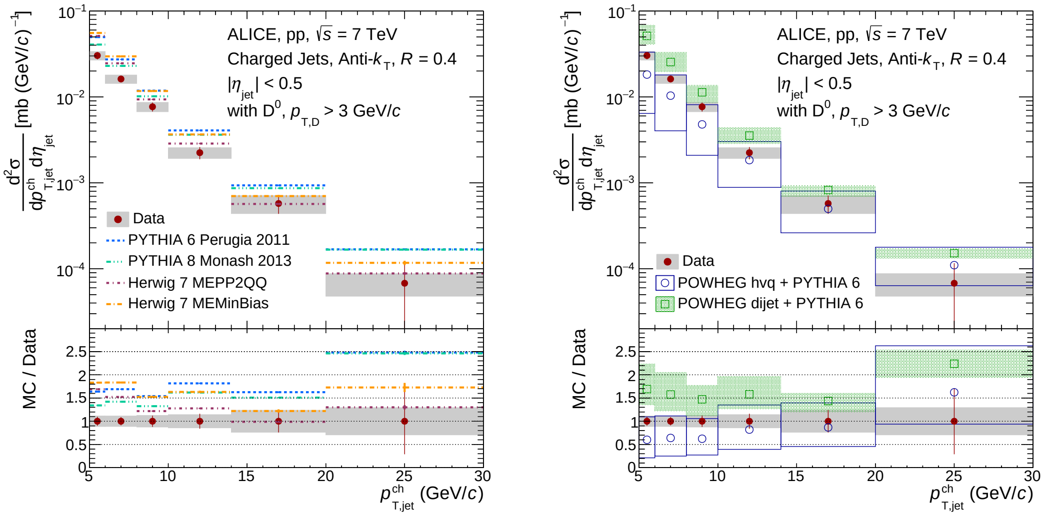

Figure 5.1: p_T-differential cross section of D^0-meson tagged jets in pp collisions at $\sqrt{s}$ = 7 TeV. The data are compared with theoretical curves obtained with PYTHIA 6 [123], PYTHIA 8 [140] and Herwig 7.0 [184, 185] (left) and with POWHEG [130–132, 159] (right).

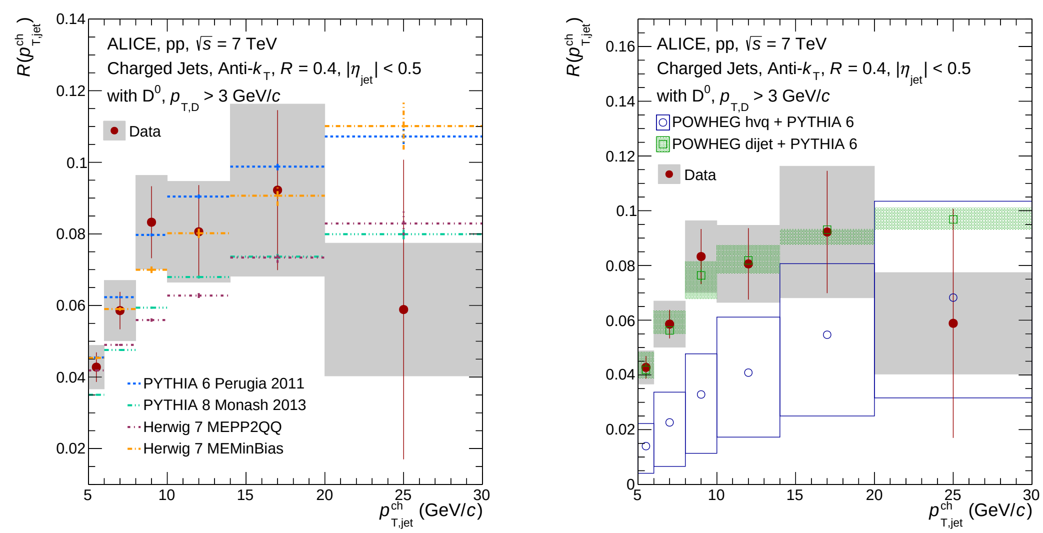

Figure 5.2: Rate of D^0-meson tagged jets in pp collisions at $\sqrt{s}$ = 7 TeV as a function of $p^{ch}_{T,jet}$. The data are compared with theoretical curves obtained with PYTHIA 6 [123], PYTHIA 8 [140] and Herwig 7.0 [184, 185] (left) and with POWHEG [130–132, 159] (right).

meson tagged and the inclusive jet measurement. In the ratio they may partially cancel, which could explain the improved agreement between the data and PYTHIA for this observable. Both Herwig processes tend to overestimate the measured cross section, with `MEPP2QQ` being closer to the data. The `MEMinBias` process reproduces well the ratio to the inclusive jet cross section[5].

As shown in Fig. 5.1 (right panel), a good agreement is found within the theoretical and experimental uncertainties between the data and the POWHEG heavy-quark implementation. The POWHEG di-jet implementation systematically overestimates the production yield by a constant factor of ≈ 1.5. In the ratio of the D^0-meson tagged jet yield over the inclusive jet yield (Fig. 5.2, right panel)[6], the opposite is true: the di-jet implementation shows a better agreement compared to the heavy-quark implementation. Notice that in the calculation of the systematic uncertainties on cross-section ratios, the variations of the perturbative scales and of the PDF were applied consistently in the numerator and in the denominator.

5.1.2 $z_{||}^{\mathrm{ch}}$-Differential Cross Section

Figures 5.3 and 5.4 show the comparisons of the data with the Monte Carlo simulations of the $z_{||}^{\mathrm{ch}}$-differential cross sections for the two $p_{\mathrm{T,jet}}^{\mathrm{ch}}$ ranges considered in this analysis. The difference between the two set of Figures is that the first is normalized as a standard cross section, while the second is normalized by the inclusive jet cross section integrated in the corresponding $p_{\mathrm{T,jet}}^{\mathrm{ch}}$ interval. As we have seen in the comparisons for the p_{T}-differential cross section, some simulations (Herwig `MEPP2QQ` and POWHEG hvq) provide a good description of the absolute cross section while others (PYTHIA, Herwig `MEMinBias` and POWHEG dijet) do a better job at describing the

5. The denominator (inclusive jet cross section) is obtained for both ratios using the `MEMinBias` process.

6. Also in this case the denominator is calculated with the di-jet implementation for both curves.

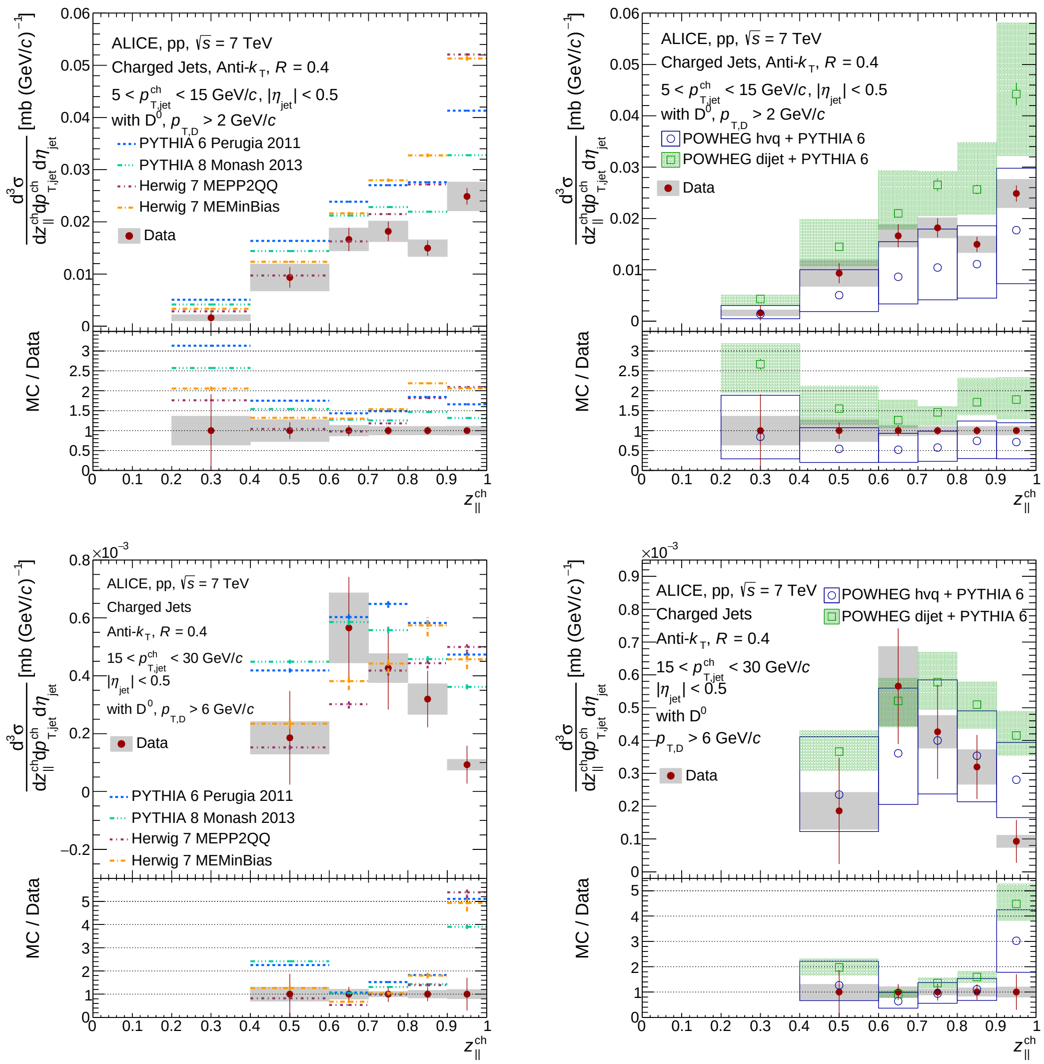

Figure 5.3: $z_{||}^{\mathrm{ch}}$-differential cross section of $\mathrm{D^0}$-meson tagged jets in pp collisions at $\sqrt{s} = 7$ TeV. The data are compared with theoretical curves obtained with Pythia 6 [123], Pythia 8 [140] and Herwig 7.0 [184, 185] (left) and with POWHEG [130–132, 159] (right).

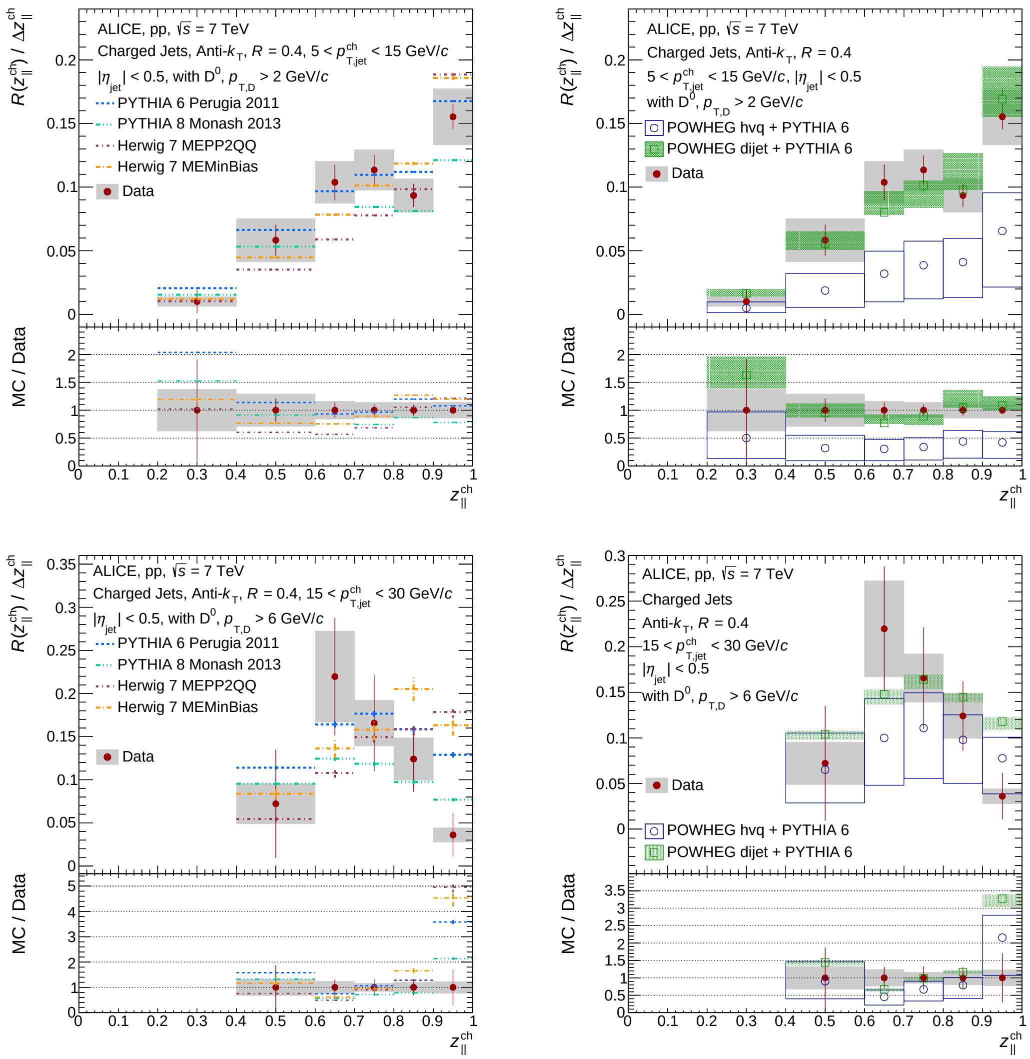

Figure 5.4: Rate of D^0-meson tagged jets in pp collisions at $\sqrt{s} = 7$ TeV as a function of $z^{ch}_{||}$. The data are compared with theoretical curves obtained with PYTHIA 6 [123], PYTHIA 8 [140] and Herwig 7.0 [184, 185] (left) and with POWHEG [130–132, 159] (right).

ratio to the inclusive jet cross section. Therefore, using both normalizations - cross section and ratio to inclusive jets - allows us to get a more complete picture of how well the models can describe the shape of the fragmentation function distribution, regardless of whether they can calculate the absolute cross section precicely.

All models show an overall good agreement with the data for jets with $5 < p_{\mathrm{T,jet}}^{\mathrm{ch}} < 15$ GeV/c, with the only exception of Herwig 7.0 `MEPP2QQ` which features a substantially harder fragmentation of D^0 mesons in jets. For jets with $15 < p_{\mathrm{T,jet}}^{\mathrm{ch}} < 30$ GeV/c models can describe the data quite well within the large uncertainties. A depletion is observed in the last $z_{||}^{\mathrm{ch}}$ bin in data compared to all models, however the discrepancy is only slightly larger than 1 σ.

5.2 Jet Suppression in Pb–Pb Collisions

The nuclear modification factor R_{AA} of jets is defined as follows:

$$R_{\mathrm{AA}} = \frac{\frac{1}{N_{\mathrm{coll}}} \frac{\mathrm{d}^2 N_{\mathrm{jets}}^{\mathrm{PbPb}}}{\mathrm{d}p_{\mathrm{T,jet}} \mathrm{d}\eta_{\mathrm{jet}}}}{\frac{1}{\sigma_{\mathrm{pp}}^{\mathrm{inel}}} \frac{\mathrm{d}^2 \sigma^{\mathrm{pp} \rightarrow \mathrm{jet+X}}}{\mathrm{d}p_{\mathrm{T,jet}} \mathrm{d}\eta_{\mathrm{jet}}}}. \tag{5.1}$$

The numerator in Eq. 5.1 represents jet p_{T} spectrum measured in Pb–Pb collisions normalized by the number of events and by the number of binary collisions expected from the Glauber Monte Carlo N_{coll}. In the denominator the jet p_{T}-differential cross section measured in pp collisions is divided by the total inelastic pp cross section $\sigma_{\mathrm{pp}}^{\mathrm{inel}}$, or alternatively (which is the same):

$$\frac{1}{\sigma_{\mathrm{pp}}^{\mathrm{inel}}} \frac{\mathrm{d}^2 \sigma^{\mathrm{pp} \rightarrow \mathrm{jet+X}}}{\mathrm{d}p_{\mathrm{T,jet}} \mathrm{d}\eta_{\mathrm{jet}}} = \frac{\mathrm{d}^2 N_{\mathrm{jets}}^{\mathrm{pp}}}{\mathrm{d}p_{\mathrm{T,jet}} \mathrm{d}\eta_{\mathrm{jet}}}. \tag{5.2}$$

In the absence of nuclear collective effects, if a Pb–Pb collision can be described as a superposition of independent N_{coll} binary collisions this ratio is unity. A deviation from unity is an indication that nuclear collective effects are at play which cannot be described as a superposition of independent nucleon-nucleon collision. A value larger than one indicates an enhancement, whereas a value smaller than one a suppression. The validity of the N_{coll} scaling has been confirmed experimentally by the measurement of the R_{AA} for electroweak probes, such us direct photons[7], Z^0 and $\mathrm{W}^{\pm}$ bosons. The measurements showed $R_{\mathrm{AA}} \approx 1$ for these probes [187–191].

The R_{AA} of $R = 0.2$ jets with a 5 GeV/c leading charged-particle requirement in the $0-10\%$ and $10-30\%$ central Pb–Pb collisions is shown in 5.5. The systematic and statistical uncertainties from the Pb–Pb and pp measurements are added in quadrature. As can be seen, jets in the measured $p_{\mathrm{T,jet}}$ range are strongly suppressed. The R_{AA} in both $0-10\%$ and $10-30\%$ central events was found to have a weak $p_{\mathrm{T,jet}}$ dependence. In the $0-10\%$ most central events the average R_{AA} is 0.28 ± 0.04 (statistical and systematic uncertainties added in quadrature). The suppression is smaller in magnitude in the $10-30\%$ central events, leading to an average R_{AA} of 0.35 ± 0.04. This centrality ordering can be interpreted as an indication that the QGP is hotter, denser and longer-lasting in the more central collisions. These results qualitatively agree with the suppression obtained from measurements using charged-particle jets [192]. Furthermore, the results are consistent with the jet R_{AA} reported by ATLAS [193] and CMS [194] at the same center-of-mass energy, as shown in Fig. 5.6 for both centrality classes.

The suppression of jet production in heavy-ion collisions is one of the cornerstones of the QGP phenomenology, together with other experimental facts related to the phenomenon of jet quenching. It is interpreted as a consequence of the interaction of the hard-scattered partons with the QGP formed in ultra-relativistic heavy-ion collisions. This interaction leads to a net transfer of energy-momentum from the hard-scattered parton to the (locally) thermalized medium. An important confirmation that the observed suppression is due to the hot nuclear medium comes from the measurement

7. $\mathrm{qg} \rightarrow \mathrm{q}\gamma$

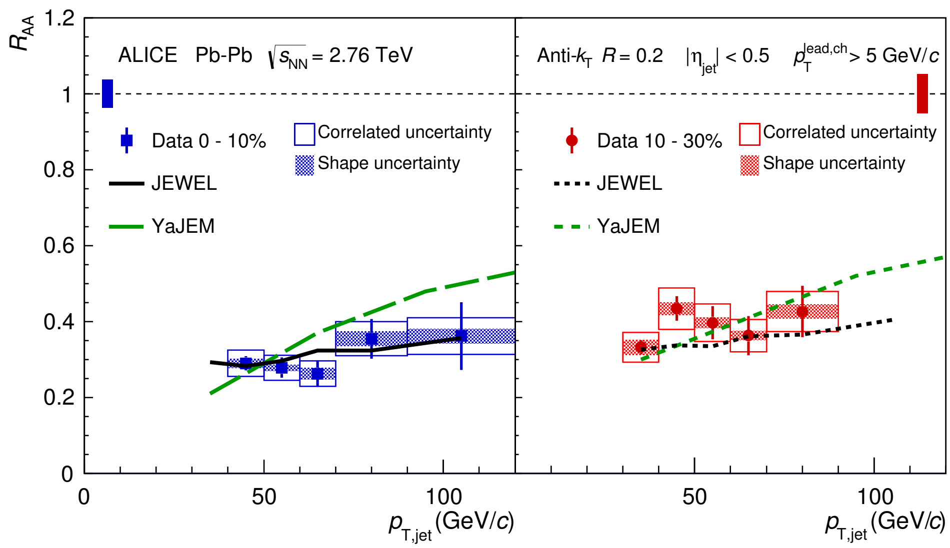

Figure 5.5: Nuclear modification factor $R_{\rm AA}$ of jets in Pb–Pb collisions at $\sqrt{s_{\rm NN}}$ = 2.76 TeV in the 0 – 10% (left) and 10 – 30% (right) most central events. The data are compared with theoretical predictions from YaJEM [200] (green dashed line) and JEWEL [201] (black solid line).

of jet production in p–Pb collisions. The p–Pb collision system is expected to be too small to lead to the formation of the QGP[8]. The presence of the Pb nucleus can interfere with the measured jet production through so-called "cold nuclear matter" effects, such as the modification of the PDF (nuclear PDF) through various mechanisms, among them the Color Glass Condensate (CGC) [195–198]. As a matter of fact, the nuclear modification factor defined for p–Pb collisions ($R_{\rm pPb}$) was found to be consistent with unity [199].

In order to interpret the results more quantitatively, a comparison of the measured jet $R_{\rm AA}$ to calculations from two different models is also shown in Fig. 5.5. Both models implement a Glauber Monte Carlo for the initial geometry and use the Pythia 6 [123] Lund model [178, 179] for the hadronization of colored partons into final-state particles. They differ both in the evolution mechanism of the medium and

8. This paradigm has been partially shaken by recent observation of QGP-like effects in the low-$p_{\rm T}$ sector [95–97]. However, no measurements attributed to jet quenching in p–Pb collisions (or other similarly small systems such as d–Au at RHIC) have been reported so far.

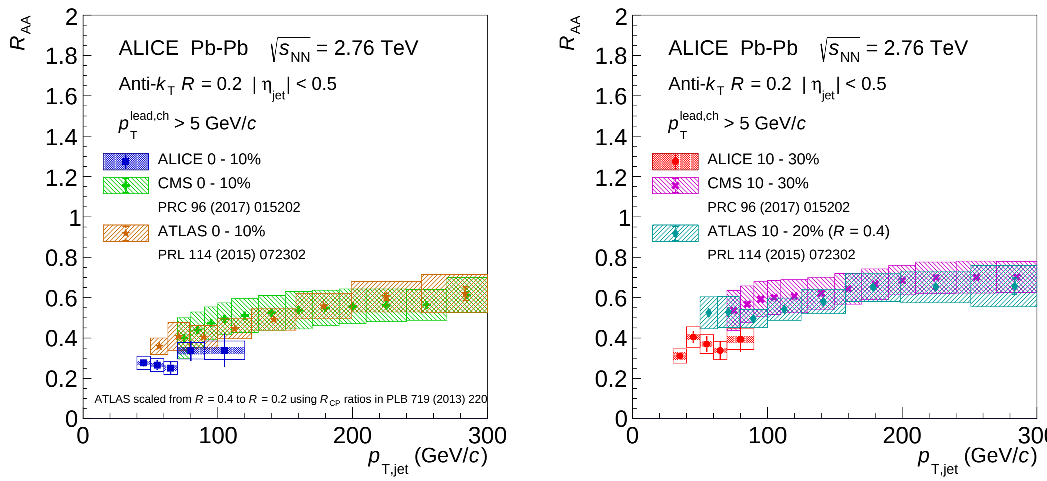

(a) $0 - 10\%$ centrality (b) $10 - 30\%$ centrality

Figure 5.6: Nuclear modification factors R_{AA} of jets in Pb–Pb collisions at $\sqrt{s_{\mathrm{NN}}} = 2.76$ TeV compared with ATLAS [193] and CMS [194], in the centrality classes indicated below each panel.

in the implementation of the parton–medium interactions.

YaJEM A 2+1D hydrodynamical calculation drives the evolution of the system. Parton showers are modified by a medium-induced increase of the virtuality during their evolution through the medium. The kinematics of the virtual partons in the evolving partonic shower were modified with a parameter related to the two transport coefficients, $\hat{q}$ and $\hat{e}$, that describes how strongly a parton of a given momentum couples to the medium by elastic scattering and induced radiation, respectively. The parameters were fixed so that the model accurately describes the R_{AA} for charged hadrons at 10 GeV/c [202], but no additional changes were made for the prediction of the jet R_{AA}. For more details see the original papers where this model is described [200, 203, 204].

JEWEL The evolution of the medium is obtained through a 1D Bjorken expansion. Hard scatters are generated according to Glauber collision geometry, and suffer from elastic and radiative energy loss in the medium. A microscopic description of the transport coefficient $\hat{q}$ is used for the implementation of the parton–medium interactions. Each scattering of the initial parton with medium partons is computed and the average over all scatters determines $\hat{q}$. Further details are available in the original paper [201].

Despite their different approaches, both calculations are found to reproduce the jet suppression. YaJEM, however, exhibits a slightly steeper increase with jet p_{T} than the data. The calculated χ^2 are 1.690 for YaJEM and 0.368 for JEWEL, obtained by comparing the models with the data, taking into account the experimental systematic and statistical uncertainties.

Chapter 6

ALICE Upgrade

6.1 Physics Program

In its Letter of Intent (LoI) [205], the ALICE Collaboration presented a rich experimental program for the LHC Run-3 (2021-2023) and Run-4 (2026-2029), making a strong case for a major upgrade of the detector. ALICE is well suited to address some of the fundamental questions of the theory of strong interactions, particularly the nature of confinement and the hadronization process, and the properties of the QCD matter at high temperature. In particular, a strong emphasis was put on heavy-flavor and jet measurements:

Thermalization (and possible thermal production) of heavy-flavor in the QGP by the measurement of the baryon-to-meson ratio and of the azimuthal-flow anisotropy of heavy-flavor mesons and baryons.

Parton-mass and color dependence of the in-medium energy loss by the measurement of the p_{T} dependence of the nuclear modification factors of charm and beauty hadrons down to low momentum ($p_{\mathrm{T}} = 0$ for charm and $p_{\mathrm{T}} \approx 2$ GeV/c for beauty) as well as the measurement of jets with heavy-flavor content, including both the p_{T} spectrum and the fragmentation function down to low $z_{||}$.

Investigate the dynamics of the energy loss and the response of the medium by measuring medium-induced modifications of the jet internal substructure, the fragmentation function of identified particles in jets, and in general by exploiting the low-momentum tracking capability of ALICE to measure the fine structure of the jets and its surroundings.

Photon-jet correlations which provide a precise calibration of the initial parton energy, and at the same time bias the jet population towards a quark-dominated one, allowing for color-dependent energy loss studies[1].

Another crucial key point of the ALICE physics program is the measurement of quarkonia states, particularly charmonia, to test the various in-medium suppression and regeneration models. The LoI highlights also the measurement of exotic objects produced in heavy-ion collisions, such us the multi-Λ hyper-nuclei ${}^{5}_{\Lambda\Lambda}\mathrm{H}$, something that is unique to ALICE. Finally, a run with low magnetic field in the ALICE central barrel is foreseen for measuring low-mass dileptons, that have the potential of shedding light on the spontaneous breaking of chiral symmetry of QCD[2] by measuring light-flavor mesons such as the ρ, as well as information on the temperature and lifetime of the QGP by measuring virtual and real photons.

For this ambitious research program, ALICE is preparing for the upgrade of its detector, which will be performed in 2019-2020 during the Long Shutdown 2 (LS2). The main upgrades regard the central barrel tracking system. The Inner Tracking System will be completely replaced by a seven-layer monolithic silicon pixel detector [158]. This brand-new state-of-the-art detector will allow for a much improved secondary vertex resolution, providing charm/beauty discrimination, with very low

1. Back-to-back photon-jet pairs are produced at LO in the process: $\mathrm{qg} \rightarrow \mathrm{q}\gamma$. Therefore the photon is expected to have the same initial momentum of the outgoing quark.

2. At high temperature quarks are expected to show their bare mass, which means that an approximate chiral symmetry would be restored between light-flavor quarks (the chiral symmetry is not perfect because of the Higgs mechanism, which gives small bare masses to light-flavor quarks).

material budget. The upgrade of the Time Projection Chamber (TPC) is crucial in order to be able to run ALICE at a much higher collision rate. The current TPC limits the event rate to about 300 Hz. The upgrade will push this limit to 50 kHz, while preserving the current tracking and PID performance. Other upgrades are planned for the readout electronics of most ALICE sub-detectors: Transition Radiation Detector (TRD), Time-Of-Flight (TOF) detector, Photon Spectrometer (PHOS), and the forward Muon Spectrometer. An important upgrade will also involve the trigger system, the High Level Trigger (HLT) computer farm, the data acquisition (DAQ) system, as well as the offline data processing infrastructure.

The approved upgrade plan will allow ALICE to collect a total of about 10^{11} Pb–Pb minimum-bias collisions, corresponding to an integrated luminosity of $10\,\mathrm{nb}^{-1}$, during the full Run-3 and Run-4 programs. ALICE will collect data in continuous mode, essentially recording every single Pb–Pb collision delivered by the LHC, at the expected peak instantaneous luminosity of $\approx 6 \times 10^{27}\,\mathrm{cm}^{-2}\mathrm{s}^{-1}$. Without the upgrades, the expected integrated luminosity collected by ALICE in the same period would have been about 100 times smaller for untriggerable observables (such as low-p_T heavy-flavor) and 10 times smaller for triggerable probes (such as high-p_T jets). These figures would have seriously limited the reach of the ALICE scientific program, as shown from the detailed projections reported in the LoI [205].

6.2 TPC Upgrade

The major limitation of the current ALICE TPC is a result of the gating grid used to suppress the ion back-flow[3]. The gating grid cycle limits the readout rate to about 3.5 Hz, insufficient to cope with the expected event rates in Run-3 and beyond. The solutions considered by the ALICE Collaboration [66, 206] aim at replacing

3. See Section 2.2.1.

the current readout system, consisting of the Multi-Wire Proportional Chambers (MWPCs) and the gating grid, with chambers constructed using stacks of Micro-Pattern Gas Detectors (MPGDs). These detectors feature intrinsically low values for ion back-flow [207, 208], which means that a gating grid is no longer required. The front-end electronics (currently limiting the readout rate further to 300 Hz) will also be completely replaced to adapt to the new readout chambers and provide higher readout rate capabilities.

After several years of R&D the solution chosen by the ALICE Collaboration was based on a stack of four Gas Electron Multiplier (GEM) detectors. The segmentation of the readout chambers is identical to the current one, consisting of two concentric crowns – the Inner Read-Out Chambers (IROCs) and the Outer Read-Out Chambers (OROCs) – of 18 sectors each. After optimization of the GEM foil choice as well as voltage settings, the quadruple GEM solution showed an ion back-flow of 0.7% with a 12% energy resolution at a gas gain of 2000 [206, 209]. These figures fulfill the requirements set by the physics program. An important contribution to these R&D efforts was brought by the Relativistic Heavy-Ion Group (RHIG) at Yale, that studied an alternative solution with chambers consisting of a stack a two GEMs and a Micromegas. Details of this R&D effort are given in Section 6.2.1.

Following the final approval of the TPC upgrade plan with the 4-GEM solution, the Yale RHIG, together with other US institutions, has undertaken the construction and commissioning of the IROCs.

6.2.1 Yale R&D

The Yale R&D efforts for the ALICE TPC upgrade focused on the exploration of a possible alternative to the 4-GEM gas amplification chamber, using a combination of GEMs stacked with a Micromegas. A series of measurements, reported in [210], were performed at Yale in 2014 on a small gas chamber prototype. The goal was to

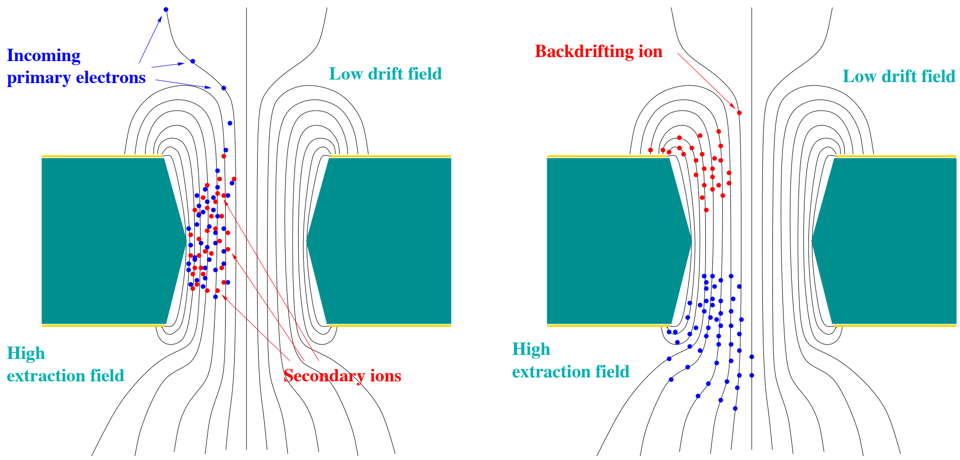

Figure 6.1: Sketch of the cross section of a GEM foil. Source: [213].

characterize the gas chamber in terms of ion back-flow (IBF) and energy resolution, varying the voltage settings of the various elements, in order to find an optimal operating condition, and verify its applicability as readout chambers of a large TPC.

Gas Chamber

GEMs [211] and Micromegas [212] are examples of MPGDs. They employ microscopic structures that concentrate electric field lines in a small volume. Gas amplification is achieved when electrons cross the high-field volume, causing an avalanche ionization. With an appropriate choice of the voltages, a large fraction of the ions produced in the avalanche are trapped by the detector itself.

GEM A thin ($\approx 50\,\mu$m) insulator foil, typically made of polyamide, is clad with copper on both sides. A large number of small holes, with a diameter of $\approx 50\,\mu$m, are etched in a regular pattern through the entire foil. A strong potential difference of $300 - 400$ V is applied between the two copper layers. A schematic picture of the working principle of the GEM is shown in Fig. 6.1. Electrons produced in the primary ionization are guided into the holes by the electric field lines of the low drift field (left). While the electrons drift to the anode, guided by the high extraction field,

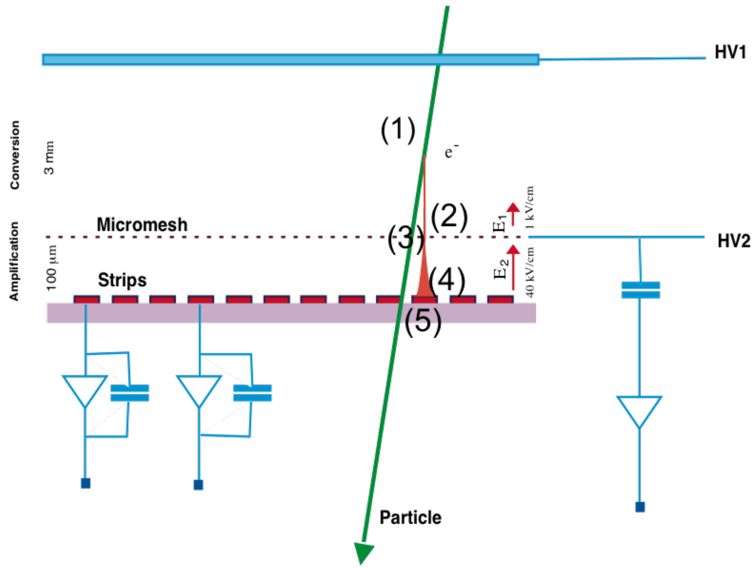

Figure 6.2: Working principle of a Micromegas detector. Source: [214].

a large fraction of the ions are trapped by the electric field lines in the top copper layer.

Micromegas The gas volume is divided in two by a metallic micro-mesh placed above the readout electrode, made of strips or pads, at a distance of about 100 μm. The working principle of the Micromegas is schematically shown in Fig. 6.2. The primary ionization produced by a particle in the gas volume above the micro-mesh (1) drifts down under the applied electric field (2). Once the electron enters the high-voltage region (3) between the mesh and the readout electrode it starts an avalanche (4), which induces a strong signal in the strips (5), read out through a charge amplifier. Ions produced in the avalanche drift back to the mesh and are largely trapped by it in a few μs.

Chamber layout The $10 \times 10\,\mathrm{cm}^2$ gas chamber prototype was assembled at Yale stacking two GEMs on top of a Micromegas[4]. The choice of this particular layout

4. The GEM foils were obtained from CERN (Switzerland) and Tech-Etch (45 Aldrin Rd, Plymouth, MA, USA), while the Micromegas came from CERN and CEA Saclay Lab (France)

serves several purposes. First, it provides a more efficient ion back-flow suppression, since ions have to drift back through multiple ion-suppressing layers. Second, it allows us to operate the Micromegas with a gas amplification factor of ~ 500, since ionization electrons are pre-amplified by the GEMs. If the full amplification of 2000, required by the ALICE TPC specifications, were to be provided by the Micromegas alone, the detector would operate in a much more unstable condition, with frequent sparks. Sparks are also suppressed by the fact that the two GEM layers spread the ionization electrons over a larger surface, reducing the probability that a dense cluster of electrons reach the Micromegas causing a discharge. This aspect is important also for another reason: in fact, if the ionization is spread over several readout pads the position of the center of the avalanche can be reconstructed more precisely through a weighted average of the positions of the pads. This improves spatial resolution to a value smaller than the pad size itself. The holes of the two GEM foils were misaligned by rotating the foils with respect to each other, in order to increase the spread of the ionization electrons and further suppress the ion back-flow.

Experimental Setup

The chamber was filled with a mix of Ne and CO_2 in the proportions 90 : 10, although other gas mixtures were tried as well. CO_2 is added to reduce the electron diffusion and partially quench UV photons created in the primary ionization. The experimental setup is sketched in Fig. 6.3 for two configurations corresponding to the measurement of the energy resolution (top) and the determination of the ion back-flow (bottom). A metallic screen was placed above the cathode and kept at the same voltage of the cathode itself. The voltages of various elements were controlled by two high voltage (HV) supplies mounted in an MPOD crate, manufactured by Wiener. The MPOD crate was connected to the local network via an Ethernet cable. It was possible to communicate with the MPOD unit via the Simple Network Management

Protocol (SNMP) from a personal computer running a Linux operating system. A comprehensive set of scripts was written in the bash language to efficiently control the voltages in a semi-automatic way. A radioactive source, was positioned on the top of the chamber to generate the primary ionization. Three regions of the chamber can be distinguished. Between the cathode and the top GEM is the drift region, characterized by a low electric field, which drifts the ionization electrons to the first GEM. The first GEM is typically operated at a low gain ~ 10. The transfer field is between the two GEMs: it has a high electric field, which is required to have a good suppression of ion back-flow from the top GEM. In all voltage configurations, the mid GEM was always operated at gain < 1. Finally the induction field, between the mid GEM and the Micromegas, has again a low field to suppress the ion back-flow from the Micromegas.

Measurement Procedure

Energy resolution measurement A ^{55}Fe source, providing x-rays with $E =$ 5.9 keV and with radioactivity strength $\sim 14\,\mu$Ci, was used for this measurement. The electric signal induced on the readout anode of the Micromegas was collected by a pre-amplifier, then passed to an amplifier and finally to a standard ADC with 1024 digital channels. The ADC was connected via USB to a Windows personal computer running a Java program (provided by the ADC manufacturer). The calibration of the electronics chain was performed by connecting the pre-amplifier to a known capacitor in order to inject fixed charges. The ^{55}Fe energy spectrum was recorded and later analyzed to extract the gas amplification factor and the resolution. Figure 6.4 shows an example of an energy spectrum obtained with such a configuration. Three peaks are visible, corresponding to a primary ionization starting in one of the three regions separated by the gain elements. The first peak corresponds to an ionization originated between the two GEMs: as mentioned earlier, the mid GEM is operated

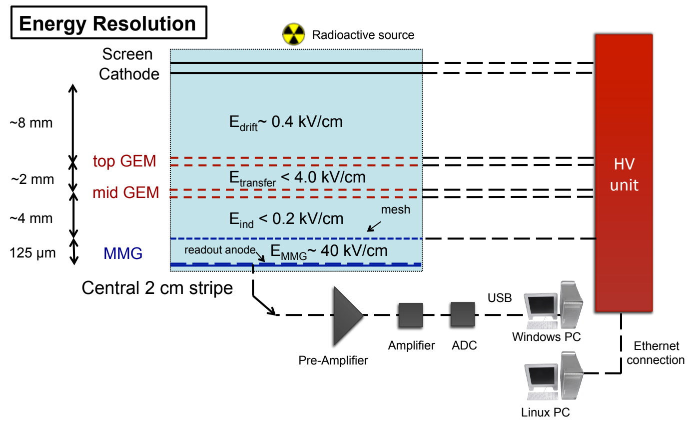

(a) Energy resolution measurement setup

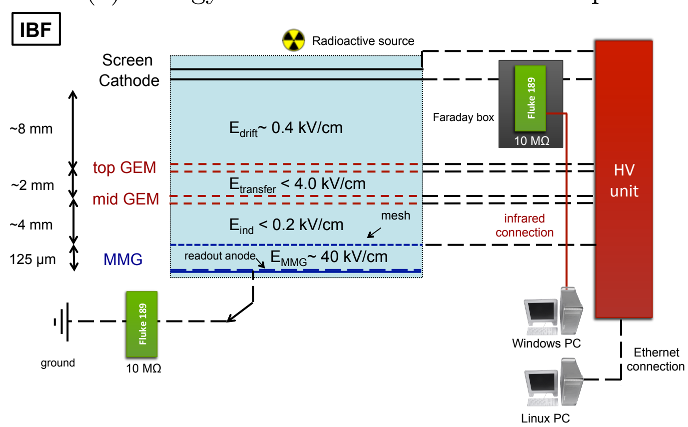

(b) IBF measurement setup

Figure 6.3: Experimental setup for a chamber with two stacked GEM foils and one MMG. The listed electric fields are the nominal values.

at a gain smaller than one. The second peak corresponds to an ionization starting just above the Micromegas. The third and main peak originates from the ionization that started between the cathode and the top GEM. The main peak was fit with a Gaussian function. The σ of the Gaussian divided by the mean was used to determine the energy resolution. The uncertainty on the energy resolution measurement was estimated to be $3-5\%$, mainly due to the choice of the fitting range.

IBF measurement A stronger radioactive source made of ^{90}Sr was used in this case. It provided β particles with $E_\beta \approx 0.5$ MeV with a rate of 2 mCi. This measurement is more delicate, since the IBF signal is small and must be collected from the

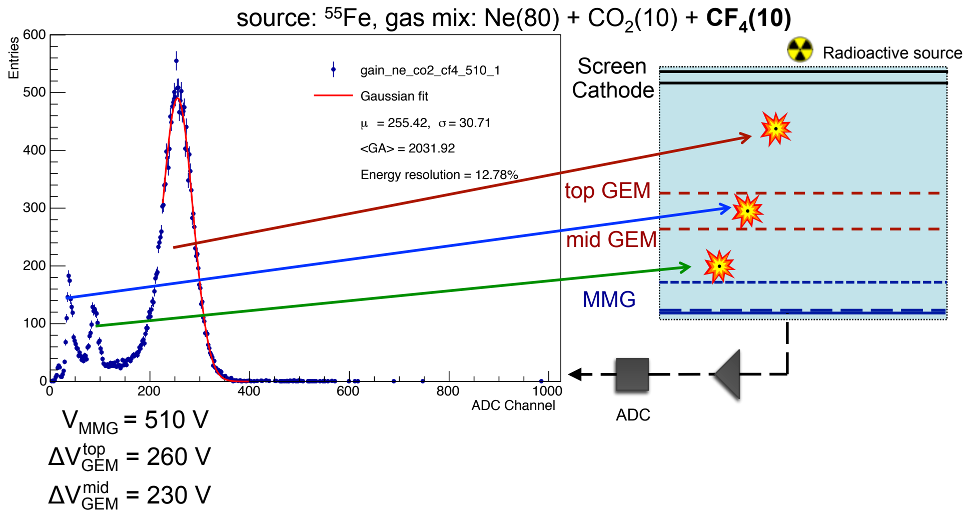

Figure 6.4: An example of the ^{55}Fe spectra showing the correspondence between the location of an X-ray absorption and each peak.

cathode that is at a high potential. The anode was connected to a Fluke 189 multimeter set with a high resistance (10 MΩ) and grounded. The cathode was connected to another Fluke 189 multimeter placed in a Faraday box. To avoid electrical interference, this multimeter was read through an infrared signal connected to a personal computer. The IBF fraction was obtained dividing the current $I_{cathode}$ measured in the cathode by the current I_{anode} measured in the anode. The overall gas amplification was estimated from the value of I_{anode}.

Results and Discussion

E-field scans First the values of the electric fields in the three regions of the chamber (drift, transfer, induction) were scanned. The scan of the drift electric field E_{drift} is shown in Fig. 6.5. Gas amplification and energy resolution are largely unaffected by changes in the drift field. The IBF scales approximately linearly with E_{drift}, because a higher drift field increases the ion extraction efficiency from the top GEM. Therefore E_{drift} should be kept as low as possible. However, TPCs are generally operated at E_{drift} = 0.4 kV/cm to have a good electron drift time, so this value was

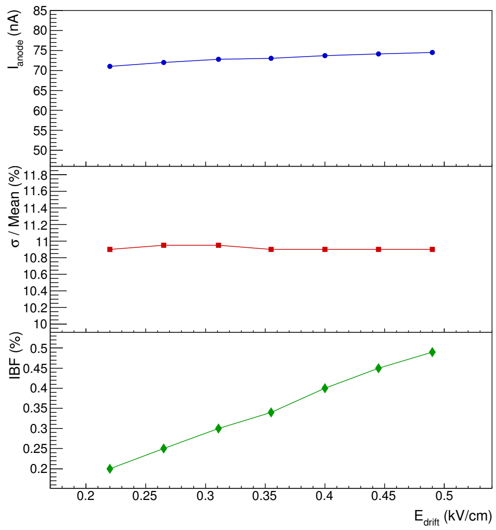

Figure 6.5: Scan of E_{drift}, $V_{MMG} = 400$ V, $\Delta V_{GEM}^{top} = 242$ V, $\Delta V_{GEM}^{mid} = 185$ V, $E_{transfer} = 2.0$ kV/cm, $E_{ind} = 0.075$ kV/cm. Gain is ≈ 2100 (corresponding to $I_{anode} \approx 74$ nA).

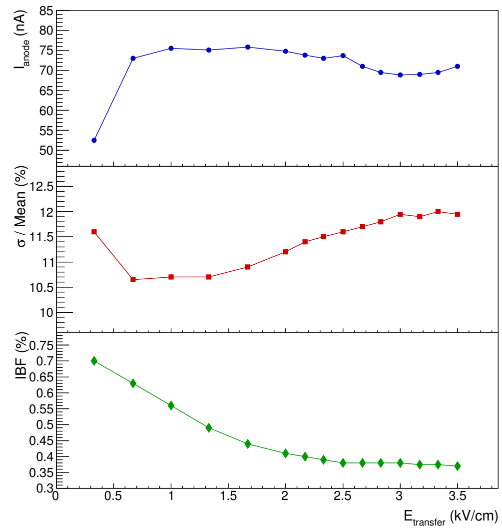

Figure 6.6: Scan of $E_{transfer}$, $V_{MMG} = 400$ V, $\Delta V_{GEM}^{top} = 242$ V, $\Delta V_{GEM}^{mid} = 185$ V, $E_{drift} = 0.4$ kV/cm, $E_{ind} = 0.075$ kV/cm.

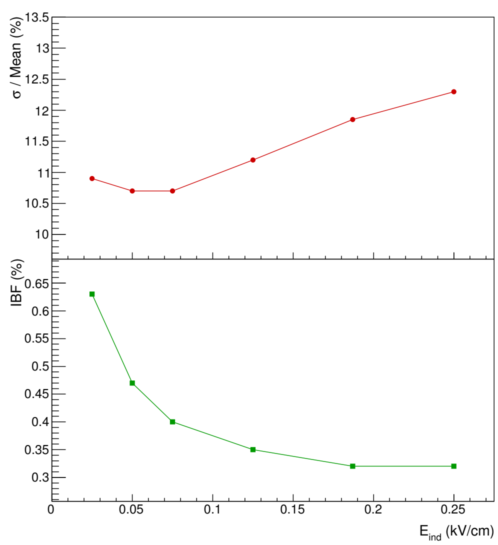

Figure 6.7: Scan of E_{ind}, $V_{MMG} = 400$ V, $E_{drift} = 0.4$ kV/cm, $E_{transfer} = 2.0$ kV/cm. ΔV_{GEM}^{top} and ΔV_{GEM}^{mid} are tuned to keep the overall gain ≈ 2000.

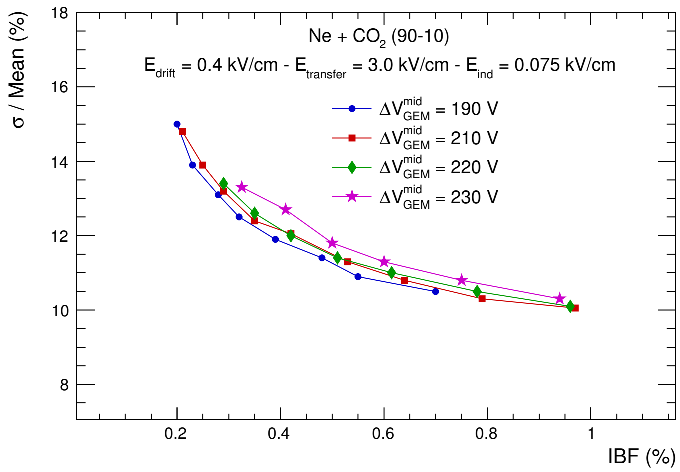

Figure 6.8: Energy resolution vs. IBF, varying V_{MMG} and $\Delta V^{\text{top}}_{\text{GEM}}$ for several fixed values of $\Delta V^{\text{mid}}_{\text{GEM}}$.

kept for all subsequent measurements. Figure 6.6 shows the measurement of $\mathrm{I}_{\text{anode}}$, energy resolution and IBF as a function of the transfer electric field $\mathrm{E}_{\text{transfer}}$. Above a certain threshold $\mathrm{E}_{\text{transfer}} \gtrapprox 0.5$ kV/cm, the gain is approximately constant, since all electrons are efficiently transported from the top GEM to the mid GEM. The IBF fraction decreases while the energy resolution becomes only slightly worse with increasing $\mathrm{E}_{\text{transfer}}$. The reduction of the IBF is due to the more efficient collection of ions from the top GEM when $\mathrm{E}_{\text{transfer}}$ is larger. Therefore a $\mathrm{E}_{\text{transfer}} \approx 3$ kV/cm is desirable to suppress IBF. Larger values are not preferred because avalanches may initiate in the transfer gap. Finally a scan of the induction field E_{ind} was performed, shown in Fig. 6.7. In this case, the gain was kept approximately constant at 2000 by tuning the voltages of the two GEMs. IBF decreases with increasing E_{ind}; however at the same time the energy resolution gets worse. Therefore a compromise choice of $\mathrm{E}_{\text{ind}} = 0.075$ kV/cm was made for the subsequent measurements.

Voltages of the amplification elements The voltages of the three gain elements, $\Delta\mathrm{V}^{\text{top}}_{\text{GEM}}$, $\Delta\mathrm{V}^{\text{mid}}_{\text{GEM}}$ and V_{MMG} were scanned in the following way. $\Delta\mathrm{V}^{\text{mid}}_{\text{GEM}}$ was kept fixed to a certain value, $\Delta\mathrm{V}^{\text{top}}_{\text{GEM}}$ was varied and V_{MMG} was tuned accordingly to keep the overall gain at about 2000. Then a different value of $\Delta V_{\mathrm{GEM}}^{\mathrm{mid}}$ and the scan was repeated. The results are reported in Fig. 6.8 in the resolution vs. IBF plane. The datasets corresponding to different values of $\Delta V_{\mathrm{GEM}}^{\mathrm{mid}}$ are reported as separate curves with different symbols. We observe an ordering as a function of $\Delta V_{\mathrm{GEM}}^{\mathrm{mid}}$, with the best performance obtained for the lowest value of $\Delta V_{\mathrm{GEM}}^{\mathrm{mid}} = 190$ V. An IBF of about 0.4% with energy resolution of about 12% is obtained setting $V_{\mathrm{MMG}} = 390$ V and $\Delta V_{\mathrm{GEM}}^{\mathrm{top}} = 225$ V. This result is in line with the ALICE TPC requirements and implies a slightly lower IBF compared to the 4-GEM setup.

Summary In conclusion, this study proved that a stack of two GEMs and a Micromegas is a suitable choice for a readout chamber of a gas drift detector, such as a TPC. Good energy resolution with low IBF can be achieved with a tuned combination of voltages and with a standard gas mixture used in conventional TPCs. However, additional tests were needed to prove that this solution was adequate for the ALICE TPC, especially regarding the discharge rate. A preliminary test at the CERN SPS facility showed discharge rates larger by $2-3$ order of magnitudes compared to the 4-GEM solution. Micromegas are more robust and they could support discharges without substantial damage. However, the discharges would temporarily make the detector unresponsive and thus increase the dead-time. Considering the timeline of the upgrade and the necessity to start the production phase in a timely fashion, the ALICE Collaboration decided to proceed with the 4-GEM solution, which appeared to be in a more mature status.

Conclusions

Jet and heavy-flavor production is a prominent aspect of the phenomenology of high-energy hadron colliders. Their fundamental origin, as the result of a high-momentum parton-parton scattering, is well understood in the framework of the perturbative expansion of QCD. This aspect makes them excellent calibrated probes for investigating the transport properties of the QGP. However, their emerging properties that come from the hadronization and fragmentation are much less under control, even in the simpler environment of a pp collision. Much work, both from the experimental and theoretical sides, is required to unravel the details of how confinement works.

This thesis presented the first analysis of charm jets tagged with D^0 mesons in ALICE. The measurement was compared with Monte Carlo event generators and with pQCD NLO calculations, showing that we understand the general features of charm jet production. The absolute cross section and some details of the fragmentation are not fully caught by the models, indicating that more refined calculations based on QCD are needed. However, the limited precision of the present measurement also calls for new data. In fact, this measurement uses a novel technique, which has now become the starting point for similar analyses performed by the ALICE Collaboration in other collision systems. Preliminary results of D^0-meson tagged jets in p–Pb and Pb–Pb collisions have been presented by ALICE at conferences, and more are underway. The plan is to measure the p_{T} spectra and fragmentation function of D-meson tagged jets in all collision systems available to ALICE from the Run-2 data:

pp at $\sqrt{s} = 5.02$ and 13 TeV, p–Pb and Pb–Pb at $\sqrt{s_{\rm NN}} = 5.02$ TeV. The inclusion of the electromagnetic calorimeter in the analysis will provide a worthwhile opportunity to measure the low-$z_{||}$ fragmentation of D mesons in intermediate- and high-$p_{\rm T}$ jets, a kinematic regime where ALICE may have an important advantage relative to its competitor experiments at the LHC. This kind of measurement is crucial to constrain some of the non-perturbative aspects of high-energy pp collisions, such as the gluon PDF and the gluon-to-D fragmentation.

Jet quenching still has many questions that remain answered. The nature of the in-medium parton energy loss is still part of a debate between different theoretical approaches. The dynamics through which the energy is transferred from the fast parton to the medium are unclear, as well as how this process modifies the internal substructure of the jets measured through the observed final state. The measurement of jet suppression in Pb–Pb collisions presented in this thesis was published in 2015. It shows that colored partons lose a significant fraction of their energy, contrary to what happens to electromagnetic probes that follow the expected scaling with the number of binary collisions. The absence of such effects in p–Pb collisions provides a strong indication that the suppression is due to the hot and dense medium, which was observed also through observables that tell us about its bulk hydrodynamical properties. Since then, significant progress has been made. The interest has shifted towards the study of the internal substructure as well as heavy-flavor jets.

Looking ahead, with the LHC Run-3 and Run-4, ALICE and the other LHC experiments will have the unique opportunity to study the QGP with unprecedented statistical precision. The ALICE upgrades are well aimed at this goal and have very good chances of making definitive progress. The measurement of jets, and particularly heavy-flavor jets, will be among the priorities of ALICE during Run-3 and beyond. In the meantime, the field is also looking at other opportunities that must be explored. In the US, the electron-ion collider project is taking shape; it will investigate the internal structure of the nucleus via Deep-Inelastic Scattering (DIS), at an energy and luminosity never reached before. These measurements will close the gap providing crucial information about the initial state of the collisions studied at hadron colliders, which up to now have to rely on extrapolations from lower energies. In Europe and in Japan, there are projects of hadron colliders at lower center-of-mass energies but higher intensities, called FAIR and J-PARC-HI, respectively. These experiments will try to investigate the nature of the QGP formed at intermediate temperature and finite baryon chemical potential, and possibly also look for a critical point of the phase transition.

In summary, the field of high-energy nuclear physics has a lot of potential to unravel fundamental properties of nature. The years to come promise to be at least as exciting as the present time.

Appendix A

Jet Finding Algorithms

In the very early jet measurements, very simple jet finding "algorithms" were adopted. Global properties of the collision event were investigated to determine how "jet-like" it was. One of the first experimental observations of jets was reported in 1975 [215]. Jet-like events were identified in hadron production by e^+e^- annihilation at energies between 3 and 7.4 GeV in the center of mass. In this pioneering measurement the jet finder consisted in the calculation of the three eigenvalues λ_1, λ_2 and λ_3 of the tensor:

$$T^{\alpha\beta} = \sum_i (\delta^{\alpha\beta}\vec{p}_i^{\,2} - p_i^\alpha p_i^\beta), \tag{A.1}$$

where $\vec{p}_i$ is the momentum of the ith particle and α, β refer to the three spatial coordinates. The smallest eigenvalue λ_3 is the minimum sum of squares of transverse momenta with respect to the direction defined by the eigenvector associated with it. This eigenvector was also defined to be the reconstructed jet axis. In order to determine how jet-like an event is, the sphericity was defined as:

$$S = \frac{3\lambda_3}{\lambda_1 + \lambda_2 + \lambda_3} = \frac{3(\sum_i p_{\perp i}^2)_{\min}}{2\sum_i \vec{p}_i^{\,2}}, \tag{A.2}$$

where $p_{\perp i}$ is the transverse momentum of the ith particle. The distribution of the S variable was found to be compatible with the "jet model" and falsified the competitor model which predicted a more isotropic particle production.

In the last four decades, thanks to the availability of ever faster computing facilities, more complex jet finding algorithms have been developed and used. Jet measurements progressed considerably contributing to our understanding of hadron production and properties of QCD.

Insofar as jet finding is an approximate attempt to invert the QCD processes of parton fragmentation and hadronization, it is not a uniquely defined procedure. In the following some of the most common jet finding algorithms are reviewed.

A.1 Jet Cone Algorithms

Early jet cone finders developed for e^+e^- collisions identified energy flow into cones spanning the space in pseudorapidity (η) and azimuth (ϕ) [216]. An iterative approach was typically employed, with criteria for merging and splitting cones. In these algorithms, directions of dominant energy flow are identified starting from "seeds" that typically coincide with some – or all – of the particles in the event. Then for each seed a list of particles in the trial cone is compiled and the sum of their 4-momenta is evaluated. The resulting 4-momentum is used as a new trial direction for the cone. This procedure is iterated until the cone direction no longer changes, i.e. until one has a "stable cone".

A.2 Infrared and Collinear Safety

Jet finding algorithms can be characterized according to the following two properties:

Infrared Safety Adding a particle of very small momentum (compared to the average momentum) does not change the outcome of the jet finding algorithm.

Collinear Safety A collinear splitting of a particle does not change the outcome of the jet finding algorithm.

The importance of these properties is related to the theoretical framework used to calculate jet production in perturbative QCD (pQCD). Both collinear splittings and low-energy gluon emissions are divergent processes in QCD. They must be cured in the perturbative expansion using renormalization techniques, ultimately suppressing them. Therefore for a meaningful comparison between experimental results and pQCD calculations it is necessary that jet finding algorithms are insensitive to the occurrence of these processes. A jet finding algorithm abiding to these properties is called IRC-safe.

Traditional iterative cone algorithms lack these two important properties. In fact, if all particles are used as seeds for the jet finding, then the addition of a particle of any momentum will add a new seed and potentially change the final outcome. On the other hand, if a low-energy cut off is applied for the seeds, a collinear splitting may bring a particle below the cut off and remove a seed, again potentially changing the final outcome. Many workarounds have been proposed in order to partially cure this problem [217, 218]. *Seedless* cone jet algorithms, which usually come with a non-iterative approach, like that used in [218], have been shown to be fully IRC-safe. Unfortunately, these algorithms are very computationally expensive and their use in large multiplicity events, such as those produced at the LHC, is prohibitive. A more recent and faster seedless cone algorithm, called SISCONE was proposed in [219].

A.3 Sequential Recombination Algorithms

One of the first collaborations to develop and use a sequential recombination algorithm to reconstruct jets was the JADE Collaboration [220] at DESY in the late eighties. More recently, several variants of the original JADE algorithm were developed: Cambridge/Aachen [221], k_{T} [222] and anti-k_{T} [142]. These jet algorithms are less intuitive, since they do not rely on an immediate "geometric" visualization; however they have the advantage of being IRC-safe without any ad-hoc "correction". In addition, modern and fast implementations have been made available recently, contributing to their success and use in practically all jet measurements since about a decade.

A sequential recombination algorithm is based on the definition of a measure:

$$d_{ij} = \min\left(k_{\mathrm{T},i}^{2p}, k_{\mathrm{T},j}^{2p}\right)\frac{\Delta_{ij}^2}{R^2} \tag{A.3a}$$

$$d_{i\mathrm{B}} = k_{\mathrm{T}i}^{2p}, \tag{A.3b}$$

where $k_{\mathrm{T}i}$, η_i and ϕ_i are, respectively, the transverse momentum, pseudo-rapidity and azimuth of particle i and

$$\Delta_{ij}^2 = (\eta_i - \eta_j)^2 + (\phi_i - \phi_j)^2. \tag{A.4}$$

R is the resolution parameter and defines the dimensional scale of the jets. It plays a role similar to the radius in the jet cone algorithms. The integer parameter p can be changed to obtain different variants of the algorithm.

The algorithm proceeds as follows. All distances between each pair of particles are calculated according to the measure defined in A.3a; in addition the distances between each particle and the beam direction are calculated according to A.3b. If the smallest of such distances is of type A.3a, then particles i and j are grouped into a "pseudo-jet". Then all the distances are recomputed and the procedure is iterated. Conversely, if the smallest distance is of type A.3b the ith pseudo-jet is removed from the set and declared a jet. Again the procedure is iterated until there are at least two pseudo-jets.

Until recent times successive recombination algorithms were not common because they were too computationally expensive. In the first implementations the execution time grew as $\mathcal{O}(N^3)$, where N is the number of particles. The computational time per event for a modern CPU (3 GHz) would be ~ 10 s at the Tevatron and $\sim 10^5$ s at the LHC. More recently [148], faster implementations have been developed with a considerably decreased execution time, making them affordable for most situations.

A.3.1 The Cambridge/Aachen Algorithm

The Cambridge/Aachen algorithm sets $p = 0$ in Eq. A.3:

$$d_{ij} = \frac{\Delta_{ij}^2}{R^2} \tag{A.5a}$$

$$d_{i\mathrm{B}} = 1. \tag{A.5b}$$

The algorithm becomes purely geometric since the p_{T} of the particles does not enter in the measure definition. The clustering starts from the nearest pair of particles and keeps clustering pseudo-jets together until they are separated by a distance larger than the radius R. It must be noted that since the distance is computed between pseudo-jets, and not between particles, jet shapes can be rather irregular, as particles that are farther away than R may end up in the same jet, if there is a continuous "path" of particles between them.

A.3.2 The k_{T} and anti-k_{T} Algorithms

The k_{T} algorithm sets $p = 1$:

$$d_{ij} = \min\left(k_{\mathrm{T},i}^2, k_{\mathrm{T},j}^2\right) \frac{\Delta_{ij}^2}{R^2} \tag{A.6a}$$

$$d_{i\mathrm{B}} = k_{\mathrm{T}i}^2. \tag{A.6b}$$

Similar to the Cambridge/Aachen algorithm, pairs of pseudo-jets are clustered together when their distance is smaller than R. However soft particles take precedence in the clustering. The shape of the resulting jets in the η, ϕ plane can be even more irregular than in the Cambridge/Aachen algorithm. It has been shown that this algorithm mimics more closely a path backwards through the QCD branching sequence, which means that reconstructed jets are more likely to collect most of the particles radiated from an original hard parton. For this reason it has been widely used to reconstruct jets produced in e^+e^- annihilations. However, the k_T algorithm is not a good choice when dealing with a noisy environment, such as that produced at hadron colliders. In a single hadron-hadron collision multiple parton-parton scatterings can occur; most of them will generate soft particles that constitute the so-called underlying event (UE). Occasionally, in a parton-parton scattering a large momentum transfer occurs, leading to jet formation. Since the k_T algorithm favors clustering of low-p_T particles first, it is clear that the presence of many uncorrelated soft particles can hinder its use in such situations. Moreover, the high luminosity achieved at the LHC has increased significantly the amount of pile-up (multiple proton-proton collisions occurring in the same event), making the environment even more noisy. The situations is much more extreme in ultra-relativistic heavy-ion collisions, where more than a thousand nucleon-nucleon collisions can occur simultaneously in a single event, generating a huge UE made of largely soft particles.

The anti-k_T algorithm sets $p = -1$:

$$d_{ij} = \min\left(\frac{1}{k_{\mathrm{T},i}^2}, \frac{1}{k_{\mathrm{T},j}^2}\right)\frac{\Delta_{ij}^2}{R^2} \tag{A.7a}$$

$$d_{i\mathrm{B}} = \frac{1}{k_{\mathrm{T}i}^2}. \tag{A.7b}$$

Contrary to the k_T algorithm, the anti-k_T algorithms favors clustering of high-p_T particles first. Then soft particles are "eaten" by high p_T pseudo-jets until they reach a certain size, which is determined by R. Jet contours tend to be more regular compared to the Cambridge/Aachen and the k_{T} algorithms, and are typically centered around high-p_{T} particles. In a way this algorithm can be described as "soft-resilient". This property is particularly important in the heavy-ion environment, where the soft particle component coming from the underlying event is dominant. For this reason the anti-k_{T} algorithm is used in almost all jet measurements performed by LHC and RHIC experiments.

A.3.3 Jet area definition

The jet area is not a trivially defined concept, especially when dealing with successive recombination algorithms. In [223] the following two different definitions of area were given:

Active area A uniform background of extremely soft massless "ghost" particles is added to the event. Ghost particles participate in the clustering together with the reconstructed particles. The area of a given jet is proportional to the number of ghosts it contains. Because the ghosts are extremely soft, the presence of the ghosts does not affect the clustering itself, provided that the algorithm is IR-safe.

Passive area A single randomly placed ghost at a time is included in the event. The procedure is repeated many times: the passive area of a jet is then proportional to the probability that a ghost is included in it.

Other alternatives exist, such as the Voronoi method, which are not described here.

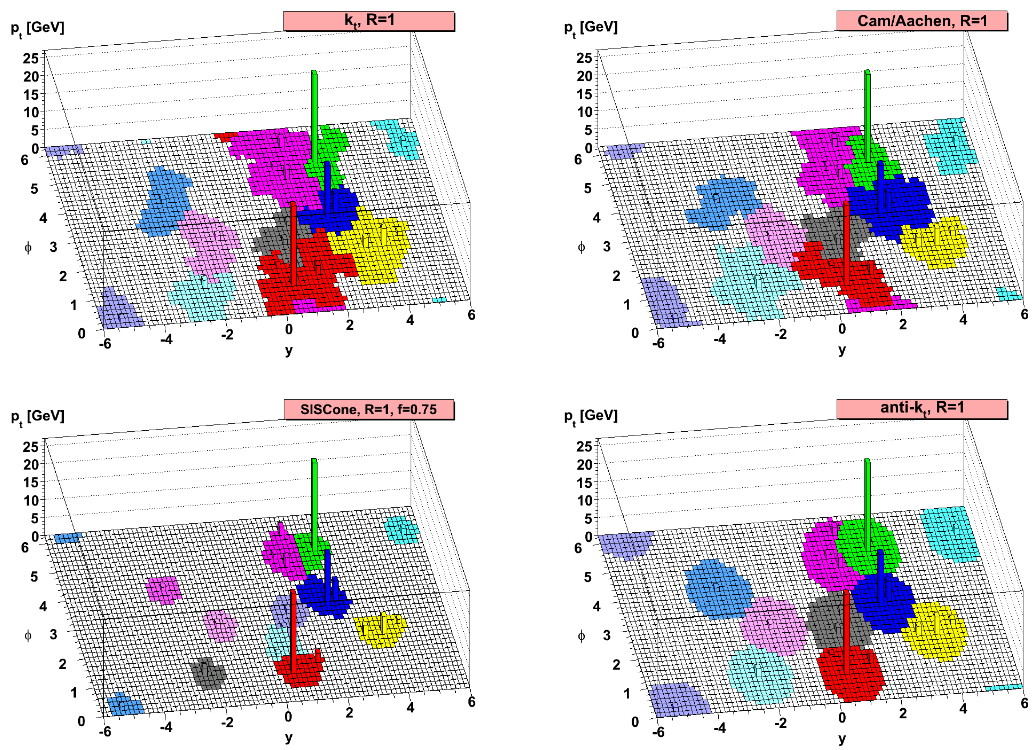

Figure A.1: A sample parton-level event, together with many random soft "ghosts", clustered with four different jet finding algorithms, illustrating the "active" catchment areas of the resulting hard jets [142]. Different colors correspond to different reconstructed jets.

A.4 Jet Finder Comparison

Figure A.1 shows four event displays of the same parton-level simulated event, clustered with different jet finder algorithms. The active area is determined through the "ghost" particle method. Note the very irregular shapes of the Cambridge/Aachen and k_{T} jets. Though the algorithms are very different, SISCone and anti-k_{T} jet collections are rather similar. The main difference is in the way they deal with overlapping jets, which can be appreciated looking at the purple and green jets: SISCone divides the jet geometrically in two halves, while anti-k_{T} makes a roundish jet around the highest particle and the rest goes into an irregular jet.

Appendix B

Unfolding Details of the $\mathbf{D^0}$-Meson $z_{||}^{\mathrm{ch}}$ Distribution

Figures B.1 and B.2 show the measured, unfolded and refolded distributions for the low and high $p_{\mathrm{T,jet}}^{\mathrm{ch}}$ ranges, respectively.

The Pearson correlation coefficients of the unfolded $z_{||}^{\mathrm{ch}}$ distributions are shown in Fig. B.3. We observe features similar to those discussed for the unfolded $p_{\mathrm{T,jet}}^{\mathrm{ch}}$ distribution.

Figure B.4 compares the unfolded results obtained starting from four different priors: Pythia 6 distribution, harder fragmentation, softer fragmentation, flat (see Fig. 3.39). No significant difference in the results is observed.

Figure B.5 shows how the unfolded spectrum evolves with increasing number of iterations. Also in this case, the procedure converges very fast: after three iterations the change in the unfolded results with any successive iteration is $< 1\%$.

Figure B.6 compares the baseline unfolded result (obtained using the Bayesian iterative approach) with the regularized SVD method and the bin-by-bin correction method. The three methods agree well with each other within statistical uncertainties.

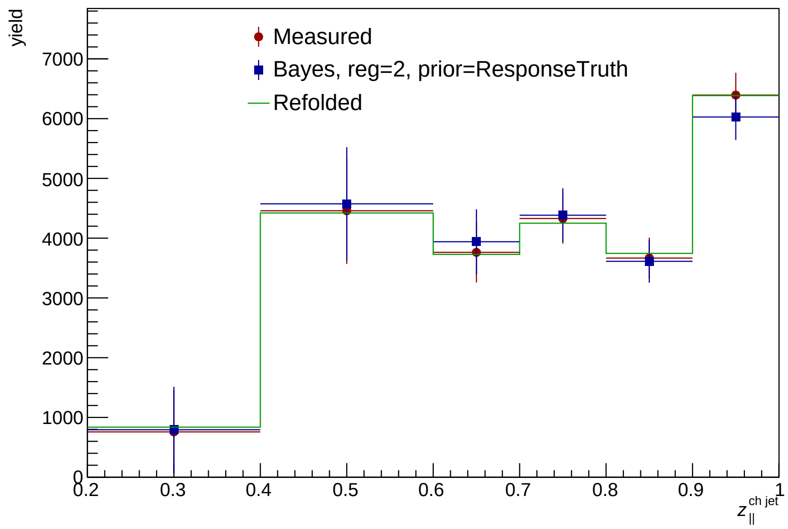

(a) Yield

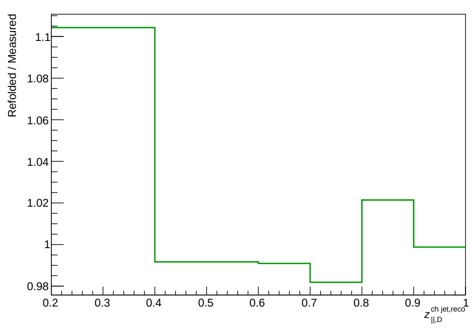

(b) Ratio Refolded / Measured

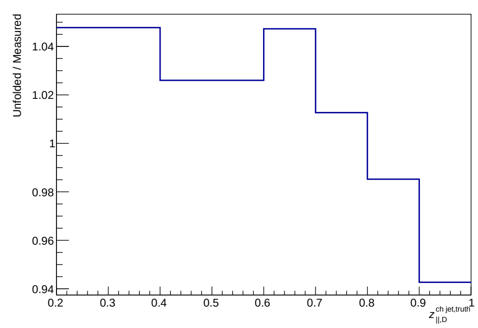

(c) Ratio Unfolded / Measured

Figure B.1: Top: measured D^0 momentum fraction distribution for $5 < p_{\mathrm{T,jet}}^{\mathrm{ch}} < 15$ GeV/c (red symbols), compared with the distribution unfolded using the Bayesian iterative method (blue symbols). The green line is the refolded distribution, which is obtained by applying the response matrix to the unfolded distribution. Bottom left: ratio between refolded and measured distributions. Bottom right: ratio between the unfolded and measured distributions.

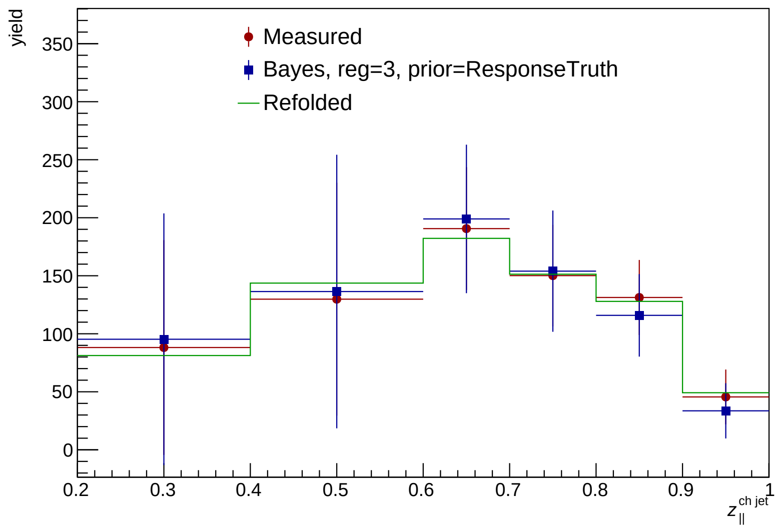

(a) Yield

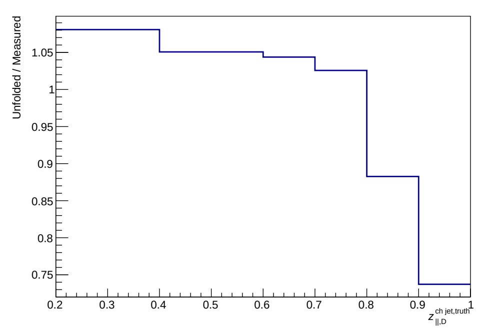

(b) Ratio Unfolded / Measured

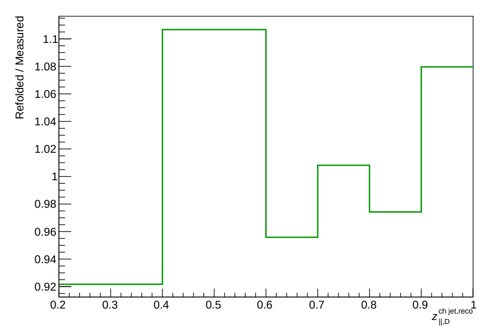

(c) Ratio Refolded / Measured

Figure B.2: Top: measured D^0 momentum fraction distribution for $15 < p_{\mathrm{T,jet}}^{\mathrm{ch}} < 30$ GeV/c (red symbols), compared with the distribution unfolded using the Bayesian iterative method (blue symbols). The green line is the refolded distribution, which is obtained by applying the response matrix to the unfolded distribution. Bottom left: ratio between refolded and measured distributions. Bottom right: ratio between the unfolded and measured distributions.

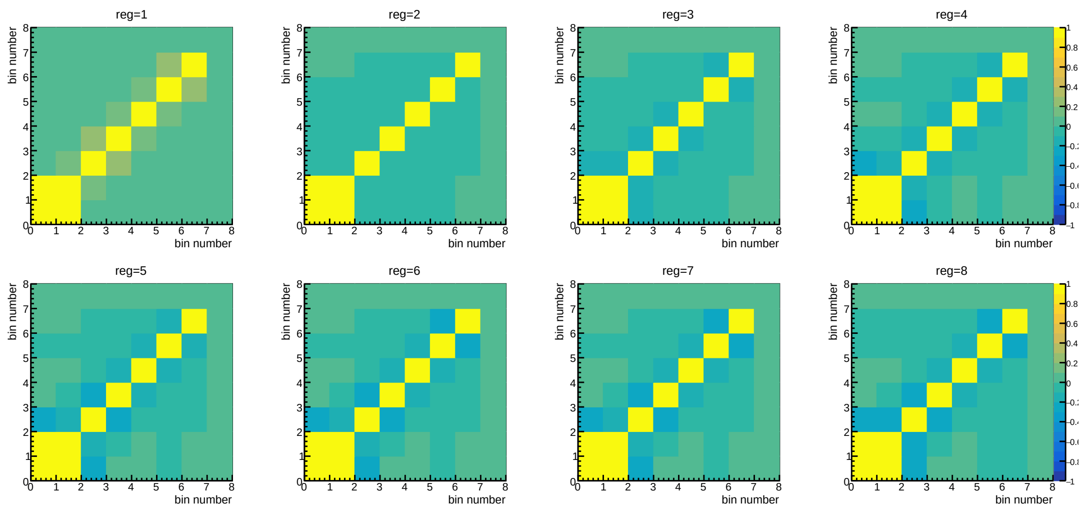

(a) $5 < p_{\mathrm{T,jet}}^{\mathrm{ch}} < 15$ GeV/c

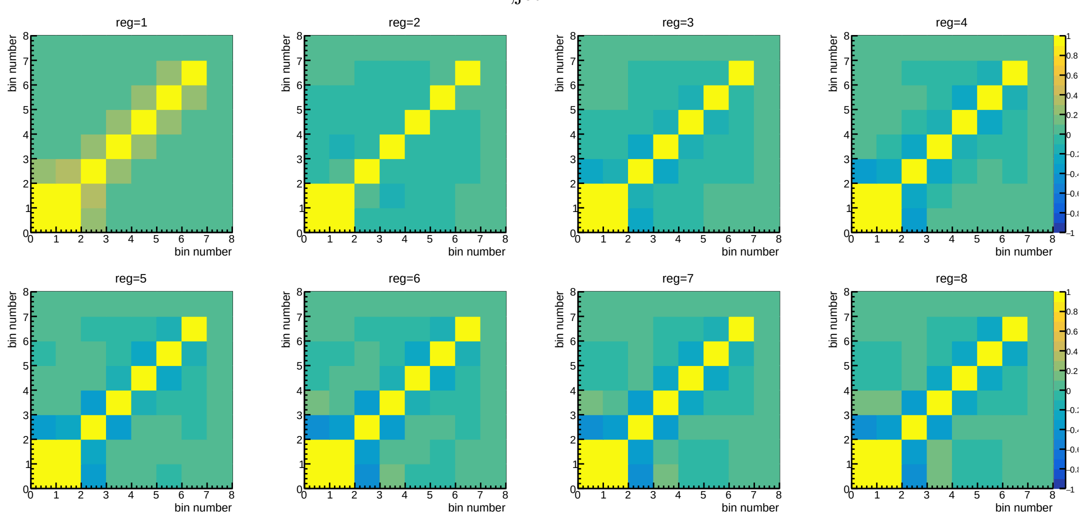

(b) $15 < p_{\mathrm{T,jet}}^{\mathrm{ch}} < 30$ GeV/c

Figure B.3: Pearson correlation coefficients obtained from the unfolding of the $z_{||}^{\mathrm{ch}}$ distributions of D^0-meson tagged jets with the Bayesian iterative method for different numbers of iterations. Starting from top left to bottom right: from 1 to 8 iterations.

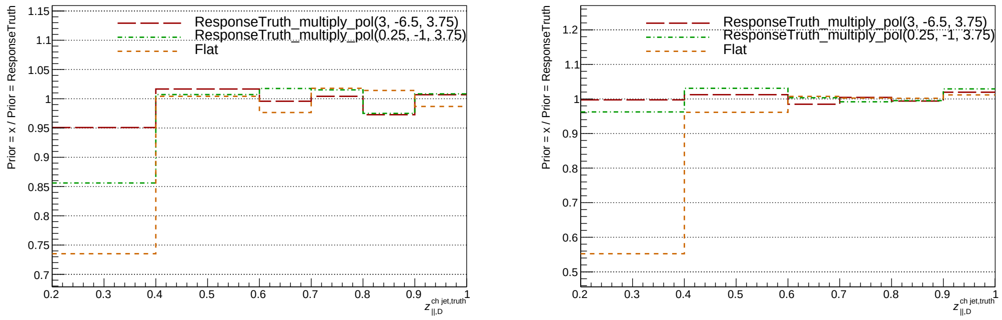

(a) $5 < p_{\mathrm{T,jet}}^{\mathrm{ch}} < 15$ GeV/c (b) $15 < p_{\mathrm{T,jet}}^{\mathrm{ch}} < 30$ GeV/c

Figure B.4: Ratios between the unfolded distributions obtained using different priors with the Bayesian iterative method: PYTHIA 6 distribution (blue), harder fragmentation (green), softer fragmentation (red), flat (orange).

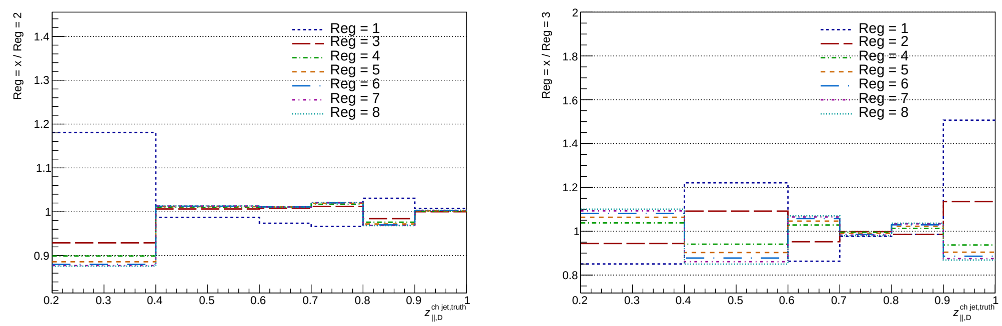

(a) $5 < p_{\mathrm{T,jet}}^{\mathrm{ch}} < 15$ GeV/c (b) $15 < p_{\mathrm{T,jet}}^{\mathrm{ch}} < 30$ GeV/c

Figure B.5: Ratios between the unfolded $z_{||}^{\mathrm{ch}}$ distributions obtained with different number of iterations of the Bayesian unfolding procedure.

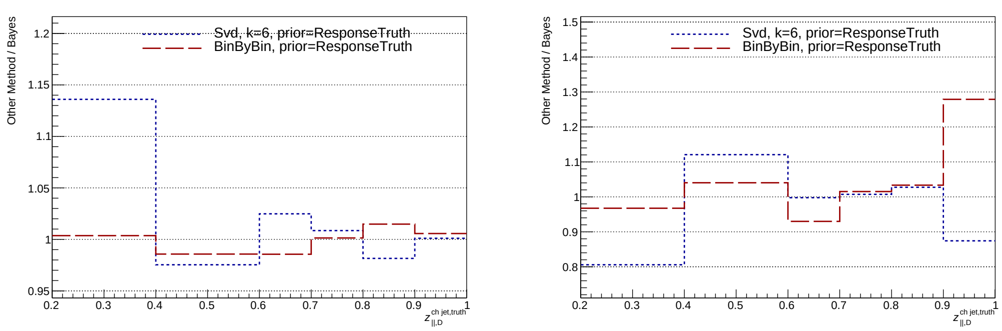

(a) $5 < p_{\mathrm{T,jet}}^{\mathrm{ch}} < 15$ GeV/c (b) $15 < p_{\mathrm{T,jet}}^{\mathrm{ch}} < 30$ GeV/c

Figure B.6: Ratios between the $z_{||}^{\mathrm{ch}}$ distributions obtained with different unfolding method. The baseline is obtained with the Bayesian iterative method.

Appendix C

Systematic Uncertainties for the Semi-Central Pb–Pb Collisions

In this Appendix a set of Figures are presented showing details of the estimation of the systematic uncertainties related to the measurement of the jet p_{T} spectrum in $10-30\%$ most central Pb–Pb collisions at $\sqrt{s_{\mathrm{NN}}} = 2.76$ TeV. At the end of the Appendix a summary with all the systematic uncertainties is presented. The description of the source of the systematic uncertainties and the methods used to estimate them is given in Section 4.6.

C.1 Correlated Uncertainties

Correlated uncertainties shift the entire jet spectrum in one direction. Figure C.1 shows the estimation of the uncertainty due to track-reconstruction efficiency. Figure C.2 shows the estimation of the uncertainty related to the EMCal clustering algorithm choice. The uncertainty due to the EMCal charged-particle correction (see Section 4.3.2) is addressed in Fig. C.3. The uncertainty related to the UE fluctuations (see Section 4.4.2) is shown in Fig. C.4. The effect of varying the limits on $p_{\mathrm{T,jet}}^{\mathrm{reco}}$ and $p_{\mathrm{T,jet}}^{\mathrm{truth}}$ are investigated in Fig. C.5 and C.6, respectively.

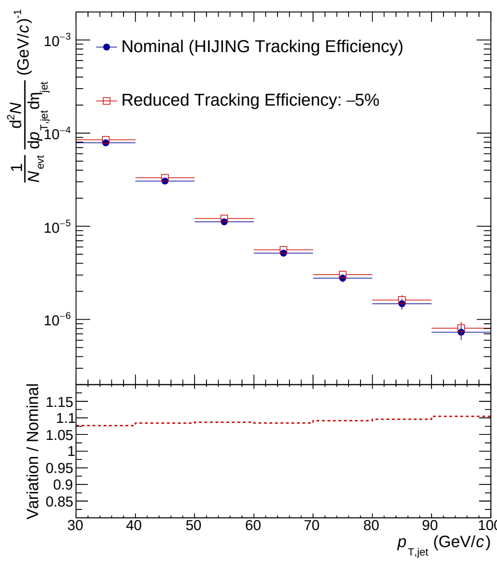

Figure C.1: Comparison of the jet p_{T} spectra in the $10-30\%$ most central Pb–Pb collisions unfolded with the nominal detector response matrix (blue solid circles) and with the matrix obtained with the reduced track-reconstruction efficiency (red open squares) for the estimation of the systematic uncertainty.

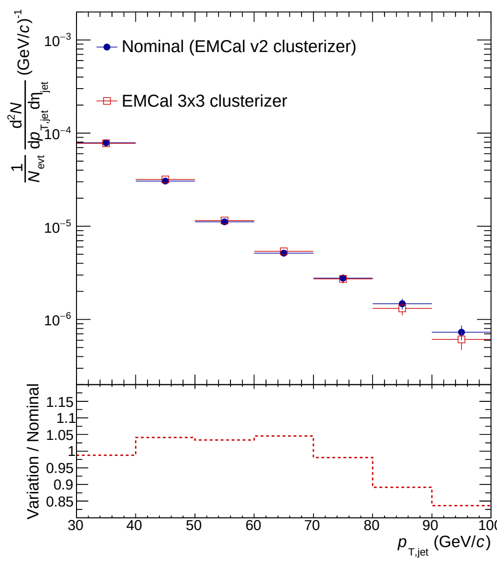

Figure C.2: Comparison of the jet p_{T} spectra in the $10-30\%$ most central Pb–Pb collisions obtained using the nominal EMCal clustering algorithm (blue solid circles) and using the 3×3 algorithm (red open squares) for the estimation of the systematic uncertainty.

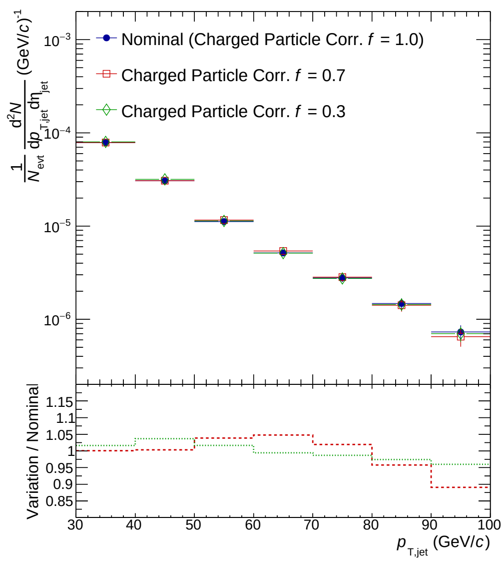

Figure C.3: Comparison of the jet p_{T} spectra in the $10-30\%$ most central Pb–Pb collisions obtained using different values of the charged-particle correction factor f (see Eq. 4.3) for the estimation of the systematic uncertainty.

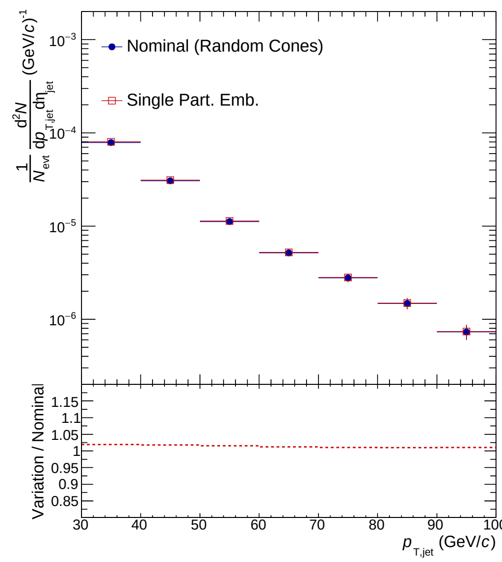

Figure C.4: Comparison of the jet p_{T} spectra in the $10-30\%$ most central Pb–Pb collisions unfolded using the UE fluctuations quantified with random cones (blue solid circles) and with single-particle embedding (red open squares) for the estimation of the systematic uncertainty.

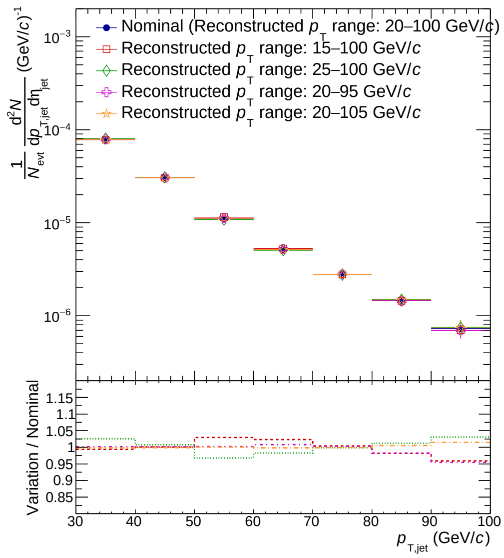

Figure C.5: Comparison of the jet p_{T} spectra in the $10-30\%$ most central Pb–Pb collisions unfolded using different limits for the reconstructed axis for the estimation of the systematic uncertainty.

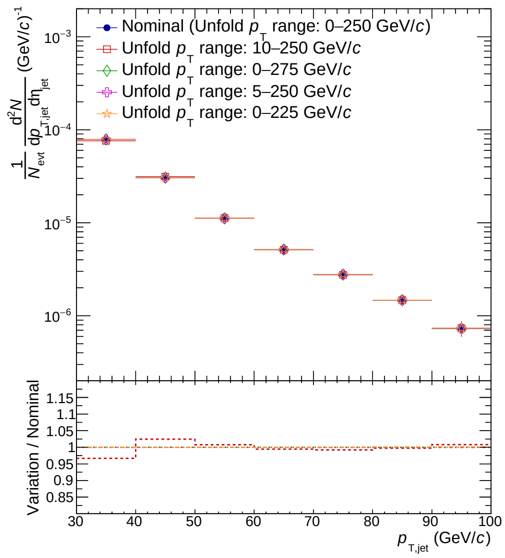

Figure C.6: Comparison of the jet p_{T} spectra in the $10-30\%$ most central Pb–Pb collisions unfolded using different limits for the unfolded axis for the estimation of the systematic uncertainty.

C.2 Shape Uncertainties

Figure C.7 show the variations of the unfolding parameters: unfolding regularization method, regularization parameter, prior choice.

C.3 Summary of the Uncertainties

The summary of all the correlated and shape uncertainties for the $10-30\%$ jet p_{T} spectrum is presented in Table C.1.

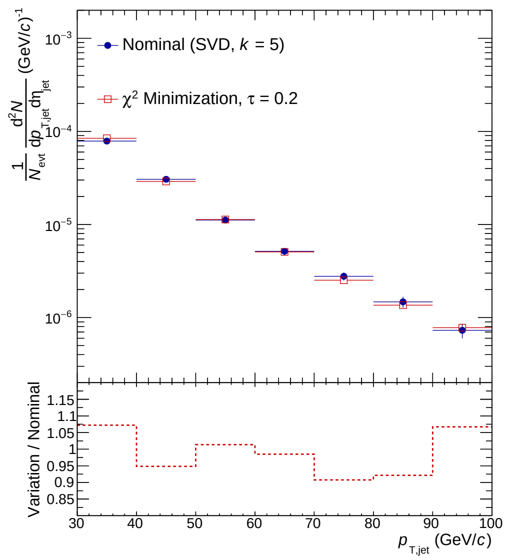

(a) Unfolding regularization method

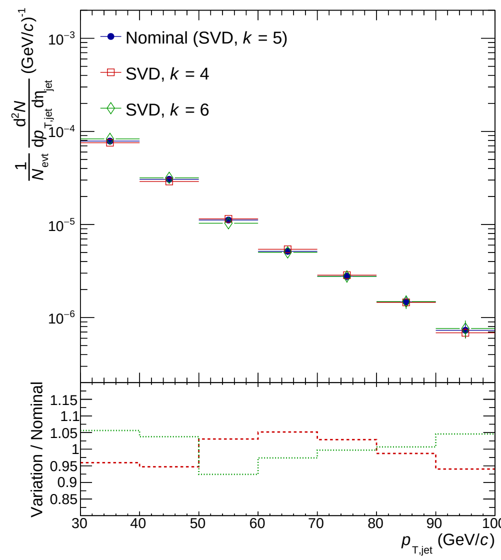

(b) SVD regularization parameter

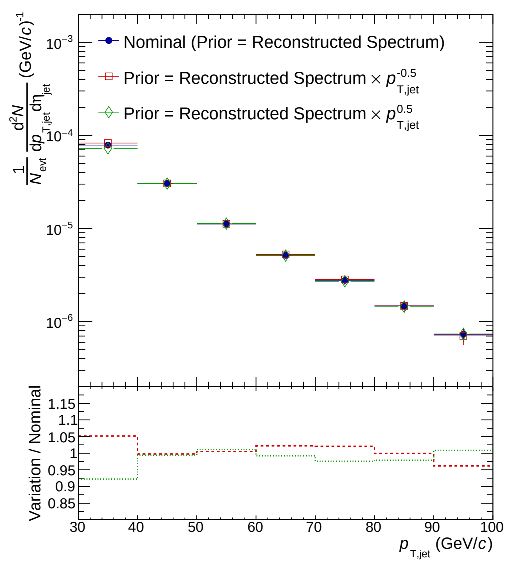

(c) Prior choice

Figure C.7: Comparison of the jet p_{T} spectra in the $10 - 30\%$ most central Pb–Pb collisions unfolded using different parameters of the unfolding procedure for the estimation of the systematic uncertainty.

Category	Relative uncertainty (%)				
	$p_{\mathrm{T,jet}}^{\mathrm{min}}$	$p_{\mathrm{T,jet}}^{\mathrm{max}}$	Min.	Max.	Avg.
Tracking efficiency	8.3	10.3	8.2	10.3	8.9
Track momentum resolution	1.0	1.0	1.0	1.0	1.0
Charged particle correction	2.0	1.8	1.8	4.4	2.8
EMCal clusterizer	1.5	4.5	0.6	4.6	3.3
EMCal resolution	4.4	4.4	4.4	4.4	4.4
Background fluctuations	2.0	1.0	1.0	2.0	1.4
Jet raw p_{T} cuts	2.3	4.2	0.5	4.2	2.2
Combinatorial jets	3.4	0.8	0.3	3.4	1.3
Total correlated	10.8	13.0	10.7	13.0	11.6
Unfolding method	7.1	5.6	1.3	9.5	5.5
SVD reg. param. $k = 4$	3.7	6.4	1.5	6.4	4.0
SVD reg. param. $k = 6$	4.9	4.6	0.6	7.3	3.7
Prior choice 1	5.0	3.7	0.1	5.0	2.0
Prior choice 2	7.7	0.7	0.6	7.7	2.3
Total shape	5.9	4.6	3.1	5.9	4.2

Table C.1: Summary of systematic uncertainties for the $10-30\%$ jet p_{T} spectrum. The first column is the uncertainty at the minimum $p_{\mathrm{T,jet}}^{\mathrm{min}}$ of 30 GeV/c, the second column is the uncertainty at the maximum $p_{\mathrm{T,jet}}^{\mathrm{min}}$ of 100 GeV/c. The minimum and maximum columns gives the extreme, and the last column gives the average systematic uncertainty over the entire p_{T} range.

Bibliography

[1] URL: `https://en.wikipedia.org/wiki/Standard_Model`.

[2] **ATLAS Collaboration**, G. Aad et al. "Observation of a new particle in the search for the Standard Model Higgs boson with the ATLAS detector at the LHC". Phys. Lett. B 716 (2012) 1.

[3] **CMS Collaboration**, S. Chatrchyan et al. "Observation of a new boson at a mass of 125 GeV with the CMS experiment at the LHC". Phys. Lett. B 716 (2012) 30.

[4] S. Bethke. "Experimental tests of asymptotic freedom". Prog. Part. Nucl. Phys. 58 (2007) 351–386.

[5] J. C. Collins, D. E. Soper, and G. F. Sterman. "Factorization of Hard Processes in QCD". Adv. Ser. Direct. High Energy Phys. 5 (1989) 1–91.

[6] V. N. Gribov and L. N. Lipatov. "Deep inelastic e p scattering in perturbation theory". Sov. J. Nucl. Phys. 15 (1972) 438–450.

[7] Y. L. Dokshitzer. "Calculation of the Structure Functions for Deep Inelastic Scattering and e^+e^- Annihilation by Perturbation Theory in Quantum Chromodynamics.". Sov. Phys. JETP 46 (1977) 641–653.

[8] G. Altarelli and G. Parisi. "Asymptotic Freedom in Parton Language". Nucl. Phys. B 126 (1977) 298–318.

[9] M. Cacciari, M. Greco, and P. Nason. "The p_{T} spectrum in heavy-flavor hadroproduction". JHEP 05 (1998) 007.

[10] M. Cacciari, S. Frixione, and P. Nason. "The p_{T} spectrum in heavy-flavor photoproduction". JHEP 03 (2001) 006.

[11] M. Cacciari et al. "Theoretical predictions for charm and bottom production at the LHC". JHEP 2012 (2012) 1–24.

[12] B. A. Kniehl et al. "Inclusive charmed-meson production at the CERN LHC". The European Physical Journal C 72 (2012) 1–10.

[13] S. Frixione, P. Nason, and G. Ridolfi. "Differential distributions for heavy flavor production at HERA". Nucl. Phys. B 454 (1995) 3–24.

[14] B. A. Kniehl and G. Kramer. "D^0, D^+, $\mathrm{D}_{\mathrm{s}}^+$, and Λ_{c}^+ fragmentation functions from CERN LEP1". Phys. Rev. D71 (2005) 094013.

[15] R. Hagedorn. "Statistical thermodynamics of strong interactions at high-energies". Nuovo Cim. Suppl. 3 (1965) 147–186. URL: `https://cds.cern.ch/record/346206`.

[16] R. Hagedorn. "Hadronic matter near the boiling point". Nuovo Cim. A56 (1968) 1027–1057.

[17] J. C. Collins and M. J. Perry. "Superdense Matter: Neutrons Or Asymptotically Free Quarks?". Phys. Rev. Lett. 34 (1975) 1353.

[18] S. A. Chin. "Transition to Hot Quark Matter in Relativistic Heavy Ion Collision". Phys. Lett. B 78 (1978) 552–555.

[19] **The DOE/NSF Nuclear Science Advisory Committee**, R. Tribble et al. "The Frontiers of Nuclear Science, A Long Range Plan". arXiv: `0809.3137 [nucl-ex]`.

[20] C. Nonaka and M. Asakawa. “Modeling a Realistic Dynamical Model for High Energy Heavy Ion Collisions”. PTEP 2012 (2012) 01A208.

[21] D. J. Schwarz. “The first second of the universe”. Annalen Phys. 12 (2003) 220–270.

[22] E. S. Fraga, A. Kurkela, and A. Vuorinen. “Interacting quark matter equation of state for compact stars”. Astrophys. J. 781 (2014) L25.

[23] J. Rafelski and B. Muller. “Strangeness Production in the Quark-Gluon Plasma”. Phys. Rev. Lett. 48 (1982) 1066.

[24] P. Koch, B. Muller, and J. Rafelski. “Strangeness in Relativistic Heavy Ion Collisions”. Phys. Rept. 142 (1986) 167–262.

[25] **WA97 Collaboration**, E. Andersen et al. “Strangeness enhancement at mid-rapidity in Pb Pb collisions at 158 AGeV/c”. Phys. Lett. B 449 (1999) 401–406.

[26] **STAR Collaboration**, B. Abelev et al. “Enhanced strange baryon production in Au+Au collisions compared to p+p at $\sqrt{s_{\mathrm{NN}}} = 200$ GeV”. Phys. Rev. C 77 (2008) 044908.

[27] **ALICE Collaboration**, B. Abelev et al. “K^0_S and Λ production in Pb-Pb collisions at $\sqrt{s_{\mathrm{NN}}} = 2.76$ TeV”. Phys. Rev. Lett. 111 (2013) 222301.

[28] **ALICE Collaboration**, B. Abelev et al. “Multi-strange baryon production at mid-rapidity in Pb-Pb collisions at $\sqrt{s_{\mathrm{NN}}} = 2.76$ TeV”. Phys. Lett. B 728 (2014) 216–227.

[29] T. Matsui and H. Satz. “J/Ψ Suppression by Quark-Gluon Plasma Formation”. Phys. Lett. B 178 (1986) 416–422.

[30] **NA50 Collaboration**, M. C. Abreu et al. “Evidence for deconfinement of quarks and gluons from the J/Ψ suppression pattern measured in Pb + Pb collisions at the CERN SPS”. Phys. Lett. B 477 (2000) 28–36.

[31] **PHENIX Collaboration**, A. Adare et al. “J/ψ Production vs Centrality, Transverse Momentum, and Rapidity in Au+Au Collisions at $\sqrt{s_{NN}} = 200$ GeV”. Phys. Rev. Lett. 98 (2007) 232301.

[32] **STAR Collaboration**, L. Adamczyk et al. “J/Ψ production at high transverse momenta in p+p and Au+Au collisions at $\sqrt{s_{NN}} = 200$ GeV”. Phys. Lett. B 722 (2013) 55–62.

[33] **ALICE Collaboration**, B. Abelev et al. “J/Ψ suppression at forward rapidity in Pb-Pb collisions at $\sqrt{s_{\mathrm{NN}}} = 2.76$ TeV”. Phys. Rev. Lett. 109 (2012) 072301.

[34] **CMS Collaboration**, S. Chatrchyan et al. “Suppression of non-prompt J/ψ, prompt J/ψ, and Y(1S) in PbPb collisions at $\sqrt{s_{NN}} = 2.76$ TeV”. JHEP 05 (2012) 063.

[35] R. L. Thews, M. Schroedter, and J. Rafelski. “Enhanced J/ψ production in deconfined quark matter”. Phys. Rev. C63 (2001) 054905.

[36] X. Zhao and R. Rapp. “Medium modifications and production of charmonia at LHC”. Nucl. Phys. A 859 (2011) 114–125.

[37] U. Heinz and M. Jacob. “Evidence for a New State of Matter: An Assessment of the Results from the CERN Lead Beam Programme”. 2000. URL: `http://newstate-matter.web.cern.ch/newstate-matter/Science.html`.

[38] **STAR Collaboration**, J. Adams et al. “Experimental and theoretical challenges in the search for the quark-gluon plasma: The STAR Collaboration’s critical assessment of the evidence from RHIC collisions”. Nucl. Phys. A 757 (2005) 102–183.

[39] **PHENIX Collaboration**, K. Adcox et al. “Formation of dense partonic matter in relativistic nucleus-nucleus collisions at RHIC: Experimental evaluation by the PHENIX Collaboration”. Nucl. Phys. A 757 (2005) 184–283.

[40] **ALICE Collaboration**, K. Aamodt et al. “Elliptic Flow of Charged Particles in Pb–Pb Collisions at $\sqrt{s_{\mathrm{NN}}} = 2.76$ TeV”. Phys. Rev. Lett. 105 (25 2010) 252302.

[41] **ALICE Collaboration**, K. Aamodt et al. “Two-pion Bose-Einstein correlations in central Pb–Pb collisions at $\sqrt{s_{\mathrm{NN}}} = 2.76$ TeV”. Phys. Lett. B 696 (2011) 328–337.

[42] **CMS Collaboration**, S. Chatrchyan et al. “Measurement of the elliptic anisotropy of charged particles produced in PbPb collisions at $\sqrt{s_{\mathrm{NN}}} = 2.76$ TeV”. Phys. Rev. C87 (1 2013) 014902.

[43] **ATLAS Collaboration**, G. Aad et al. “Measurement of the distributions of event-by-event flow harmonics in lead-lead collisions at $\sqrt{s_{\mathrm{NN}}} = 2.76$ TeV with the ATLAS detector at the LHC”. JHEP 1311 (2013) 183.

[44] D. d’Enterria. “Jet quenching”. Relativistic Heavy Ion Physics Chapter 6.2 (2010) 471. Ed. by R. Stock.

[45] **STAR Collaboration**, J. Adams et al. “Evidence from d + Au measurements for final state suppression of high-p_{T} hadrons in Au+Au collisions at RHIC”. Phys. Rev. Lett. 91 (2003) 072304.

[46] **STAR Collaboration**, J. Adams et al. “Transverse-momentum and collision-energy dependence of high-p_{T} hadron suppression in Au+Au collisions at ultrarelativistic energies”. Phys. Rev. Lett. 91 (17 2003) 172302.

[47] **PHENIX Collaboration**, S. S. Adler et al. “Suppressed π^0 production at large transverse momentum in central Au+Au collisions at $\sqrt{s_{\mathrm{NN}}} = 200$ GeV”. Phys. Rev. Lett. 91 (2003) 072301.

[48] **ALICE Collaboration**, K. Aamodt et al. "Suppression of charged particle production at large transverse momentum in central Pb–Pb collisions at $\sqrt{s_{\mathrm{NN}}} = 2.76$ TeV". Phys. Lett. B 696 (2011) 30.

[49] **CMS Collaboration**, S. Chatrchyan et al. "Dependence on pseudorapidity and centrality of charged hadron production in Pb–Pb collisions at a nucleon-nucleon centre-of-mass energy of 2.76 TeV". JHEP 1108 (2011) 141.

[50] **ATLAS Collaboration**, G. Aad et al. "Observation of a centrality-dependent dijet asymmetry in Pb–Pb collisions at $\sqrt{s_{\mathrm{NN}}} = 2.76$ TeV with the ATLAS Detector at the LHC". Phys. Rev. Lett. 105 (2010) 252303.

[51] **CMS Collaboration**, S. Chatrchyan et al. "Observation and studies of jet quenching in Pb–Pb collisions at $\sqrt{s_{\mathrm{NN}}} = 2.76$ TeV". Phys. Rev. C84 (2 2011) 024906.

[52] **CMS Collaboration**, S. Chatrchyan et al. "Studies of jet quenching using isolated-photon+jet correlations in Pb–Pb and pp collisions at $\sqrt{s_{\mathrm{NN}}} = 2.76$ TeV". Phys. Lett. B 718 (2013) 773–794.

[53] **CMS Collaboration**, S. Chatrchyan et al. "Measurement of jet fragmentation into charged particles in pp and Pb–Pb collisions at $\sqrt{s_{NN}} = 2.76$ TeV". JHEP 1210 (2012) 087.

[54] **CMS Collaboration**, S. Chatrchyan et al. "Modification of jet shapes in PbPb collisions at $\sqrt{s_{NN}} = 2.76$ TeV". Phys. Lett. B 730 (2014) 243–263.

[55] H. A. Andrews et al. "Novel tools and observables for jet physics in heavy-ion collisions". arXiv: `1808.03689 [hep-ph]`.

[56] O. S. Bruning et al. "LHC Design Report Vol.1: The LHC Main Ring". URL: `https://cds.cern.ch/record/782076`.

[57] O. Bruning et al. "LHC Design Report Vol.2: The LHC infrastructure and general services". URL: `https://cds.cern.ch/record/815187`.

[58] M. Benedikt et al. “LHC Design Report Vol.3: The LHC injector chain”. URL: `https://cds.cern.ch/record/823808`.

[59] **ALICE Collaboration**, K. Aamodt and other. “The ALICE experiment at the CERN LHC”. JINST 3 (2008) S08002.

[60] **ATLAS Collaboration**, G. Aad et al. “The ATLAS Experiment at the CERN Large Hadron Collider”. JINST 3 (2008) S08003.

[61] **CMS Collaboration**, S. Chatrchyan et al. “The CMS Experiment at the CERN LHC”. JINST 3 (2008) S08004.

[62] **LHCb Collaboration**, A. A. Alves Jr. et al. “The LHCb Detector at the LHC”. JINST 3 (2008) S08005.

[63] S. Myers. “The Large Hadron Collider 2008-2013”. Int. J. Mod. Phys. A28 (2013) 1330035.

[64] **ALICE Collaboration**, B. Abelev et al. “Performance of the ALICE Experiment at the CERN LHC”. Int. J. Mod. Phys. A29 (2014) 1430044.

[65] **ALICE Collaboration**, K. Aamodt et al. “Alignment of the ALICE Inner Tracking System with cosmic-ray tracks”. JINST 5 (2010) P03003.

[66] **ALICE Collaboration**, B. Abelev et al. “Upgrade of the ALICE Time Projection Chamber”. Tech. rep. CERN-LHCC-2013-020. ALICE-TDR-016. CERN, 2014. URL: `https://cds.cern.ch/record/1622286`.

[67] **Particle Data Group Collaboration**, M. Tanabashi et al. “Review of Particle Physics”. Phys. Rev. D98 (2018) 030001.

[68] **ALICE Collaboration**, J. Adam et al. “Production of light nuclei and anti-nuclei in pp and Pb-Pb collisions at energies available at the CERN Large Hadron Collider”. Phys. Rev. C93 (2016) 024917.

[69] **ALICE Collaboration**, B. Abelev et al. “Production of charged pions, kaons and protons at large transverse momenta in pp and Pb–Pb collisions at $\sqrt{s_{\mathrm{NN}}}$ =2.76 TeV”. Phys. Lett. B 736 (2014) 196–207.

[70] **ALICE Collaboration**, J. Adam et al. “Determination of the event collision time with the ALICE detector at the LHC”. Eur. Phys. J. Plus 132 (2017) 99.

[71] **ALICE Collaboration**, J. Adam et al. “Measurement of pion, kaon and proton production in proton–proton collisions at $\sqrt{s} = 7$ TeV”. Eur. Phys. J. C 75 (2015) 226.

[72] **ALICE EMCal Collaboration**, U. Abeysekara et al. “ALICE EMCal Physics Performance Report”. Tech. rep. CERN, 2010.

[73] M. Cacciari, M. L. Mangano, and P. Nason. “Gluon PDF constraints from the ratio of forward heavy-quark production at the LHC at $\sqrt{s} = 7$ and 13 TeV”. The European Physical Journal C 75 (2015) 1–20.

[74] Y. Dokshitzer and D. Kharzeev. “Heavy-quark colorimetry of QCD matter”. Phys. Lett. B 519 (2001) 199–206.

[75] S. Batsouli et al. “Does the charm flow at RHIC?”. Phys. Lett. B 557 (2003) 26–32.

[76] V. Greco, C. M. Ko, and R. Rapp. “Quark coalescence for charmed mesons in ultrarelativistic heavy ion collisions”. Phys. Lett. B 595 (2004) 202–208.

[77] M. Djordjevic et al. “Influence of bottom quark jet quenching on single electron tomography of Au + Au”. Phys. Lett. B 632 (2006) 81–86.

[78] N. Armesto et al. “How sensitive are high-p_{T} electron spectra at RHIC to heavy quark energy loss?”. Phys. Lett. B 637 (2006) 362–366.

[79] **PHENIX Collaboration**, S. Adler et al. “Nuclear modification of electron spectra and implications for heavy quark energy loss in Au+Au collisions at $\sqrt{s_{\rm NN}} = 200$ GeV”. Phys. Rev. Lett. 96 (2006) 032301.

[80] **STAR Collaboration**, B. Abelev et al. “Transverse momentum and centrality dependence of high-$p_{\rm T}$ non-photonic electron suppression in Au+Au collisions at $\sqrt{s_{\rm NN}} = 200\,$GeV”. Phys. Rev. Lett. 98 (2007) 192301.

[81] **PHENIX Collaboration**, A. Adare et al. “Energy Loss and Flow of Heavy Quarks in Au+Au Collisions at $\sqrt{s_{\rm NN}} = 200$ GeV”. Phys. Rev. Lett. 98 (2007) 172301.

[82] **ALICE Collaboration**, B. Abelev et al. “Suppression of high transverse momentum D mesons in central Pb–Pb collisions at $\sqrt{s_{\rm NN}} = 2.76$ TeV”. JHEP 09 (2012) 112.

[83] **ALICE Collaboration**, J. Adam et al. “Centrality dependence of high-$p_{\rm T}$ D meson suppression in Pb–Pb collisions at $\sqrt{s_{\rm NN}} = 2.76$ TeV”. JHEP 11 (2015) 205.

[84] **ALICE Collaboration**, J. Adam et al. “Transverse momentum dependence of D-meson production in Pb–Pb collisions at $\sqrt{s_{\rm NN}} = 2.76$TeV”. JHEP 2016 (2016) 1–43.

[85] **ALICE Collaboration**, J. Adam et al. “Measurement of electrons from beauty-hadron decays in p-Pb collisions at $\sqrt{s_{\rm NN}} = 5.02$ TeV and Pb-Pb collisions at $\sqrt{s_{\rm NN}} = 2.76$ TeV”. JHEP 07 (2017) 052.

[86] **CMS Collaboration**, V. Khachatryan et al. “Suppression and azimuthal anisotropy of prompt and nonprompt J/Ψ production in PbPb collisions at $\sqrt{s_{_{\rm NN}}} = 2.76$ TeV”. Eur. Phys. J. C 77 (2017) 252.

[87] **CMS Collaboration**, A. M. Sirunyan et al. “Nuclear modification factor of D^0 mesons in PbPb collisions at $\sqrt{s_{NN}} = 5.02$ TeV”. Phys. Lett. B 782 (2018) 474–496.

[88] **ALICE Collaboration**, B. Abelev et al. “Azimuthal anisotropy of D meson production in Pb-Pb collisions at $\sqrt{s_{NN}} = 2.76$ TeV”. Phys. Rev. C90 (2014) 034904.

[89] **ALICE Collaboration**, S. Acharya et al. “D-meson azimuthal anisotropy in midcentral Pb-Pb collisions at $\sqrt{s_{NN}} = 5.02$ TeV”. Phys. Rev. Lett. 120 (2018) 102301.

[90] **CMS Collaboration**, A. M. Sirunyan et al. “Measurement of prompt D^0 meson azimuthal anisotropy in Pb-Pb collisions at $\sqrt{s_{NN}} = 5.02$ TeV”. Phys. Rev. Lett. 120 (2018) 202301.

[91] P. B. Gossiaux et al. “Competition of Heavy Quark Radiative and Collisional Energy Loss in Deconfined Matter”. J. Phys. G 37 (2010) 094019.

[92] J. Uphoff et al. “Elliptic Flow and Energy Loss of Heavy Quarks in Ultra-Relativistic heavy Ion Collisions”. Phys. Rev. C 84 (2011) 024908.

[93] S. K. Das et al. “Heavy-flavor in-medium momentum evolution: Langevin versus Boltzmann approach”. Phys. Rev. C90 (2014) 044901.

[94] J. Uphoff et al. “Elliptic flow and nuclear modification factor in ultrarelativistic heavy-ion collisions within a partonic transport model”. Phys. Rev. Lett. 114 (2015) 112301.

[95] **CMS Collaboration**, S. Chatrchyan et al. “Observation of long-range near-side angular correlations in proton-lead collisions at the LHC”. Phys. Lett. B 718 (2013) 795–814.

[96] **ALICE Collaboration**, B. Abelev et al. “Long-range angular correlations on the near and away side in p-Pb collisions at $\sqrt{s_{\mathrm{NN}}} = 5.02$ TeV”. Phys. Lett. B 719 (2013) 29–41.

[97] **ATLAS Collaboration**, G. Aad et al. “Observation of Associated Near-Side and Away-Side Long-Range Correlations in $\sqrt{s_{\mathrm{NN}}}$=5.02 TeV Proton-Lead Collisions with the ATLAS Detector”. Phys. Rev. Lett. 110 (2013) 182302.

[98] **ATLAS Collaboration**, G. Aad et al. “Observation of Long-Range Elliptic Azimuthal Anisotropies in $\sqrt{s}$ =13 and 2.76 TeV pp Collisions with the ATLAS Detector”. Phys. Rev. Lett. 116 (2016) 172301.

[99] **CMS Collaboration**, V. Khachatryan et al. “Measurement of long-range near-side two-particle angular correlations in pp collisions at $\sqrt{s}$ =13 TeV”. Phys. Rev. Lett. 116 (2016) 172302.

[100] **ALICE Collaboration**, J. Adam et al. “Enhanced production of multi-strange hadrons in high-multiplicity proton-proton collisions”. Nature Phys. 13 (2017) 535–539.

[101] **ATLAS Collaboration**, “D-meson production and long-range azimuthal correlation in 8.16 TeV p+Pb collisions with ATLAS”. Tech. rep. CERN, 2017. URL: `https://cds.cern.ch/record/2285811`.

[102] **ALICE Collaboration**, S. Acharya et al. “Azimuthal anisotropy of heavy-flavour decay electrons in p-Pb collisions at $\sqrt{s_{\mathrm{NN}}} = 5.02$ TeV”. arXiv: `1805.04367 [nucl-ex]`.

[103] **ALICE Collaboration**, B. Abelev et al. “Measurement of Prompt D-Meson Production in p–Pb Collisions at $\sqrt{s_{\mathrm{NN}}} = 5.02$ TeV”. Phys. Rev. Lett. 113 (23 2014) 232301.

[104] **ALICE Collaboration**, J. Adam et al. "Measurement of charm and beauty production at central rapidity versus charged-particle multiplicity in proton-proton collisions at $\sqrt{s} = 7$ TeV". JHEP 2015 (2015) 1–46.

[105] **ALICE Collaboration**, J. Adam et al. "Measurement of electrons from heavy-flavour hadron decays in p-Pb collisions at $\sqrt{s_{\mathrm{NN}}} = 5.02$ TeV". Phys. Lett. B 754 (2016) 81–93.

[106] **ALICE Collaboration**, J. Adam et al. "D-meson production in p–Pb collisions at $\sqrt{s_{\mathrm{NN}}}$ =5.02 TeV and in pp collisions at $\sqrt{s}$ =7 TeV". Phys. Rev. C94 (2016) 054908.

[107] **ALICE Collaboration**, J. Adam et al. "Measurement of D-meson production versus multiplicity in p-Pb collisions at $\sqrt{s_{\mathrm{NN}}} = 5.02$ TeV". JHEP 08 (2016) 078.

[108] R. Gauld et al. "Charm production in the forward region: constraints on the small-x gluon and backgrounds for neutrino astronomy". arXiv: `1506.08025 [hep-ph]`.

[109] A. Bhattacharya et al. "Perturbative charm production and the prompt atmospheric neutrino flux in light of RHIC and LHC". JHEP 6 (2015) 1–19.

[110] **CDF Collaboration**, D. Acosta et al. "Measurement of prompt charm meson production cross sections in $p\bar{p}$ collisions at $\sqrt{s} = 1.96$ TeV". Phys. Rev. Lett. 91 (2003) 241804.

[111] **STAR Collaboration**, L. Adamczyk et al. "Measurements of D^0 and D^{*+} production in pp Collisions at $\sqrt{s} = 200$ GeV". Phys. Rev. D86 (2012) 072013.

[112] **ALICE Collaboration**, B. Abelev et al. "Measurement of charm production at central rapidity in proton-proton collisions at $\sqrt{s} = 7$ TeV". JHEP 2012 (2012) 1–30.

[113] **ALICE Collaboration**, B. Abelev et al. “$\mathrm{D_s}$ meson production at central rapidity in proton–proton collisions at $\sqrt{s} = 7$ TeV”. Phys. Lett. B 718 (2012) 279–294.

[114] **ATLAS Collaboration**, G. Aad et al. “Measurement of $\mathrm{D}^{*\pm}$, $\mathrm{D}^{\pm}$ and $\mathrm{D}_\mathrm{s}^{\pm}$ meson production cross sections in pp collisions at $\sqrt{s} = 7$ TeV with the ATLAS detector”. Nucl. Phys. B 907 (2016) 717–763.

[115] **ALICE Collaboration**, S. Acharya et al. “Measurement of D-meson production at mid-rapidity in pp collisions at $\sqrt{s} = 7$ TeV”. Eur. Phys. J. C 77 (2017) 550.

[116] **LHCb Collaboration**, R. Aaij et al. “Prompt charm production in pp collisions at $\sqrt{s} = 7$ TeV”. Nucl. Phys. B 871 (2013) 1–20.

[117] **LHCb Collaboration**, R. Aaij et al. “Measurements of prompt charm production cross-sections in pp collisions at $\sqrt{s} = 13$ TeV”. JHEP 03 (2016) 159.

[118] **LHCb Collaboration**, R. Aaij et al. “Measurements of prompt charm production cross-sections in pp collisions at $\sqrt{s} = 5$ TeV”. JHEP 06 (2017) 147.

[119] D. d’Enterria et al. “Confronting current NLO parton fragmentation functions with inclusive charged-particle spectra at hadron colliders”. Nucl. Phys. B 883 (2014) 615.

[120] **CDF Collaboration**, F. Abe et al. “Measurement of D^* production in jets from $\mathrm{p\overline{p}}$ collisions at $\sqrt{s} = 1.8$ TeV”. Phys. Rev. Lett. 64 (4 1990) 348–352.

[121] **UA1 Collaboration**, C. Albajar et al. “A study of the D^* content of jets at the CERN pp collider”. Phys. Lett. B 244 (1990) 566.

[122] **STAR Collaboration**, B. Abelev et al. “Measurement of D^* mesons in jets from pp collisions at $\sqrt{s} = 200$ GeV”. Phys. Rev. D 79 (2009) 112006.

[123] T. Sjöstrand, S. Mrenna, and P. Skands. "PYTHIA 6.4 physics and manual". JHEP 5 (2006) 1.

[124] **PHENIX Collaboration**, C. Aidala et al. "Correlations of $\mu\mu$, $e\mu$, and ee pairs in pp collisions at $\sqrt{s} = 200$ GeV and implications for $\mathrm{c\bar{c}}$ and $\mathrm{b\bar{b}}$ production mechanisms". Submitted to: Phys. Rev. Lett. (2018).

[125] **CMS Collaboration**, V. Khachatryan et al. "Measurement of $\mathrm{B\bar{B}}$ angular correlations based on secondary vertex reconstruction at $\sqrt{s} = 7\,\mathrm{TeV}$". JHEP 3 (2011) 136.

[126] **ATLAS Collaboration**, G. Aad et al. "Measurement of $\mathrm{D}^{*\pm}$ meson production in jets from pp collisions at $\sqrt{s} = 7\,\mathrm{TeV}$ with the ATLAS detector". Phys. Rev. D 85 (2012) 052005.

[127] G. Corcella et al. "HERWIG 6: An Event generator for hadron emission reactions with interfering gluons (including supersymmetric processes)". JHEP 01 (2001) 010.

[128] G. Corcella et al. "HERWIG 6.5 Release Note". arXiv: `0210213 [hep-ph]`.

[129] P. Nason. "A new method for combining NLO QCD with shower Monte Carlo algorithms". JHEP 11 (2004) 040.

[130] S. Frixione, P. Nason, and C. Oleari. "Matching NLO QCD computations with Parton Shower simulations: the POWHEG method". JHEP 11 (2007) 070.

[131] S. Alioli et al. "A general framework for implementing NLO calculations in shower Monte Carlo programs: the POWHEG BOX". JHEP 2010 (2010) 1–58.

[132] S. Alioli et al. "Jet pair production in POWHEG". JHEP 04 (2011) 081.

[133] R. Thorne and R. Roberts. “A variable flavour number scheme for charged current heavy flavour structure functions”. The European Physical Journal C 19 (2001) 339–349.

[134] D. P. Anderle et al. “Using hadron-in-jet data in a global analysis of D^* fragmentation functions”. Phys. Rev. D 96 (3 2017) 034028.

[135] H.-M. Chang et al. “Calculating Track-Based Observables for the LHC”. Phys. Rev. Lett. 111 (10 2013) 102002.

[136] **ATLAS Collaboration**, G. Aad et al. “Performance of the ATLAS Trigger System in 2010”. Eur. Phys. J. C 72 (2012) 1849.

[137] **ALICE Collaboration**, B. Abelev et al. “Measurement of inelastic, single- and double-diffraction cross sections in proton–proton collisions at the LHC with ALICE”. Eur. Phys. J. C 73 (2013) 2456.

[138] P. Z. Skands. “Tuning Monte Carlo Generators: The Perugia Tunes”. Phys. Rev. D82 (2010) 074018.

[139] S. van der Meer. “Calibration of the Effective Beam Height in the ISR”. Tech. rep. 1968. URL: `https://cdsweb.cern.ch/record/296752/files/196800064.pdf`.

[140] T. Sjostrand, S. Mrenna, and P. Z. Skands. “A Brief Introduction to PYTHIA 8.1”. Comput. Phys. Commun. 178 (2008) 852–867.

[141] R. Brun, F. Carminati, and S. Giani. “GEANT Detector Description and Simulation Tool”. Tech. rep. CERN, 1994. URL: `https://cds.cern.ch/record/1082634`.

[142] M. Cacciari, G. Salam, and G. Soyez. “The anti-k_T jet clustering algorithm”. JHEP 04 (2008) 063.

[143] **ALICE Collaboration**, P. Saiz et al. “AliEn - ALICE environment on the GRID”. Nucl. Instrum. Meth. A 502 (2003) 437–440.

[144] **ALICE Collaboration**, M. Zimmermann. “The ALICE analysis train system”. J. Phys. Conf. Ser. 608 (2015) 012019.

[145] “ROOT - A Data Analysis Framework”. URL: `https://root.cern.ch/`.

[146] “AliRoot git repository”. URL: `https://github.com/alisw/AliRoot`.

[147] “AliPhysics git repository”. URL: `https://github.com/alisw/AliPhysics`.

[148] M. Cacciari and G. P. Salam. “Dispelling the N^3 myth for the k_t jet-finder”. Phys. Lett. B 641 (2006) 57–61.

[149] M. Cacciari, G. P. Salam, and G. Soyez. “FastJet User Manual”. Eur. Phys. J. C 72 (2012) 1896.

[150] URL: `https://github.com/aiola/alice-yale-hfjet`.

[151] T. Adye. “Unfolding algorithms and tests using RooUnfold”. arXiv: `1105.1160 [physics.data-an]`.

[152] R. Fruhwirth. “Application of Kalman filtering to track and vertex fitting”. Nucl. Instrum. Meth. A 262 (1987) 444–450.

[153] **ALICE Collaboration**, B. Abelev et al. “Measurement of the inclusive differential jet cross section in pp collisions at $\sqrt{s} = 2.76$ TeV”. Phys. Lett. B 722 (2013) 262.

[154] **ALICE Collaboration**, B. Abelev et al. “Charged jet cross sections and properties in proton–proton collisions at $\sqrt{s} = 7\,\mathrm{TeV}$”. Phys. Rev. D91 (11 2015) 112012.

[155] **ALICE Collaboration**, B. Abelev et al. “Measurement of charged jet suppression in Pb–Pb collisions at $\sqrt{s_{\mathrm{NN}}} = 2.76$ TeV”. JHEP 1403 (2014) 013.

[156] **ALICE Collaboration**, J. Adam et al. "Measurement of jet suppression in central Pb–Pb collisions at $\sqrt{s_{\mathrm{NN}}} = 2.76$ TeV". Phys. Lett. B 746 (2015) 1–14.

[157] **CDF Collaboration**, D. Acosta et al. "Heavy flavor properties of jets produced in $\mathrm{p\overline{p}}$ interactions at $\sqrt{s} = 1.8$TeV". Phys. Rev. D69 (7 2004) 072004.

[158] **ALICE Collaboration**, B. Abelev et al. "Technical Design Report for the Upgrade of the ALICE Inner Tracking System". J. Phys. G 41 (2014) 087002.

[159] S. Frixione, G. Ridolfi, and P. Nason. "A positive-weight next-to-leading-order Monte Carlo for heavy flavour hadroproduction". JHEP 2007 (2007) 126.

[160] A. Buckley et al. "LHAPDF6: parton density access in the LHC precision era". The European Physical Journal C 75 (2015) 132.

[161] H.-L. Lai et al. "New parton distributions for collider physics". Phys. Rev. D 82 (2010) 074024.

[162] D. J. Lange. "The EvtGen particle decay simulation package". Nucl. Instrum. Meth. A 462 (2001) 152–155.

[163] G. Cowan. "A Survey of Unfolding Methods for Particle Physics". *Proc. Advanced Statistical Techniques in Particle Physics*. Durham, 2002. URL: `http://www.ippp.dur.ac.uk/Workshops/02/statistics/proceedings/cowan.ps`.

[164] G. D'Agostini. "A multidimensional unfolding method based on Bayes' theorem". Nucl. Instrum. Meth. A 362 (1995) 487.

[165] G. D'Agostini. "Improved iterative Bayesian unfolding". arXiv: `1010.0632 [physics.data-an]`. URL: `http://inspirehep.net/record/1672893/files/1010.0632.pdf`.

[166] A. Hocker and V. Kartvelishvili. "SVD approach to data unfolding". Nucl. Instrum. Meth. A 372 (1996) 469–481.

[167] A. D. Martin et al. “Parton distributions for the LHC”. Eur. Phys. J. C 63 (2009) 189–285.

[168] M. L. Miller et al. “Glauber modeling in high energy nuclear collisions”. Ann. Rev. Nucl. Part. Sci. 57 (2007) 205–243.

[169] **ALICE Collaboration**, B. Abelev et al. “Centrality determination of Pb–Pb collisions at $\sqrt{s_{\mathrm{NN}}} = 2.76$ TeV with ALICE”. Phys. Rev. C88 (2013) 044909.

[170] X.-N. Wang and M. Gyulassy. “HIJING: A Monte Carlo model for multiple jet production in pp, pA and AA collisions”. Phys. Rev. D44 (1991) 3501–3516.

[171] M. Gyulassy and X.-N. Wang. “HIJING 1.0: A Monte Carlo program for parton and particle production in high-energy hadronic and nuclear collisions”. Comput. Phys. Commun. 83 (1994) 307.

[172] R. Kunnawalkam Elayavalli and K. C. Zapp. “Medium Recoils and background subtraction in JEWEL”. Nucl. Part. Phys. Proc. 289-290 (2017) 368–371.

[173] R. Kunnawalkam Elayavalli and K. C. Zapp. “Medium response in JEWEL and its impact on jet shape observables in heavy ion collisions”. JHEP 07 (2017) 141.

[174] M. Cacciari and G. P. Salam. “Pileup subtraction using jet areas”. Phys. Lett. B 659 (2008) 119–126.

[175] R. Ma. “Jet measurements in pp and Pb–Pb collisions in ALICE”. English. PhD thesis. 2014, 171. URL: `https://search.proquest.com/docview/1542099165`.

[176] V. Blobel. “Unfolding Methods in High-energy Physics Experiments”. *Proceedings, CERN School of Computing: Aiguablava, Spain, September 9-22 1984*. 1984. URL: `http://cds.cern.ch/record/161223`.

[177] T. Sjöstrand et al. "An Introduction to PYTHIA 8.2". Comput. Phys. Commun. 191 (2015) 159–177.

[178] B. Andersson et al. "Parton Fragmentation and String Dynamics". Phys. Rept. 97 (1983) 31–145.

[179] B. Andersson. "The Lund model". Camb. Monogr. Part. Phys. Nucl. Phys. Cosmol. 7 (1997) 1–471.

[180] P. Skands, S. Carrazza, and J. Rojo. "Tuning PYTHIA 8.1: the Monash 2013 Tune". Eur. Phys. J. C 74 (2014) 3024.

[181] **CTEQ Collaboration**, H. L. Lai et al. "Global QCD analysis of parton structure of the nucleon: CTEQ5 parton distributions". Eur. Phys. J. C 12 (2000) 375–392.

[182] **NNPDF Collaboration**, R. D. Ball et al. "Parton distributions with LHC data". Nucl. Phys. B 867 (2013) 244–289.

[183] M. R. Whalley, D. Bourilkov, and R. C. Group. "The Les Houches accord PDFs (LHAPDF) and LHAGLUE". arXiv: `hep-ph/0508110 [hep-ph]`.

[184] M. Bahr et al. "Herwig++ physics and manual". The European Physical Journal C 58 (2008) 639–707.

[185] J. Bellm et al. "Herwig 7.0/Herwig++ 3.0 release note". The European Physical Journal C 76 (2016) 196.

[186] **ALICE Collaboration**, S. Acharya et al. "Charged jet cross section and fragmentation in proton-proton collisions at $\sqrt{s} = 7$ TeV". Submitted to PRD (2018).

[187] **CMS Collaboration**, S. Chatrchyan et al. "Study of Z boson production in PbPb collisions at $\sqrt{s_{\mathrm{NN}}} = 2.76$ TeV". Phys. Rev. Lett. 106 (2011) 212301.

[188] **CMS Collaboration**, S. Chatrchyan et al. "Measurement of isolated photon production in pp and PbPb collisions at $\sqrt{s_{\mathrm{NN}}} = 2.76$ TeV". Phys. Lett. B 710 (2012) 256–277.

[189] **CMS Collaboration**, S. Chatrchyan et al. "Study of W boson production in PbPb and pp collisions at $\sqrt{s_{\mathrm{NN}}} = 2.76$ TeV". Phys. Lett. B 715 (2012) 66–87.

[190] **ATLAS Collaboration**, G. Aad et al. "Measurement of Z boson Production in Pb+Pb Collisions at $\sqrt{s_{\mathrm{NN}}} = 2.76$ TeV with the ATLAS Detector". Phys. Rev. Lett. 110 (2013) 022301.

[191] **ATLAS Collaboration**, G. Aad et al. "Centrality, rapidity and transverse momentum dependence of isolated prompt photon production in lead-lead collisions at $\sqrt{s_{\mathrm{NN}}} = 2.76$ TeV measured with the ATLAS detector". Phys. Rev. C93 (2016) 034914.

[192] **ALICE Collaboration**, B. Abelev et al. "Centrality Dependence of Charged Particle Production at Large Transverse Momentum in Pb–Pb Collisions at $\sqrt{s_{\mathrm{NN}}} = 2.76$ TeV". Phys. Lett. B 720 (2013) 52–62.

[193] **ATLAS Collaboration**, G. Aad et al. "Measurements of the Nuclear Modification Factor for Jets in Pb+Pb Collisions at $\sqrt{s_{\mathrm{NN}}} = 2.76$ TeV with the ATLAS Detector". Phys. Rev. Lett. 114 (2015) 072302.

[194] **CMS Collaboration**, V. Khachatryan et al. "Measurement of inclusive jet cross sections in pp and PbPb collisions at $\sqrt{s_{\mathrm{NN}}} = 2.76$ TeV". Phys. Rev. C 96 (2017) 015202.

[195] R. V. Gavai and R. Venugopalan. "Lattice computations of small x parton distributions in a model of parton densities in very large nuclei". Phys. Rev. D 54 (1996) 5795–5803.

[196] E. Iancu. “The colored glass condensate and extreme QCD”. arXiv: `hep-ph/0010317 [hep-ph]`.

[197] J. Bjoraker and R. Venugopalan. “From colored glass condensate to gluon plasma: Equilibration in high-energy heavy ion collisions”. Phys. Rev. C 63 (2001) 024609.

[198] F. Gelis et al. “The Color Glass Condensate”. Ann. Rev. Nucl. Part. Sci. 60 (2010) 463–489.

[199] **ALICE Collaboration**, J. Adam et al. “Measurement of charged jet production cross sections and nuclear modification in p–Pb collisions at $\sqrt{s_{\mathrm{NN}}} = 5.02$ TeV”. Phys. Lett. B 749 (2015) 68–81.

[200] T. Renk. “Physics probed by the P_T dependence of the nuclear suppression factor”. Phys. Rev. C 88 (2013) 014905.

[201] K. C. Zapp, F. Krauss, and U. A. Wiedemann. “A perturbative framework for jet quenching”. JHEP 03 (2013) 080.

[202] **CMS Collaboration**, S. Chatrchyan et al. “Study of high-p_{T} charged particle suppression in PbPb compared to pp collisions at $\sqrt{s_{\mathrm{NN}}} = 2.76$ TeV”. The European Physical Journal C 72 (3 2012) 1–22.

[203] T. Renk. “Parton shower evolution in a 3-d hydrodynamical medium”. Phys. Rev. C 78 (2008) 034908.

[204] T. Renk. “A Comparison study of medium-modified QCD shower evolution scenarios”. Phys. Rev. C 79 (2009) 054906.

[205] **ALICE Collaboration**, B. Abelev et al. “Upgrade of the ALICE Experiment: Letter Of Intent”. J. Phys. G 41 (2014) 087001.

[206] **ALICE Collaboration**, J. Adam et al. "Addendum to the Technical Design Report for the Upgrade of the ALICE Time Projection Chamber". Tech. rep. CERN-LHCC-2015-002. ALICE-TDR-016-ADD-1. CERN, 2015. URL: http://cds.cern.ch/record/1984329.

[207] P. Colas, I. Giomataris, and V. Lepeltier. "Ion backflow in the Micromegas TPC for the future linear collider". Nucl. Instrum. Meth. A 535 (2004) 226–230.

[208] F. Sauli, L. Ropelewski, and P. Everaerts. "Ion feedback suppression in time projection chambers". Nucl. Instrum. Meth. A 560 (2006) 269–277.

[209] **ALICE TPC Collaboration**, M. M. Aggarwal et al. "Particle identification studies with a full-size 4-GEM prototype for the ALICE TPC upgrade". Nucl. Instrum. Meth. A 903 (2018) 215–223.

[210] S. Aiola et al. "Combination of two Gas Electron Multipliers and a Micromegas as gain elements for a time projection chamber". Nucl. Instrum. Meth. A 834 (2016) 149–157.

[211] F. Sauli. "GEM: A new concept for electron amplification in gas detectors". Nucl. Instrum. Meth. A 386 (1997) 531–534.

[212] Y. Giomataris et al. "MICROMEGAS: A High granularity position sensitive gaseous detector for high particle flux environments". Nucl. Instrum. Meth. A 376 (1996) 29–35.

[213] M. Ball et al. "Technical Design Study for the PANDA Time Projection Chamber". arXiv: 1207.0013 [physics.ins-det].

[214] URL: https://en.wikipedia.org/wiki/MicroMegas_detector.

[215] G. Hanson et al. "Evidence for Jet Structure in Hadron Production by e^+e^- Annihilation". Phys. Rev. Lett. 35 (1975) 1609–1612.

[216] G. Sterman and S. Weinberg. "Jets from Quantum Chromodynamics". Phys. Rev. Lett. 39 (23 1977) 1436–1439. URL: http://link.aps.org/doi/10.1103/PhysRevLett.39.1436.

[217] G. C. Blazey and B. L. Flaugher. "Inclusive Jet and Dijet Production at the Tevatron". Ann. Rev. Nucl. Part. Sci. 49 (1999) 633.

[218] G. C. Blazey et al. "Run II jet physics". *QCD and weak boson physics in Run II. Proceedings, Batavia, USA, March 4-6, June 3-4, November 4-6, 1999*. 2000, 47–77. URL: http://lss.fnal.gov/cgi-bin/find_paper.pl?conf-00-092.

[219] G. P. Salam and G. Soyez. "A Practical Seedless Infrared-Safe Cone jet algorithm". JHEP 05 (2007) 086.

[220] Bartel et al. "Experimental studies on multijet production in e^+e^- annihilation at PETRA energies". English . Zeitschrift für Physik C Particles and Fields 33 (1 1986) 23–31.

[221] Y. L. Dokshitzer et al. "Better jet clustering algorithms". JHEP 08 (1997) 001.

[222] S. D. Ellis and D. E. Soper. "Successive combination jet algorithm for hadron collisions". Phys. Rev. D48 (1993) 3160–3166.

[223] M. Cacciari, G. P. Salam, and G. Soyez. "The Catchment Area of Jets". JHEP 04 (2008) 005.